# Polymer Solutions in Complex Flows:

# Fibrils, Filaments, and Flocs

A DISSERTATION

SUBMITTED TO THE FACULTY OF THE GRADUATE SCHOOL

OF THE UNIVERSITY OF MINNESOTA

BY

Athena Eugenia Metaxas

IN PARTIAL FULFILLMENT OF THE REQUIREMENTS

FOR THE DEGREE OF

DOCTOR OF PHILOSOPHY

Professor Cari S. Dutcher, *advisor*

August 2020

# Acknowledgements

It is said that it takes a village to raise a child, and I would argue that the same is true for writing and defending a dissertation. What follows is just a small list of folks who have helped me on this journey.

First, I would like to acknowledge my advisor, Cari Dutcher, who has guided me on my path to be a more competent and confident scientist. She took a chance on me, even though I did not come from an engineering background. She has allowed me relative freedom to explore my interests and work with others to accomplish my research goals. Additionally, I have become incredibly picky with presentations, and I can now see slight differences in font and formatting thanks to Cari. :) I would also like to thank my PhD Defense Committee: Prof. Lorraine Francis, Prof. Phil Buhlmann, and Prof. Michelle Calabrese.

Next, I would like to thank all the people with whom I have had the privilege to work together. A big thanks is in order to the Dutcher group, both past and present: Andrew Metcalf, Archit Dani, Hallie Boyer, Nick Wilkinson, Lucy Nandy, Ellie Raethke, Yun Chen, Ben Micklavzina, Shweta Narayan, Priyatanu Roy, Shihao Liu, Tom Neumiller, Vishal Panwar, Nikhil Sethia, Yaroslav Makhnenko, Maggie House, and Rana Bachnak. I would like to give special shoutouts to Nick, for taking me under his wing and making work enjoyable (even though he would make fun of me incessantly), and to Shweta, who became a good friend and someone to confide in during my time here (and who squeals over baby animals on Instagram with me). A huge thank you goes out to the undergraduate students I have worked with and had the honor of mentoring: Dion Casey, Patrick McCauley, Nancy Bautista, Ruth Olson, Clay Hansen, Ryan Bell, and Audrey Sebastian. I

have also been blessed to work with incredible peers and scientists at UMN, some of whom include the CaBER Crew (Prof. Sveta Morozova and Dr. Peter Schmidt), David Giles, Jim Marti, Dr. Javier Garcia Barriocanal, and Prof. Chris Macosko.

In addition to folks at UMN, I have been incredibly lucky to have mentors from undergrad and high school would laid the foundation for my graduate career. To Mrs. Lawrence, my AP Chemistry teacher, who recognized my inclination for science and pushed me to major in chemistry. To Prof. Stacia Rodenbusch, my first research mentor at UT Austin, who encouraged my choice to pursue research and for caring about the process just as much, if not more, than the results. To Prof. John Stanton, who listened to my worries about my future and suggested I change disciplines when applying to graduate school. To Dr. John Cort, whose egalitarian mentorship influenced my own mentoring style and whose support has continued past my time working at Pacific Northwest National Laboratory.

Finally, I would like to thank my family for keeping me somewhat sane by offering their endless love and support. To my little bro, Thanos, and my sis-in-law, Meredith, thank you for letting me incessantly complain to y'all and sending me pictures of my precious fur nephew, Beau. To my mother, Deena, and my father, Costas, for raising me to be the person I am today. You managed to create a successful life for yourselves as immigrants in this country, and your story continues to motivate me. Thank you for also sending me pictures of my precious fur baby, Haroula.

If there is one thing I will take away from this journey, it is that I am leaving with more questions unanswered than answered, and that is perfectly fine. To quote Plato's account of Socrates, "*Εν οίδα ότι ουδέν οίδα"* ("All I know is that I know nothing").

# Dedication

Για τους αγαπημένους μου γονείς. Αυτή η διατριβή είναι αφιερωμένη σε σας. Χωρίς την υπομονή σας, την υποστήριξή σας, και την αγάπη σας, δεν θα μπορούσα να την πετύχω.

# Abstract

The behavior of polymers in solution under complex physicochemical and hydrodynamic flow fields is of interest to a variety of industrial processes. Of particular interest here are applications which involve polymer-polymer or polymer-particulate interactions and assembly in flow, such as those found in polymer processing and water treatment, among others. In this thesis, two main areas are presented which examine polymer interactions under various physicochemical and flow conditions in aqueous environments: (1) self-association of polymer chains in flow (Chapters 2 and 3), resulting in the formation of fibrils and filaments and (2) association of polymer chains with suspended particulate (Chapters 4, 5, and 6), resulting in the formation of flocs. More detail on the types of processes where these flows occur and how the polymeric response and assembly can be probed are introduced in Chapter 1.

In the first area, the extensional properties of polymer methylcellulose (MC) solutions were characterized using Capillary Breakup Extensional Rheometry (CaBER), as described in Chapter 2. The addition of NaCl to MC solutions results in the formation of MC fibrils, which imparts elastic characteristics to the solution. The extensional relaxation time and extensional viscosity due to these fibrils were found to increase with increasing MC concentration. While the results presented in Chapter 2 represent the first sets of characterization of NaCl-induced fibril formation for MC solutions, a disadvantage of the CaBER approach is that its resolution is limited by solution viscosity. Therefore, in Chapter 3, a microfluidic filament stretching device was used to further characterize extensional

properties for lower molecular weight and lower viscosity MC solutions, where it was found that the extensional viscosity increased with increasing NaCl concentration.

In the second area, the flocculation of charged polymers with bentonite clay was studied in complex flow fields using jar tests and Taylor-Couette (TC) flows. The custom-built TC cell used in these studies is capable of radial injection of fluids into the gap between two concentric cylinders, thus allowing for introduction of the polymeric solutions into the particle-laden flow to investigate *in-situ* floc nucleation and growth. Chapter 4 discusses the effects of hydrodynamic flow states on flocculation in the TC cell, where faster floc growth rates and decreased 2-D perimeter-based fractal dimensions were observed for higher order flow states, indicating improved mass transfer of the polymer flocculant and shear rounding of the flocs, respectively. Chapter 5 builds on the work in Chapter 4 by investigating the effects of ionic strength and polyelectrolyte molecular weight on flocculation in the TC cell, where increasing charge screening from increasing ionic strength results in an interplay between initial bentonite aggregate size and ability for the polyelectrolyte to bridge multiple aggregates due to its decreasing persistence length. Finally, Chapter 6 investigates the effects of adding an additional organic component to the flocculation system, humic acid, using jar tests, where changes in solution pH results in competitive flocculation between the bentonite and the humic acid with the polyelectrolyte.

Overall, this thesis seeks to provide additional understanding of how polymers assemble in solution under a variety of physicochemical conditions and flow. Understanding the rheological behavior of associating polymer chains into fibrils due to changing solution conditions broadens their processing capabilities by understanding chain and fibril dynamics in solution. Likewise, consideration of physicochemical properties and flow parameters in the flocculation of a particulate-laden suspension with polyelectrolytes could aid in the improvement of process predictive capabilities and, ultimately, process performance in applications such as water treatment.

# Table of Contents

# List of Tables

# List of Figures

# Chapter 1
# Global Introduction

## *1.1. Motivation*

The behavior of soft materials, such as polymers and colloidal materials, under complex physicochemical and hydrodynamic flow conditions is of interest to a variety of processes, such as extrusion, coatings, printing, spraying, flocculation of particulate-laden systems, and many more.[1–7] While there are many combinations of variables that can be studied in a wide variety of systems, the focus on this thesis is on polymer assembly in solution at two different length scales. The first area examines the microscale extensional rheological behavior of methylcellulose solutions, whose chains associate with themselves to form structures known as fibrils in the presence of NaCl at room temperature. The extensional behavior of this class of polymers is not as well understood as its shear behavior is. Therefore, these studies open an already commercially relevant material to several other processes and continue to make the case that a thorough rheological characterization is necessary to predict and optimize processes. The second area examines the mesoscale flocculation behavior of polyelectrolytes, which are charged polymers, with suspended particulates under a variety of solution conditions using Taylor-Couette (TC) flows. The wide range of flow states accessible in a TC cell vary in both turbulent intensity and kinetic flow type (a measure of the degree of rotation, shear, and extension in the flow). Consideration of physicochemical properties and flow type parameters in the flocculation

can potentially improve process predictive capabilities and ultimately, process performance in drinking water treatment, which is a basic global need.

## *1.2. Extensional Rheology of Polymer Solutions*

### *1.2.1. Extensional Rheology Methods*

The two basic flows used to study rheological properties of materials are shear flow and extensional flow. In shear flow, adjacent layers of the fluid move parallel to each other at different speeds, resulting in a velocity gradient. In extensional flow, the velocity profile in a specific direction is independent of the other spatial dimensions in the system, and polymer chains and particles will align in the direction of the flow.[8] Just as shear viscosity can be measured for fluids, extensional viscosity can be measured as well. The Trouton ratio, which is the ratio of extensional viscosity to the shear viscosity, can be used to compare the extensional behavior to the shear behavior of a fluid. For Newtonian fluids, the Trouton ratio is 3 for axisymmetric elongation and 4 for planar elongation, whereas for non-Newtonian fluids, such as polymer melts and solutions, the Trouton ratio is anywhere from one to several orders of magnitude larger.[9,10]

In theory, it is easy to imagine how one would apply an extensional flow to a material, particularly a polymer melt, by "grabbing onto" the ends of a sample and pulling in a single direction. In practice, there have been many obstacles in developing methods to accurately measure extensional viscosity, largely due to challenges with generating a homogeneous extensional flow field. Even more challenging was method development for solution-based materials, which cannot be "grabbed onto" like a polymer melt. Fortunately, many advances have been made in developing both commercially available and laboratory-based methods that can reliably measure extensional properties of materials. The major methods are highlighted in **Figure 1.1** and are classified by the accessible shear and extensional viscosity ranges. Methods that can measure higher viscosity samples such as the Versatile Accurate Deformation Extensional Rheometer (VADER) or the Extensional Viscosity Fixture (EVF) for the ARES-G2 rheometer will not be discussed here as these methods work best for higher viscosity solutions (greater than 100 Pa·s) or polymer melts whereas the focus of this work is on lower viscosity polymer solutions.

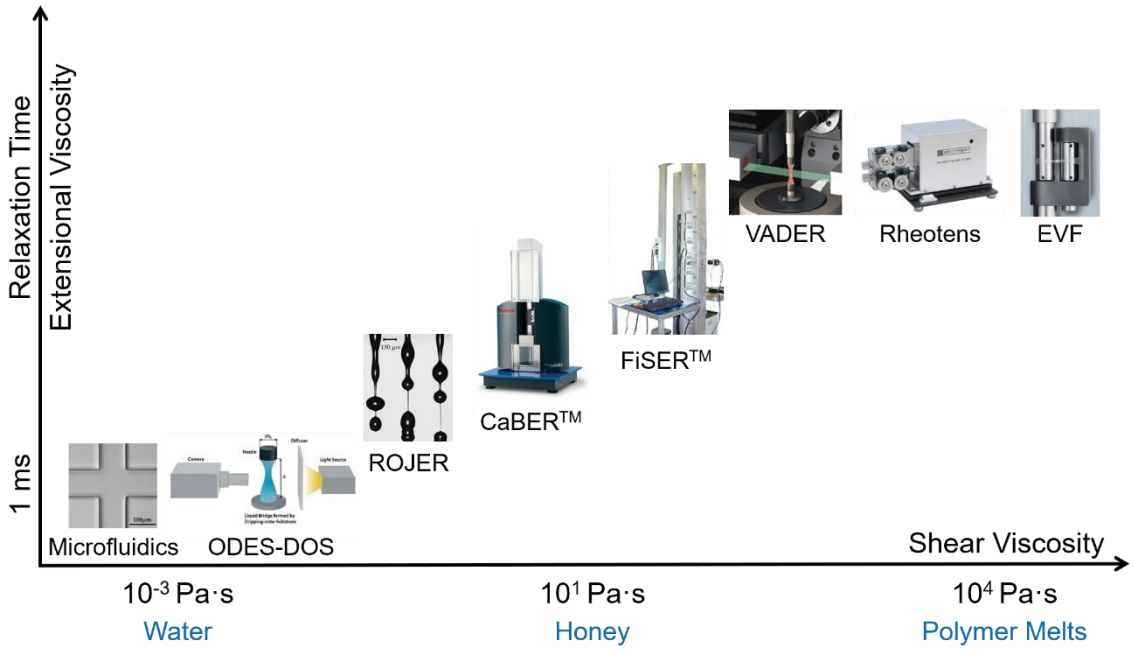


**Figure 1.1**: Extensional rheometry process window categorized by shear and extensional viscosity (or relaxation time in some cases). The microfluidic device featured here is an example of a cross-slot geometry. The Optically-Detected Elastocapillary Self-Thinning Dripping-onto-Substrate (ODES-DOS) extensional rheometer was developed by Sharma and colleagues.[11,12] The Rayleigh Ohnesorge Jetting Extensional Rheometer (ROJER) was developed by McKinley and colleagues.[13,14] The Capillary Breakup Extensional Rheometer (CaBER™) and the filament stretching extensional rheometer (FiSER™) were developed by the Cambridge Polymer Group (MA, USA) and commercialized by ThermoFisher Scientific (MA, USA) and the Cambridge Polymer Group, respectively. The Versatile Accurate Deformation Extensional Rheometer (VADER) was developed by Huang and colleagues[15,16] and commercialized by Rheo Filament (PA, USA and Copenhagen, Denmark). The Rheotens was commercialized by Göttfert (Buchen, Germany). The Extensional Viscosity Fixture (EVF) was commercialized by TA Instruments (DE, USA). Adapted by permission from Springer Nature Customer Service Centre GmBH: Springer, *Microfluidics and Nanofluidics*, *14*, Microdevices for extensional rheometry of low viscosity elastic liquids: a review, F. J. Galindo-Rosales and M. A. Alves, Copyright (2013).

One of the earlier methods developed to measure the extensional viscosity of polymer solutions is the Filament Stretching Extensional Rheometer (FiSER). The sample fluid is placed between two plates, and the top plate moves up with an exponentially increasing velocity with constant strain rate. This deformation forms a filament, and its diameter and applied force can be measured as a function of time and position.[17,18] The FiSER is appropriate to use for samples with shear viscosities between 1 – 1000 Pa·s. For

samples with shear viscosities between 0.01 – 10 Pa·s, the Capillary Breakup Extensional Rheometer (CaBER) can be used to measure extensional properties. In this apparatus, a step strain is imposed on a fluid sandwiched between two plates and the resulting filament self-thins due to capillary forces. The filament thinning progresses with an extensional strain rate dictated by the properties of the fluid. What is unique about CaBER is that unlike FiSER, it does not measure a force; rather, the information that is collected is the midpoint diameter of the thinning filament with time.[18,19]

While both FiSER and CaBER are both relatively easy methods to obtain extensional properties, such as extensional viscosity and extensional relaxation time, there are still some limitations to consider. It was already mentioned that FiSER cannot accurately measure fluids with viscosities below 1 Pa·s (and this is pushing the limitations of the instrument). Even CaBER, which is capable of measuring fluids with lower viscosities, can only reach a lower viscosity limit around 20 mPa·s and a lower relaxation time limit of 1 ms, although these values are close to the limitations of the instrument, hence there is some question on the reliability of the measurement at these viscosity limits. Furthermore, these two techniques cannot achieve high strain rates (*e.g.*, greater than 1000 $s^{-1}$), and there is some concern that chains fail to reach their full extension.[8,20] In addition to these limitations, inertial effects become increasingly difficult to ignore as solution viscosities decrease. The addition of high-speed cameras and the slow retraction method developed by Clasen *et al.*[21] have been shown to reliably push the limits of CaBER for lower viscosity solutions to avoid inertial effects. Even with continued improvement to CaBER to measure lower viscosity fluids, there are still concerns about distortion of the thinning filament due to gravitational effects.[8]

An alternative technique that addresses restrictions associated with inertial effects from CaBER is the Rayleigh Ohnesorge Jetting Extensional Rheometer (ROJER). This device uses stroboscopic imaging to measure thinning liquid bridges in a continuous jet without the use of a high-speed camera.[13,14] A disadvantage of this technique is that it is prone to frequent blockages in the nozzles used to jet the fluid. One study by Greiciunas *et al.*[22] utilized disposable needles in the nozzle design so that the needle can be replaced with another one should a blockage occur. Even with this improvement in the ROJER design,

the higher shear rates associated with fluid jetting could potentially preshear the fluid, thus altering the results. To mitigate the potential pitfalls of inertial effects by imposing a step-strain or preshear for lower viscosity solutions, a recent technique known as Optically-Detected Elastocapillary Self-Thinning Dripping-onto-Substrate (ODES-DOS) extensional rheometry was developed by Dinic *et al*.[11,12] For DOS experiments, a pre-determined volume of fluid is slowly deposited onto a substrate. The unstable liquid bridge that forms undergoes capillary-driven thinning recorded by a high-speed camera. This technique is capable of measuring extensional viscosities of low viscosity (shear viscosities < 20 mPa·s), low elasticity (relaxation times < 1 ms) fluids, which is nearly impossible to achieve using CaBER, as the fluid tends to pinch-off before the liquid bridge can be properly stretched.[21,23]

Another method that can measure the extensional properties of low viscosity, low relaxation fluids is microfluidics. One difference between DOS and microfluidics is that the viscoelastic behavior can be enhanced and higher strain rates can be imposed on the fluids due to the significantly decreased size of microfluidics[8,24–27]. There are several different geometries that can be used, such as cross-slot devices, hyperbolic contractions, and flow-focusing devices, which possess different ranges of accessible strains and strain rates. Measurements can either be made with high-speed cameras in two-phase systems (typically, a continuous, outer phase of oil or buffer is used, depending on the test fluid, and this is seen in flow-focusing and cross-slot devices) or by pressure drops across the channel (which is the case for hyperbolic contraction devices). Another advantage to using microfluidics is that they have high throughput that results in large datasets from relatively small sample volumes. In this thesis, CaBER was used to study the extensional behavior of higher viscosity methylcellulose solutions containing fibrils, while a flow-focusing microfluidic device was used to study their lower viscosity analogs.[28]

### *1.2.2. Methylcellulose Chemistry and Properties*

Methylcellulose (MC) is a methoxy-substituted cellulose ether derivative commonly used as a rheology modifier in a variety of food, pharmaceutical, and consumer products. The structure of MC is shown in **Figure 1.2**. For the commercial grade of MC used in this thesis, each anhydroglucose unit is substituted with a degree of substitution of

1.7 to 2.2 methoxy groups out of 3 hydroxyl groups. The partial substitution of the hydroxyl groups with methoxy groups disrupts the intra- and intermolecular hydrogen bonds, which renders MC soluble in water at temperatures below 50°C.[29]

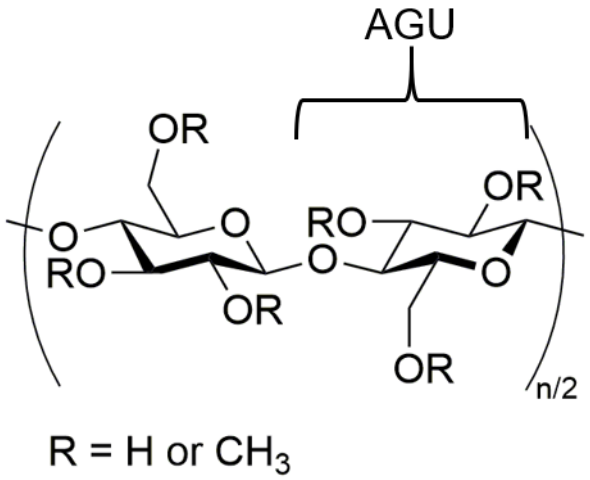


**Figure 1.2**: Chemical structure of methylcellulose (MC). The degree of substitution, *DS*, for each anhydroglucose (AGU) unit is between 1.7-2.2 for the commercial variant used in this thesis.

Arguably the most unique property of MC is that it can reversibly transition to a turbid hydrogel upon heating or upon the introduction of a salt, such as NaCl, into solution around room temperature.[30–33] There was much debate over the mechanism of gelation, where everything from micelle formation to crosslinking and finally, to trapped phase separation was proposed.[34–37] It was not until cryo-transmission electron microscopy (cryo-TEM) was used to directly visualize the gelled MC in combination with small angle X-ray and neutron scattering that the consensus for the cause of thermoreversible gelation was established.[32,33,38] The prevailing theory is that the MC chains associate into nanometer-scale structures known as fibrils, and this fibrillar network is thought to be responsible for the observed gelation. The shear rheological behavior of MC has been extensively studied, but the extensional rheological behavior was not reported prior to the studies discussed in this thesis.[39–41]

This concludes the background information for the first area of this thesis, where the aim is to study the extensional rheological behavior of a polymer, such as MC, that associates with itself, when the NaCl content of the solution is changed. The next and final

area of this thesis will look at studying the interactions of a polymer, such as a polyelectrolyte, with suspended particulates as a function of physicochemical and hydrodynamic properties.

## *1.3. Polymer-particle Flocculation in Flow*

### *1.3.1. Polyelectrolytes and Their Role in Flocculation*

Polyelectrolytes, which are water-soluble polymers with charged functional groups, are used in a variety of applications such as drag reduction, enhanced oil recovery (EOR), paper manufacturing, and both drinking- and waste-water treatment.[42–45] While flocculation is relevant in a variety of industries, this thesis will primarily focus on how the information developed from the studies impacts drinking water treatment applications. Polyelectrolytes are particularly useful for removal of nano- and microscale suspended charged contaminants by combining with these particulates to form mesoscale structures known as *flocs*. The resultant flocs can then be readily separated and removed from water through filtration or sedimentation. Compared to less-expensive mineral coagulants such as alum, smaller doses of polyelectrolyte are required to form both larger and breakage-resistant flocs, resulting in more efficient separation processes during water treatment.[44,46] Flocculation is critical in the water treatment process because potentially harmful contaminants, such as heavy metals, bacteria, and viruses, can adsorb to solid particulate and be removed from potable water.

Rapid floc growth is enabled by orthokinetic aggregation, where the particulates with adsorbed polyelectrolyte collide and grow due to the shear gradients present in the flow.[47–49] There are several different mechanisms for polymer-particle adsorption and flocculation events, including charge neutralization, polymer bridging, charge-patch flocculation, and polymer depletion.[50–53] A schematic of a generalized flocculation process and two of the primary mechanisms for polyelectrolyte-mediated flocculation is shown in **Figure 1.3**. The aqueous environment impacts the underlying flocculation mechanism through highly interrelated physicochemical properties including the suspension composition (pH, ionic strength, and salt valency),[54] coagulant type,[55,56] particle surface properties,[57] and the dosing and mixing conditions.[58–60] These complex interdependencies on the floc assembly kinetics and final floc microstructure are not well understood and can

result in poorly optimized polymeric dosing, which is one of the major technical issues in water treatment plant operations. Under-dosing results in insufficient particulate removal and over-dosing results in particulate re-stabilization, which is undesirable as it can be cost-prohibitive in water treatment (for reference, cationic flocculants cost roughly $3000 dollars per metric ton, which is not an insignificant cost).[44,46] Fragmented flocs from shear can be re-suspended and are often more difficult to remove than the initial particulate. For optimal separation, large, hydrodynamically robust flocs are desired to readily settle out under gravity, as well as withstand turbulent stresses in the flow with little to no fragmentation.[61,62]

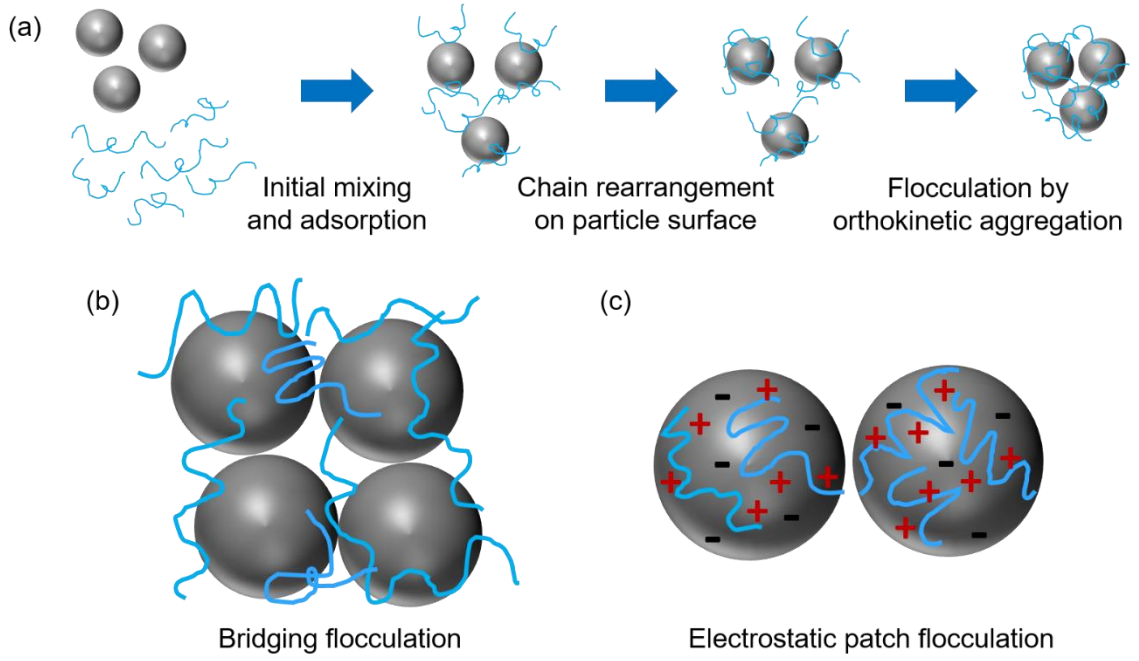


**Figure 1.3**: (a) A schematic of a generalized flocculation process where the gray spheres represent solid particulate and the blue chains represent free polyelectrolyte in solution. (b) A schematic of bridging flocculation, where free end segments of polyelectrolyte already adsorbed to particulate can adsorb to others, thus "bridging" the particles, and (c) a schematic of electrostatic patch flocculation, where there are localized regions of opposing charges on the surface that allow for the particles to attach to each other.

### *1.3.2. Particulate Systems*

Surface waters contain a variety of particulates such as clays, organic materials, salts, heavy metals, and living organisms. Studying the interactions between all these

particulates is nontrivial, therefore model systems of NaCl, humic acid, and bentonite will be used to isolate key solute interactions. Bentonite is an anisotropic smectite clay commonly found in surface waters with a high adsorption capacity for water and has been used in other flocculation studies.[7,63–65] The general chemical formula for bentonite is $Na_{0.7}Al_{3.3}Mg_{0.7}Si_8O_{20}(OH)_4 \bullet nH_2O$ and individual bentonite particles can be visualized as thin sheets composed of an octahedral layer of aluminum, magnesium, or iron oxide sandwiched between two tetrahedral layers of silicon oxide, $(SiO_4)^{4-}$ as shown in **Figure 1.4**.[66] Within a bentonite sheet, $Al^{3+}$ can substitute for $Si^{4+}$ in the tetrahedral layer and $Mg^{2+}$ can substitute for $Al^{3+}$ in the octahedral layer, creating a permanent negative charge on the faces, with counter-ions intercalated between the bentonite sheets.[66,67]

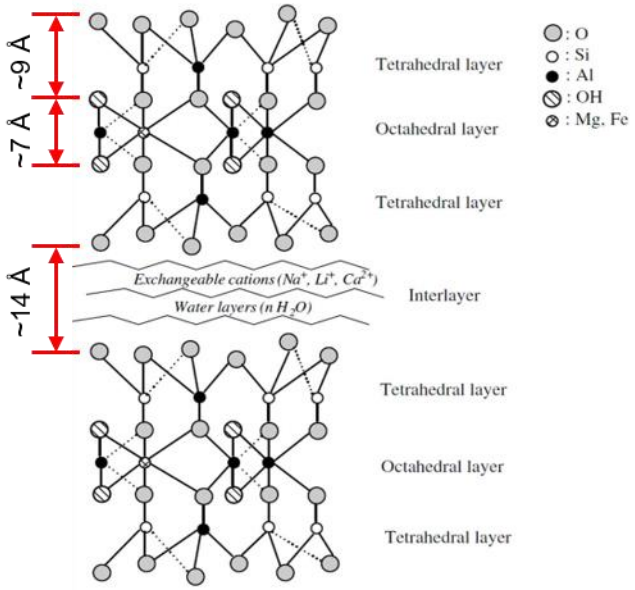


**Figure 1.4**: A schematic of the molecular structure of bentonite. Reprinted from *Microporous and Mesoporous Materials*, *33*, O. Duman and S. Tunç, Electrokinetic and rheological properties of Na-bentonite in some electrolyte solutions, 331-338, Copyright (2009), with permission from Elsevier.

The edges of the bentonite sheets have pH-sensitive hydroxyl groups, which are positively charged at lower solution pH (pH < 6) and negatively charged at higher solution pH (pH > 8).[68,69] As a result, bentonite sheets can be arranged in a porous, edge-face arrangement, an edge-edge arrangement, or ultimately a dense, face-face structure.[70,71] Generally, all three of these interactions occur within a bentonite aggregate. Scanning

electron microscopy studies have also shown that with increasing ionic strength, bentonite structure changes from a more porous, edge-face arrangement to a much denser, face-face arrangement.[71,72] These variations in aggregate surface morphology more than likely result in different polyelectrolyte adsorption capacities and interaction potentials due to the uneven charge distribution of the functional edge groups.[73]

In addition to inorganic particulates such as bentonite, organic humic substances (HS) such as humic acid from biodegradation of organic matter are widely present in aquatic systems and may interact with the bentonite particles to modify polyelectrolyte adsorption to the clay.[74,75] Removing HS from source waters via flocculation is a non-trivial process as the HS need to be converted from a soluble form to an insoluble form. Adsorption of HS onto the clay is highly dependent on solution conditions, and generally proceeds via ion exchange and surface complexation mechanisms.[75–77] Addition of cationic polyelectrolytes only partially removes HS from surface waters, but the presence of suspended solids such as bentonite has shown increased removal from water.[74] Removal of HS is critical to the health and safety of human populations because improper removal prior to the chlorination step of the water treatment process could potentially result in the reaction of HS with chlorination chemicals to form toxic byproducts.[78,79]

### *1.3.3. Methods for Studying Floc Properties as a Function of Mixing Hydrodynamics*

To further complicate matters, the effects of local hydrodynamic conditions on flocculation performance, flocculation mechanism, polyelectrolyte-particle assembly kinetics, and final floc microstructure remain largely uncertain. The velocity gradient during the mixing process depends on the nature of the fluid flow (*i.e.*, constant in laminar flow and spatially and temporally dependent in turbulent flow).[47–49] As the flocs are formed and grow during the flocculation process, they can eventually break due to fluid shear forces.[59,61] After some time, the flocs will approach a steady state between floc growth and breakage. Too much shear at the beginning of the mixing process, particularly in turbulent conditions, can break the polymer chains and prevent initial floc formation.[58,80] The local hydrodynamics around a growing floc also affect the conformation of the polymer on the surface. Extensional forces in particular can stretch the polymer from the surface to lengths

greater than the radius of gyration of the free polymer in solution, increasing the bridging capability of the polymer.[81]

There have been some studies on determining floc properties after a mixing process by using small angle light scattering, but these results only yield final floc size and fractal dimensions.[56,82–84] Several computational fluid dynamics studies have been used to simulate the effects of laminar and turbulent shear on the flocculation process to potentially achieve optimal flocculation conditions, but the models remain largely limited due to the complexities associated with turbulent flow.[47,85,86] Jar tests, which typically use flocculators featuring impeller blades, replicate scaled-down industrial mixing tanks and are a relatively rapid, easy technique to obtain a large amount of information about the flocculation processes using turbidity measurements, particle sizing, microscopy, and image analysis.[59,61,87–91] Unfortunately, a major disadvantage of jar tests is their lack of homogeneous spatial and temporal flow features that are needed to precisely study floc strength as a function of hydrodynamic flow.[59] In addition to their inability to precisely generate a variety of flow states, the shear stresses within the fluid in a jar test cannot be accurately controlled to determine where floc breakage occurs.[62,92]

A potential solution to address the issues associated with jar tests is the use of Taylor-Couette (TC) cells. TC cells consist of two concentric cylinders, where the outer cylinder is typically made of a transparent material, such as glass, for observation and for image analysis. Precise laminar and turbulent hydrodynamic flow states defined by the rotational speeds of either the inner cylinder or the co- and counter-rotation of the outer cylinder offer an experimental method to study flocculation with the ability to precisely control the hydrodynamics. Prior flocculation studies with TC cells were limited in that flocs had to be pre-formed outside of the cell.[55,87,93] The Dutcher group has developed a Taylor-Couette cell (**Figure 1.5**) that offers the unique ability to directly inject fluids into the annulus without disturbing the flow itself.[94,95] This unique ability is particularly advantageous as it allows for studies on hydrodynamic effects of floc formation in well-controlled flow fields throughout the entire mixing process.

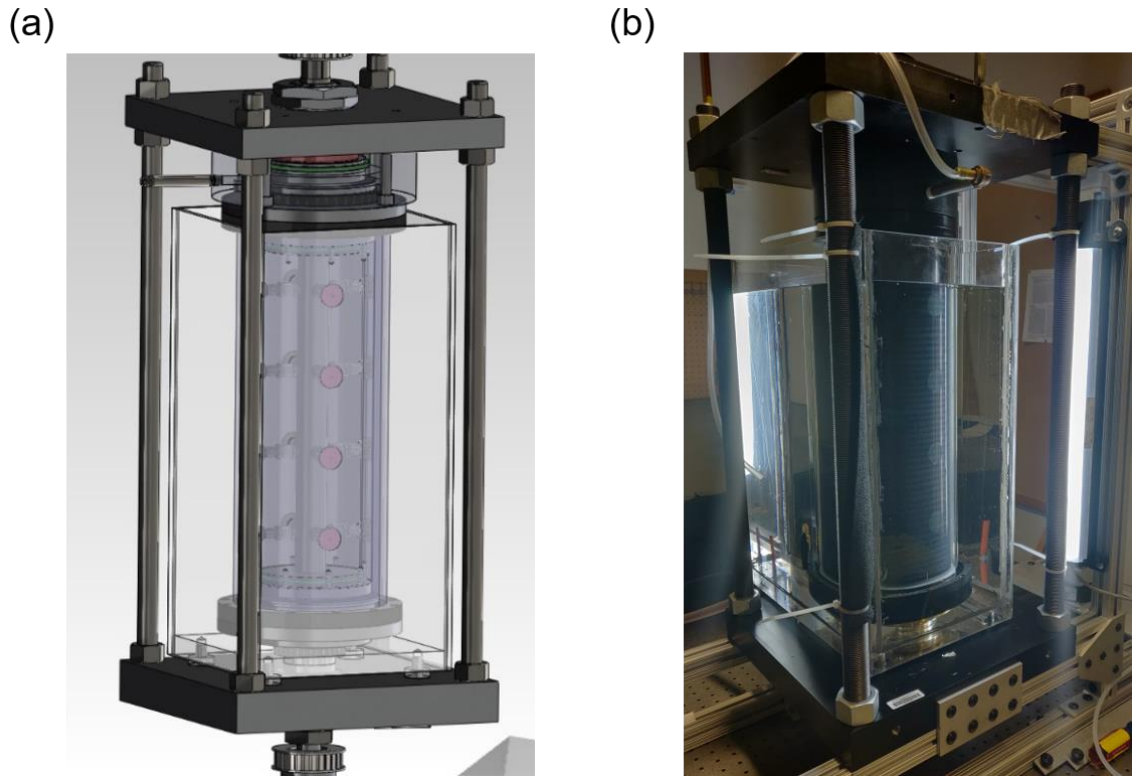


**Figure 1.5**: (a) SolidWorks model of the Taylor-Couette cell, where the inner cylinder is capable of radial fluid injection used in the flocculation studies. The red circles arranged axially and azimuthally along the inner cylinder are the injection port covers. (b) Image of the Taylor-Couette cell during operation. The fluid encased in the rectangular Plexiglass container is paraffin oil, whose index of refraction matches that of the glass outer cylinder to eliminate that curved surface while imaging.

## *1.4. Central Goal and Structure of Thesis*

The central goal of this thesis is to provide additional understanding of how polymers assemble in solution under a variety of physicochemical conditions and flow. The thesis is broadly divided into two sections, based on the assembly type and length-scale probed. Chapters 2 and 3 seek to understand the extensional rheological behavior of self-associating methylcellulose polymers in solution, which form fibrils as a function of polymer concentration and NaCl content. Both milliscale capillary thinning (Chapter 2) and microscale filament thinning (Chapter 3) were used to probe into the difficult-to-characterize low molecular weight, low viscosity regime. Knowledge of this behavior potentially broadens its processing capabilities while further studying chain and fibril dynamics in solution. In chapters 4, 5 and 6, polymer-particle assemblies are studied in

mixed macroscale flows, where each chapter deals with the increasing chemical complexity of the solution, with the goal of describing the optimal process flocculation performance in applications from drinking water treatment to paper manufacturing. In all chapters, the role of solution ionic strength of the polymer confirmation and assembly is central. Chapter 7 provides a summary as well as commentary on potential future work stemming from the projects discussed in Chapters 2-6.

# Chapter 2

# Extensional Flow Behavior of Methylcellulose Solutions Containing Fibrils[†]

[†]Portions of this chapter are reprinted with permission from S. Morozova, P. W. Schmidt, A. Metaxas, F. S. Bates, T. P. Lodge, and C. S. Dutcher, Extensional Flow Behavior of Methylcellulose Solutions Containing Fibrils, *ACS Macro Letters, 7,* 347-352, Copyright (2018) American Chemical Society.

## *2.1. Introduction*

Cellulose ethers are a class of chemical compounds in which the hydroxyl groups on cellulose are partially substituted with alkoxy groups. These synthetic derivatives are widely used in commercial products as rheology modifiers. Methylcellulose (MC) is substituted on average with 1.7 – 2.2 out of 3 hydroxyl groups per anhydroglucose unit.[29] At this degree of substitution (DS), the methoxy substituents disrupt the inter- and intramolecular hydrogen bonds which makes cellulose insoluble in water. As a result, MC can dissolve in water at low temperatures and can be readily used in a variety of food, pharmaceutical, construction, and consumer applications.

In addition to aqueous solubility at low temperature, MC reversibly transitions to a turbid hydrogel upon heating. The mechanism of this thermo-reversible process has been debated for decades; however, recent work has unequivocally demonstrated that the gelation transition is concurrent with the formation of long fibrils with a consistent

diameter of ca. 15 nm.[32,33] Both linear and non-linear shear viscoelastic studies have demonstrated that the fibrillar network dictates the mechanical properties of the high temperature gel.[39]

The MC fibril offers an enticing design component to expand the use of MC in applications not previously considered. Extensional flow is essential in a variety of polymer solution processes, including fiber spinning, printing, porous media flows, extrusion, coating, molding, spraying, film blowing, and more.[1–4,96–98] Control over the extensional behavior of MC promises to broaden the already impressive range of applications of MC, while simultaneously improving understanding of MC chain and fibril dynamics in aqueous solutions. While MC has been extensively studied using shear rheology, the extensional flow properties have only been reported for cellulose in ionic liquids, cellulose ether, and other polysaccharide solutions.[14,99–101]

Recently there has been a renaissance in methods developed for characterizing the extensional properties of polymer melts, polymer solutions, and complex fluids.[8,11–13,22,26,102–104] Of particular interest to polymer solutions is utilizing capillary-driven thinning to extract a characteristic extensional relaxation time and apparent extensional viscosity.[105–108] The Capillary Breakup Extensional Rheometry (CaBER) method provides a rapid, facile method to determine relevant extensional parameters of polymer solutions. Understanding and controlling the viscous and elastic forces in a fluid is crucial for a diverse range of applications that take advantage of free-surface flow. In this chapter, a first study of the influence of fibrils on the extensional flow behavior of MC solutions is presented. One strategy for creating such solutions at room temperature is the use of NaCl. The addition of NaCl has been widely reported to impact the gel temperature, such that it decreases monotonically with increasing concentration of NaCl.[30,31,34,109–113] The results from CaBER experiments demonstrate that the addition of MC fibrils into MC solutions causes a transition from a shear-thinning power-law fluid behavior to an elastic-like fluid deformation.

## *2.2. Materials and Methods*

### *2.2.1. Materials and Solution Preparation*

For rheological studies, aqueous MC solutions were made using an established protocol.[32,33,114] The methylcellulose was graciously provided by the Dow Chemical Company, and all other reagents were purchased from Sigma-Aldrich and used without further purification. MC ($DS \approx 1.8$, $M_w = 530$ kg·mol$^{-1}$, $Đ = 4.1$) was first dried at 50°C under vacuum (~100 mTorr) for 24 h. To prepare NaCl-free aqueous solutions, 0.75 or 1 g of MC were dissolved in 50 mL Milli-Q de-ionized 60°C water and stirred for 10 min in a 100 mL jar. The remaining quantity of the room-temperature water was then added to make up a total solution weight of 100 g. The solutions were stirred at room temperature for 10 min, followed by stirring on ice for 10 min. When finished, the solutions were stored at –20°C for at least 24 h. To prepare MC solutions in 8 wt% NaCl, 8 g of NaCl was dissolved along with MC in 50 mL Milli-Q de-ionized 60°C water and stirred for 10 min in a 100 mL jar. The rest of the procedure was equivalent to the NaCl-free solution protocol. MC solutions in 8 wt% NaCl were annealed at room temperature for 24 h prior to rheological studies.

### *2.2.2. Steady Shear and Oscillatory Shear Rheology*

Shear and oscillatory rheology were measured on an TA Instruments AR-G2 rheometer using a 2° steel 40 mm cone and a Peltier plate geometry for steady state shear flows and a DIN bob and cup geometry for oscillatory measurements. For steady state shear, the shear viscosity was measured after torque values reached an equilibrium for each shear rate from 0.1 – 1000 s$^{-1}$. Two oscillatory tests were performed: a temperature ramp of 1 °C·min$^{-1}$ at 3% strain from 0°C to 80°C at 1 rad·s$^{-1}$ and a frequency sweep from 0.1 – 10 rad·s$^{-1}$ at 3% strain every 2 h for 24 h.

### *2.2.3. Capillary Breakup Extensional Rheology*

For capillary breakup experiments, the HAAKE CaBER was used. For all experiments, 4 mm diameter plates were used at a 30 – 50 ms strike time. The sample was first loaded between the plates at an initial separation distance of 2 mm. The plates then

rapidly separated to a final height of 8 to 9 mm with an exponentially increasing rate over 30 to 50 ms to impart a step strain on the fluid. Other conditions (*e.g.*, longer strike times, linear strike profiles, and varied final separations) were found to result in filaments that broke up immediately after the power law decay or instabilities, such as the formation of the beads on a string. After the plates come to a stop, the fluid bridge flows due to a resulting force balance between surface tension and capillary-thinning forces. The midpoint of the liquid filament diameter is recorded over time as raw data.[19] The capillary thinning and breakup profile depend on the fluid type, and a constitutive model can be used to extract relevant extensional parameters.

## *2.3. Results and Discussion*

### *2.3.1. Effect of MC Fibrils on Shear Properties*

The sol-gel transition for aqueous MC solutions has been studied extensively by investigating the shear rheological properties as a function of temperature.[114] For NaCl-free MC solutions, the elastic modulus increases rapidly by several orders of magnitude at ~60°C, indicating formation of a fibrillar network (**Figure 2.1b**, red curve). This has been previously confirmed by cryogenic transmission electron microscopy and small-angle scattering.[32,33] The addition of NaCl decreases the temperature at which fibrils form and dissolve and therefore decreases the temperature at which the sol-gel and gel-sol transitions takes place A cartoon representation of fibril formation from free MC chains in solution upon heating or the addition of NaCl is shown in **Figure 2.1a**.

To directly compare the sol-gel transition for aqueous MC solutions with and without NaCl, the complex modulus magnitude, $|G^*|$, was measured as a function of temperature as shown in **Figure 2.1b**. The addition of 8 wt% NaCl leads to an approximately 30°C decrease in the sol-gel transition temperature, when the MC solutions are heated at $1°C \cdot min^{-1}$ (**Figure 2.1b**, blue curve). The gel-sol transition, which is believed to be the lower limit in temperature at which fibril formation can occur, also decreased below room temperature.[115] When annealing 1 wt% MC in 8 wt% NaCl at 25°C for 24 h, both the storage modulus, $G'$, and the loss modulus, $G''$, increase with time by an order of magnitude as shown in **Figure 2.1c**. $G'$ and $G''$ still show a distinct dependence on

frequency after 24 h, and the solution still flows as indicated by the shear viscosity measurements in **Figure 2.2**. The increase in both moduli is consistent with the formation of fibrils near the gelation transition.

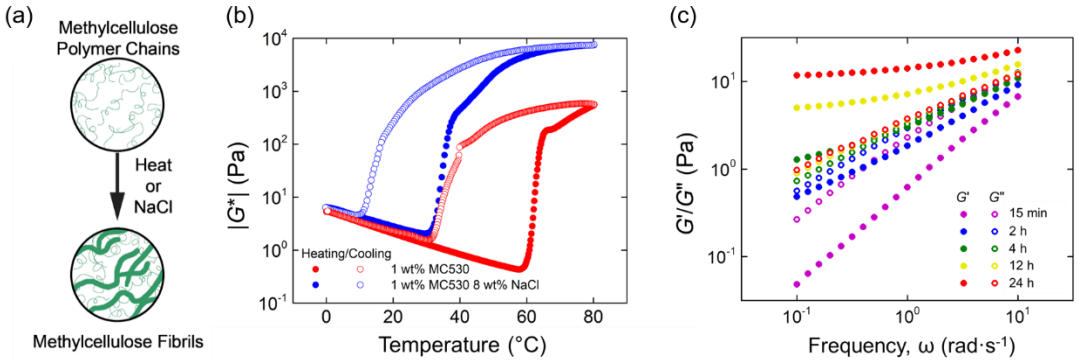


**Figure 2.1**: Rheological evidence of fibril formation. (a) Heating, or the addition of NaCl to MC solutions, leads to fibril formation. This study uses NaCl addition to create viscous solutions of MC fibrils embedded within the entangled MC polymer chain solution. (b) Complex modulus magnitude, $|G^*|$, of 1 wt% MC530 as a function of temperature with and without NaCl. The addition of 8 wt% NaCl depresses the gel temperature by ~30°C. (c) $G'$ and $G''$ as a function of frequency when annealing the 1 wt% MC in 8 wt% NaCl solution at 25°C for 15 min to 24 h.

The steady shear behavior of MC solutions is also modified by the presence of fibrils. **Figure 2.2** shows an overlay of the shear viscosity, $\eta_s$, as a function of shear rate for MC solutions at 1 wt% without added NaCl and 0.5 – 1wt % MC solutions in 8 wt% NaCl. Although highly viscous, the solutions still flow at 25°C. The 1 wt% solution without added NaCl shows the expected shear thinning behavior previously observed for MC solutions. At low shear rates, the viscosity asymptotes to the zero-shear viscosity value of 1.6 Pa·s. At high shear rates, the viscosity starts to decrease as the sample shear thins. To determine the flow behavior index, $n$, a power law can be fit to the higher shear rate values:

$$\eta_s = K\dot{\gamma}^{n-1} \tag{2.1}$$

where $K$ is the flow consistency index. Without NaCl, the power law index is $n$ = 0.33.

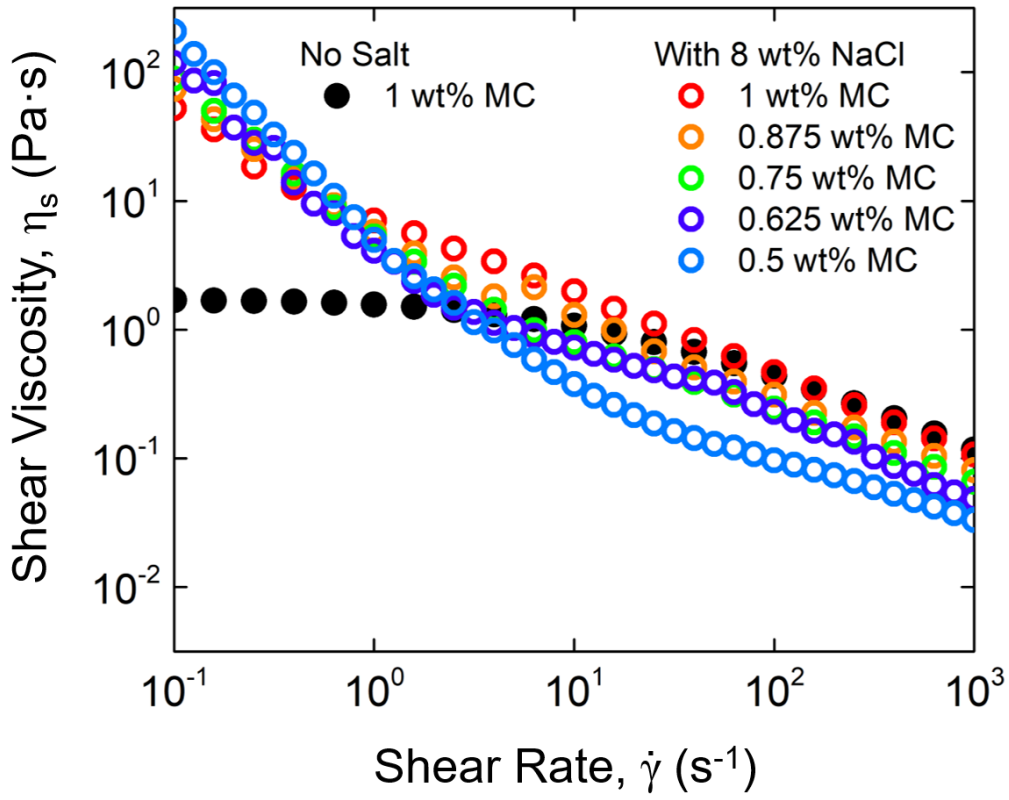


**Figure 2.2**: Shear viscosity in a cone and plate (40 mm) geometry as a function of shear rate at 25°C. For solutions with no NaCl (closed symbols) only MC coils contribute to the viscosity, which exhibits shear thinning behavior at larger shear rates. With the addition of NaCl (open symbols), two shear thinning regions are present, one at high frequency due to shear thinning effects of MC coils and the other at long time scales due to shear thinning effects of MC fibers.

For the MC solutions in 8 wt% NaCl, the flow behavior was modified. Instead of observing a constant, "zero-shear" viscosity regime at low shear rates, a second shear thinning regime was observed for all concentrations of MC in 8 wt% NaCl. At higher shear rates, the samples shear thin in a similar way to the control (NaCl-free MC). The two shear thinning regimes are indicative of a mixture of high molecular weight aggregates, which are responsible for the low shear rate behavior, and free MC chains, which dictate the shear thinning at high shear rates. This behavior corroborates the oscillatory behavior from **Figure 2.1c**. The addition of 8 wt% NaCl leads to partial aggregation of free MC chains

into fibrils after annealing at room temperature for 24 h. Fitting **Eqn. 2.1** to both shear thinning regimes, the low shear rate behavior is consistent with the highest possible shear thinning for all concentrations, where *n* approaches zero. At the highest shear rates, $n$ = 0.33, 0.36, 0.48, 0.33, and 0.55, for 0.5 – 1 wt%, respectively. Overall, the presence of fibrils increases the low shear rate (0.1 $s^{-1}$) viscosity in a dramatic way, from 1.6 Pa·s to approximately 100 Pa·s for the 1 wt% solution, consistent with large molecular weight anisotropic aggregates.

### *2.3.2. Effect of MC Fibrils on Extensional Properties*

The consequence of the presence of viscosity-modifying fibrils on the extensional flow behavior is dramatic. **Figure 2.3** shows this comparison: the light green curve is from a 0.75 wt% MC solution without added NaCl, whereas the dark green curve is for an 0.75 wt% MC solution in 8 wt% NaCl. Fibrils modify the CaBER profile in two ways. Firstly, the liquid bridge flows more slowly and breaks up at later times. Secondly and more significantly, after the initial shear-thinning power-law behavior, solutions with fibrils now exhibit elastic fluid behavior, as the power-law thinning segues into exponential filament thinning at later times when the polymers or fibrils disentangle and orient.[19,98,105,116,117] **Figure 2.3** also shows CaBER profiles for 0.5, 0.625, 0.875, and 1 wt% MC solutions in 8 wt% NaCl after annealing at room temperature for 24 h. The solutions first flow according to a visco-capillary force balance, for which the non-slender viscous power-law constitutive model for power-law exponents $n < 0.6$ can be written as

$$\frac{D(t)}{D_0} = A(t_c - t)^n \tag{2.2}$$

where $D(t)$ is the liquid bridge midpoint diameter, $D_0$ is the plate diameter, $t_c$ is the critical transition time between the power-law and exponential thinning regimes, $t$ is time, $n$ is the power-law exponent determined previously from **Figure 2.2**, and $A$ is a numerical pre-factor.[12,117,118]

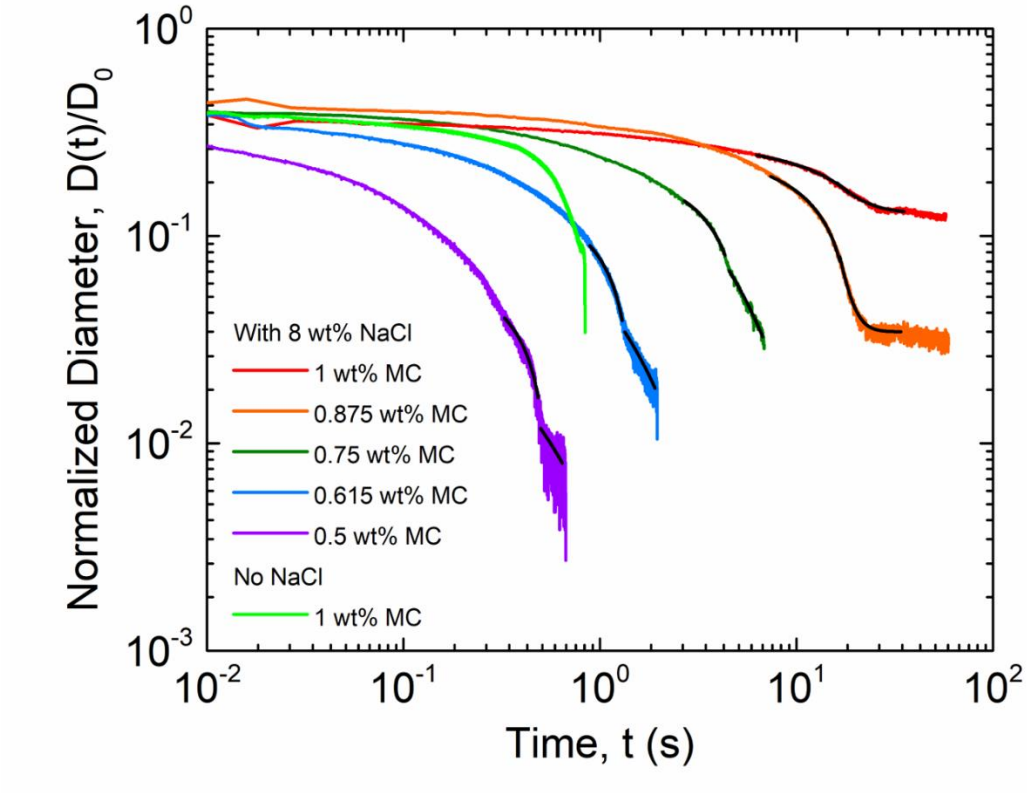


**Figure 2.3**: CaBER liquid neck diameter normalized by the plate diameter as a function of time and total MC concentration at 25°C for 0 wt% and 8 wt% NaCl solutions. The time for liquid bridge breakup increases drastically as does the diameter where elastic extensional behavior, characterized by an exponential thinning of the neck diameter, is observed. The black lines represent fits to **Eqns. 2.2** and **2.3** for each concentration. The measurements were taken with a plate diameter of 4 mm, initial plate separation of 2 mm, final strike height of 8 to 9 mm, and an exponential strike time of 30 to 50 ms.

With the presence of fibrils, the visco-capillary balance power law thinning leads into an elasto-capillary force balance, with the liquid bridge thinning with a characteristic extensional relaxation time

$$\frac{D(t)}{D_0} = \left(\frac{GD_0}{4\sigma}\right)^{\frac{1}{3}} \exp\left(-\frac{t}{3\lambda_E}\right) \tag{2.3}$$

where $G$ is the shear modulus, $\sigma$ is the surface tension, and $\lambda_E$ is the extensional relaxation time.[119] The term $\left(\frac{GD_0}{4\sigma}\right)^{\frac{1}{3}}$ is treated as a fitting constant. The formation of fibrils creates conditions such that elastic and capillary stresses dominate the overall stress balance within the flowing liquid bridge. Elastic forces oppose any capillary stresses and arise from polymer or fibril stretching, orientation, and conformational changes.

**Figure 2.4** shows details of the fits for all repeated trials. The $t_c$ values from the fits to **Eqn. 2.2** are plotted in **Figure 2.4a**. The variable $t_c$ marks the critical time at which the flow transitions from a visco-capillary power-law balance to an elasto-capillary balance.[19,105,119] As the concentration of MC increases, so does $t_c$, from 0.4 s for 0.5 wt% to 26 s for 1 wt% MC solutions. The critical radius at this transition can be estimated as $R_{crit} \sim 0.2127 \frac{\lambda_E \sigma}{\eta}$.[119] For 0.5 wt% MC in 8 wt% NaCl solutions $R_{crit}/R_0$ is 0.03 and increases to 0.18 for 1 wt% MC 8 wt% NaCl solutions as shown in **Figure 2.4b**. Beyond $R_{crit}$, the neck diameter decays exponentially with time; this behavior is fitted with **Eqn. 2.3.** As shown in **Figure 2.4c**, the relaxation time, $\lambda_E$, for the decay increases with MC concentration for solutions with NaCl, from 0.04 s for 0.5 wt% MC to 3.9 s for 1 wt% MC. At the highest MC concentrations, the samples are so viscous that the filament stabilized at a finite diameter. For these samples, a constant was added to **Eqn. 2.3** for the fit to accommodate this flow behavior.

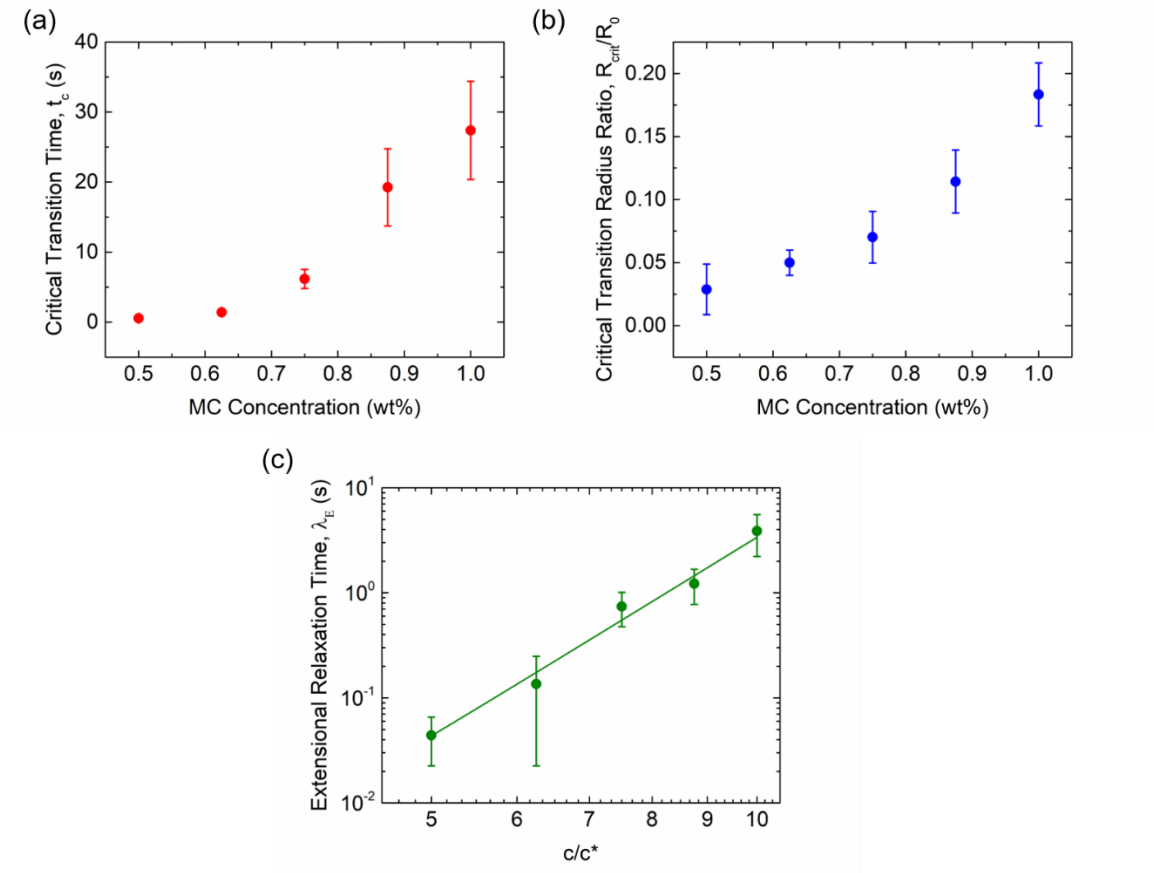


**Figure 2.4**: Summary of fit results. Error bars indicate the range. The errors are most likely due to variations in sample loading. (a) The breakup time from fits to **Eqn. 2.2.** (b) Observed $R_{crit}/R_0$ the critical diameter at which there is an observed transition from the visco-capillary to the elasto-capillary balance. (c) The relaxation times from fits to **Eqn. 2.3,** using an estimated c* = 0.1 wt%. The solid line represents a fit to 0.001 + 1.7 x $10^{-6}$ $(c/c^*)^{6.3 \pm 1.4}$.

The relaxation time scales are strongly concentration dependent, as shown by **Figure 2.4c**. For MC of molecular weight 530 kg·mol$^{-1}$, the overlap concentration is estimated as

$$c^* = \frac{3M_w}{4\pi N_A R_g^3} \sim 0.1\ wt\% \tag{2.4}$$

where $R_g$ is the radius of gyration that depends on the number of monomers, $N$, in the polymer chains and the length of each polymer, $b$, such that $R_g \approx bN^{\nu}$.[114] For the MC

solutions used in this study, $c > 5c^*$, and therefore, the polymer chains interpenetrate significantly. It is also expected that the MC chains, especially when heavily strained at the end of the flow, entangle significantly. Clasen *et al.*,[108] Sachsenheimer *et al.*,[120] Arnolds *et al.*,[121] and Liu *et al.*[122] have previously determined that for such cases, reptation dynamics dominate the time scales and that the longest relaxation time depends on the correlation length, a length scale beyond which hydrodynamic interactions are screened. Considering the concentration dependence of the correlation length, the longest relaxation time has a power law dependence on concentration

$$\frac{\lambda_E}{\lambda_0} \sim \left(\frac{c}{c^*}\right)^{\frac{3.4-3\nu}{3\nu-1}} \tag{2.5}$$

where $\lambda_0$ is the Zimm dynamic relaxation time of a strand between entanglements and $\nu$ is the Flory exponent.[122–125]

The exponent from the power law fit in **Figure 2.4c** is 6.3 ± 1.4, which is consistent with $\nu = 0.44$. The power law exponent is much larger than 3.8, which is the power law exponent reported previously for cellulose in ionic liquids and is consistent with $\nu = 0.5$.[99] This may be ascribed to at least two factors: (1) the lower Flory exponent is consistent with the poor solvent quality of MC in 8 wt% NaCl solutions, and (2) the mixture of fibrils and free MC chains is a complex solution and it is beyond the scope of this study to determine the exact composition (*i.e.*, fibril vs. chain) as a function of time and concentration. Despite the complications, the evident concentration dependence is consistent with polymer reptation in a highly entangled solution.

In addition to the extensional relaxation time, the apparent extensional viscosity can be calculated from the exponentially thinning region of the profile.[119,126] The relationship used to calculate the apparent extensional viscosity, $\eta_{E,app}$, is

$$\eta_{E,app} = \frac{2\sigma/D(t)}{d\varepsilon(t)/dt} \tag{2.6}$$

where σ is the surface tension and $d\varepsilon(t)/dt$ is the extensional strain rate, which is defined as

$$\frac{d\varepsilon(t)}{dt} = -\frac{2}{D(t)}\frac{dD(t)}{dt} = \frac{2}{3\lambda_E} \tag{2.7}$$

The surface tension of the 8 wt% NaCl MC solutions was estimated using a semi-empirical model developed by Dutcher *et al.*[127] At a temperature of 25°C, the surface tension was calculated as 74.4 mN·m$^{-1}$. This value for surface tension is most likely an overestimation, however conventional pendant drop methods were unable to successfully measure a surface tension for the samples as it failed to equilibrate to a constant value.

Using the determined value for $\lambda_E$ and the calculated value for the surface tension in the presence of 8 wt% NaCl, the apparent extensional viscosities were determined for all five MC concentrations. The values were plotted as a function of Hencky strain, defined as $\varepsilon_H = 2\ln\left(\frac{D_0}{D(t)}\right)$, in **Figure 2.5a**. The apparent extensional viscosity increases drastically with concentration, from 40 Pa·s for 0.5 wt% MC to 1300 Pa·s for 1 wt% MC as shown in **Figure 2.5b** at $R_{crit}$. As the liquid bridge thins, the apparent extensional viscosity increases linearly with the Hencky strain, indicating a nearly constant extension rate, as expected from **Eqn. 2.7**.

**Figure 2.6** summarizes the important findings: while NaCl-free MC solutions at room temperature are strongly shear-thinning, the addition of fibrils increases the viscosity drastically such that elasto-capillary filament thinning is observed starting at 0.5 wt% MC. This difference can be quantified by the elasto-capillary number

$$Ec = \frac{\lambda_E \sigma}{\eta_s R_{crit}} \tag{2.8}$$

which compares the time scales of elastically controlled thinning with the viscous time scales, which drive the capillary flow.[98,119] $Ec$ is expected to be close to 1 at the transition between visco-capillary power-law balance and elasto-capillary balance. With increasing MC concentration, $R_{crit}$ and $\lambda_E$ increase such that $Ec$ is 1, 4, 0.6, 0.6, 0.6 for 0.5 wt % to

1 wt% MC solutions in 8 wt% NaCl, respectively. The value is order unity as expected, with differences from unity within the error of the measurements.

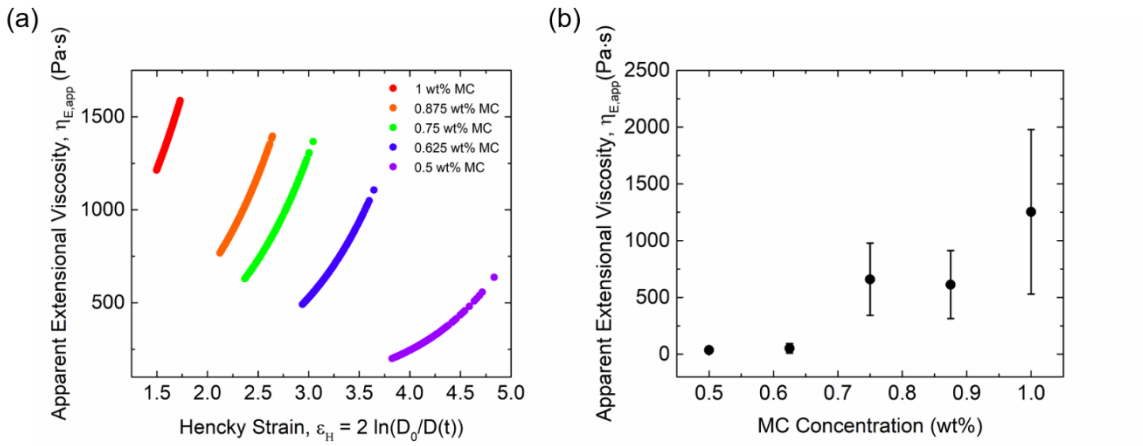


**Figure 2.5**: (a) The apparent extensional viscosity, calculated using **Eqns. 2.6** and **2.7**, as a function of Hencky strain for the exponentially thinning region. (b) The average viscosity for all trials in 8 wt% NaCl at $R_{crit}$. The extensional viscosity at the critical strain increases rapidly with concentration.

For MC solutions without NaCl, only shear thinning profiles are observed because of the low Deborah numbers of the flows at $R_{crit}$. The Deborah number, $De$, compares the elastic stress relaxation time scales to the Rayleigh time scale for inertia-capillary breakup of a fluid jet.[23,98] $De$ can be defined as

$$De = \frac{\lambda_E \sqrt{\sigma}}{\sqrt{\rho R_{crit}^3}} \tag{2.9}$$

where $\rho$ is the MC solution density. For all 8 wt% NaCl MC solutions, $De > 1$, and is equal to 26 for 0.5 wt% MC, 80 for 0.625 wt% MC, 121 for 0.75 wt% MC, 100 for 0.875 wt% MC, and 155 for 1 wt% MC in 8 wt% NaCl.

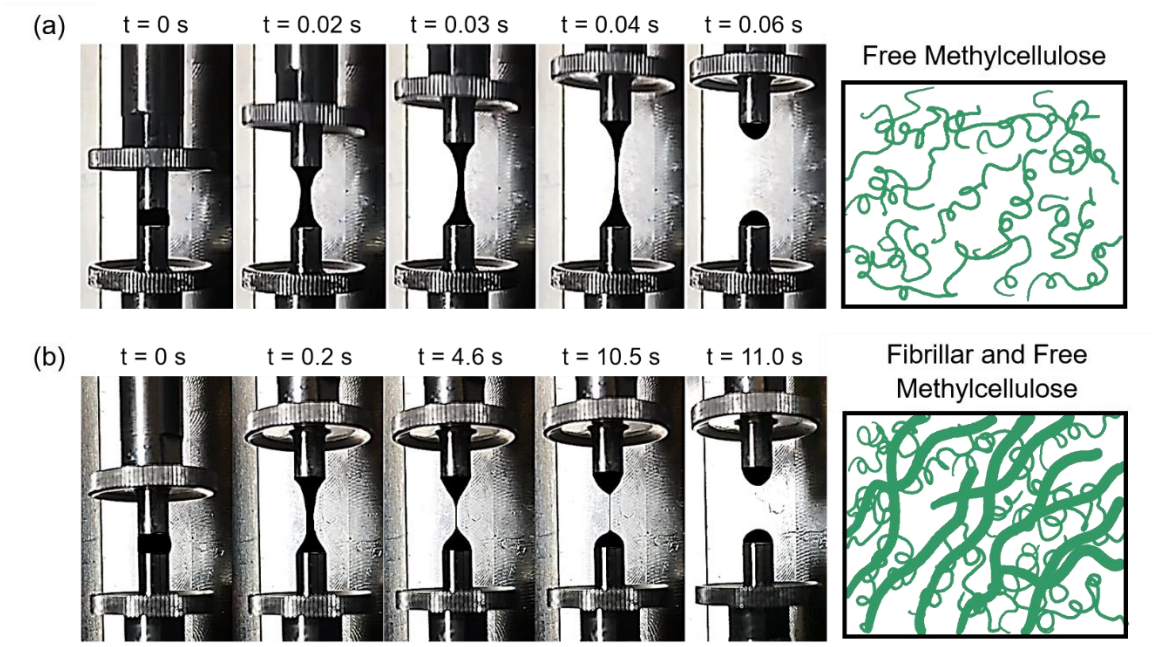


**Figure 2.6**: Schematic and experimental snapshots of 0.75 wt% MC behavior as a result of applied extensional flow from the CaBER. (a) In the case of NaCl-free MC solutions, the power law fluid profiles indicate only free MC chains were present. (b) In the case of MC solutions with 8 wt% NaCl, elastic behavior was observed because MC fibrils are present in addition to free MC chains. For these images, the initial height between the plates was 2 mm, the final height was 13 mm, and the exponential strike time was 30 ms to capture the disparate behavior between MC solutions with and without NaCl. The images were extracted from videos recorded at 120 fps. The fluid between the top and bottom plates was false colored with black to depict the filament more clearly.

Without NaCl, the largest possible estimated $De$ for a 1 wt% MC solution is ~7 and decreases steadily for lower concentrations, using estimated values for the Zimm relaxation time, $\lambda_{Zimm}$, and a hypothetical $R_{crit}$. To estimate the latter values, $R_{crit}$ is expected to be at 0.1 mm for 1 wt% MC solutions without NaCl, based on the viscosity of the solution, and the estimated Zimm relaxation time, $\lambda_{Zimm} \sim \frac{0.5[\eta]\eta_s M_w}{N_A k_B T} \sim 0.03\ s$, where $[\eta]$ is the intrinsic viscosity, $k_B$ is Boltzmann's constant, and $N_A$ is Avogadro's number.[23] For MC solutions in water, $[\eta]$ is equal to 1100 mL·g$^{-1}$ for MC of $M_w$ = 530 kg·mol$^{-1}$, and $\eta_s$ is 0.001 Pa·s.[29] For lower concentrations, $R_{crit}$ is higher due to a decrease in viscosity. For low $De$, characteristic flow times are much faster and generalized Newtonian-like breakup dynamics are observed. The 0.75 wt% MC solution with no NaCl (**Figure 2.6a** shows a

"cusp-like" profile for the duration of the CaBER experiment, which is indicative of power-law behavior. The 0.75 wt% MC solution with 8 wt% NaCl (**Figure 2.6b** initially has this same "cusp-like" profile). This profile eventually transitions to a thin filament at the end of the flow, which is indicative of elasto-capillary behavior.

## *2.4. Conclusion*

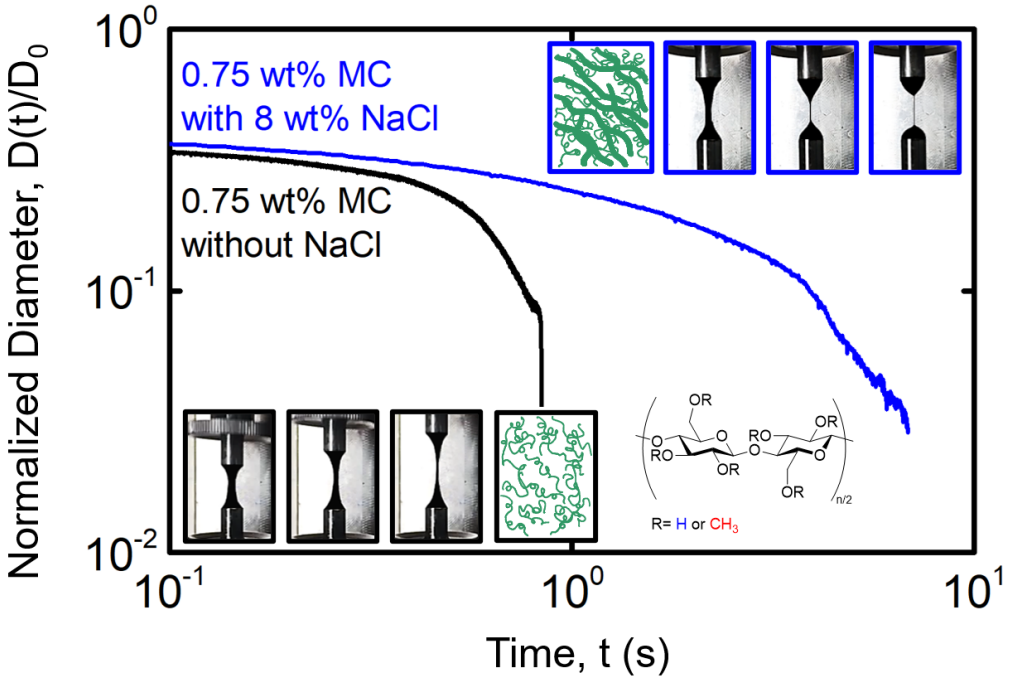


**Figure 2.7**: Summary of the CaBER studies for MC with and without NaCl. The presence of fibrils in the MC solution containing NaCl results in a CaBER profile and fluid profile (inset images) indicative of elasto-capillary behavior, which the MC solution without NaCl does not exhibit.

Self-association of MC into fibrils controls the extensional flow properties of MC solutions in several key ways. Without fibrils, the Deborah number of MC solutions is too low and fluid flow times are much faster than polymer relaxation times. Consequently, 0.5 – 1 wt% MC solutions with no NaCl show a power-law "cusp-like" CaBER profile as shown in **Figure 2.6a**. The addition of NaCl to the MC solutions to form fibrils increases the relaxation times, viscosity, and $R_{crit}$ of the solution such that elasto-capillary regime becomes accessible and experimentally tunable. The distinct thin filament shown in **Figure**

**2.6b** is characteristic for elasto-capillary thinning behavior of elastic fluids. This difference in behavior is summarized in **Figure 2.7**. Varying the MC and NaCl concentrations accesses a regime of stable extensional flows, which have never before been characterized for aqueous MC solutions. These flows open the already commercially relevant polymer to a myriad of other processes, such as fiber spinning and extrusion.

# Chapter 3

# Microfluidic Filament Thinning of Aqueous, Fibrillar Methylcellulose Solutions[†]

[†]Portions of this chapter includes work in A. E. Metaxas, M. L. Coughlin, C. K. Hansen, F. S. Bates, T. P. Lodge, and C. S. Dutcher, Microfluidic filament thinning of aqueous, fibrillar methylcellulose solutions, *Physical Review Fluids* (2020) Submitted.

## *3.1. Introduction*

Extensional flow fields observed in nozzles and contracting channels are relevant in many industrial applications, including printing, fiber spinning, extrusion, coatings, spraying, and film blowing.[1–4,97,98] However, establishing the non-Newtonian behavior of fluids in extensional flow fields can be challenging, especially for low-viscosity, weakly elastic solutions. The information obtained from the thinning and progressive breakup of an initially stable fluid filament with time is a key method to studying complex flows for droplets,[128,129] emulsions,[130–132] and polymer solutions.[11,13,14,104] For example, a typical macro-scale method for determining extensional properties of polymer solutions is Capillary Breakup Extensional Rheology (CaBER), where a step-strain is applied to a fluid or semi-solid between two parallel plates and the fluid filament flows and thins due to a balance between viscous and/or elastic stresses and capillary action. The diameter of the thinning filament is measured as a function of time by a laser housed in the device or by image analysis with a high-speed camera, where properties such as extensional relaxation

time and extensional viscosity can be inferred. Although convenient, CaBER only reliably determines these properties of solutions with shear viscosities above 100 mPa·s, as lower viscosity solutions tend to break up before relevant quantitative information can be collected.[108,119,126]

Microfluidic flow-focusing devices, such as the device used by Arratia *et al.*[133,134] and shown in **Figure 3.1**, are much smaller in scale than the CaBER. Combined with high-speed imaging, flow-focusing devices offer a potential solution to the drawbacks associated with CaBER. Because the ratio of elastic to inertial forces, defined as the elasticity number $El = \lambda\eta_s/(\rho l)^2$, where $\lambda$ is the relaxation time, $\eta_s$ is the solution (shear) viscosity, and $\rho$ is the fluid density, scales with the inverse square of the characteristic length scale of a device, $l$, the viscoelastic behavior of a polymer solution can be enhanced in a microfluidic device.[27] The range of measurable extensional strain rates in a microfluidic device is also extended by several orders of magnitude from those accessible by CaBER.[19,26,102,135–137] In addition, the presence of an oil phase surrounding the thinning filament can help regulate temperature and suppress evaporation, as those can also be concerns in a method such as CaBER. Finally, the microfluidic device set-ups require very small volumes of solution and are high throughput, providing large datasets from small sample amounts.

The extensional behavior of methylcellulose (MC) is of interest due to processing that involves extensional deformation. Methylcellulose is used as a rheology modifier in a variety of food, pharmaceutical, and consumer product industries because of its unique properties. MC is cellulose partially substituted with methoxy groups (on average 1.7 – 2.2 out of 3 hydroxyl groups per anhydroglucose unit), which renders it soluble in water at temperatures below about 50°C.[29] In addition to its solubility in water at lower temperatures, MC can reversibly transition to a turbid hydrogel upon heating or with the introduction of NaCl into solution around room temperature.[30,31] The current consensus for the thermoreversible gelation mechanism involves the formation of MC fibrils. Extensive work using cryogenic transmission electron microscopy (cryo-TEM), rheological measurements, and small angle X-ray and neutron scattering (SAXS and SANS) support

the hypothesis that the fibrillar network is responsible for the mechanical response of this material.[32,33,39,114,115]

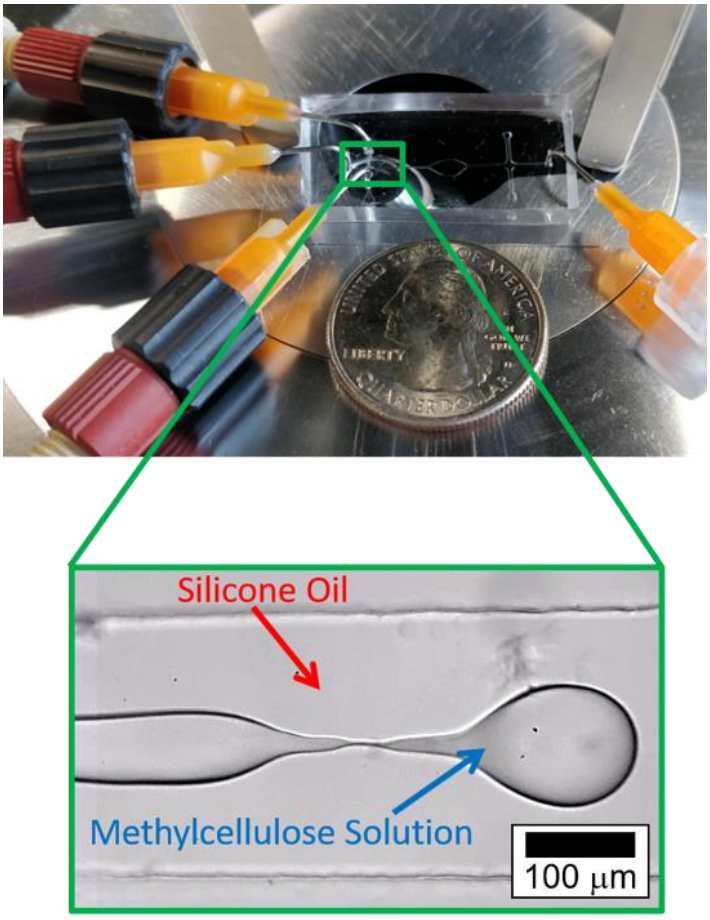


**Figure 3.1**: Filament thinning of aqueous methylcellulose (MC) solutions in flow-focusing microfluidic devices can generate transient changes in filament diameter, which can be used to calculate the extensional viscosity of each solution.

Prior studies have successfully vitrified MC solutions after annealing above the gel point in solutions that did not contain salt. Cryo-TEM images obtained from these glassy thin films showed fibrils with an average diameter of *ca*. 15 nm, which was further corroborated by SAXS and SANS on these solutions.[32,39,41,115] Recent simulations support the proposal that the fibrils are composed of a core of axially oriented chains with polymers wrapped around the core to form twisted bundles, which are formed by chain bending and water-mediated inter-chain interactions.[138–141] A recent experimental study using SAXS, medium- and wide-angle X-ray scattering (MAXS and WAXS) on oriented gel samples

confirm that the average chain axis is oriented along the fibril axis, and that the fibrils include crystalline regions.[142]

The study by Morozova *et al*.[28], which was discussed in Chapter 2, examined the extensional behavior of methylcellulose solutions using CaBER as a function of MC concentration and NaCl concentration. The study found that the presence of NaCl resulted in an elasto-capillary regime, from which the extensional relaxation time and apparent extensional viscosity were calculated from Hencky strains ranging from 1.5 to 5. The emergence of this elasto-capillary regime was attributed to the formation of fibrils in solution at room temperature. Unfortunately, CaBER can only reliably resolve MC solutions with molecular weights of 250 $kg \cdot mol^{-1}$ and higher, as shown in **Figure 3.2**, as lower molecular weight samples have viscosities and relaxation times that render the CaBER technique ineffective.

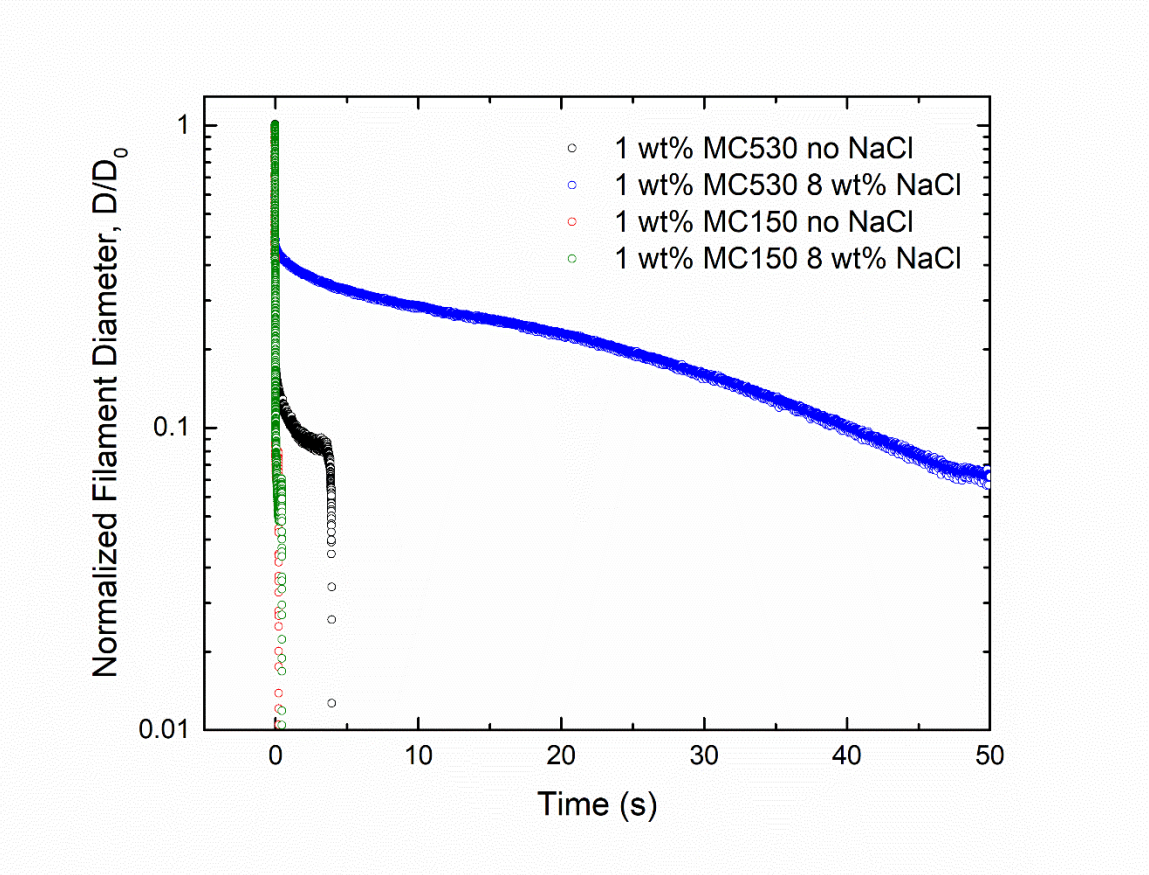


**Figure 3.2**: CaBER traces for 1 wt% MC530 and 1 wt% MC150 solutions in both 0 wt% and 8 wt% NaCl. While CaBER is readily able to resolve the extensional behavior of the higher molecular weight MC530 solutions, it cannot be used to resolve the extensional features of the MC150 solutions. The filament diameter was normalized to the initial diameter at time = 0 s. An exponential strike time of 30 ms was used with 4 mm diameter plates and an initial height to plate diameter ratio of 0.5.

Recently, Micklavzina *et al.*[143] used hyperbolic microfluidic contractions to extend the range of extensional rheology measurements of MC solutions to lower viscosities, and resolved extensional viscosities between 0.01-1 Pa·s using pressure drop measurements. However, a drawback of the single phase contraction channel is the dominant contribution of viscous losses in the contraction.[24,144] The present study couples the advantage of MC solution filament thinning by the surrounding outer fluid extensional flow with the advantage of the improved strain rate range accessible in microfluidic devices. The extensional properties of MC solutions were examined over a range of NaCl concentrations by using microfluidic flow-focusing devices to generate dynamically thinning filaments.

The work discussed here presents a relatively straightforward method to obtaining extensional properties that were previously unattainable to expand the understanding of MC behavior under extensional flow fields.

## *3.2. Materials and Methods*

### *3.2.1. Methylcellulose Solution Preparation*

Methylcellulose ($M_w$ = 150 kg·mol$^{-1}$, $Đ$ = 3.6, degree of methyl substitution, DS ≈ 1.8) was provided by The Dow Chemical Company. NaCl is ACS grade from Fisher Scientific and used as received. MC was dried under vacuum (~100 mTorr) at 50°C for 24 h to eliminate any excess water. The concentration of MC for all solutions in this study was 1 wt%, which for MC150 in water is approximately five times the overlap concentration $c^*$ of 0.21 wt%.[114,145] To prepare the solutions, 0.5 g of MC was dissolved in 25 g of HPLC grade chromatography water (Fisher Scientific) at 60°C and stirred for 10 min in a 50 mL glass jar. For solutions with NaCl, samples containing 1 g (2 wt%), 2.5 g (5 wt%), or 4 g (8 wt%) of the salt were dissolved with the MC in water at 60°C. The remaining quantity of water at room temperature (~23°C) was added to yield a total solution weight of 50 g, and stirred for an additional 10 min. The solutions were placed into an ice bath, stirred for 10 min, and then stored in a refrigerator at 2°C for at least 24 h. These samples can be used for up to a month after preparation. The solutions were annealed at room temperature for 24 h prior to any measurements using cryo-TEM, steady shear and oscillatory rheology or microfluidic filament thinning.

### *3.2.2. Steady Shear and Oscillatory Shear Rheology*

Shear and oscillatory rheology experiments were conducted on a TA Instruments AR-G2 rheometer. For steady shear experiments, a 2° steel 40 mm cone and Peltier plate geometry were used. The shear viscosity for each 1 wt% MC solution (with 0, 2, 5, or 8 wt% NaCl) was measured after the torque signal reached an equilibrium state, for shear rates ranging from 0.1 to 5000 $s^{-1}$. The temperature was kept constant at 23°C for all experiments. Oscillatory experiments were taken using a cup and bob geometry (rotor o.d. 14 mm, rotor height 42 mm, cup i.d. 15 mm, and gap height 5 mm) from 0°C to 80°C and

80°C to 0°C at a temperature ramp rate of 1°C·min$^{-1}$ at 1% strain amplitude with an angular frequency of 1 rad·s$^{-1}$.

### *3.2.3. Cryogenic Transmission Electron Microscopy (Cryo-TEM)*

NaCl-free and 8 wt% NaCl solutions of 0.1 wt% MC were prepared as described in Section 3.2.1. To vitrify the samples, an FEI Vitrobot Mark IV vitrification system was used with the climate control chamber set to 25°C and 100% humidity. Lacy carbon/Formvar grids (Ted Pella, 300 mesh) were cleaned and hydrophilized using a PELCO easiGlow discharge cleaning system. Five μL of each sample were pipetted onto separate grids, and the grids were annealed in the Vitrobot chamber for 1 s before the grid was blotted for 1 s with a blot force set to –1, equilibrated for 1 s, and plunged into liquid ethane cooled by liquid nitrogen. The vitrified grids were stored in liquid nitrogen prior to imaging. The sample grids were transferred to a Gatan-626 single tilt cryo-holder and imaged using an FEI Tecnai G2 Spirit BioTWIN microscope operated at 120 kV coupled with an FEI Eagle charge-coupled device camera (2048 × 2048 pixels). Images were obtained from multiple areas of the grid to determine if fibrils were formed in the MC solutions.

### *3.2.4. Extensional Filament Thinning in Microfluidic Devices*

The microfluidic device for extensional filament thinning measurements was fabricated using standard soft-lithography techniques described extensively in the literature.[146–148] A photolithography mask of the flow-focusing device was drawn using 2D CAD software (Draftsight) and printed on a 20,000 dpi high-resolution printer (CAD/Art Services, Inc.), as shown in **Figure 3.3a**. In the clean room, a blank silicon wafer was cleaned using a piranha solution and spin-coated with a negative photoresist (SU-8 2050, Microchem). After a pre-exposure bake, a mask aligner (Karl Süss) was used to expose the photoresist to UV light and developed to form an SU-8 mold of the flow-focusing device. Prior to pouring poly(dimethylsiloxane) (PDMS, SYLGARD 184 silicone elastomer, 10:1 elastomer to crosslinker ratio, Dow Corning Corporation), the surface of the mold was rinsed with isopropanol, dried with compressed air, and treated with silanes ((tridecafluoro-1,1,2,2-tetrahydrootcyl)trichlorosilane, Gelest) to allow for easy removal of the PDMS

device from the surface of the silicon wafer. Approximately 20 μL of the silanes were pipetted into a watchglass and placed with the cleaned wafer into a desiccator and held for 20 min under vacuum.

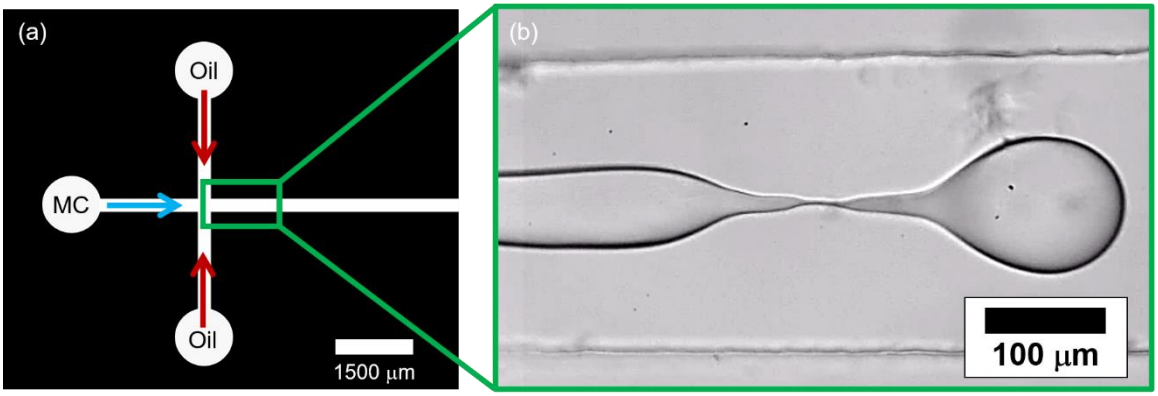


**Figure 3.3**: (a) Schematic of the microfluidic flow-focusing device. The MC solution flows through the leftmost entrance port and is surrounded by a continuous phase of 50 cSt silicone oil. (b) A movie at 20,000 fps is recorded to capture the filament thinning behavior as shown. Edge detection is then applied to obtain the filament diameter with time.

After treating the wafer surface, the PDMS was poured onto the mold and baked overnight at 70°C to allow the PDMS to harden. To seal the bottom of the PDMS device and mitigate wetting effects, a glass coverslip was spin-coated with PDMS and allowed to bake overnight. The device was then cut out from the mold and holes were punched into the three inlets (two side arms for the continuous silicone oil phase and one central arm for the MC solution, as shown in **Figure 3.3a** and one outlet) using a 0.75 mm OD biopsy punch (World Precision Instruments). The PDMS device and PDMS-coated glass coverslip were rinsed with methanol, isopropanol, distilled water, and dried with compressed air. The device and coverslip were plasma-treated (Harrick Plasma), sealed, and baked for a minimum of 2 h in an oven at 70°C to render the channel walls hydrophobic and prevent the aqueous MC solutions from adhering to the walls. The device channel width is 250 μm while the device channel height is 120 μm, which was confirmed with optical microscopy and ImageJ.

The device was then mounted on the stage of an inverted microscope (Olympus IX73) for bright field imaging using a 20× objective lens. Pressure-driven flow is generated

using syringe pumps (Harvard Apparatus) with gas-tight glass syringes connected to perfluoroalkoxy tubing (PFA, i.d. 0.02 in, o.d. 0.0625 in, IDEX Corporation) and curved needles hermetically sealed to the device inlets and outlet. The continuous phase of 50 cSt silicone oil (Fisher Scientific) was pumped in at a specified volumetric flow rate (see **Table 3-1**) and allowed to flow through the device for several minutes prior to pumping in the MC solution. The silicone oil was Newtonian, as confirmed by steady shear measurements. The dispersed phase flow rate was held constant at 0.008 $cm^3 \cdot min^{-1}$ for all MC solutions. The field of view was adjusted near the cross junction to record movies at 20,000 frames per second (fps) on a Photron FASTCAM Mini UX100 high-speed camera. A frame from a sample movie is shown in **Figure 3.3b**.

Once the movies were recorded, they were processed in MATLAB using an in-house code to apply an intensity threshold to the interface between the continuous, silicone oil phase and the dispersed, aqueous MC150 solution phase. Sample movie frames with applied thresholding for the solution containing 0 wt% NaCl, 2 wt% NaCl, 5 wt% NaCl, and 8 wt% NaCl are shown in **Figure 3.4b**, **Figure 3.5b**, **Figure 3.6b**, and **Figure 3.7b**, respectively. The filament diameter, $D(t)$, can be calculated in terms of pixels for each frame of the movie and converted to a μm length-scale since the channel width is known. The filament diameter measurements were collected at five user-defined locations in an Eulerian frame, as represented by the vertical white lines in **Figure 3.4b**. The transient region occurs at times less than 10 ms, as the drop passes, and this is not used in the calculation. In contrast, for times over 10 ms, the thinning behavior is nearly identical across the region of interest, regardless of where the image analysis is performed within the thinning region shown. The orange, dashed box in **Figure 3.4a** shows the portion of the trace that is used for extensional viscosity calculations, as the filament diameters are below the channel height and therefore not in a confined state. Multiple filament breakup events were further analyzed to calculate extensional strain rate and flow-driven extensional viscosity, to be discussed later. Repeat runs for each solution can be found in **Figure 3.8**.

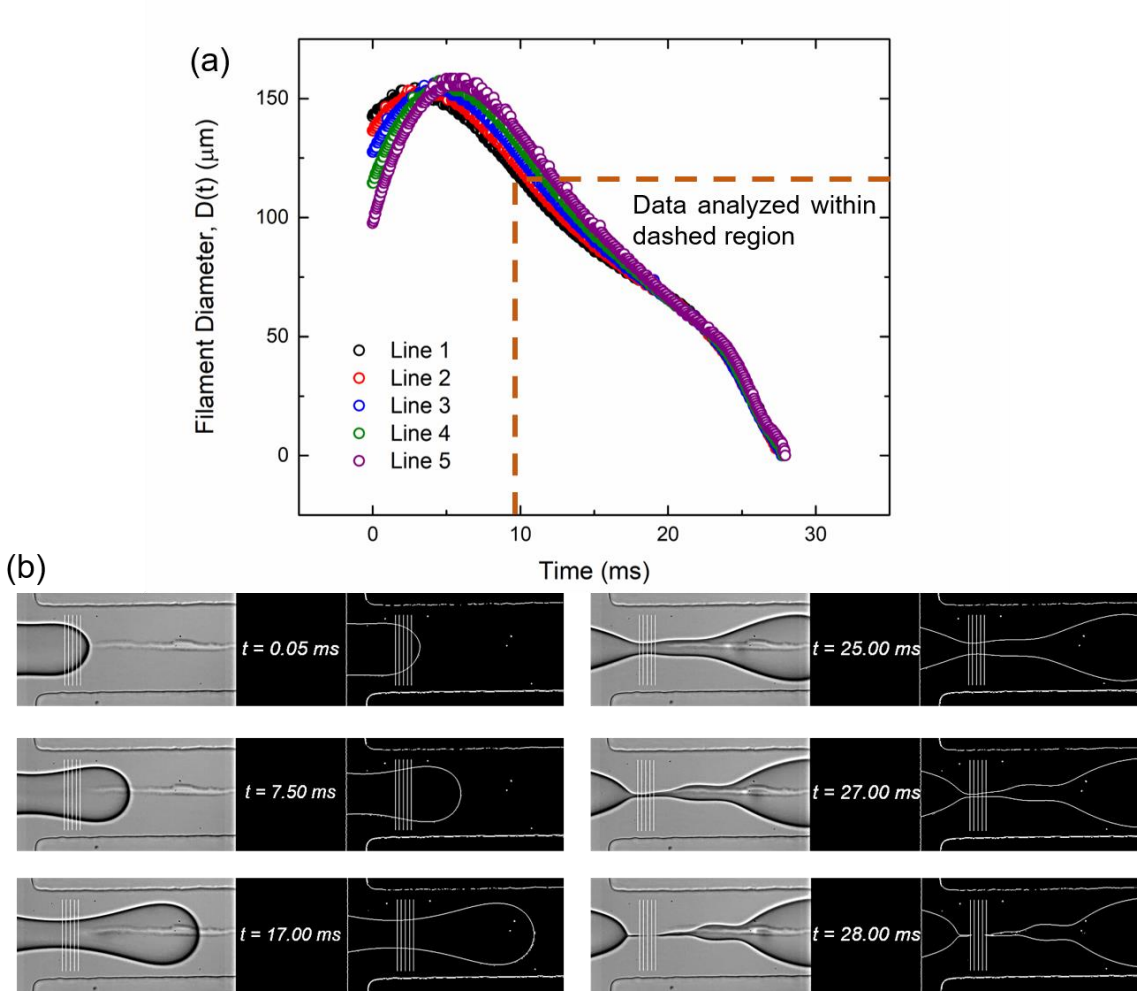


**Figure 3.4**: (a) Filament diameter of the fluid front for 1 wt% MC150 in 0 wt% NaCl passing through all five white, vertical lines in the snapshots of a sample movie shown in (b). The raw movie frame is on the left-hand side of each column, while the frame with applied thresholding is shown on the right-hand side of each column in (b). The vertical white lines indicate where the filament diameter, *D(t)*, can be measured. The channel width is 250 μm in all frames shown here. The area boxed in with the orange dashed lines indicates the region where the data were analyzed, described in the Results and Discussion.

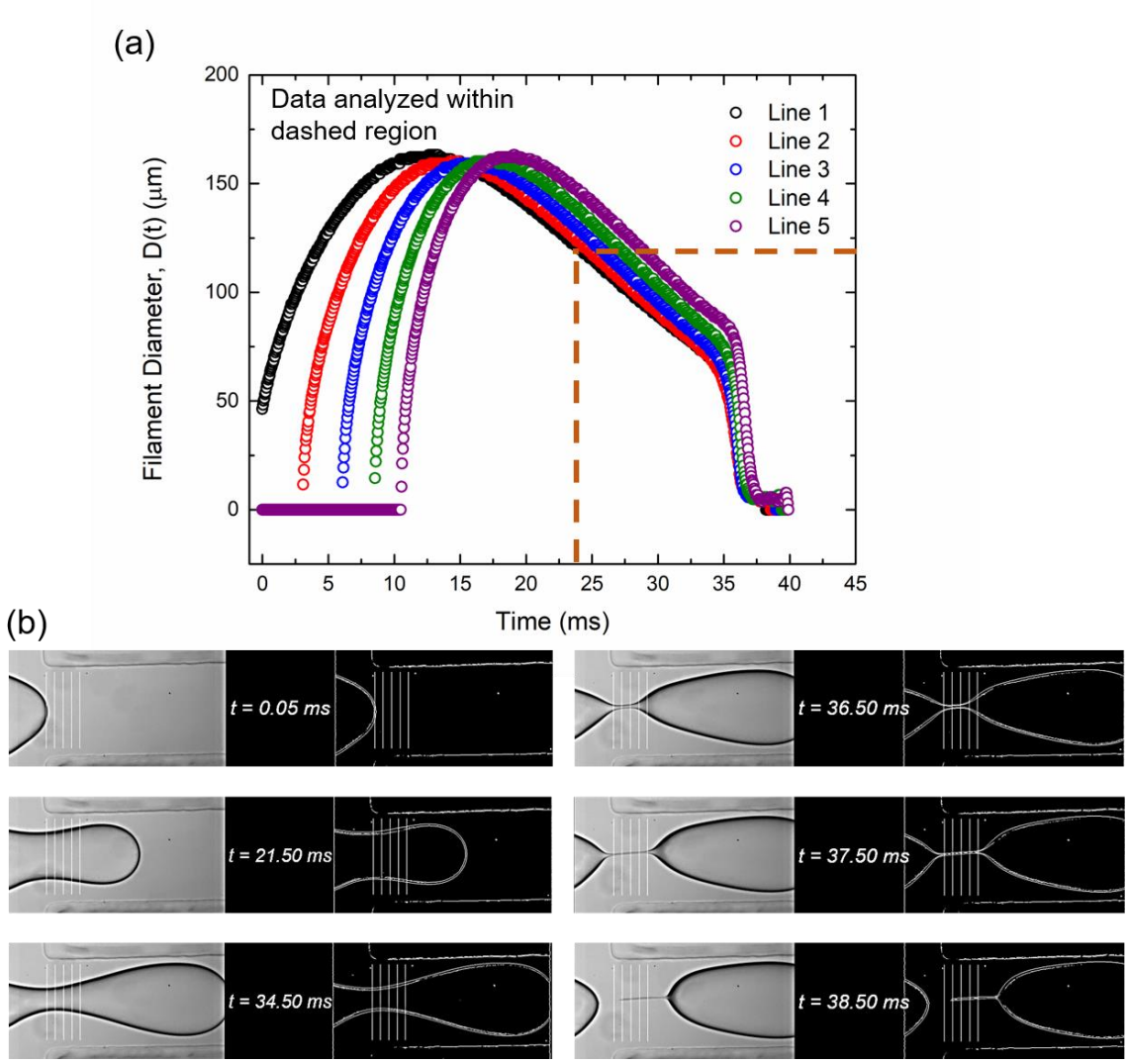


**Figure 3.5**: (a) Filament diameter of the fluid front for 1 wt% MC150 in 2 wt% NaCl passing through all five white, vertical lines in the snapshots of a sample movie shown in (b). The raw movie frame is on the left-hand side of each column, while the frame with applied thresholding is shown on the right-hand side of each column in (b). The vertical white lines indicate where the filament diameter, *D(t)*, can be measured. The channel width is 250 μm in all frames shown here. The area boxed in with the orange dashed lines indicates the region where the data were analyzed.

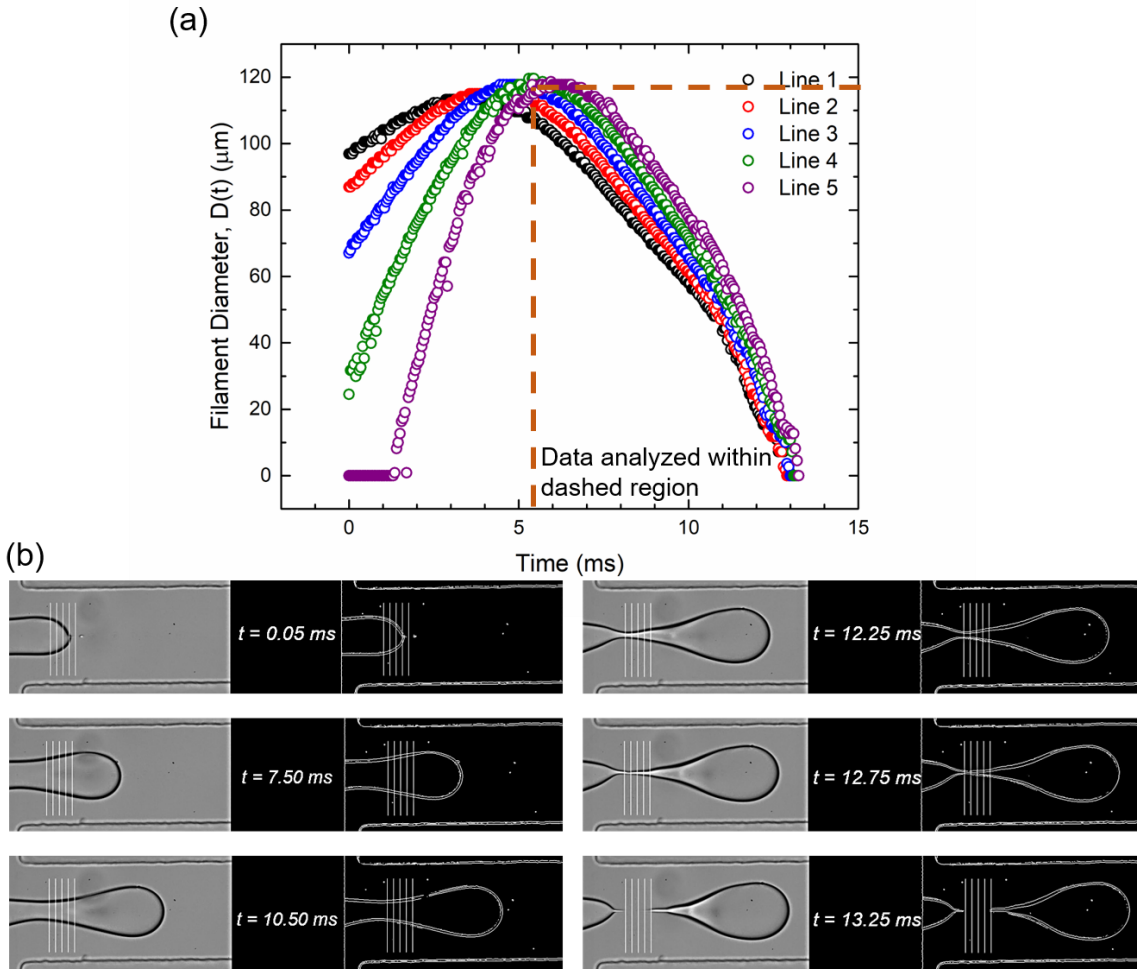


**Figure 3.6**: (a) Filament diameter of the fluid front for 1 wt% MC150 in 5 wt% NaCl passing through all five white, vertical lines in the snapshots of a sample movie shown in (b). The raw movie frame is on the left-hand side of each column, while the frame with applied thresholding is shown on the right-hand side of each column in (b). The vertical white lines indicate where the filament diameter, *D(t)*, can be measured. The channel width is 250 μm in all frames shown here. The area boxed in with the orange dashed lines indicates the region where the data were analyzed.

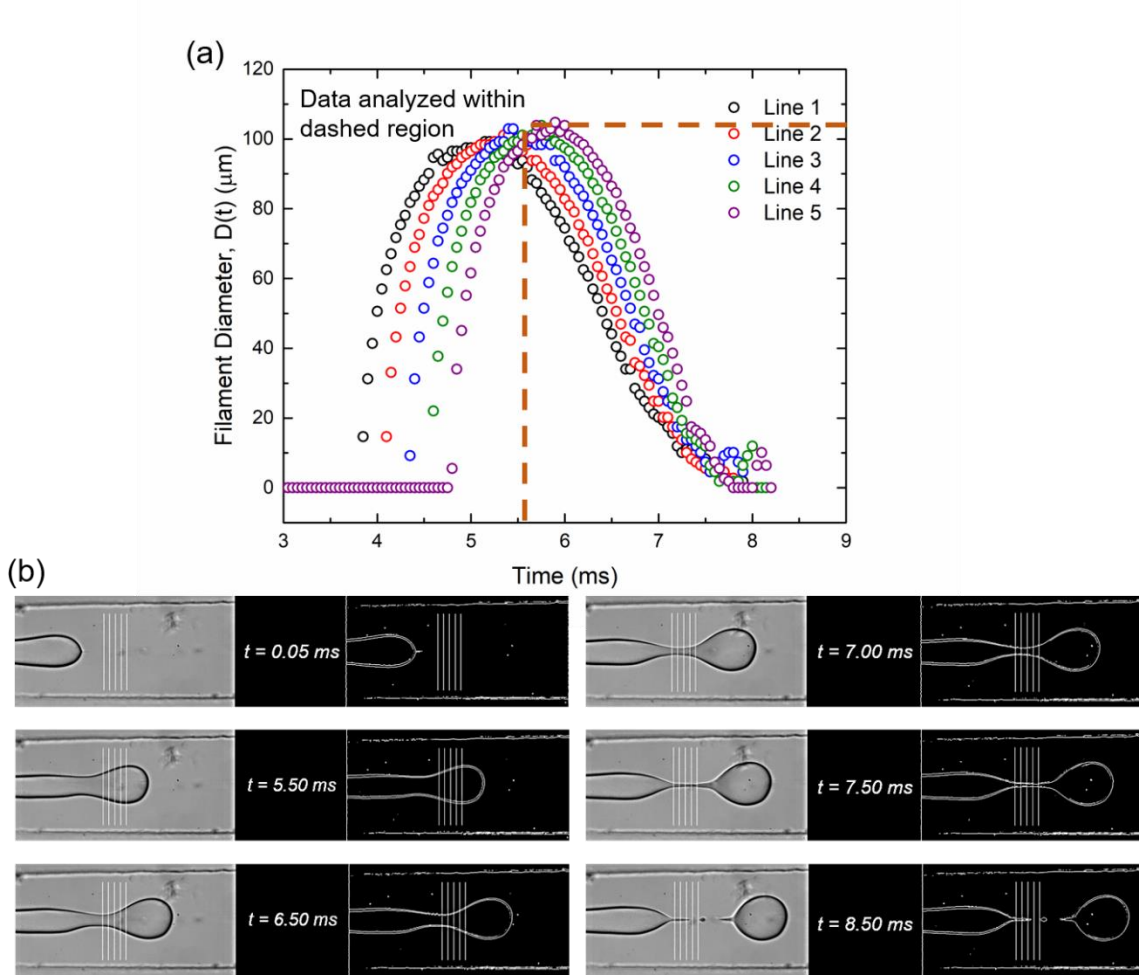


**Figure 3.7**: (a) Filament diameter of the fluid front for 1 wt% MC150 in 8 wt% NaCl passing through all five white, vertical lines in the snapshots of a sample movie shown in (b). The raw movie frame is on the left-hand side of each column, while the frame with applied thresholding is shown on the right-hand side of each column in (b). The vertical white lines indicate where the filament diameter, *D(t)*, can be measured. The channel width is 250 μm in all frames shown here. The area boxed in with the orange dashed lines indicates the region where the data were analyzed.

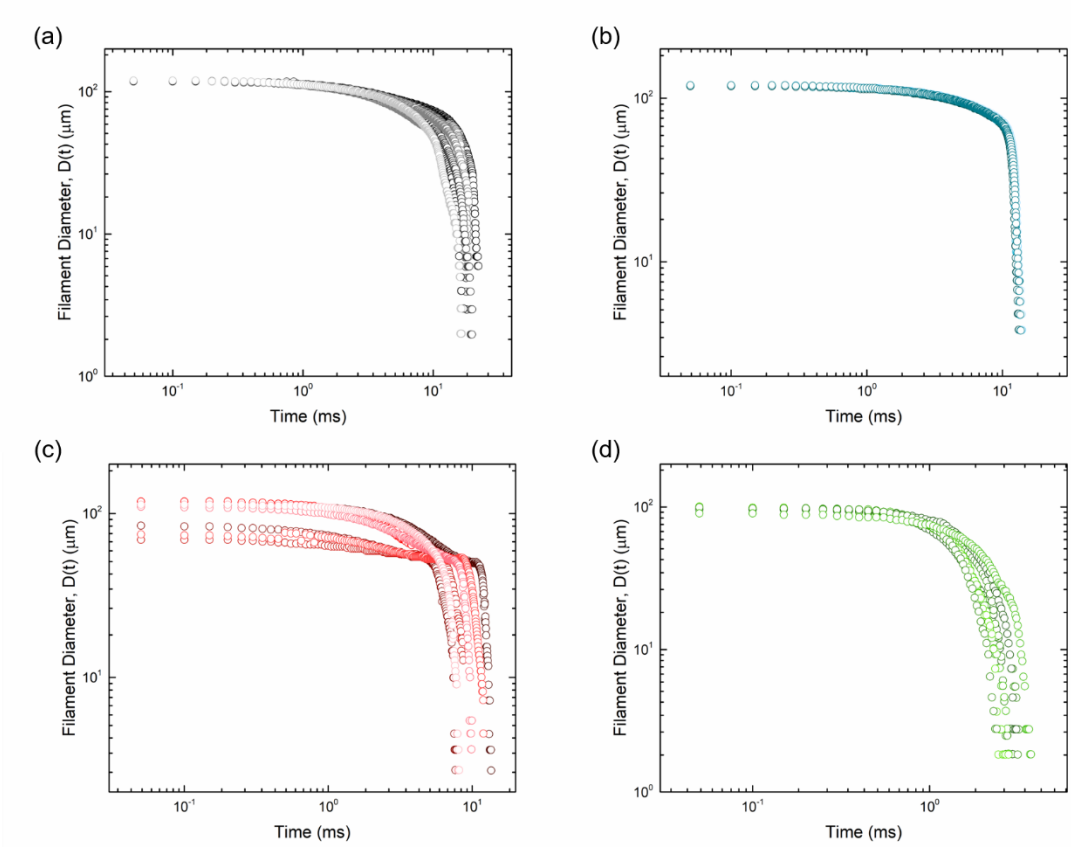


**Figure 3.8**: All transient filament diameter traces for (a) 0 wt% NaCl, (b) 2 wt% NaCl, (c) 5 wt% NaCl, and (d) 8 wt% NaCl.

## *3.3. Results and Discussion*

### *3.3.1. Shear Rheology of Aqueous Methylcellulose Solutions*

The viscoelastic properties of MC150 solutions as a function of temperature and NaCl concentration were measured using small-amplitude oscillatory shear. Solutions of 1 wt% MC150 at concentrations of NaCl ranging from 0 wt% to 8 wt% were heated from 0°C to 80°C and back at a temperature ramp rate of 1°C·min$^{-1}$. **Figure 3.9** shows that all MC150 solutions at varying NaCl concentrations undergo a sol-gel transition upon heating, as signified by the large increase in magnitude of the complex modulus, $|G^*|$. This is followed by a gel-sol transition upon cooling, as reflected in the large decrease in magnitude of $|G^*|$. These drastic changes in the complex modulus are attributed to the

formation of MC fibrils upon heating and their dissolution upon cooling, indicating that the process is thermoreversible, albeit with substantial hysteresis.[33,114]

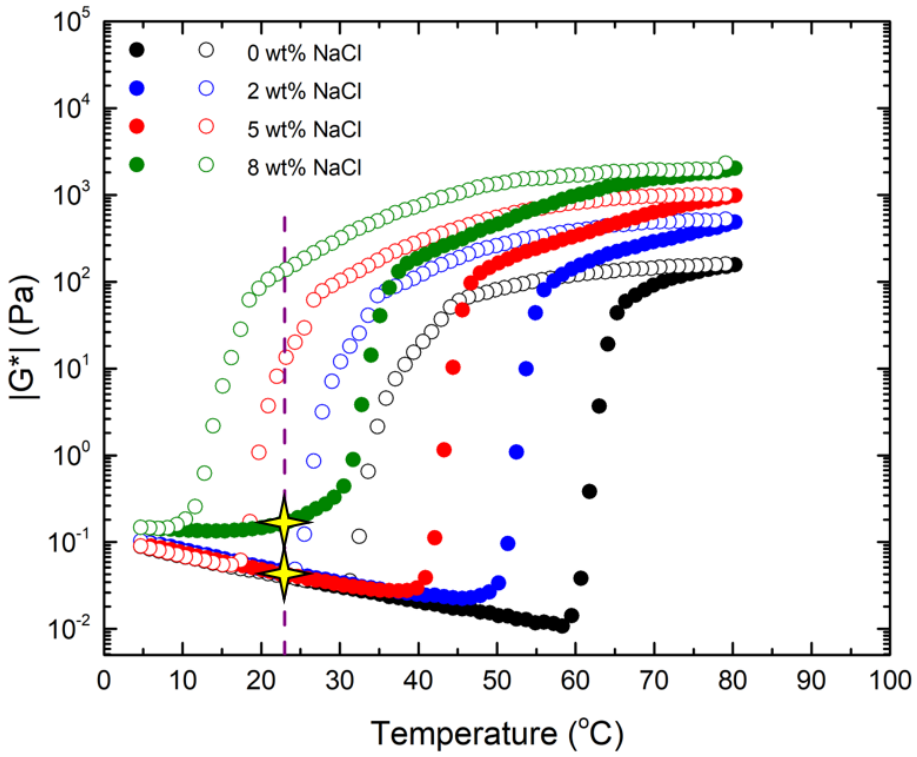


**Figure 3.9**: Complex moduli for 1 wt% MC150 solutions in 0, 2, 5, and 8 wt% NaCl at 1% strain, 1 rad·s$^{-1}$, and heating and cooling rates of 1 °C·min$^{-1}$. The filled and open symbols refer to heating and cooling traces, respectively. The purple, dashed line denotes the operating temperature of all microfluidic filament thinning experiments (23°C). The MC solutions for the filament thinning experiments were removed from the refrigerator and allowed to warm to 23°C (room temperature), thus falling on the "heating" trace as indicated by the yellow stars.

The addition of NaCl decreases both the gel temperature ($T_{gel}$), which is taken as the midpoint of the overall sharp increase in the complex modulus upon heating and the sol temperature, ($T_{sol}$) taken here as the midpoint of the sharp decrease in the complex modulus upon cooling, which is attributed to the transition of MC fibrils to dissolved chains. With sufficient NaCl, fibrils can be formed at lower temperatures. Indeed, there is a ~30°C difference between the sol-gel and gel-sol transitions between the two extreme

NaCl concentrations. The gel-sol transition, the lower temperature limit for fibril formation, is at or below room temperature for the 5 and 8 wt% NaCl solutions.[115] This behavior is consistent with what was observed for higher molecular weight MC solutions.[28,41] One aspect to note is that even at the highest concentration of NaCl, the solution still flows freely as the yield stress is only around 1 Pa as shown in **Figure 3.10**. This ability for the MC solutions to flow freely is imperative for pumping the solution through the microfluidic filament thinning device to maintain a Reynolds number, *Re*, of less than 1.

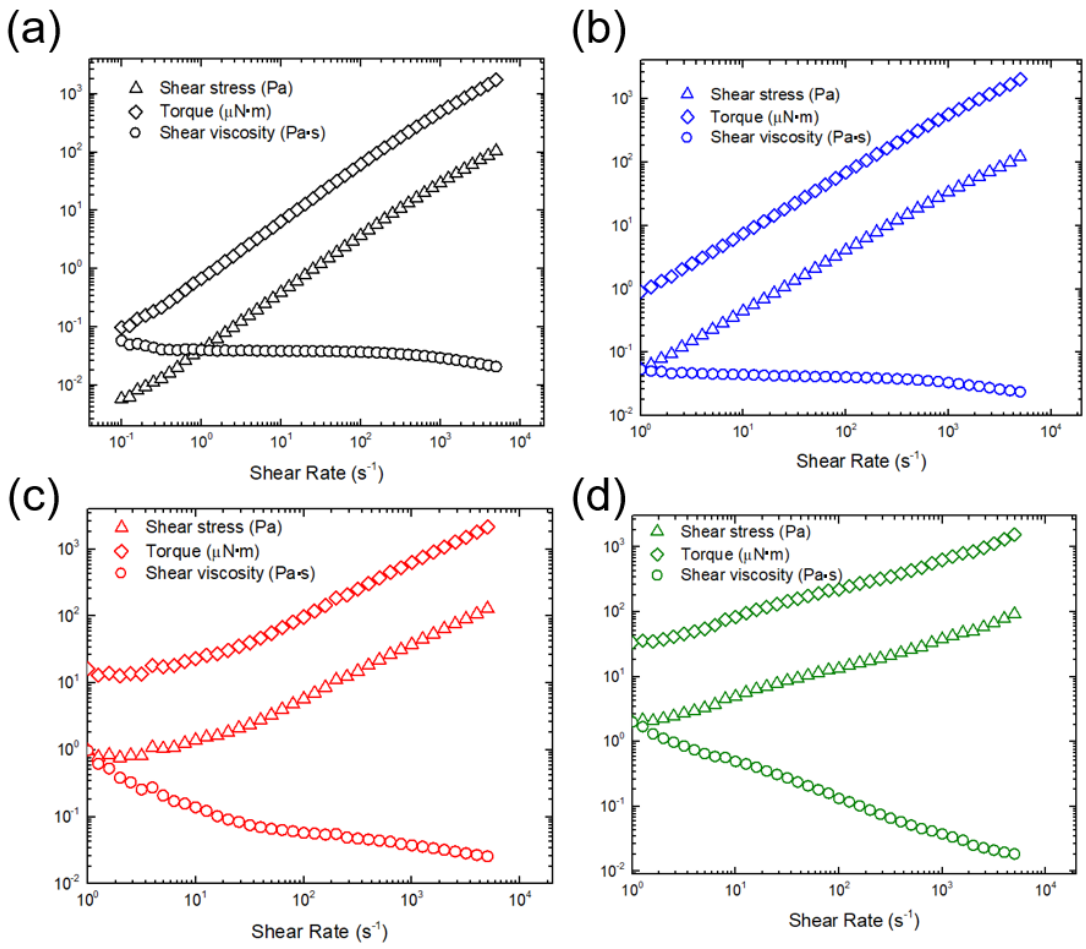


**Figure 3.10**: Shear stress, torque, and shear viscosity traces for 1 wt% MC150 in (a) 0 wt% NaCl, (b) 2 wt% NaCl, (c) 5 wt% NaCl, and (d) 8 wt% NaCl.

The steady shear behavior of the 1 wt% MC150 solutions is also modified by the presence of fibrils to varying degrees depending upon the NaCl concentration in solution.

The shear viscosity as a function of shear rate at room temperature (23°C) for each solution is shown in **Figure 3.11**. The shear thinning observed at higher shear rates > 250 $s^{-1}$ in all solutions is similar to what was observed at higher molecular weights of MC and is attributable to free (non-fibrillar) MC chains.[144] Similar behavior has also been observed by Dinic *et al*.[149] in an another cellulose ether analog, hydroxyethyl cellulose. At these higher shear rates, the shear viscosity decreases, and the flow behavior index, $n$, can be determined by fitting the higher shear rate values from 250 $s^{-1}$ to 5000 $s^{-1}$:

$$\eta_s = K\dot{\gamma}^{n-1} \tag{3.1}$$

where $\eta_s$ is the shear viscosity, $K$ is the flow consistency index, and $\dot{\gamma}$ is the shear rate. The flow behavior index decreases with increasing NaCl concentration, where $n$ = 0.831 ± 0.007, 0.821 ± 0.006, 0.793 ± 0.006, and 0.446 ± 0.009 for 0 – 8 wt% NaCl, respectively, as reported in **Table 3-1**. The power-law fits can be seen in **Figure 3.12**. The decreasing values of $n$ indicate more shear thinning with increasing NaCl concentration. At lower shear rates, the shear viscosity of the 0 wt% NaCl asymptotes to a zero-shear viscosity of 0.05 Pa·s. The shear viscosity behavior for the MC150 solutions containing NaCl, however, is not constant with shear rate. A second "shear thinning" regime is observed at lower shear rates (below 200 $s^{-1}$), attributed to the presence of fibrils. These differences in shear thinning behavior across the solutions will become important in the last section where the extensional rheological behavior of these solutions is discussed.

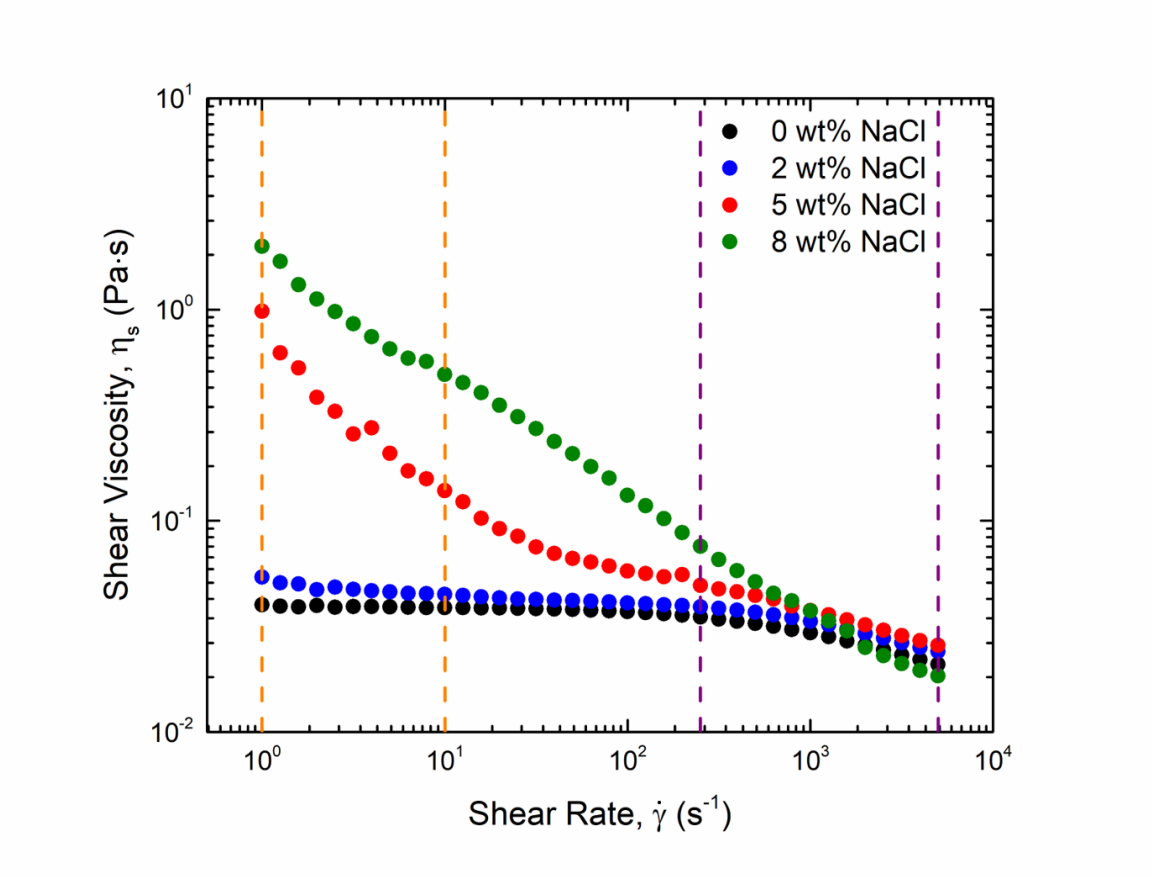


**Figure 3.11**: Steady shear viscosity as a function of shear rate for 1 wt% MC150 solutions in 0, 2, 5, and 8 wt% NaCl at 23°C. Two shear thinning regions separated by the vertical, dashed lines are present in the traces with NaCl: one at lower shear rates due to the shear thinning effects of the fibrils (orange, dashed lines) and one at higher shear rates due to the shear thinning effects of MC coils in solution (purple, dashed lines).

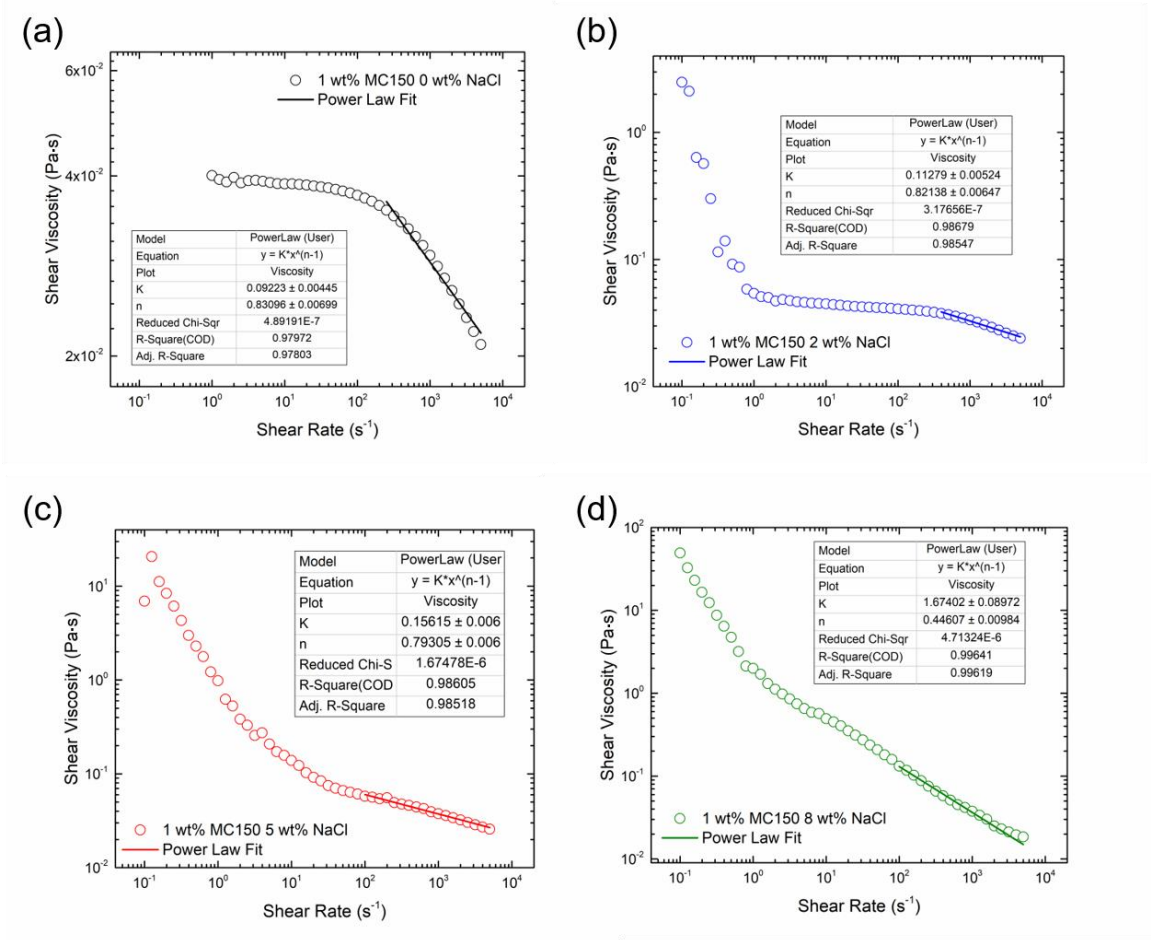


**Figure 3.12**: Power-law fits of the higher shear rates for each 1 wt% MC150 solution in (a) 0 wt% NaCl, (b) 2 wt% NaCl, (c) 5 wt% NaCl, and (d) 8 wt% NaCl. The fit is applied over a shear rate range from 250 $s^{-1}$ to 5000 $s^{-1}$, which is the data within the linear torque regime. The flow behavior index, *n*, and the consistency index, *K*, can be found from these fits.

### *3.3.2. Visualization of Methylcellulose Fibrils Annealed at Room Temperature*

As previously noted, the formation of MC fibrils is responsible for the onset of gelation and mechanical response of these samples. While the shear behavior suggests that intermolecular association occurs to give the response seen in **Figure 3.9** and **Figure 3.11**, it cannot produce a direct measure of the fibril structure. Cryogenic transmission electron microscopy (cryo-TEM) was therefore used to directly image the fibril structure.[32,33] Here, the occurrence of MC fibrils in the presence of NaCl for systems annealed at room temperature prior to vitrification was verified. **Figure 3.13a** depicts a 0.1 wt% MC150

solution with 0 wt% NaCl annealed for 24 h at room temperature prior to vitrification. As expected from the location of the sol-gel and gel-sol temperatures in **Figure 3.9** and the shear behavior in **Figure 3.11**, no fibrils are present. For the 0.1 wt% MC solution in 8 wt% NaCl, variations in contrast in the form of darker cylindrical objects, which are MC fibrils, on the lighter substrate can be seen in **Figure 3.13b**. As documented in a prior study by Schmidt *et al.*[41], the average fibril diameter remains constant regardless of molecular weight or concentration of the filament, but it does change with the amount of salt in solution. Because the fibrils contain water, the presence of NaCl increases the osmotic pressure, which ultimately extracts the water and therefore decreases the filament diameter from approximately 15 nm from prior SAXS and ImageJ analysis of cryo-TEM images to 11 nm using ImageJ analysis in this study. Similar behavior has been observed in other gel systems, where the presence of dissolved ions decreases the diameter of the respective structures.[150–152]

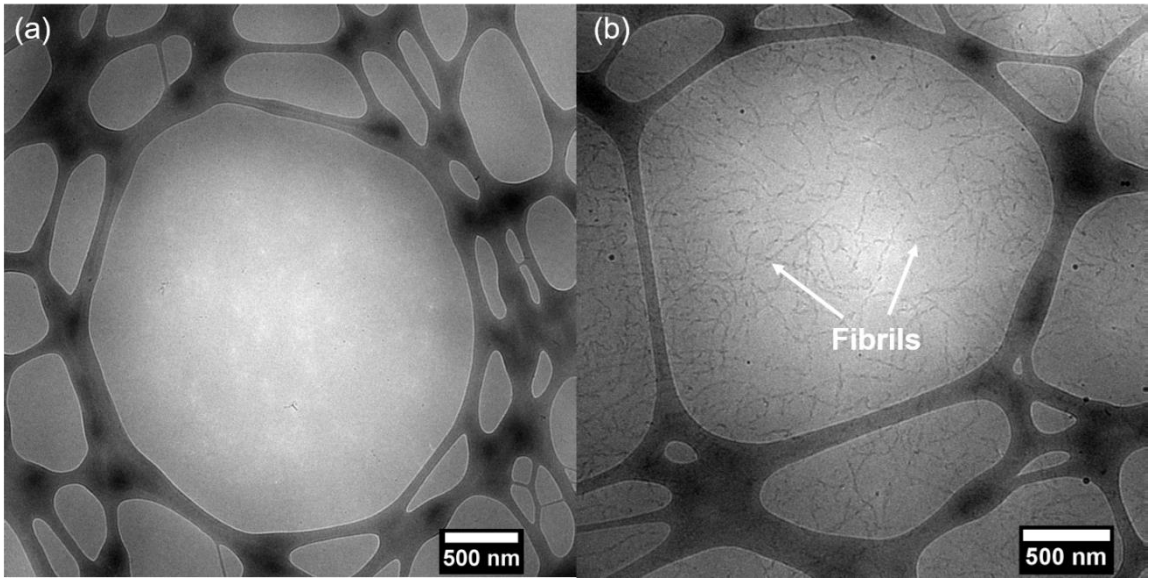


**Figure 3.13**: Cryo-TEM images of 0.1 wt% MC solutions in (a) HPLC-grade water and (b) 8 wt% NaCl annealed at 23ºC for 24 hours. Fibrils, denoted by the arrows, are only present for solutions with added NaCl at room temperature. The fibril diameters were measured using ImageJ to obtain an average diameter of 11 ± 1 nm.

### *3.3.3. Filament Thinning of Aqueous Methylcellulose to Measure Extensional Viscosity*

The filament thinning profiles of the MC solutions in the microfluidic devices generated from the movies are shown in **Figure 3.14a** as filament diameter, $D(t)$, as a function of time. As the NaCl concentration increased, the MC solution viscosity increased as shown in **Figure 3.11**, which required higher volumetric flow rates of the continuous silicone oil phase to form a filament, as shown in **Table 3-1**. This accounts for the progressively shorter breakup times as the NaCl concentration increased.[137] The volumetric flow rate for the dispersed aqueous MC150 phase remained constant for all experiments. Note that all flows are maintained in the laminar flow regime, as the Reynolds numbers range from *Re* = 0.012 at the lowest continuous phase flow rate to *Re* = 0.48 at the highest continuous phase flow rate. With this particular geometry, there is no dependence on the evolution of $D(t)$ with axial position as seen in **Figure 3.4-3.7**.[134]

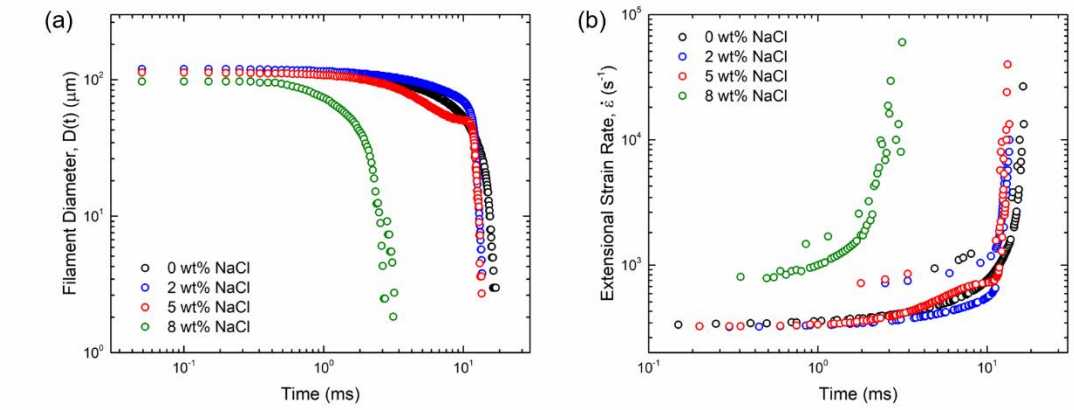


**Figure 3.14**: (a) Filament thinning of the MC solution at varying concentrations of NaCl with time. Measurements shown here are taken from a single point in the microfluidic device at 20,000 fps. (b) Calculated extensional strain rate of each MC solution with time. The strain rate drastically increases toward the end of the filament thinning process.

From the filament diameter data, the extensional strain rate of the filament can be calculated by the following relationship:

$$\dot{\varepsilon} = -\left(\frac{2}{D(t)}\right)\left(\frac{dD(t)}{dt}\right) \tag{3.2}$$

where $D(t)$ is the filament diameter, $t$ is time, and $\dot{\varepsilon}$ is the extensional strain rate of the MC filament. This form of extensional strain rate assumes that the filament is homogeneous in the axial direction.[153,154] Realistically, there is some variation in the filament diameter in the axial direction that would require an additional term to calculate the extensional strain rate. However, in these experiments, the local spatial rate of change in filament thickness is much smaller than the temporal rate of change, so the additional term can be neglected. To a good approximation, the filament can be treated as spatially uniform and **Eqn. 3.2** can be used to calculate the extensional strain rate, as seen in **Figure 3.14b**.[134]

**Figure 3.14b** shows that the extensional strain rate is initially independent of time, before sharply increasing by orders of magnitude. Both regimes ("flow-driven" filament thinning, where the extensional strain rate is constant with time, and "capillary-driven" filament thinning, where the extensional strain rate rapidly changes with time) contain information about the extensional viscosity of the solutions. In this regime, the filament diameter thins exponentially with time as seen in **Figure 3.14a**. Because the filament thinning is driven by the continuous phase (silicone oil) viscous stresses normal to the dispersed phase (MC solution) and pressure drag imparted by the droplet at the end of a thinning filament, a stress balance can be calculated across the interface between the two phases

$$\eta_E \dot{\varepsilon} = \eta_{E,oil} \dot{\varepsilon}_{oil} + \frac{F_{drag}}{\pi \left(\frac{D(t)}{2}\right)^2} \tag{3.3}$$

where the left-hand side represents the extensional stress of the MC solution and includes the extensional viscosity, $\eta_E$. The first term on the right-hand side represents the viscous stress the silicone oil applies to the MC solution, and the second term represents the reactive force acting on the filament due to the pressure drag exerted by the oil on the confined leading droplet, defined later with **Eqn. 3.5**.[97,155]

The extensional viscosity of the silicone oil, $\eta_{E,oil}$, can be found using the Trouton ratio, where the extensional viscosity is three times the shear viscosity. The calculated

extensional viscosity is 0.165 Pa·s at 23°C from cone and plate measurements. The extensional strain rate of the oil, $\dot{\varepsilon}_{oil}$, can be approximated using the strain rate from the cross region found by dividing the volumetric flow rate of the oil by the product of the square of the channel width by the channel height.[133,156] However, since the filament itself occupies a portion of the width and height, the extensional strain rate of the oil can be calculated with the following relationship

$$\dot{\varepsilon}_{oil} = \frac{U_{oil}}{W - D(t)} = \frac{Q_{oil}/[HW - \pi\left(\frac{D(t)}{2}\right)^2]}{W - D(t)} \tag{3.4}$$

where $U_{oil}$ is the cross-sectional velocity of the silicone oil, $W$ is the channel width, $H$ is the channel height, $D(t)$ is the filament diameter with time determined by image analysis, and $Q_{oil}$ is the volumetric flow rate of the silicone oil (see **Table 3-1**). The thinning filament can be thought of as cylindrical in shape as it is unconfined below the channel height, therefore the cross-sectional area is circular. **Figure 3.15** shows that the centerline velocity of the confined, leading droplet increases with increasing volumetric flow rate of the silicone oil as shown in **Table 3-1**.

**Table 3-1**: Summary of relevant parameters for shear and extensional rheological characterization of MC solutions. The error for density represents one standard deviation from the mean, the error for the power law index is from the power law fit, and the errors for the extensional viscosity and Trouton ratio represent a 95% confidence interval. The Trouton ratio calculated for each sample at a Hencky strain of 0.1 using the method discussed with **Eqn. 3.6**.

| NaCl Conc. (wt%) | Power Law Index, $n$ | Dispersed Phase Volumetric Flow Rate, $Q_d$ ($cm^3 \cdot min^{-1}$) | Continuous Phase Volumetric Flow Rate, $Q_c$ ($cm^3 \cdot min^{-1}$) | Flow-Driven Extensional Viscosity, $\eta_E$ (Pa·s) | Trouton Ratio |
|---|---|---|---|---|---|
| 0 | 0.831 ± 0.007 | 0.008 | 0.015 | 0.947 ± 0.005 | 26.9 ± 0.3 |
| 2 | 0.821 ± 0.006 | 0.008 | 0.015 | 1.62 ± 0.01 | 40.5 ± 0.3 |
| 5 | 0.793 ± 0.006 | 0.008 | 0.050 | 2.7 ± 0.4 | 56 ± 13 |
| 8 | 0.446 ± 0.009 | 0.008 | 0.600 | 15.1 ± 0.6 | 271 ± 35 |

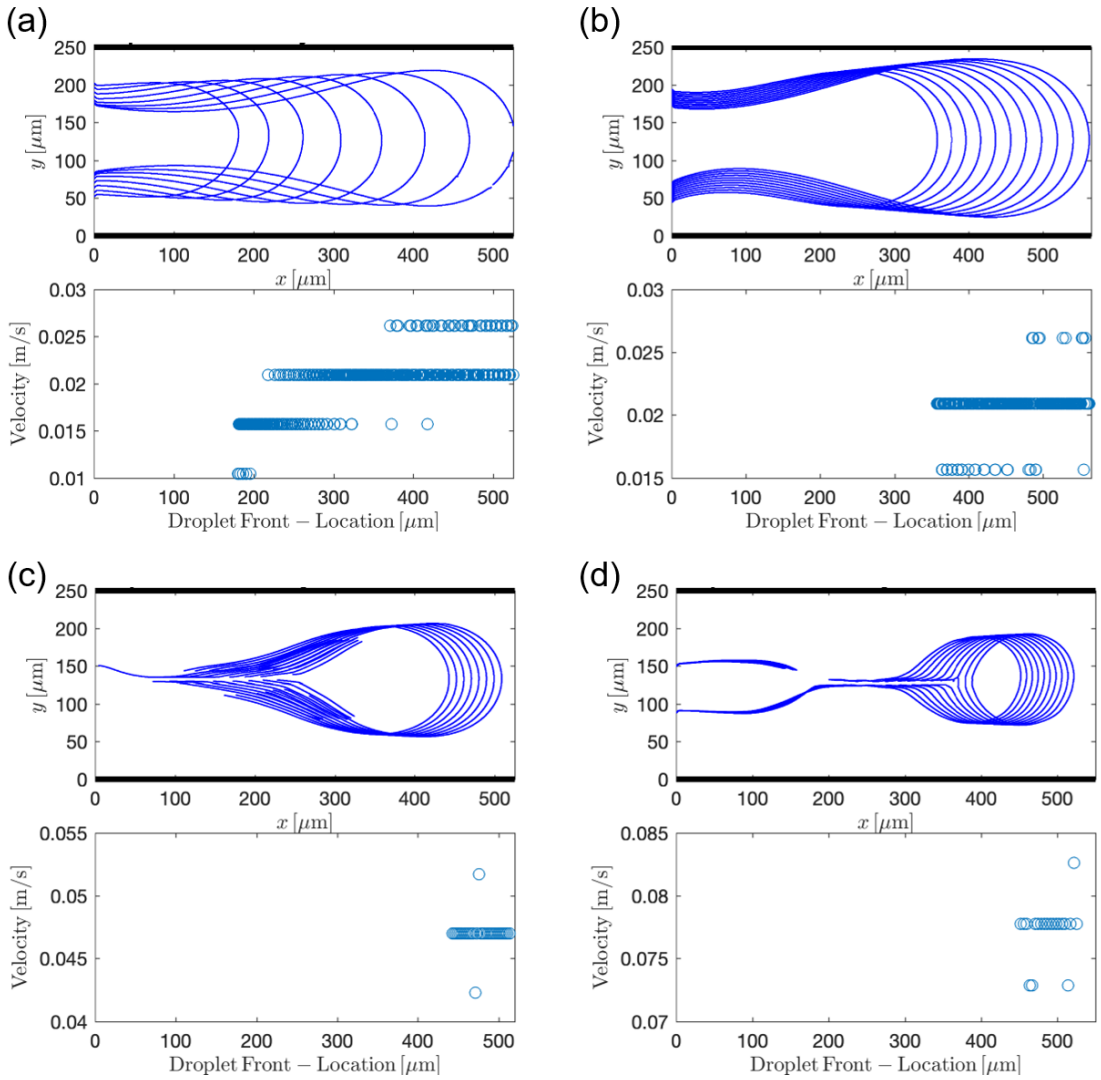


**Figure 3.15**: Leading droplet positions (top) and velocity (bottom) calculations using edge detection for 1 wt% MC150 in (a) 0 wt% NaCl, (b) 2 wt% NaCl, (c) 5 wt% NaCl, and (d) 8 wt% NaCl. The centerline velocity was used for drag force calculations described in the main text. The centerline velocities were 0.021 $m \cdot s^{-1}$ for both the 0 wt% and 2 wt% NaCl solutions, 0.047 $m \cdot s^{-1}$ for the 5 wt% NaCl solution, and 0.078 $m \cdot s^{-1}$ for the 8 wt% NaCl solution. The maximum sizes of the leading droplets were 185 μm, 195 μm, 160 μm, and 125 μm at 0 wt% NaCl, 2 wt% NaCl, 5 wt% NaCl, and 8 wt% NaCl, respectively.

To determine the drag force and ultimately axial stress due to drag on the overall stress balance across the thinning filament, the confined nature of the droplet must be considered. Although all experiments occur in the $Re < 1$ regime, Stokes' drag is not a good approximation to use here as the confined nature of the leading droplet resembles a

"pancake" rather than a sphere. The "pancake" geometry of the leading droplet is assumed here because in all cases, the diameter of the droplet is greater than the channel height of 120 μm (ranging from 125 μm at the smallest to 195 μm at the largest). In cases like these with a confined droplet where the radius of the droplet is larger than the channel height, the pressure drag will dominate over viscous drag, and for a fully confined case, there is no viscous drag contribution.[155,157,158] The pressure drag force component can be expressed as

$$F_{drag} = \frac{24\pi\eta_{s,oil}U_r R^2}{H} \tag{3.5}$$

where $F_{drag}$ is the pressure drag force specifically for a confined "pancake" droplet, $\eta_{s,oil}$ is the shear viscosity of the silicone oil, $U_{relative}$ is the relative velocity between the oil and the leading MC droplet ($U_r = U_{oil} - U_{droplet}$, with droplet velocity $U_{droplet}$ determined with image analysis, see **Figure 3.15**), and $R$ is the projected radius of the leading droplet. To calculate the axial stress, the drag force is then divided by the cross-sectional area of the thinning filament. One caveat here is that the droplets are only partially confined because for a fully confined case, $R/H > 4$.[159] Therefore, the true drag force and resultant extensional viscosity may be slightly modified as a result.

The quantity $\frac{\eta_{E,oil}\dot{\varepsilon}_{oil} + F_{drag}/\pi\left(\frac{D(t)}{2}\right)^2}{\dot{\varepsilon}}$, which is a rearranged expression from **Eqn. 3.3** and shares the same units as extensional viscosity, was calculated for all MC solutions as a function of time, and a representative set of results is shown in **Figure 3.16**. In the region where this quantity is nearly constant with time and therefore where the extensional strain rate of the MC is also nearly constant with time, the values can be averaged to determine the flow-driven apparent extensional viscosity.[134] The average flow driven extensional viscosities are shown with 95% confidence intervals in **Table 3-1**, and increase from 0.947 ± 0.005, 1.62 ± 0.01, 2.7 ± 0.4, and 15.1 ± 0.6 Pa·s as the concentration of NaCl increases from 0, 2, 5, to 8 wt%, respectively. These results are comparable to results obtained by Micklavzina *et al.*[143] using pressure drop measurements in a hyperbolic microchannel. The increase in extensional viscosity by an order of magnitude from 0 to 8

wt% NaCl is attributed to the formation of fibrils in the solution with NaCl. This effect was also seen in capillary breakup extensional rheology (CaBER) studies of higher molecular weight MC530.[28]

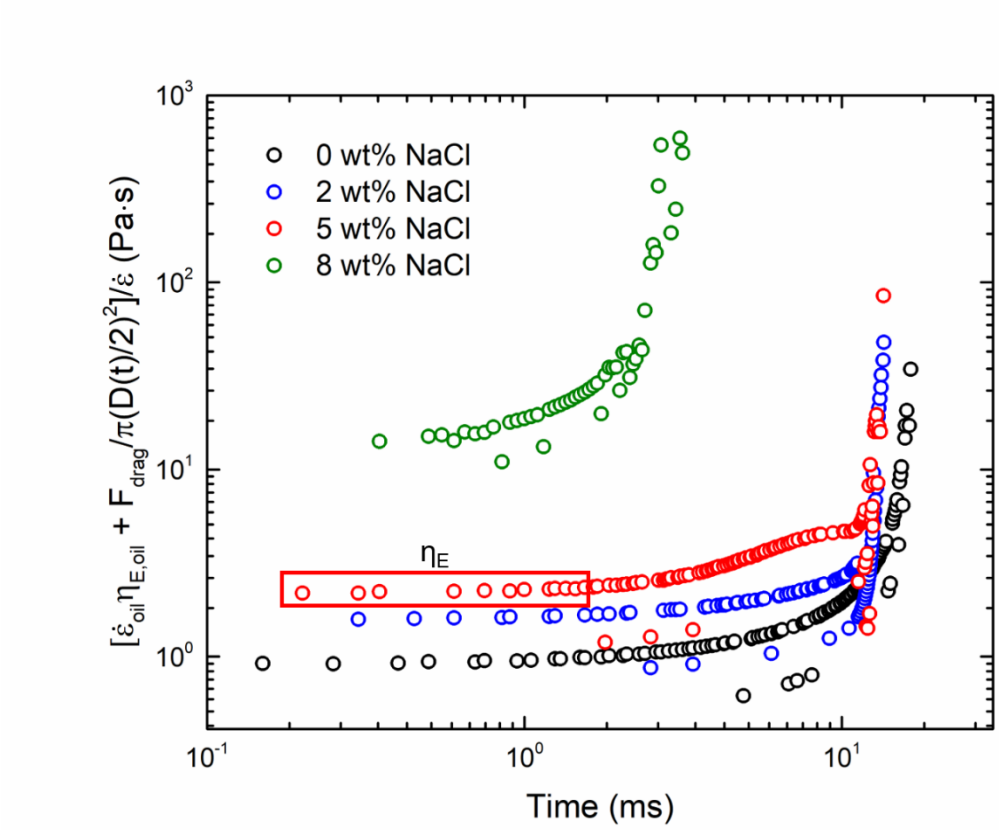


**Figure 3.16**: Stress balance of the outer, continuous oil phase with the inner, dispersed phase of the MC solutions with time. The portions of the plot where the quantity is nearly constant with extensional strain rate and time is the flow-driven extensional viscosity, $\eta_E$. The red box shows an example of this flow-driven region, and the values for each MC solution are reported in **Table 3-1**.

Prior studies using CaBER with MC solutions and the filament stretching technique used here with other polymer solutions show that the extensional viscosity increases above a certain extensional strain rate due to polymer chains aligning and elongating with the direction of the extensional flow field.[28,134] However, the extensional strain rates that were used in those studies were much smaller (*e.g.*, 50 $s^{-1}$ from Arratia *et al.*[134]) than the extensional strain rates used in the present study and by Micklavzina *et al.*[143] (*e.g.*, 10,000

$s^{-1}$). To quantify the relationship between the extensional and shear viscosities, the Trouton ratio was calculated considering uniaxial extensional flow using the following equation

$$Tr = \frac{\eta_e(\dot{\varepsilon}_H)}{\eta(\dot{\varepsilon_H}\sqrt{3})} \tag{3.6}$$

where the extensional viscosity, $\eta_e$, and the shear viscosity, $\eta$, are evaluated at the Hencky strain rate, $\dot{\varepsilon}_H$, and the shear rate equivalent to $\dot{\varepsilon_H}\sqrt{3}$. Approximating the thinning filament as cylindrical, the Hencky strain, $\varepsilon_H$, can be calculated using,

$$\varepsilon_H = 2\ln\left(\frac{D}{D(t)}\right) \tag{3.7}$$

and the derivative at different time points can be used to calculate the Hencky strain rate from the Hencky strain values.[22,160] The Trouton ratios calculated using **Eqns. 3.6** and **3.7**, shown in **Table 3-1**, are found to be 26.9 ± 0.3, 40.5 ± 0.3, 56 ± 13, and 271 ± 35 for 0 wt%, 2 wt%, 5 wt%, and 8 wt% NaCl, respectively. Trouton ratios larger than 3 for non-Newtonian fluids such as the MC solutions tested here are generally expected.

One should note that the extensional strain rate using the filament thinning device in this study is fixed by the ratio of the volumetric flow rates of the dispersed and continuous phases. Further studies would be needed to explore how the extensional viscosity would depend on strain rate. While this could result in commonly observed extensional thickening, it is also possible to expect extensional thinning seen with similar MC solutions and other entangled and branched polysaccharide systems.[10,143,161–163] From the study of the extensional properties of MC solutions, the presence of fibrils continues to have a major effect on the flow-driven extensional viscosity even for low viscosity, weakly elastic MC solutions whose extensional viscosities cannot be measured using traditional macroscale techniques.

## *3.4. Conclusion*

This study has shown that the extensional viscosity of low molecular weight and low viscosity MC solutions can be determined using a flow-focusing microfluidic device

at room temperature, with values comparable to other work that utilized microchannels to elucidate extensional viscosity. The increase in apparent extensional viscosity by an order of magnitude from 0.947 Pa·s to 15.1 Pa·s as the NaCl concentration increased from 0 to 8 wt% was attributed to the presence of a fibrillar MC network in solution at room temperature. The presence of a fibrillar network that forms because of the addition of NaCl to the solution was confirmed by cryo-TEM and shear rheology experiments, corroborating prior studies using macroscale techniques to determine extensional viscosity. This technique provides the opportunity to study extensional viscosity in solutions with lower viscosities and higher extensional strain rates than are accessible with other commercial techniques, including the CaBER.

# Chapter 4

# *In Situ* Polymer Flocculation and Growth in Taylor-Couette Flows†

†Portions of this chapter consist of a journal article cited as A. Metaxas, N. Wilkinson, E. Raethke, and C. S. Dutcher, *In situ* polymer flocculation and growth in Taylor-Couette flows, *Soft Matter*, 14, 8627-8635 (2018), reproduced by permission of The Royal Society of Chemistry.

## *4.1. Introduction*

The removal of solid particulates using polyelectrolyte-driven flocculation is a common process in a variety of applications including paper manufacturing and drinking water treatment.[44,45,50] Despite its widespread use, the process remains poorly understood due to the complexity of the system. Therefore, treatment plants rely on highly empirical methods to determine polymer flocculant dosing levels. Charged polymers are added to a fluid system during mixing to bind onto suspended particulates, thus forming flocs. Rapid floc growth is then enabled by orthokinetic aggregation, where the polymer-coated particulates collide due to fluid motion and the velocity gradient during the mixing process depends on the nature of the fluid flow.[47–49] The local hydrodynamics around a growing floc is one of the key factors that affects the conformation of the polymer on the surface. Extensional forces in particular can stretch the polymer from the surface to lengths greater than the radius of gyration, $R_g$, of the free polymer in solution, increasing the bridging

capability of the polymer.[54,81] As the flocs are formed and grow during the flocculation process, they can eventually break due to fluid shear forces.[59,61] After some time, the flocs will approach a steady state between floc growth and breakage.[58,80,164]

There are several different molecular-level mechanisms for polymer-particle adsorption and flocculation events, including charge neutralization, polymer bridging, charge-patch flocculation, and polymer depletion.[44,50–53] The aqueous environment affects the underlying flocculation mechanism through highly interrelated physicochemical properties including the suspension composition (pH, ionic strength, and salt valency),[54] coagulant type,[55,56] particle surface properties,[57] and dosing and mixing conditions.[58–60] In this study, bentonite was used as the solid particulate of interest. Bentonite is an anisotropic smectite clay commonly found in surface waters with a high adsorption capacity for water and has been used in other flocculation studies.[7,63–65] Individual bentonite particles can be visualized as thin sheets with negatively charged faces and either positively or negatively charged edges depending on the solution pH.[68,69] As a result, bentonite sheets can be arranged in a porous, edge-face arrangement, an edge-edge arrangement, or a dense, face-face structure.[70,71] Variations in aggregate surface morphology more than likely result in different polyelectrolyte adsorption capacities and interaction potentials due to the uneven charge distribution of the functional edge groups.

These complex interdependencies on the floc assembly kinetics and final floc microstructure are not well understood and can result in poorly optimized polymeric dosing, which is one of the major technical issues treatment plants face. Under-dosing results in insufficient particulate removal and over-dosing results in particulate restabilization. Both are undesirable outcomes, which can be cost-prohibitive in water treatment.[46] Flocs fragmented resulting from shear forces can be re-suspended and are often more difficult to remove than the initial particulate. For optimal separation, large hydrodynamically robust flocs are desired for flocs to readily settle out due to gravity, as well as withstand turbulent stresses in the flow with little to no fragmentation.[44,61,62]

The effects of physicochemical and hydrodynamic conditions on final floc microstructure have been examined using small angle light scattering, yielding final floc

size and fractal dimensions.[82–84] These studies found that the longer characterization length scales accessible by static light scattering work well to determine mass fractal dimensions. However, interpretation of the scattering patterns can be difficult, and static light scattering works best for smaller aggregates with loosely packed structures. Recently, advanced image analysis techniques have been used to study the dynamic flocculation behavior using jar tests and impellers, which offers a more non-intrusive method of studying the flocs as compared to obtaining and preparing a sample for light scattering experiments.[59] Jar tests replicate scaled-down industrial water treatment conditions but lack homogeneous spatial and temporal flow features that are needed to precisely study floc strength as a function of hydrodynamic flow. In addition to the lack of varied flow states, the shear stresses within the fluid cannot be accurately controlled in a jar test to determine the point where floc breakage occurs.[62,92]

Unlike jar tests, Taylor-Couette (TC) cells, devices consisting of two concentric cylinders with a specified gap width, offer an experimental method to study mixing events with the ability to precisely control the hydrodynamics. TC cells can generate a wide variety of flow states as a function of either or both cylinder speeds, and they range from laminar types to turbulent types.[165–170] Four different flow states were used in this study in order of increasing inner cylinder speed: (1) laminar Taylor vortex flow (LTV), (2) laminar wavy vortex flow (LWV), (3) turbulent wavy vortex flow (TWV), and (4) turbulent Taylor vortex flow (TTV). Laminar Taylor vortex flow consists of axisymmetric, toroidal vortices with a characteristic spatial frequency but no temporal frequency, whereas laminar wavy vortex flow consists of a characteristic temporal and spatial frequency.[171] From a qualitative perspective, LTV flow look like a series of parallel bands whereas LWV flow appears as parallel waves. The turbulent cases of these two flow states physically resemble their laminar counterparts with additional turbulent features such as eddies. The wide variety of flow states accessible by a TC cell, in addition to optical access via the transparent outer cylinder has made it an ideal tool to study a variety of processes such as polymer drag reduction, catalysis, filtration, and liquid-liquid mixing.[172–174] TC cells have

also been used to study flocculation, although prior studies with TC cells were limited in that flocs had to be pre-formed outside of the cell.[61,87,93,175]

To study the entirety of the mixing process in an in-situ manner, a modified TC cell has been designed and built by Wilkinson and Dutcher[94] to directly inject the polymer flocculant into the annulus. Unlike other TC cells where the injection was in a single location or protruded into the annulus, using the cell built by Wilkinson and Dutcher, one has the ability to inject flocculant at multiple, precisely spaced axial and azimuthal locations to allow for larger volume injections and smoothing of any azimuthal concentration gradients.[94,173,176,177] The injection ports are built into the inner cylinder and the port covers lie flush against the surface of the inner cylinder and are contour-matched to prevent any alteration of the flow profile. Additional studies with this modified TC cell recently published by Wilkinson and Dutcher[95] have been conducted to determine the stability of flow vortices to injection, and the flow states tested in this study are stable over a wide range of cylinder speeds, injection drive pressures, and injection times. The advantages this modified TC cell offers over other cell designs include the ability to explore initial mixing effects in flocculation of bentonite clay with a polyelectrolyte flocculant. Optical access allows for image analysis techniques to calculate the size, morphology, and growth rate of flocs in a precise hydrodynamic flow state. The goal of this study is to determine the effect of changing speed, and therefore flow state, on floc size, growth rate, and morphology.

## *4.2. Materials and Methods*

### *4.2.1. Materials*

The polymer flocculant, or polyelectrolyte, used in this study is a commercially available cationic polyacrylamide (FLOPAM FO 4190 SH, SNF Polydyne) with 10 mol% quaternary ammonium cation monomer charge groups and a molecular weight of 4-6 x $10^6$ $g \cdot mol^{-1}$. A 0.2 wt% polymer solution was made by using a Jiffy mixer attachment to mix the solid polymer pellets into distilled water for 30 min. The polymer rested in a refrigerator overnight prior to use and was remade every 2 weeks as necessary per supplier instructions. The distilled water used was from Premium Waters, Inc. Powdered Na-Bentonite was ACS

grade from Fisher Scientific and was used as received. The kinematic viscosity of the 30 mg·L$^{-1}$ bentonite suspension was 1.00 ± 0.05 cSt from steady shear experiments as shown in **Figure 4.1**, which showed Newtonian behavior in the frequency regions relevant to the speeds tested in this study.

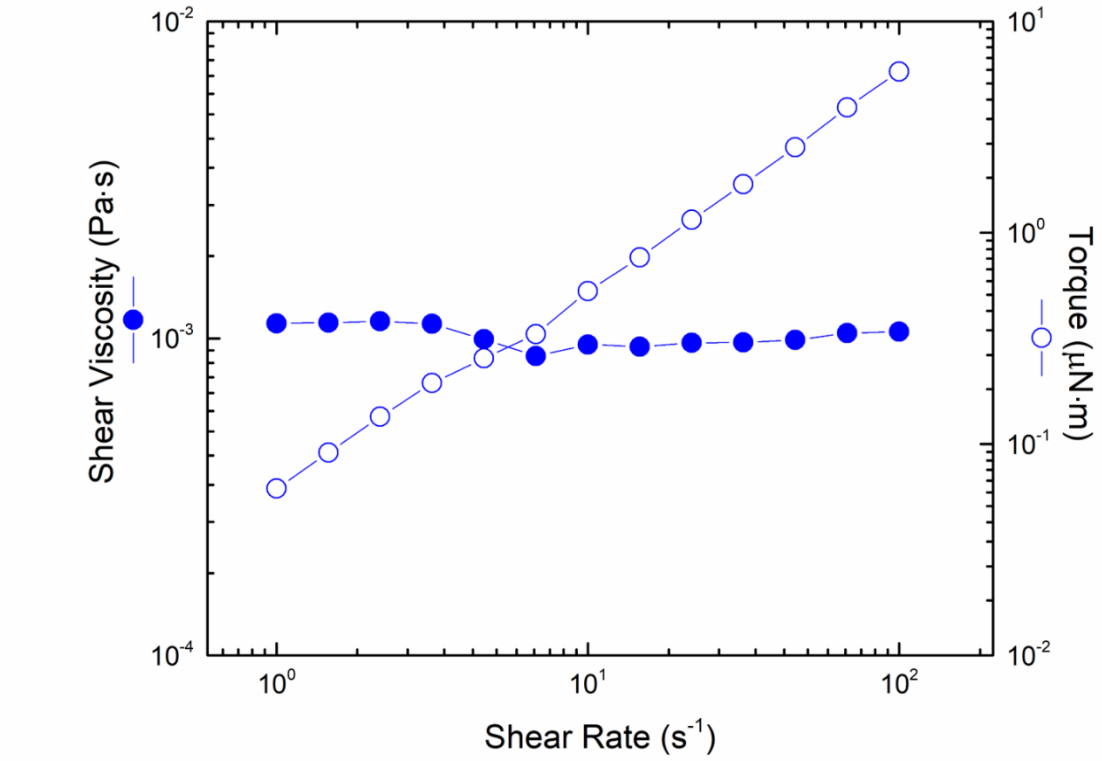


**Figure 4.1**: Steady shear viscosity and torque response traces of 30 mg·L$^{-1}$ bentonite in distilled water from shear rates of 1 s$^{-1}$ to 100 s$^{-1}$. The temperature was kept constant at 23ºC. The experiment was performed using a cup and bob geometry to mimic the TC cell geometry.

*4.2.2. Sample Loading into TC Cell Annulus and Spatial Calibration*

The TC cell used in these experiments consists of a total of 16 injection ports evenly distributed axially and azimuthally into the inner cylinder. Because the injection ports do not protrude into the annulus and the port covers are contour-matched to the inner cylinder, the flow profile of the resultant vortices are not modified during operation as shown by

Wilkinson and Dutcher.[94] Additional details on the TC cell design, with inner cylinder diameter of 13.5407 ± 0.0025 cm, gap width of 0.84 cm, inner cylinder radius to outer cylinder radius ratio of 0.891, and injection assembly can be found elsewhere.[94] To make the bentonite suspensions, 30 mg of bentonite was transferred to a 2 L beaker filled with 1 L of water. This process was repeated to make a total of 2 L of 30 $mg \cdot L^{-1}$ bentonite suspensions. The bentonite was dispersed using a VELP Scientifica JTL4 Flocculator for 30 min at 300 RPM. The pH of the resultant suspensions is approximately 6.6 due to the interaction of dissolved carbon dioxide in water and bentonite.[178] Since the size and morphology of bentonite, an anisotropic particle, is dependent on solution ionic strength and pH, respectively, these two parameters were kept consistent between all experiments in this study[90,91]. Once finished, the bentonite suspensions were immediately transferred to the annulus of the TC cell by way of tubing attached to the base of the cylinder assembly as seen in **Figure 4.2**.

Once the bentonite was loaded, refractive index-matching paraffin oil was poured into the Plexiglass tank holding the apparatus to eliminate the curved glass surface of the outer cylinder. The cell was axially illuminated with a flicker-free LED light strip (Metaphase 19 in Exo2 Light) to better visualize the injection port covers for spatial calibration for image analysis. A spatial calibration image of the bottom-most port cover of the inner cylinder was captured using a Basler Ace camera (1280 × 1024 pixels, 60 fps maximum frame rate) with a Tamron 25 mm c-mount lens. ImageJ was then used to calculate the pixel-to-mm ratio of the spatial calibration image.

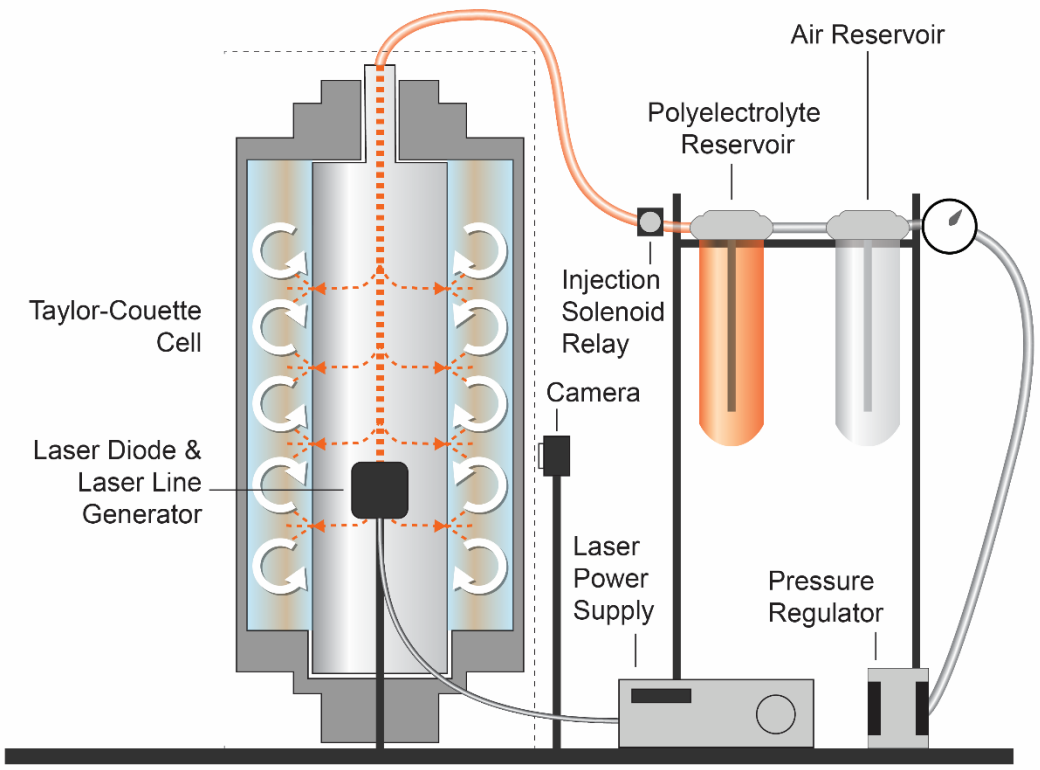


**Figure 4.2**: Flocculation experimental set-up in the TC cell. The bentonite suspension is loaded into the annulus by way of tubing attached to a Swagelok valve at the bottom of the cylinder base. The polyelectrolyte is held in a reservoir and is injected at the top of the inner cylinder by way of a solenoid valve, which is controlled by a LabView program. The stepper motor for the inner cylinder is controlled separately by a motor controller. Under normal operating conditions, the Plexiglass tank surrounding the TC cell is filled with paraffin oil to match the index of refraction of the glass outer cylinder, which eliminates its curved surface during recording.

### *4.2.3. Flocculation Experiment Protocol*

The inner cylinder is rotated by a stepper motor (Applied Motion Products HT34-497 2 phase stepper motor with a STAC5-S-E120 controller) equipped with a 7:1 gear reducer (Applied Motion Products 34VL007) for inertial balance between the motor and the cylinder. To remove unwanted flow dislocations in the vortices, flow priming was conducted by way of a motor control script to ramp down from a speed higher than the required speed to the intended speed.[95] A laser diode (Thorlabs, 450 nm, 1600 mW max) combined with a laser line generator was used to create a laser light sheet tangential to the

inner cylinder as shown in **Figure 4.3a**. The cationic polyacrylamide injection process and movie recording were operated using LabView. For all experiments, the drive pressure was set to 30 psi to inject cationic polyacrylamide from the injection ports into the annulus at a calibrated injection rate of 1.115 $g \cdot s^{-1}$ for 6 as reported in Wilkinson *et al*.,[94] which corresponds to the optimal polymer dose for the bentonite-distilled water of ~8 ppm as reported elsewhere.[90] The camera was vertically adjusted such that the field of view was between the third and fourth injection port covers from the bottom of the annulus. The frame rate of the camera was set to 30 fps with an exposure time of 8 ms for all experiments.

As discussed later, flocculation mixing protocols typically have two speeds – an initial "Mix" speed (Stage 1), followed by a slower "Growth" speed (Stage 2). However, these standard names may be misleading: some growth can occur in the early "Mix" stage, and mixing can occur in the later "Growth" stages. In this study, the early Stage 1 steady "Mix" speeds were 0.04 $s^{-1}$, 0.17 $s^{-1}$, 0.50 $s^{-1}$, 1.10 $s^{-1}$, and 1.47 $s^{-1}$, and the later Stage 2 steady "Growth" speed is fixed at 0.46 $s^{-1}$. After flow priming, the initial inner cylinder Stage 1 rotational speed was set, and the recording started. After a 30 s delay, the polymer was injected and mixed at this Stage 1 speed for 3 min to distribute the polymer throughout the annulus. After 3 min at the Stage 1 speed, the inner cylinder speed was then set to the Stage 2 speed of 0.46 $s^{-1}$ at a quick ramp rate of 0.92 rotations$\cdot s^{-2}$ for 30 min to allow the flocs to grow. The value of 0.46 $s^{-1}$ was chosen as it was the slowest speed tested which was able to suspend enough flocs throughout the duration of the flocculation process for image analysis. Once each experiment was completed, the annulus was drained, and the inner cylinder was removed from the apparatus for cleaning with a dilute solution of Micro-90. The inner cylinder drive shaft and ports were re-primed with cationic polyacrylamide. Once reassembled, the annulus was refilled with distilled water prior to the next experiment.

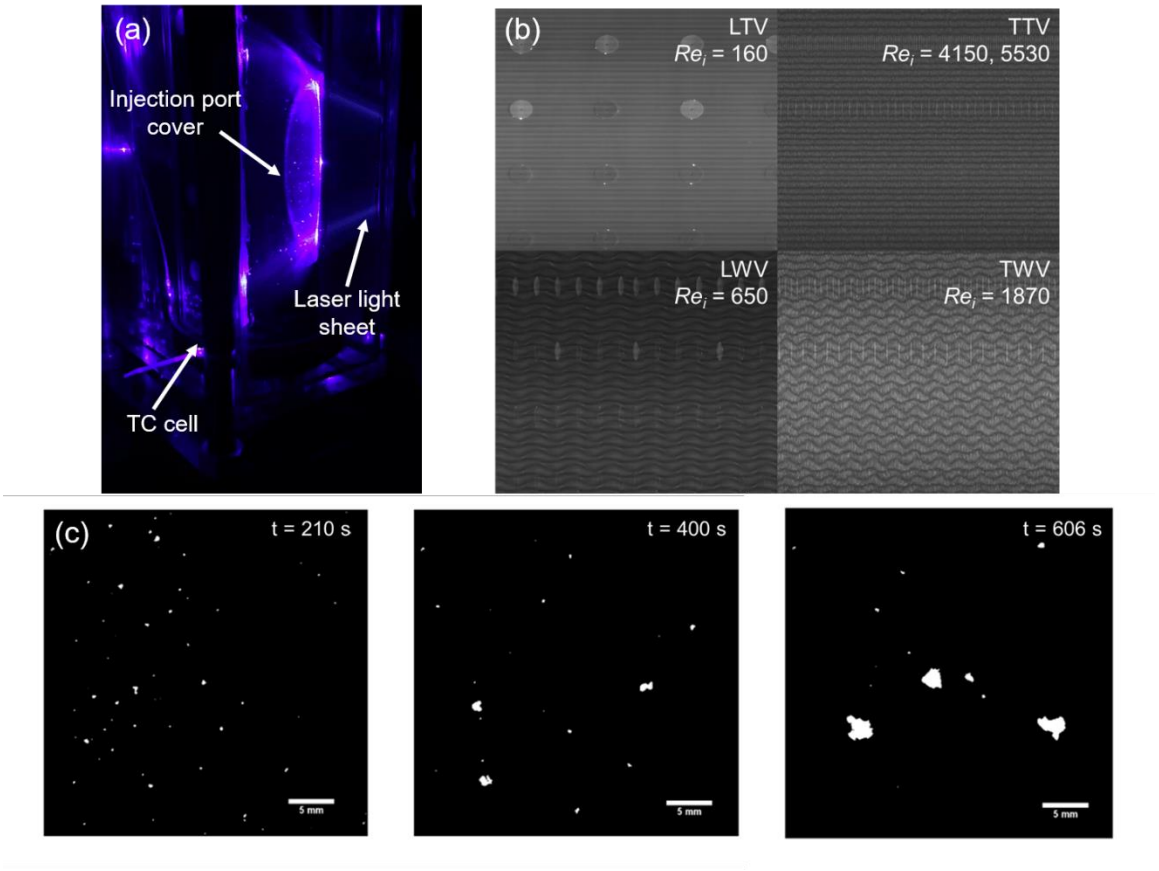


**Figure 4.3**: (a) Laser light sheet generated from laser diode illuminating the injection port cover and bentonite flocs. (b) The four wave states with their vortex type and speed in terms of Re. There are two laminar types (Laminar Taylor Vortex, LTV, and Laminar Wavy Vortex, LWV) and two turbulent types (Turbulent Taylor Vortex, TTV and Turbulent Wavy Vortex, TWV). The gray circles present in the image are the injection port covers. (c) Binarized images of bentonite flocs from at 210 s, 400 s, and 606 s into flocculation at an inner cylinder Growth Speed of $Re_i$ = 4150. Scale bars are all 5 mm in length.

### *4.2.4. Image Analysis of Flocculation Experiments*

The movies were analyzed in MATLAB using a process adapted from Vlieghe *et al.*[61] to obtain floc size and morphology information as a function of time. The raw images were converted to grayscale images and binarized for all experiments as shown in **Figure 4.3c**. Size was reported in terms of the radius of gyration, $R_g$, of the floc as calculated by the following equation,

$$R_g^2 = \frac{1}{N_p}\sum_{i=1}^{N_p}[(x_i - x_c)^2 + (y_i - y_c)^2] \quad (4.1)$$

where $N_p$ is the number of pixels making up each floc, $(x_i, y_i)$ are the individual pixel coordinate pair, and $(x_c, y_c)$ is the centroid coordinate pair. The area average for all flocs in a 10 s interval (300 frames) was computed.

To quantify the morphology of the flocs, a surface-based 2-D fractal dimension, $D_{sf}$, was calculated using the following relationship as reported by Vlieghe *et al.*[61]

$$A \propto P^{2/D_{sf}} \quad (4.2)$$

where *A* is the cross-sectional floc area, and *P* is the floc perimeter. The fractal dimension varies in value from 1 to 2, where a value of 1 indicates a circular shape and a value of 2 indicates a rod-like shape. A linear regression was performed on each 10 s set of data (A, P) to determine $D_{sf}$.

## *4.3. Results and Discussion*

### *4.3.1. Effect of Hydrodynamics on Floc Size and Growth Rate*

In water treatment processes, it is preferable to rapidly mix the flocculant for a short period of time with the solid particulate of interest to disperse the polymer throughout the suspension as quickly and evenly as possible. This faster mixing step (Stage 1) is followed by a slower mixing step (Stage 2) for a longer time period to allow for continued floc growth.[179] To test the effect of both mixture speed and vortex flow on the growth of the flocs, four different flow regimes were selected for Stage 1 mixing. A set of laminar flow states with corresponding Taylor and wavy vortex types (LTV and LWV, respectively), and a set of turbulent flow states with corresponding Taylor and wavy vortex types (labeled TTV and TWV, respectively) were used for this study as shown in **Figure 4.3b**. The flow states were reported in terms of the inner cylinder Reynolds number, $Re_i$. The Re for TC flow is defined by the following equation

$$Re_i = \frac{\Omega_i R_i d}{\nu} \quad (4.3)$$

where $Re_i$ and $\Omega_i$ are the inner cylinder radius and rotational speed, respectively, $d$ is the gap width between the inner and outer cylinders, and $\nu$ is the kinematic viscosity of the sample.[180] The Stage 2 mixing speed was kept constant for all experiments at $Re_i$ of 1680 (TWV). For this particular TC cell, the ranges for the flow states in terms of $Re_i$ are 124 to 167 for LTV, 251 to 870 for LWV, 1400 to 2924 for TWV, and above 2924 for TTV.

**Figure 4.4** depicts the time-dependent radius of gyration, $R_g$, for the bentonite flocs as a function of time and vortex flow type. The radius of gyration of the flocs increases in all runs after the initial injection of cationic polyacrylamide at time = 30 s, until a plateau value of $R_g$ is obtained. The plateau values of $R_g$ were approximately 1.1 mm in the LWV, TWV, and TTV cases while the plateau value was approximately 0.7 mm in the LTV case. Shear breakage of the flocs due to velocity gradients present in the flow limit the maximum floc size.[49,55,59,87] Interestingly, the curves for the $Re_i$ of 4150 and 5530 cases show nearly identical growth behavior, most likely due to their having the same vortex type.

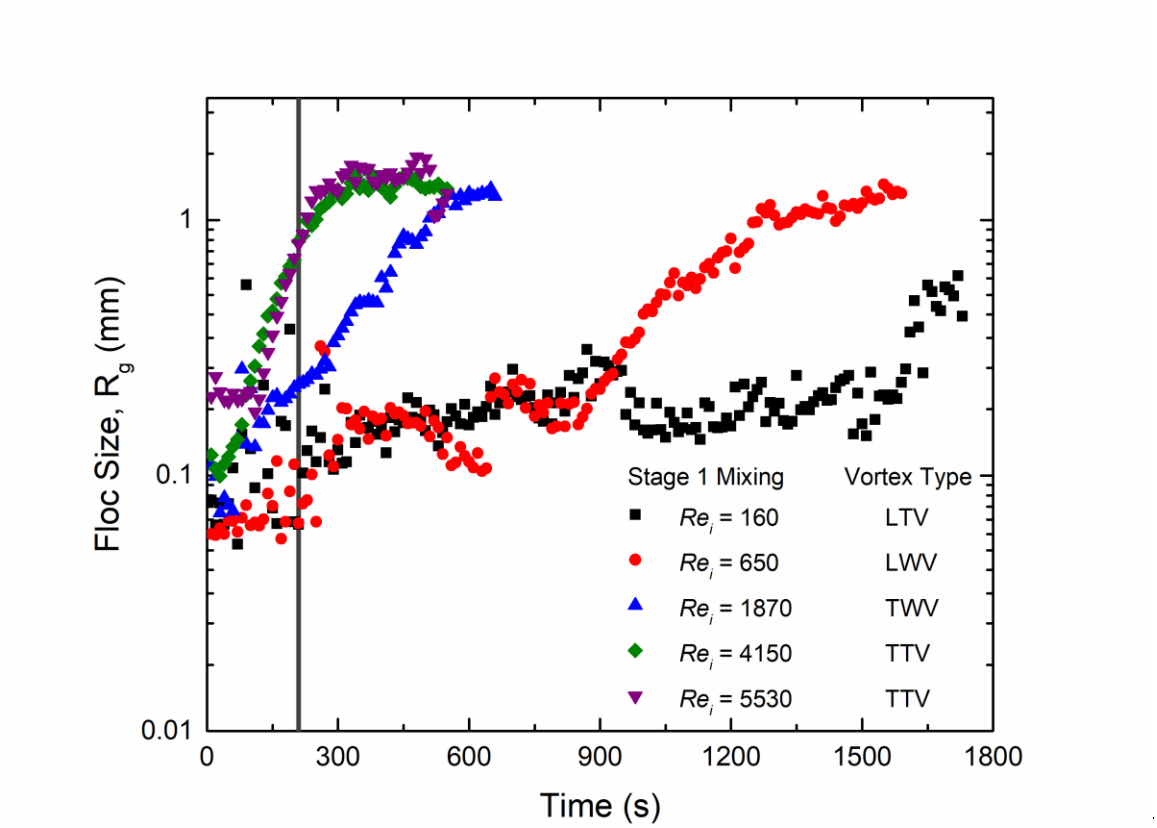


**Figure 4.4**: Bentonite floc size as a function of time and Stage 1 mixing speed in terms of the inner cylinder rotational speed. The corresponding vortex type is listed next to the speed. The vertical, dark gray line denotes the point in time where the speed changes from the Stage 1 speed to Stage 2 speed, which is held constant for all experiments at 0.46 $s^{-1}$ ($Re_i$ = 1680). Each point represents data averaged from 300 frames of the movie (10 s at a frame rate of 30 fps).

The floc growth rate can be quantified from the data by using a modified version of the logistic growth equation

$$\frac{R_g(t)}{R_{g,max}} = \frac{1}{1 + \left( \frac{1}{R_{g,0}/R_{g,max}} - 1 \right) e^{-rt}} \tag{4.4}$$

where $R_g$ is the radius of gyration at a given time in mm, $R_{g,max}$ is the maximum value of $R_g$ in the fitting range in mm, $R_{g,0}$ is the initial value of $R_g$ at the beginning of the fitting range in mm, $r$ is the growth rate in mm·$s^{-1}$, and $t$ is time in seconds. While this model is

typically used for quantifying growth rates in microbial and ecological studies, it has also been used to quantify floc growth as the flocs tend to reach a “carrying capacity” in their population in the form of a maximum floc size.[181–184]

The logistic growth equation was fit to the portion of the plot where there was a marked increase in the floc size with time. The logistic growth fits to the relevant portion of the data are presented in **Figure 4.5**. In addition to the fits, the residuals between the measured values and calculated values from the logistic growth equation are present to show how well the logistic growth equation fits the data points. For the LWV, TWV, and TTV experiments, the model fits the data well based on the residuals but was not a good fit for the LTV experiment. This was most likely due to the relatively poor mass transfer of the polymer flocculant associated with the LTV flow state, which is discussed in the following section.

Previous investigations have shown that maximum floc size is on the order of the Kolmogorov microscale, and floc size decreases with increasing global velocity gradient via the global dissipation rate of turbulent kinetic energy.[59,87,185] A point of interest about the floc size results from the present study is that maximum floc size did not vary much between the different inner cylinder speeds, with the exception of the lowest speed. Prior flocculation studies in the literature, however, explored mixing hydrodynamics on flocculation in stirred tanks with impellers or in TC cells under uncontrolled mixing conditions, which have been shown to possess inhomogeneities over spatial and temporal flow features.[61,87]

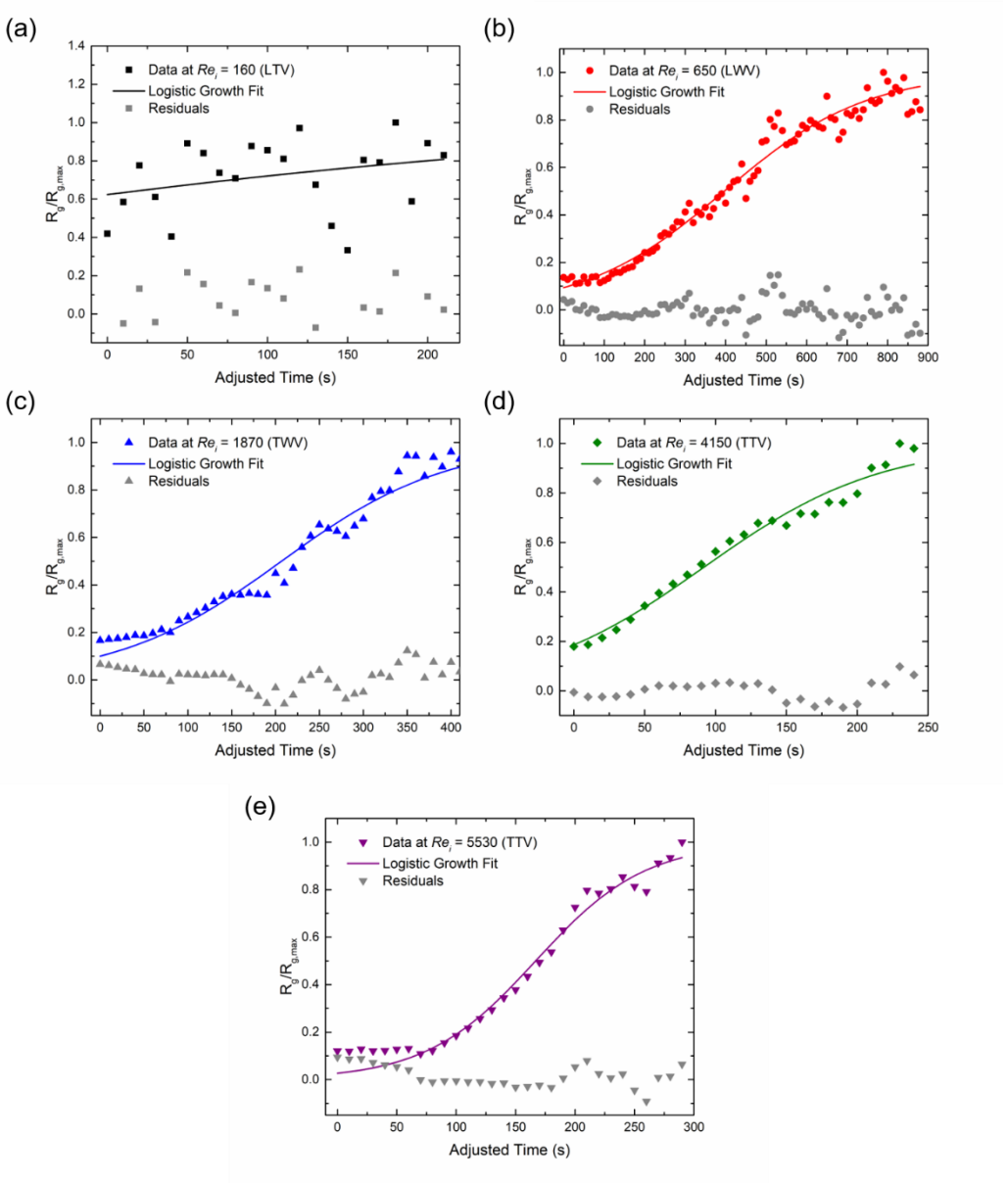


**Figure 4.5**: Logistic growth fit to floc size data at inner cylinder speeds of (a) 0.04 $s^{-1}$ ($Re_i$ = 160, LTV), (b) 0.17 $s^{-1}$ ($Re_i$ = 650, LWV), (c) 0.50 $s^{-1}$ ($Re_i$ = 1870, TWV), (d) 1.10 $s^{-1}$ ($Re_i$ = 4150, TTV), and (e) 1.47 $s^{-1}$ ($Re_i$ = 5530, TTV) over time. The non-gray, solid symbols represent the $R_g$ data points collected during the experiment normalized by the maximum value of $R_g$ in the fitting range ($R_g/R_{g,max}$). The solid line indicates the logistic growth fit. The gray data points are the residuals of the fit, which are derived by the logistic growth model subtracted from the original data at the corresponding point in time.

*4.3.2. Effect of Hydrodynamics on Polymer Flocculant Mass Transfer*

**Figure 4.4** shows a delay in the growth of the flocs as a function of inner cylinder speed. The lag time is defined as the point in time where the slope of the growth curve instantaneously increased rapidly from zero slope. This delay, or lag time, in growth can be attributed to the intervortex mass transfer of the cationic polyacrylamide. Intervortex mass transfer can be quantified by an effective dispersion coefficient, $D_z^*$, recently determined for this particular TC cell by Wilkinson and Dutcher[95]

$$D_z^* = 2\lambda k_{cb} \tag{4.5}$$

where $\lambda$ is the axial wavelength of the vortex, and $k_{cb}$ is the intermixing coefficient.[186] Intervortex mass transfer refers to mass transfer of the polyacrylamide between individual vortex bands versus intravortex mass transfer, which refers to mass transfer of the polyacrylamide within a single vortex. To compare the effect of intervortex mixing during the flocculation process, the lag time was plotted against the effective dispersion coefficient for the initial mixing step as shown in **Figure 4.6**. The lag times varied from 40 s for the highest order flow state (TTV) up to 1600 seconds for the lowest order flow state (LTV). $D_z^*$ increases approximately an order of magnitude from $1.12 \times 10^{-5}$ $m^2 \cdot s^{-1}$ to $2.16 \times 10^{-4}$ $m^2 \cdot s^{-1}$ over the range of $Re_i$ used in this study, indicating improved mass transfer of the polymer as the inner cylinder speed increased.

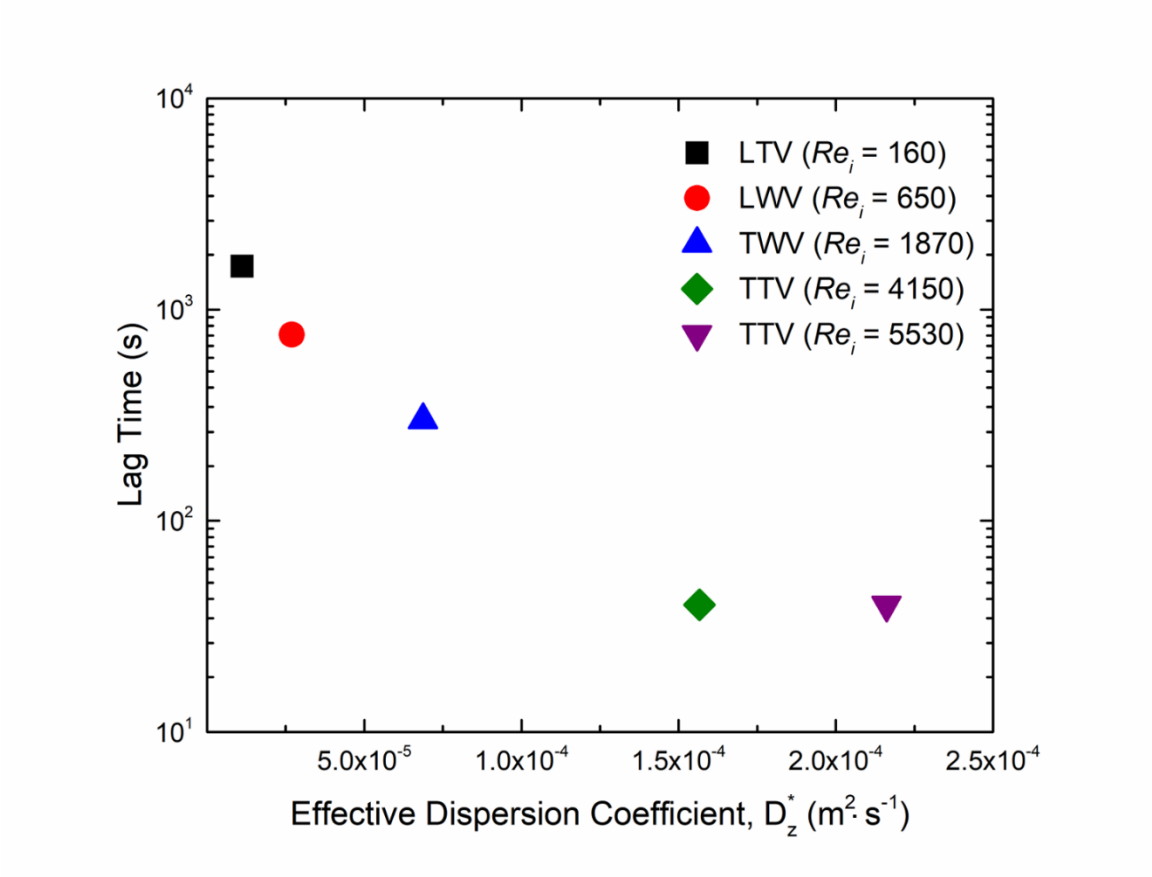


**Figure 4.6**: Lag time of floc growth verse the effective dispersion coefficient, $D_z^*$. Lag time refers to the point in time during flocculation where the flocs commence growth. The Reynolds number, $Re_i$, and the dispersion coefficient, $D_z^*$, correspond to Stage 1 mixing.

The lag time strongly depends on the initial Stage 1 speed. For the higher "Mix" speeds with $Re_i$ of 4150 and 5530 cases (TTV), most of the growth curve from **Figure 4.4** is contained within the initial Stage 1 mixing portion of the plot, which are represented by the data to the left of the solid gray line. The growth curve for the $Re_i$ of 1870 (TWV) begins before the solid gray line in the Stage 1 region and continues past the line into the Stage 2 mixing region to the right of the dark gray line. Unlike the turbulent cases, the growth for the $Re_i$ of 160 (LTV) and $Re_i$ of 650 (LWV) cases commences well past the speed transition between Stage 1 and Stage 2. As the mass and therefore, global concentration, of polymer injected into the system is consistent across all trials, this difference in the initiation of floc growth is due to the reduced mass transfer ability of the laminar flow states compared to their corresponding turbulent flow states. The decrease in

effective dispersion coefficient and increase in lag time of the LTV and LWV states compared to the TWV and TTV states are therefore largely due to the reduced ability of the LTV flow state to intermix the polymer flocculant with the bentonite to form flocs. In addition to reduced mass transfer ability based on $Re_i$, the presence of an "unmixed core" in the laminar flow states observed and discussed previously could also be an explanation for poorer mixing compared to the corresponding TWV flow state.[95,173,176,177,187] Evidence of this "unmixed core" was not present in the turbulent flow states.

### *4.3.3. Effect of Hydrodynamics on Floc Morphology*

In addition to floc size, hydrodynamics play a key role in floc morphology. Solid particulate removal efficiency via sedimentation and filtration depends on the floc structure as morphology is related to both floc size and density.[62] Velocity gradients in the mixing process can alter the floc structure with time, which can also have consequences for removal efficiency. Floc morphology can be quantified using fractal dimensions. Previous studies used light scattering techniques to obtain a mass fractal dimension, which gives three-dimensional information about the floc structure.[164,188,189] However, using light scattering requires removal of sample flocs from their original environment. In order to measure floc structure in a non-intrusive manner, image analysis can be used to calculate a two-dimensional fractal dimension, $D_{sf}$.[61,62,190]

The two-dimensional fractal dimension was obtained by linearly regressing a plot of the log of the area versus log of the perimeter for each ten second data set. The closer the $D_{sf}$ value is to 1, the more circular the floc is in profile whereas the closer $D_{sf}$ is to 2, the more linear and rod-like the floc is in profile. **Figure 4.7** shows the evolution of $D_{sf}$ with time at each Stage 1 mixing speed. In all cases, $D_{sf}$ decreases with time until $D_{sf}$ plateaus during the later Stage 2 portion of the plot. The plateau value of $D_{sf}$ at the end of the flocculation experiment is largest for the slowest speed ($Re_i$ = 160) and decreases with increasing inner cylinder speed. This decrease in $D_{sf}$ with increasing inner cylinder speed is caused by the larger velocity gradients present in more turbulent flow types (higher speeds), which at longer mixing times shear the edges of the flocs and subsequently round them.

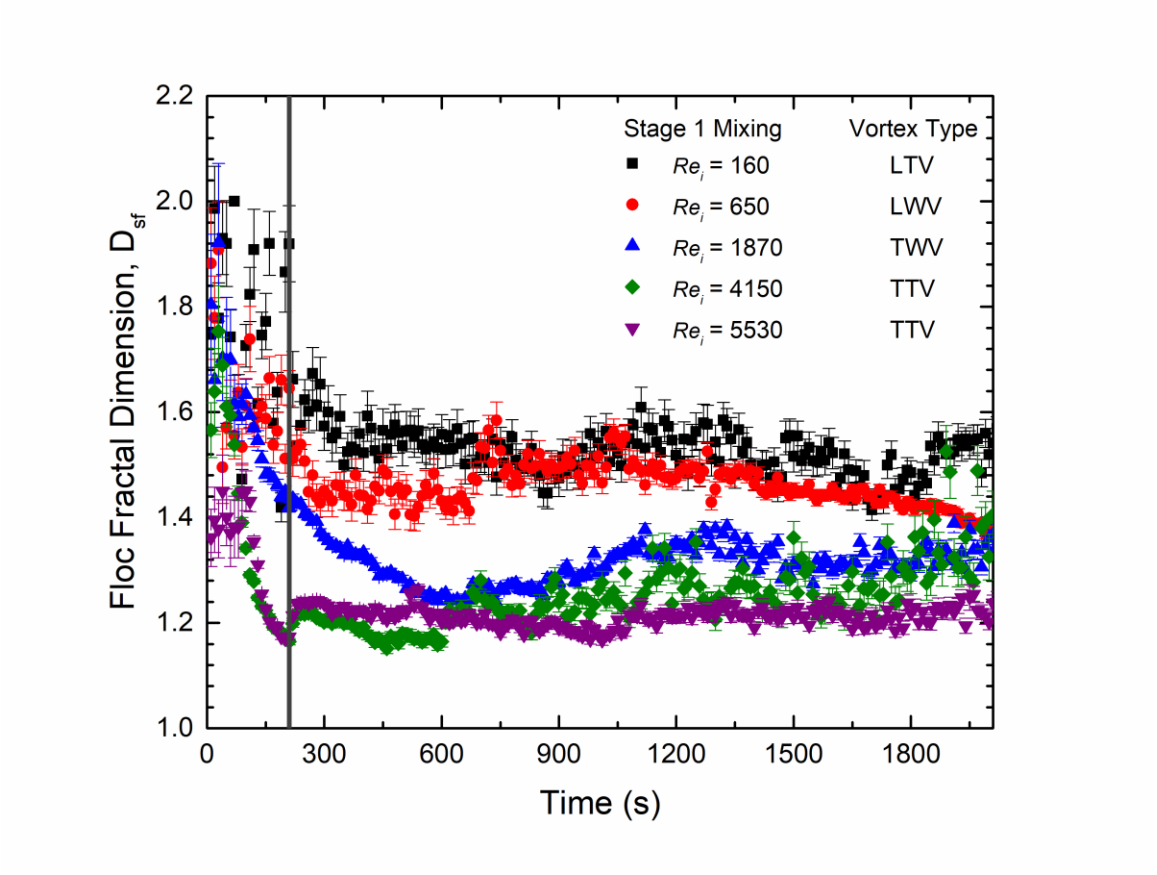


**Figure 4.7**: Bentonite morphology quantified as a 2-D perimeter-based fractal dimension, $D_{sf}$, as a function of time and Stage 1 mixing speed. The corresponding vortex type is listed next to the speed. The vertical, dark gray line denotes the point in time where the speed changes from the "Mix" Speed to the "Growth" Speed, which is held constant for all experiments at 0.46 $s^{-1}$ ($Re_i$ = 1680). Each point represents data averaged from 300 frames of the movie (10 s at a frame rate of 30 fps).

The absence of a particle imaging velocimetry setup (PIV) does not allow for a precise distribution of the velocity gradient. However, a global velocity gradient term at each inner cylinder speed can be calculated using the following equations:

$$G = \sqrt{\frac{\langle \varepsilon \rangle}{\nu}} \tag{4.6}$$

where $G$ is the global velocity gradient, $\langle\varepsilon\rangle$ is the global viscous dissipation of the turbulent kinetic energy, and $\nu$ is the kinematic viscosity of the bentonite suspension.[87] The viscous dissipation of turbulent kinetic energy can be calculate using the following equation:

$$\langle\varepsilon\rangle = \nu\left(\frac{dU}{dx}\right)^2 \approx \nu\left(\frac{U_{inner} - U_{outer}}{d}\right)^2 \tag{4.7}$$

where $U_{inner}$ is the rotational speed of the inner cylinder and $U_{outer}$ is the rotational speed of the outer cylinder. Since the outer cylinder is stationary for all experiments, $U_{outer}$ is reduced to zero. The global velocity gradient was calculated for each Stage 1 mixing speed and are listed here in order of increasing mixing speed: 2.0 $s^{-1}$, 8.6 $s^{-1}$, 25.3 $s^{-1}$, 55.7 $s^{-1}$, 74.4 $s^{-1}$. The Stage 2 global velocity gradient is 23.3 $s^{-1}$.

During the flocculation process in water treatment, the flocculant is mixed at higher speeds (which implies a higher global velocity gradient) into the suspension to rapidly disperse the flocculant, which subsequently also allows for more aggregate-aggregate collisions to form the initial flocs. Certainly increasing the mixing speed would initially result in aggregates with morphologies that are less circular ($D_{sf}$ values tending toward 2 rather than 1) due to increased aggregate-aggregate collisions from orthokinetic aggregation compared to diffusion alone.[58,190] However, here we should note that with sufficient speeds and mixing times, the $D_{sf}$ values decrease asymptotically to unity (more circular floc morphology), suggesting that the shear-induced rounding overwhelms aggregate-aggregate collisions in determining floc morphology in turbulent flows at longer mixing times.

## *4.4. Conclusion*

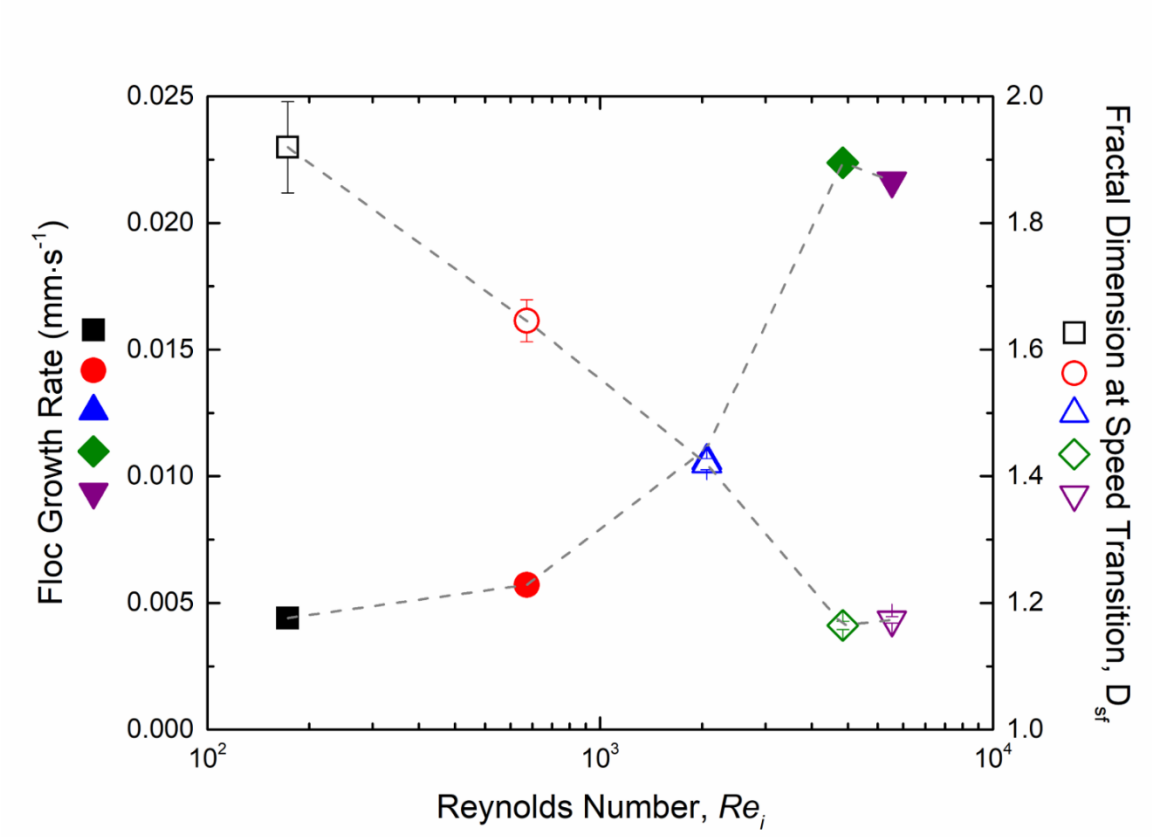


**Figure 4.8**: Summary of floc growth rate (closed symbols) and floc fractal dimension (open symbols) as functions of inner cylinder speed. The $Re_i$ listed here corresponds to the cylinder speed during Stage 1 mixing. The error bars on the floc fractal dimension represent the 95% confidence interval, and the points were taken at the speed transition between the "Mix" speed and the "Growth" speed. The gray dashed line is there to guide the eye to observe the increasing trend in flow growth rate and decreasing floc fractal dimension with increasing $Re_i$. The solid blue triangle is behind the open blue triangle. Several of the error bars are obscured by the symbols.

The unique ability for this TC cell to non-intrusively inject one fluid into another fluid offers unprecedented access to the entire mixing process during flocculation. To summarize the overall effects on flocculation of bentonite clay with cationic polyacrylamide in distilled water at four different flow states generated by the TC cell, the floc growth rate and $D_{sf}$ at the speed transition have been plotted for each inner cylinder speed as shown in **Figure 4.8**. As the inner cylinder speed increases, the flocs more rapidly

increase in size and become more spherical in shape. The differences in floc growth rate and morphology are largely attributed to the global velocity gradients associated with each flow state, which also affect the dispersion of the polymer flocculant. The intermixing coefficients calculated and shown in **Figure 4.6**, which describe turbulent dispersion, rather than molecular diffusion of the polyacrylamide in solution, are several orders of magnitude larger than the diffusion coefficients of polymers similar to the one used in this study.[191] Even though the growth rate was the fastest at the highest speeds tested, the fractal dimension of the flocs was more circular, indicating more shear rounding and breakage at the surfaces of the flocs. Based on the results, a balance between faster growth rate and shear rounding is necessary to satisfy the criteria for large, hydrodynamically robust flocs. **Figure 4.9** summarizes these major findings from the study in a graphical manner.

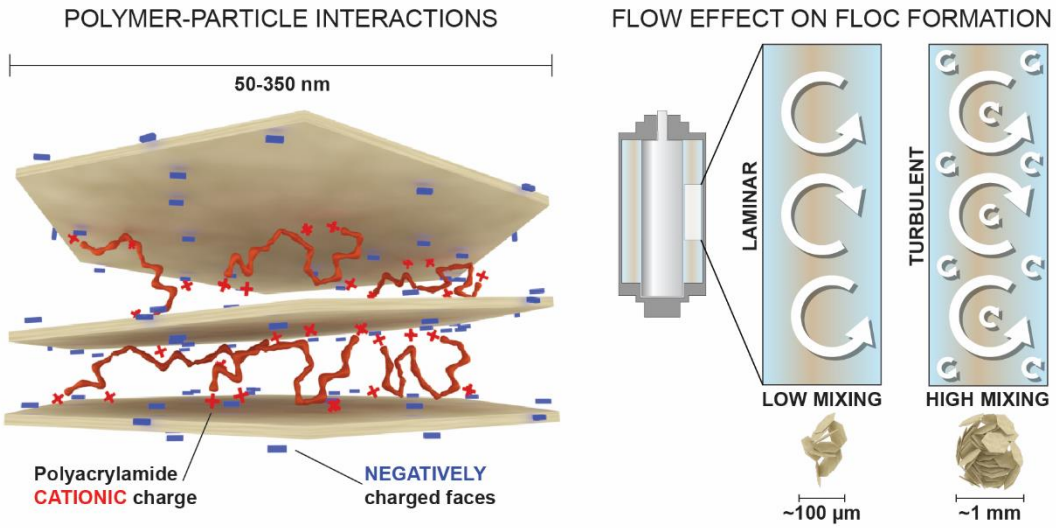


**Figure 4.9**: Graphical summary of findings. Transient, in-situ polymer-particle flocculation and growth were studied as a function of hydrodynamic flow state using a modified Taylor-Couette cell.

Flocculation is a largely non-equilibrium process that is dependent on a variety of physicochemical and hydrodynamic properties. The unique ability to directly inject a flocculant into a particulate-laden suspension in this TC cell offers the ability to study the entirety of the flocculation process in a hydrodynamically controlled fashion. While only one type of polymer flocculant was used here and the ionic strength and pH of the water

were kept consistent, these process variables critical to the flocculation process can be altered for future experimental studies. Fundamental understanding of the effects of these process variables on flocculation can potentially be used to optimize water treatment operations.

# Chapter 5

# Ionic Strength and Molecular Weight Effects on Floc Formation and Growth in Taylor-Couette Flows†

†Portions of this chapter includes work in A. E. Metaxas, V. Panwar, R. L. Olson, and C. S. Dutcher, Ionic strength and molecular weight effects on floc formation and growth in Taylor-Couette flows, *Soft Matter* (2020) Submitted.

## *5.1. Introduction*

Polyelectrolytes, or polymers with charged functional groups, are used in a variety of applications such as drag reduction, enhanced oil recovery, paper manufacturing, and flocculation in drinking water treatment.[42–45,50] In flocculation, polyelectrolytes are added to a particulate-laden suspension so that they adsorb to multiple suspended particulates, forming structures known as flocs that can be readily separated from solution. Rapid floc growth occurs during mixing by orthokinetic aggregation, where the particulates with adsorbed polyelectrolyte collide and grow due to the shear gradients present in the flow.[47–49] The variation in chemical composition of the aqueous solutions along with the complexity of the hydrodynamics involved in mixing make understanding the process of flocculation difficult to understand. This results in reliance of highly empirical methods to

determine polyelectrolyte flocculant dosing amounts in applications like drinking water treatment.

The particulate of interest in this study is bentonite, a clay particle commonly found in surface waters that has been used in prior flocculation studies.[7,63–65] Bentonite itself is an aggregate of many thin sheets, where the basal planes consist of permanent negative charges, and the edges consist of hydroxyl groups where the charge can vary with pH.[68,69] Due to these surface charges, the morphology of the bentonite aggregate is susceptible to changes in solution ionic strength or pH. In particular, an increase in solution ionic strength results in a change in the bentonite structure from a more porous morphology to a denser morphology. This change in aggregate structure has been indirectly confirmed with rheological measurements and confocal microscopy and directly confirmed with scanning electron microscopy.[70–72,89–91,169,192] Changes in solution ionic strength also have consequences for bentonite aggregate size. A previous study by Wilkinson et al.[90] showed that an increase in solution ionic strength resulted in an increase by two orders of magnitude of the initial bentonite aggregate size, which is attributed to the decrease in Debye length between bentonite sheets. This allows aggregation of the bentonite sheets to form denser, face-face morphologies and larger bentonite aggregates in solution.[48,193]

The variations in bentonite aggregate surface morphology and aggregate size due to changes in solution ionic strength result in different adsorption capacities and interaction potentials with the polyelectrolyte flocculant added to a bentonite-laden suspension, thus increasing the complexity of fundamentally understanding flocculation.[73] In addition to charge screening affecting the aggregate structure of the bentonite, the polyelectrolyte present in solution will also change conformation depending on the ionic strength. At lower ionic strengths, the charged moieties along the polymer backbone are not sufficiently screened, and the polymer chains adopt an expanded conformation, resulting in larger persistence lengths. At higher ionic strengths, the charged moieties are now screened, and the polymer chains adopt a coil-like conformation, resulting in smaller persistence lengths.[50,194,195]

The mixing environmental also influences the flocculation behavior. One method to test for flocculation performance is with jar tests, which replicate scaled-down industrial mixing tanks for flocculation. Jar tests are a relatively rapid, easy technique to obtain a lot of information about flocculation processes, but they lack homogeneous spatial and temporal flow features and possess un-controlled shear stresses, thus making it difficult to attribute certain floc properties to a specific flow features.[62,92] Instead, Taylor-Couette (TC) cells, which consists of two concentric cylinders with a specified gap width, can be used as they can generate a controlled variety of laminar and turbulent flow states as a function of cylinder speed.[165–170] Prior flocculation studies using a TC cell were limited in that the flocs had to be pre-formed outside of the cell.[87,93,196] A TC cell with a glass outer cylinder for imaging and an inner cylinder modified for radial injection was recently constructed to directly inject the polymer flocculant into the annulus, so that the full flocculation process can be studied in-situ.[94,95] This unique TC cell was used previously by the authors in Metaxas et al.[88] as described in Chapter 4 to test the effects of initial mixing speed, which corresponds to a specific vortex type in the TC cell, on the flocculation of bentonite with a cationic polyacrylamide flocculant. It was found that an increase in the early mixing speed results in an increased floc growth rate, but the maximum floc sizes were very similar in size.

While *in-situ* bentonite-polyelectrolyte flocculation work by Metaxas et al.[88] enabled a first study of flocculation in varying TC flows, the influence of changes in solution chemical composition was not examined as the ionic strength of the suspension, the polyelectrolyte molecular weight, and the concentration of polyelectrolyte were constant. However, the known ionic strength-dependence of size and morphology of the bentonite aggregate as well as the ionic strength-dependence of polyelectrolyte persistence length and conformation adds an important additional complexity to understanding flocculation dynamics. The ionic strength-induced changes in polyelectrolyte chain conformation will modify the extent that extensional forces present in the flow field around the polymer act to stretch the polyelectrolyte chains and enhance the bridging capability of the polyelectrolyte.[54,81] In this work, we vary ionic strength and molecular weight to

understand the effects of these properties on the flocculation process, specifically the floc size, floc growth rate, and floc morphology, in well-controlled flow conditions.

## *5.2. Materials and Methods*

### *5.2.1. Materials*

The polymer flocculants, or organic polyelectrolytes, used in this study are both commercially available cationic polyacrylamides (FLOPAM FO 4190SH and FLOPAM FO 4190SSH, SNF Polydyne) with 10 mol% of the monomer groups containing a quaternary ammonium cation with a permanent positive charge in solution. The FLOPAM 4190SH has a molecular weight of 4-6 x $10^6$ g·mol$^{-1}$ and the FLOPAM 4190SSH has a molecular weight of 8-11 x $10^6$ g·mol$^{-1}$. For both cationic polyacrylamides (CPAM), a 0.2 wt% solution was made by mixing the solid polymer pellets with a Jiffy mixer attachment in distilled water for 30 min. The solutions rested in a refrigerator overnight prior to use and were remade every 2 weeks as necessary as indicated by the supplier. Before any experiment was performed, the solution was removed from the refrigerator and allowed to warm to room temperature (~23°C). The distilled water was purchased from Premium Waters, Inc. Powdered Na-Bentonite and NaCl are ACS grade from Fisher Scientific and were used as received.

### *5.2.2. Jar Tests*

To perform a jar test, the appropriate amount of NaCl needed to obtain ionic strengths, [I], of 0 mM (no NaCl), 1.3 mM, 10 mM, and 100 mM was added to 1 L of distilled water in a 2 L Pyrex beaker, or jar. A VELP Scientifica JTL4 flocculator was used to mix the solution for 5 min at 300 RPM to fully dissolved the NaCl. The bentonite was then added to the jar to mix for 30 min at 300 RPM to evenly distribute it. For all jar tests, the concentration of bentonite was kept constant at 30 mg·L$^{-1}$. The mixing speed was then lowered to 200 RPM, and a pre-specified volume of polyelectrolyte flocculant was injected into the suspension and mixed for 3 min to disperse the flocculant. To allow the flocs to grow, the mixing speed was lowered to 30 RPM and the suspension was mixed for an additional 30 min. Once the mixing stopped, the jars sat for 5 min before the turbidity in nephelometric turbidity units (NTU) was measured with a LaMotte turbidity meter. This

was performed for a range of polyelectrolyte flocculant concentrations to obtain the optimal dose, which is the global minimum in a turbidity curve. The optimal dose for each ionic strength and polyelectrolyte type is shown in **Table 5-1**. The steady shear viscosities of each suspension with the optimal dose of polyelectrolyte were measured using the cup and bob geometry fixture of an AR-G2 rotational rheometer from 1 $s^{-1}$ to 250 $s^{-1}$ at 23°C as shown in **Figure 5.1** and were found to be Newtonian for the range of shear rates experienced in the annulus of the TC cell.

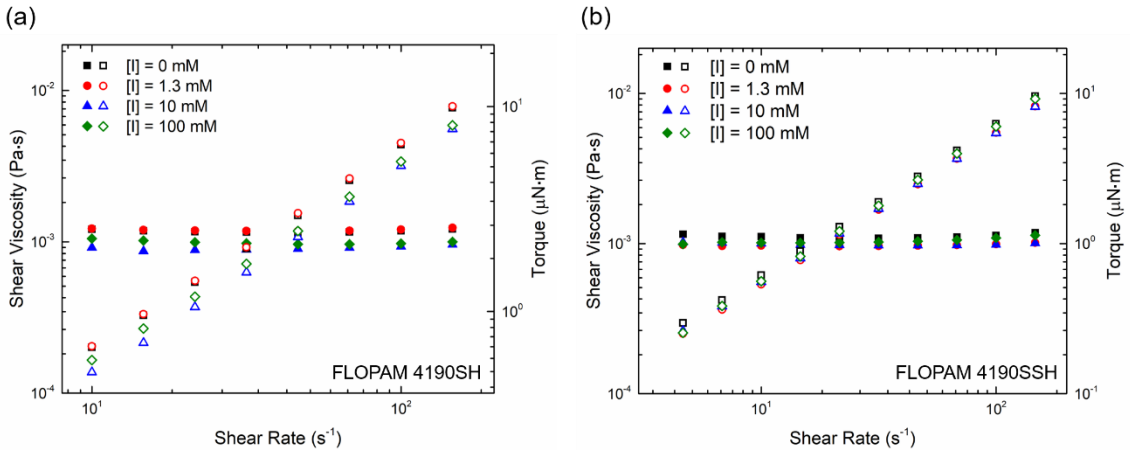


**Figure 5.1**: Steady shear viscosity (closed symbols) and torque response traces (open symbols) as a function of solution ionic strength with shear rate for the (a) lower molecular weight cationic polyacrylamide flocculant (4190SH) and the (b) higher molecular weight cationic polyacrylamide flocculant (4190SSH). The temperature was kept constant at 23ºC. The experiment was performed using the cup and bob geometry to mimic the Taylor-Couette cell geometry.

### *5.2.3. Suspension Loading into TC Cell Annulus and Spatial Calibration*

The TC cell used in this study injects flocculant through a total of 16 precisely spaced axial and azimuthal injection ports along the inner cylinder to smooth any azimuthal concentration gradients.[94,173,176,177] These injection ports do not protrude into the annulus and the port covers are contour-matched to the inner cylinder so that the flow profile of the resultant vortices are not modified during operation.[95] Additional details on the TC cell design, with inner cylinder diameter diameter ($D_i = 2R_i$) of 13.5407 ± 0.0025 cm, gap width ($d$) of 0.84 cm, and the injection assembly can be found elsewhere.[94] To make the bentonite suspensions, the appropriate amount of NaCl was added to two separate 2 L jars each filled

with 1 L distilled water to obtain solutions with ionic strengths of 0 mM (no NaCl), 1.3 mM, 10 mM, or 100 mM. The NaCl was mixed using a VELP Scientifica JTL4 Flocculator for 5 min at 300 RPM. Once the NaCl was dissolved, 30 mg of bentonite was transferred to each jar to have a total of 2 L of 30 $mg \cdot L^{-1}$ bentonite suspensions. The bentonite was dispersed using the flocculator for 30 min at 300 RPM. The pH of the suspensions in all cases was approximately 6.6 due to the interaction of dissolved carbon dioxide in water and bentonite.[178] Once finished, the bentonite suspensions were immediately transferred to the annulus of the TC cell by way of tubing attached to the base of the cylinder assembly. This process is also detailed in Chapter 4, which is based on a previous study by Metaxas *et al*.[88]

### *5.2.4. Flocculation Experiment Protocol*

A stepper motor (Applied Motion Products HT34-497 2 phase stepper motor with a STAC5-S-E120 controller) rotates the inner cylinder and is equipped with a 7:1 gear reducer (Applied Motion Products 34VL007) for inertial balance between the motor and the cylinder. A laser diode (Thorlabs, 450 nm, 1600 mW max) in combination with a laser line generator was used to create a laser light sheet tangential to the inner cylinder. The Basler Ace camera (1280 × 1024 pixels, 60 fps maximum frame rate) with a Tamron 25 mm c-mount lens was vertically adjusted such that the field of view was between the third and fourth injection port covers from the bottom of the TC cell. The frame rate on the camera was set to 30 fps with an exposure time of 8 ms for all experiments. A LabView code was used to simultaneously inject the polyelectrolyte flocculant from the inner cylinder ports into the annulus and record the entire flocculation process. For all experiments, the drive pressure was set to 30 psi to inject the 0.2 wt% polyelectrolyte solution at a calibrated injection rate of $1.115 \pm 0.089$ $g \cdot s^{-1}$ for the 4190SH flocculant and $0.772 \pm 0.039$ $g \cdot s^{-1}$ for the 4190SSH flocculant as shown in **Figure 5.2**. The injection time was based on the required mass of flocculant needed to obtain the concentrations shown in **Table 5-1**.

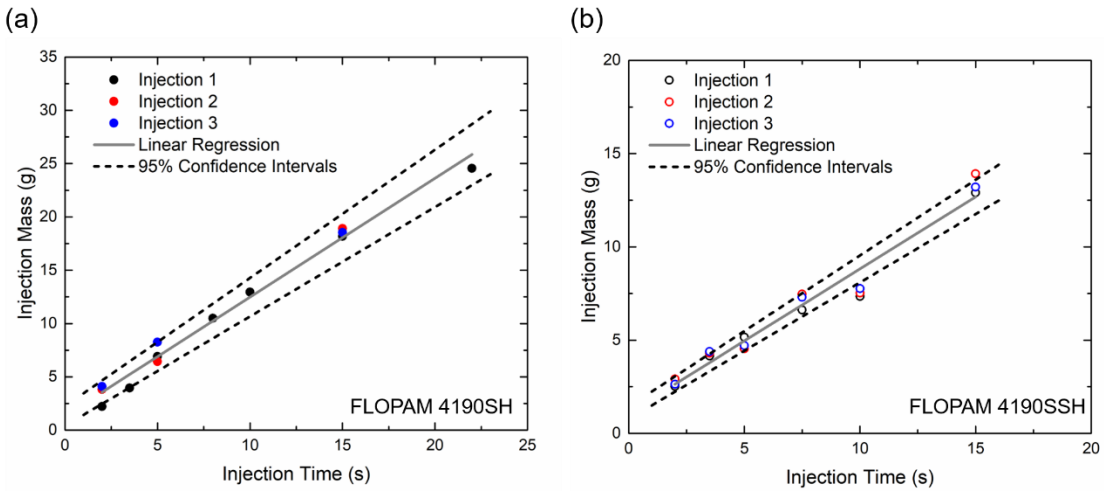


**Figure 5.2**: Flow rate calibration curves for polyelectrolyte injection from the inner cylinder of the TC cell at a drive pressure of 30 psi. The closed symbols represent the (a) lower molecular weight cationic polyacrylamide flocculant (4190SH) while the closed symbols represent the (b) higher molecular weight cationic polyacrylamide flocculant (4190SSH). The solid gray line represents a linear regression of the data points while the dashed black lines represent upper and lower 95% confidence intervals. The slope of the linear regression is the flow rate in $g \cdot s^{-1}$ that was used to calculate the drive time needed to inject the required mass of polyelectrolyte into the annulus to obtain the required concentration shown in **Table 5-1**. The linear fit equations are (a) Injection Mass = (1.115 ± 0.089)·Injection Time + (1.330 ± 0.922), $R^2$ = 0.99 and (b) Injection Mass = (0.772 ± 0.039)·Injection Time + (1.098 ± 0.330), $R^2$ = 0.96.

Many flocculation applications preform the mixing with a two-stage protocol. First, there is an initial faster "Mix" speed (Stage 1), followed by a slower "Growth" speed (Stage 2), although growth can occur during both Stage 1 and Stage 2. In this study, the Mix and Growth speeds were set to constant rotation speeds of 0.50 $s^{-1}$ and 0.46 $s^{-1}$, respectively. To begin an experiment, the inner cylinder drive shaft and injection ports were primed with flocculant. The initial Stage 1 speed was set, and the recording was started. After a delay of 30 s, the polymer was injected from the inner cylinder into the annulus and mixed at this Stage 1 speed for 3 min. After this, a step change in speed occurred to reach the Stage 2. This stage was maintained for 30 min to allow the flocs to grow. The speed of 0.46 $s^{-1}$ was chosen as it was the slowest speed tested that allowed flocs to be suspended throughout the 30 min duration of Stage 2 mixing. The times (3 min for

Stage 1 and 30 for min Stage 2) used here mimic those used in the jar tests described in Section 5.2.2. After completion, the TC cell was disassembled and cleaned.

### *5.2.5. Image Analysis*

Physicochemical and hydrodynamic effects on final floc microstructure have been examined using techniques such as small angle light scattering, which yields final floc size and fractal dimensions.[82–84] The longer characterization length scales accessible by static light scattering typically work well to determine mass fractal dimension determination. However, interpretation of the scattering patterns can be difficult, and static light scattering works best for small aggregates with loosely packed structures, which is not always the case during flocculation. In more recent years, advanced image analysis techniques have been used to study the dynamic flocculation behavior using jar tests and impellers. Image analysis offers a non-intrusive method of studying the flocs as compared to obtaining and preparing a sample for light scattering experiments.[59]

To eliminate the curved glass surface of the outer cylinder during imaging, refractive index-matching paraffin oil was poured into the Plexiglass tank surrounding the TC cell prior to making the bentonite suspension. The cell was illuminated using a flicker-free LED light strip (Metaphase 19 in Exo2 Light) to visualize the bottom-most port cover of the inner cylinder. An image of the port cover was captured with the Basler camera. ImageJ was then used to determine the pixel-to-mm ratio of the port cover for spatial calibration of the flocculation movies.

The movies were post-processed using MATLAB to obtain time-dependent floc size and morphology based on an analysis by Vlieghe *et al*.[61] The raw movie frames were first binarized to clearly show the floc (shown as white shapes in **Figure 5.3** and **Figure 5.4**), and the centroid of each floc ($x_c$,$y_c$) was determined. A metric of floc size, the radius of gyration, $R_g$, of the non-spherical floc is calculated via

$$R_g^2 = \frac{1}{N_p}\sum_{i=1}^{N_p}[(x_i - x_c)^2 + (y_i - y_c)^2] \tag{5.1}$$

where $N_p$ is the number of pixels making up each floc with coordinate pair ($x_i$, $y_i$). The resulting radii of gyration were averaged for each 10 s interval (300 frames).

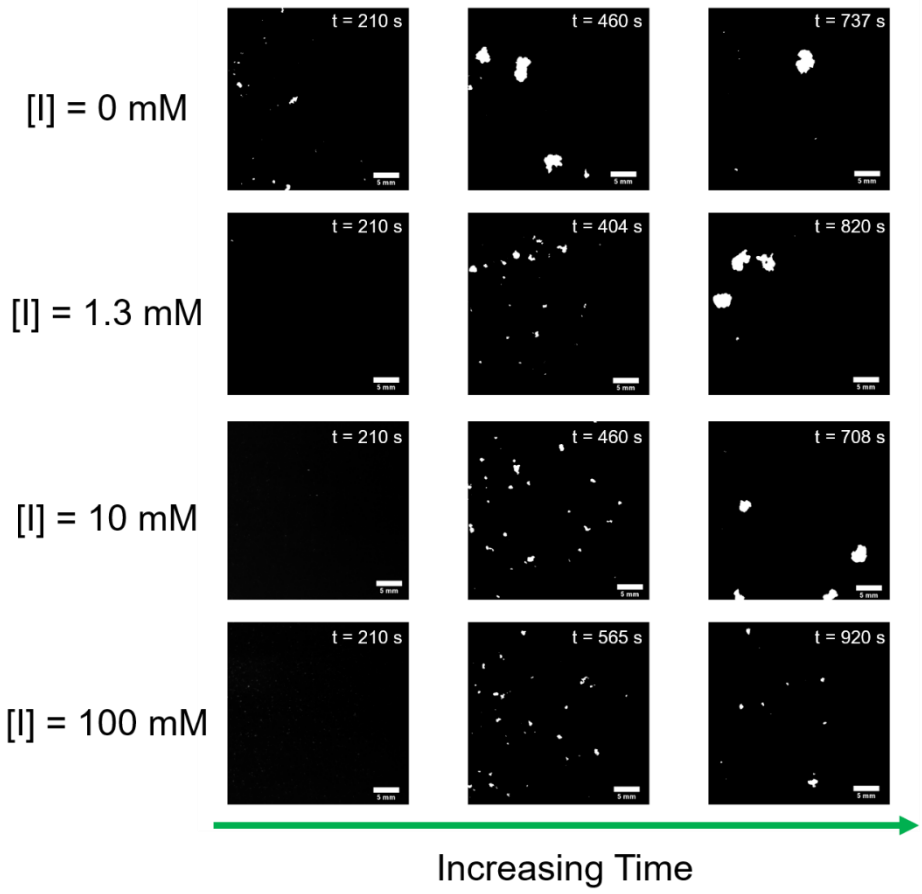


**Figure 5.3**: Time lapse of binarized images of bentonite-cationic polyacrylamide flocs (here, the 4190SH flocculant was used) as a function of ionic strength. The first image in each row is at 210 s, which is the onset of the inner cylinder speed change. The last image in each row occurs where the floc size plateaus. The middle image in each row occurs at the midpoint time between the times associated with the first and last images. The white scale bar in the lower right-hand corner of each image represents 5 mm.

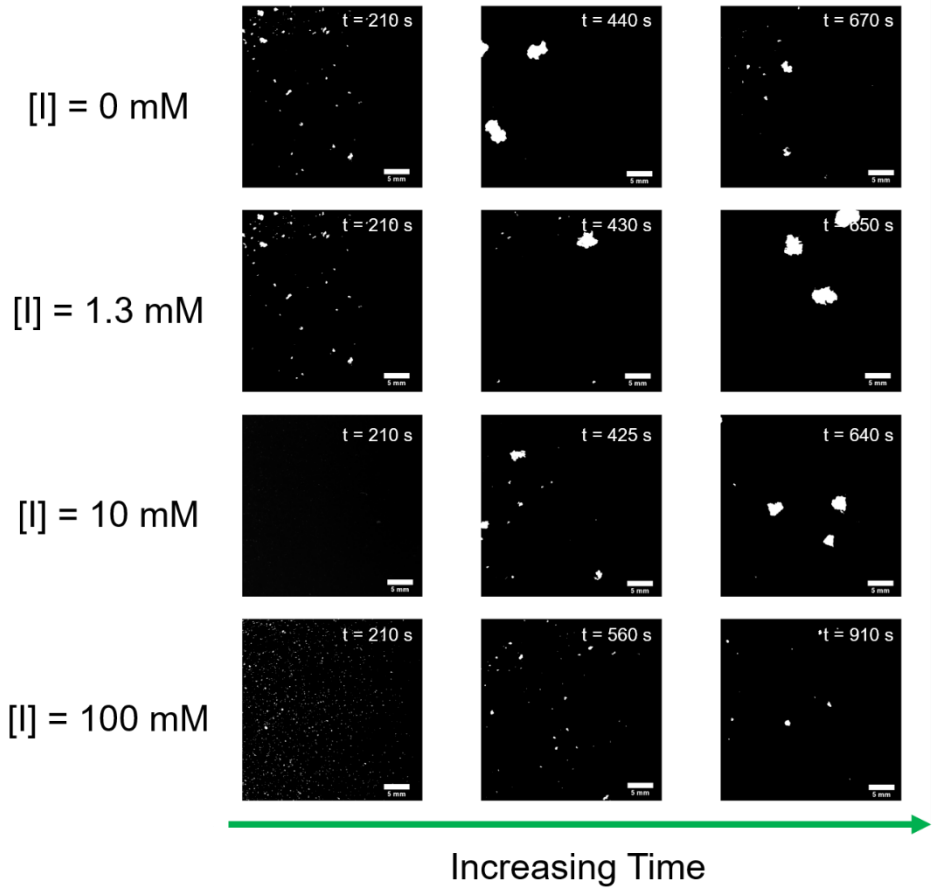


**Figure 5.4**: Time lapse of binarized images of bentonite-cationic polyacrylamide flocs (here, the 4190SSH flocculant was used) as a function of ionic strength. The first image in each row is at 210 s, which is the onset of the inner cylinder speed change. The last image in each row occurs where the floc size plateaus. The middle image in each row occurs at the midpoint time between the times associated with the first and last images. The white scale bar in the lower right-hand corner of each image represents 5 mm.

A 2-D surface-based fractal dimension, $D_{sf}$, was used to quantify the morphology of the flocs. This quantity was calculated using the cross-sectional floc area, $A$, and the floc perimeter, $P$, using the relationship by Vlieghe *et al.*[61]

$$A \propto P^{2/D_{sf}} \tag{5.2}$$

The fractal dimension varies between the limits of 1, which indicates a circular floc cross-section, and 2, which indicates a rod-like floc cross-section. For each 10 s set of data, a linear regression was performed to determine $D_{sf}$. The number of flocs as a function of

time were also calculated for each experiment. All experiments were conducted in triplicate for error analysis. All runs for both the 4190SH and 4190SSH flocculants are shown in **Figure 5.5** and **Figure 5.6**, respectively.

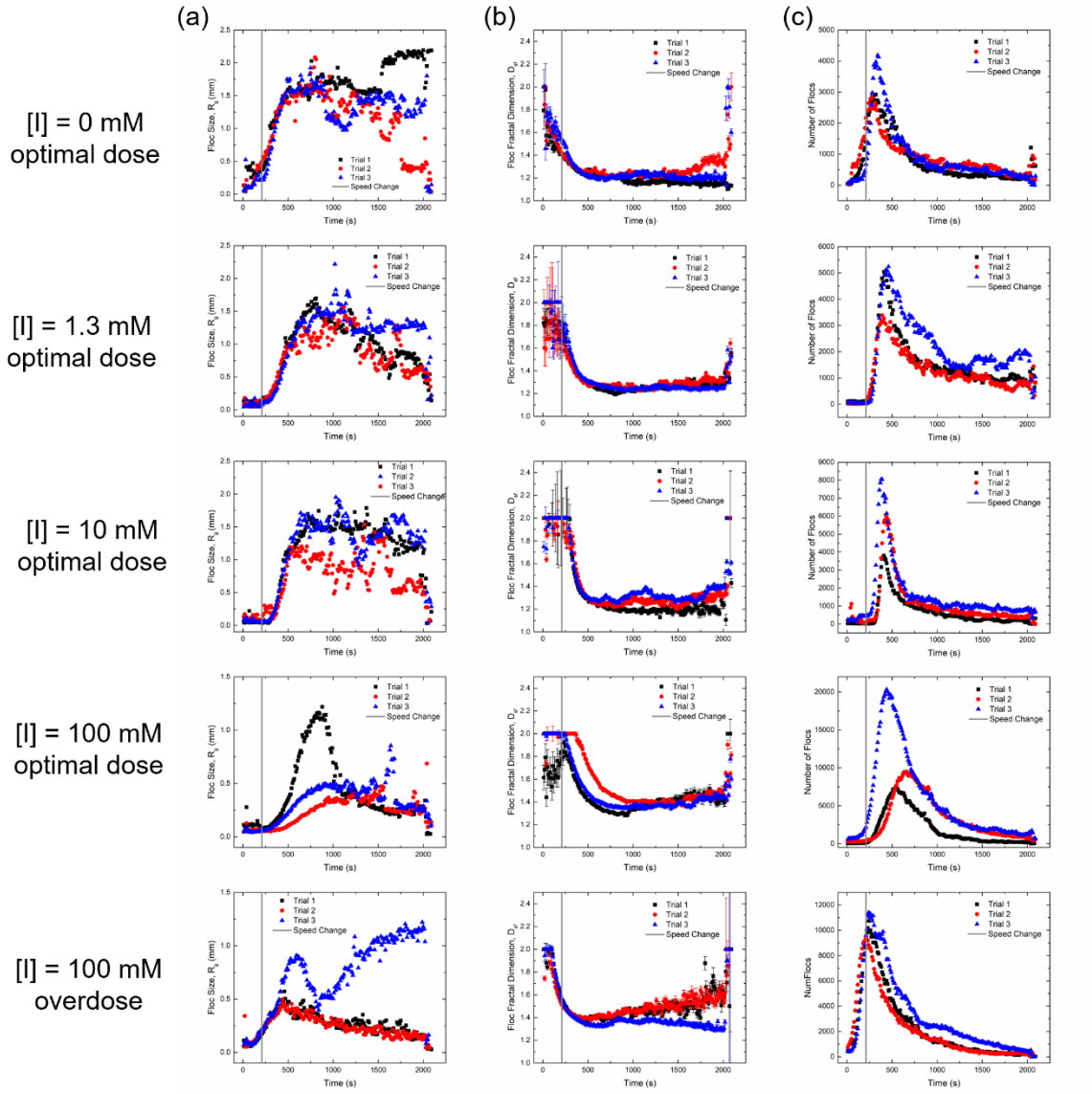


**Figure 5.5**: All trials for the (a) floc sizes expressed as radius of gyration, $R_g$, (b) 2-D floc fractal dimension, and (c) number of flocs as a function of ionic strength with time for the lower molecular weight cationic polyacrylamide flocculant (4190SH). The vertical gray line depicts the point where the inner cylinder speed transitions from $\Omega_i$ = 0.5 $s^{-1}$ to $\Omega_i$ = 0.46 $s^{-1}$.

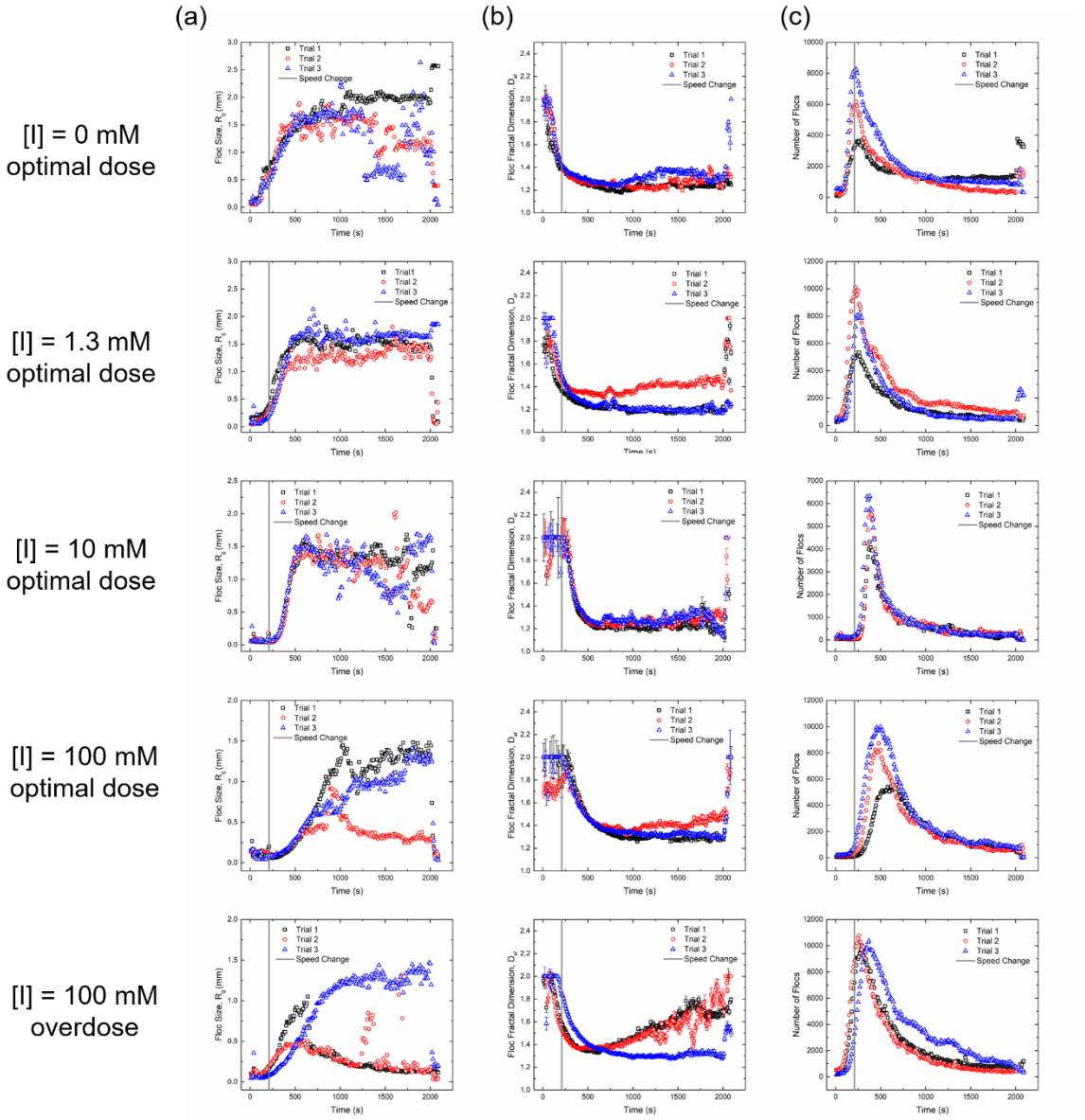


**Figure 5.6**: All trials for the (a) floc sizes expressed as radius of gyration, $R_g$, (b) 2-D floc fractal dimension, and (c) number of flocs as a function of ionic strength with time for the lower molecular weight cationic polyacrylamide flocculant (4190SSH). The vertical gray line depicts the point where the inner cylinder speed transitions from $\Omega_i$ = 0.5 $s^{-1}$ to $\Omega_i$ = 0.46 $s^{-1}$.

## 5.3. *Results and Discussion*

### *5.3.1. Optimal Dose Determination of Polyelectrolyte Flocculants*

Jar tests were performed to determine the optimal dose of polyelectrolyte required as a function of both the solution ionic strength and the polyelectrolyte type. The optimal dose occurs where there is a global minimum in the turbidity curve. Determining the optimal dose is critical because under-dosing results in insufficient particulate removal and over-dosing results in particulate restabilization, both undesirable outcomes which can be cost-prohibitive in water treatment.[46,197,198] **Figure 5.7** shows the results from these jar tests for both the lower molecular weight (4190SH) and higher molecular weight (4190SSH) cationic polyacrylamides. The optimal dose decreases as the ionic strength increases for both polyelectrolytes as reported in **Table 5-1**. The global minimum in the final turbidity indicates that more solid particulate (in this the case, bentonite) has settled out of solution because of the presence of the flocculant and the increase in ionic strength of the solution. The shape of the turbidity curves also differs with ionic strength, where there is a distinct minimum in the curve below [I] = 10 mM and a loss of the distinct minimum at [I] = 10 mM and above. This suggests the restabilization of bentonite due to overdosing as previously mentioned.

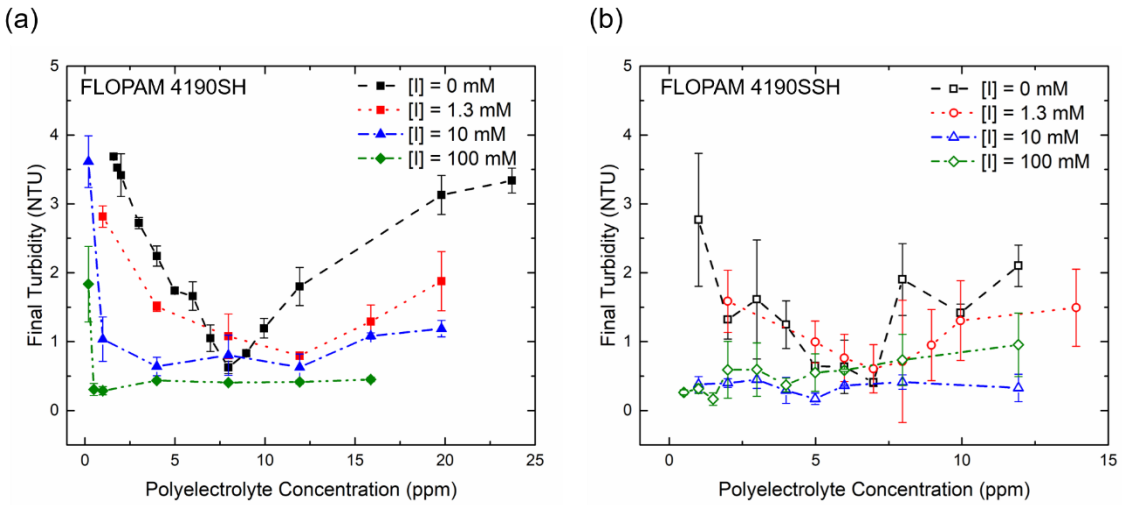


**Figure 5.7**: Jar test results as a function of solution ionic strength using the (a) lower molecular weight cationic polyacrylamide flocculant (4190SH) and the (b) higher molecular weight cationic polyacrylamide flocculant (4190SSH). The final turbidity in

terms of nephelometric turbidity units (NTU) is expressed as a function of the polyelectrolyte dose, or concentration, in parts per million (ppm). The global minimum in each curve denotes the optimal dose for a set of solution conditions.

The previously mentioned study by Wilkinson *et al.*[90] showed that an increase in solution ionic strength resulted in an increase in the bentonite aggregate size from ~0.04 μm at [I] = 0 mM to ~9 μm at [I] = 100 mM, which is attributed to the decrease in Debye length between bentonite sheets. In brief, the net negative charge of the bentonite platelets is screened by an increase in positive $Na^+$ ions added as NaCl into solution, which decreases the repulsive, electrostatic force between the bentonite platelets, allowing them to aggregate to form larger bentonite aggregates.[48,193] Aggregation of the bentonite clay is aided just by the presence of additional NaCl in the solution, which means less of the polyelectrolyte is required to promote flocculation efficiency. The optimal doses of the higher molecular weight CPAM at each solution ionic strength were generally lower than those of the lower molecular weight CPAM. Because both polyelectrolytes in the study consist of the same monomer unit, the higher molecular weight polyelectrolyte is longer in length and therefore able to bridge more bentonite aggregates, requiring less of the polymer in solution to produce similar flocculation efficiencies.[44,199]

### *5.3.2. Ionic Strength and Molecular Weight Effects on Floc Size and Growth Rate*

Once the optimal doses were determined for each polyelectrolyte at a particular solution ionic strength and the TC cell was calibrated to inject the correct mass of polyelectrolyte (see **Figure 5.2**), the flocculation experiments were conducted in the TC cell with radial injection capabilities. As described in the Methods section, during a routine flocculation processes, the flocculant is first rapidly mixed (Stage 1) to disperse the polymer quickly, followed by a slower mix (Stage 2) to allow appreciable floc growth.[179] For this study, the inner cylinder rotational speed, $\Omega_i$, for Stage 1 and Stage 2 mixing were both kept constant at 0.5 $s^{-1}$ and 0.46 $s^{-1}$ respectively.

While $\Omega_i$ remained constant for both the Stage 1 and Stage 2 mixing, there is some variation in the non-dimensionalized velocity, given by the Reynolds number ($Re_i = \Omega_i R_i d/\nu$), due to slight differences in the kinematic viscosity $\nu$ of each suspension. The

Stage 1 $Re_i$ range from 1517, 1518, 1956, and 1785 for the lower molecular weight CPAM and from 1593, 1822, 1792, and 1709 for the higher molecular weight CPAM as ionic strength increases. The Stage 2 $Re_i$ range from 1404, 1405, 1810, and 1654 for the lower molecular weight CPAM and from 1474, 1687, 1659, and 1582 for the higher molecular weight CPAM as ionic strength increases. Even though the $Re_i$ vary, they all fall within the range for the turbulent wavy vortex (TWV) flow type, which the $Re_i$ range for TWV flow for this specific TC geometry falls between 1400 and 2924. The prior TC flocculation study by Metaxas et al.[88] tested two different $Re_i$ within a vortex flow type and found no statistical difference in the floc size, growth rate, and floc morphology, therefore it can be assumed that the same holds true in this study.

**Figure 5.8** depicts a representative example of the transient floc size, expressed as the radius of gyration $R_g$, and was a function of solution ionic strength and polyelectrolyte molecular weight. The radius of gyration of the flocs increases in all runs after the initial injection of cationic polyacrylamide at 30 s until a plateau value of $R_g$ is obtained. Shear gradients present in the flow and a finite amount of bentonite and flocculant limit the maximum floc size.[49,55,59,87] The maximum floc size generally decreases as ionic strength increases from 1.8 ± 0.3 mm at [I] = 0 mM to 0.7 ± 0.9 mm at [I] = 100 mM for the lower molecular weight CPAM (4190SH) and from 1.9 ± 0.2 mm at [I] = 0 mM to 0.9 ± 1.0 mm at [I] = 100 mM for the higher molecular weight CPAM (4190SSH) (**Table 5-1**). The floc sizes tend to be slightly larger for the 4190SSH CPAM compared to the 4190SH CPAM as the 4190SSH variant is higher in molecular weight and therefore is longer in length, allowing it to bridge more bentonite aggregates.[7,44,199] All experimental runs for each molecular weight of polyelectrolyte are shown in **Figure 5.5** and **Figure 5.6**.

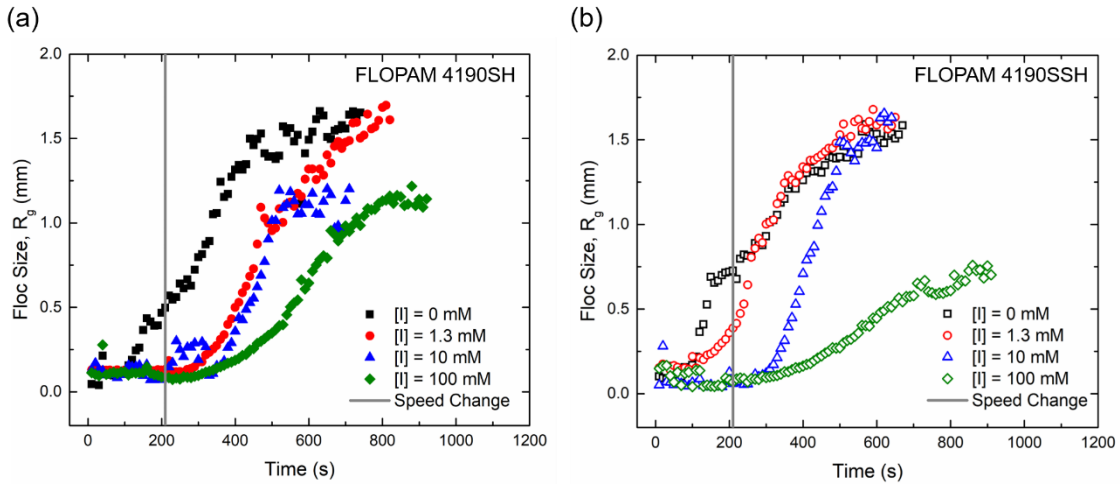


**Figure 5.8**: Floc size expressed as radius of gyration, $R_g$, as a function of ionic strength with time for the (a) lower molecular weight cationic polyacrylamide flocculant (4190SH) and the (b) higher molecular weight cationic polyacrylamide flocculant (4190SSH). The vertical gray line depicts the point where the inner cylinder speed transitions from $\Omega_i$ = 0.5 $s^{-1}$ to $\Omega_i$ = 0.46 $s^{-1}$.

The floc growth rate can be calculated from the experimental data using a modified version of the logistic growth equation

$$\frac{R_g(t)}{R_{g,max}} = \frac{1}{1 + \left( \frac{1}{R_{g,0}/R_{g,max}} - 1 \right) e^{-rt}} \tag{5.3}$$

where $R_g$ is the radius of gyration at a given time in mm, $R_{g,max}$ is the maximum value of $R_g$ in the fitting range in mm, $R_{g,0}$ is the initial value of $R_g$ at the beginning of the fitting range in mm, $r$ is the growth rate in mm $s^{-1}$, and $t$ is time in seconds. This model is typically used for quantifying growth rates in microbial and ecological studies, but it can also be applied to quantify floc growth rates as the flocs eventually plateau in growth, which is akin to a "carrying capacity."[88,182,183,200] The logistic growth equation was fit to where there was a marked increase in the floc size with time. An example of the logistic growth fit is shown **Figure 5.9**, and all fits are shown **Figure 5.10** and **Figure 5.11**. In addition to the fits, the residuals between the measured values and calculated values from the

modified logistic growth equation are presented to show how well the logistic growth equation fits the data points.

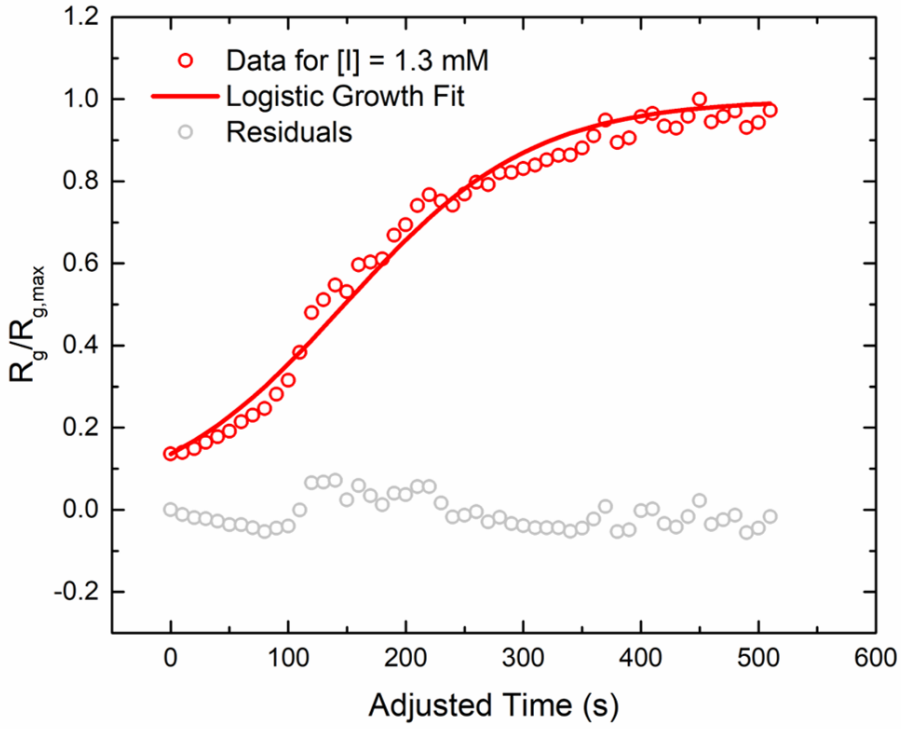


**Figure 5.9**: Representative example of the logistic growth fit to floc size data over time using the higher molecular weight polyelectrolyte (4190SSH) at a solution ionic strength of [I] = 1.3 mM. The open red circles represent the $R_g$ experimental data points normalized by the maximum value of $R_g$ in the fitting range at the floc size plateau. The solid red line indicates the logistic growth fit. The open gray circles represent the residuals of the fit, which are calculated using the logistic growth model and subtracted from the original data at each corresponding time point. The time was adjusted so that the beginning of floc growth occurs at t = 0 s. Logistic growth fits for all systems can be found in **Figure 5.10** and **Figure 5.11**.

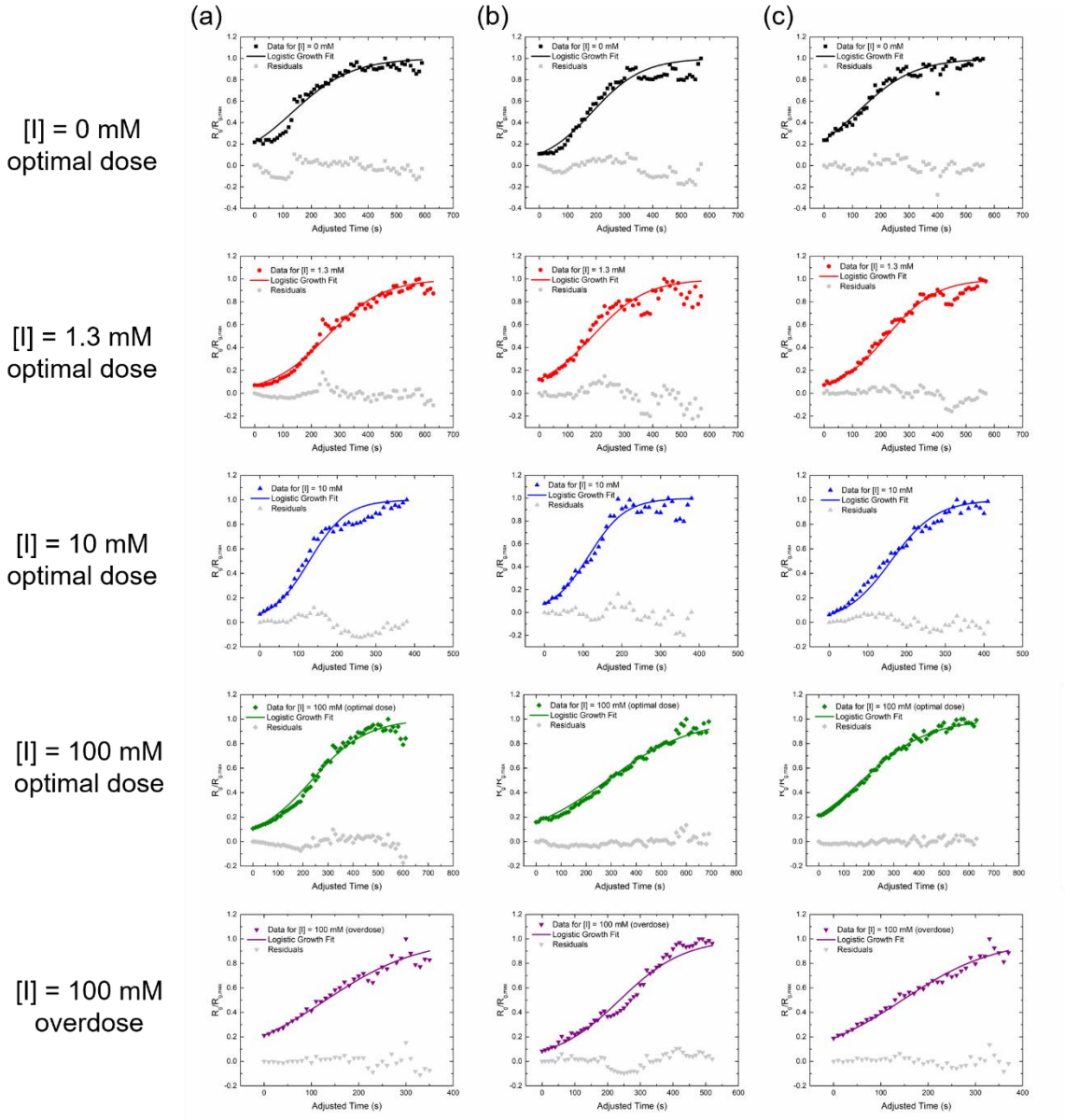


**Figure 5.10**: Logistic growth fits to floc size data over time for (a) trial 1, (b) trial 2, and (c) trial 3. The fits represent the solutions with the lower molecular weight polyelectrolyte (4190SH) at all solution ionic strengths tested in this study. For each plot, the closed, colored circles represent the $R_g$ data points collected during the experiment, normalized by the maximum value of $R_g$ in the fitting range at the floc size plateaus. The solid, colored line indicates the logistic growth fit. The closed gray circles represent the residuals of the fit, which is the calculated data point, using the logistic growth model subtracted from the original data at each corresponding time point. The time was adjusted such that the beginning of floc growth occurs at t = 0 s.

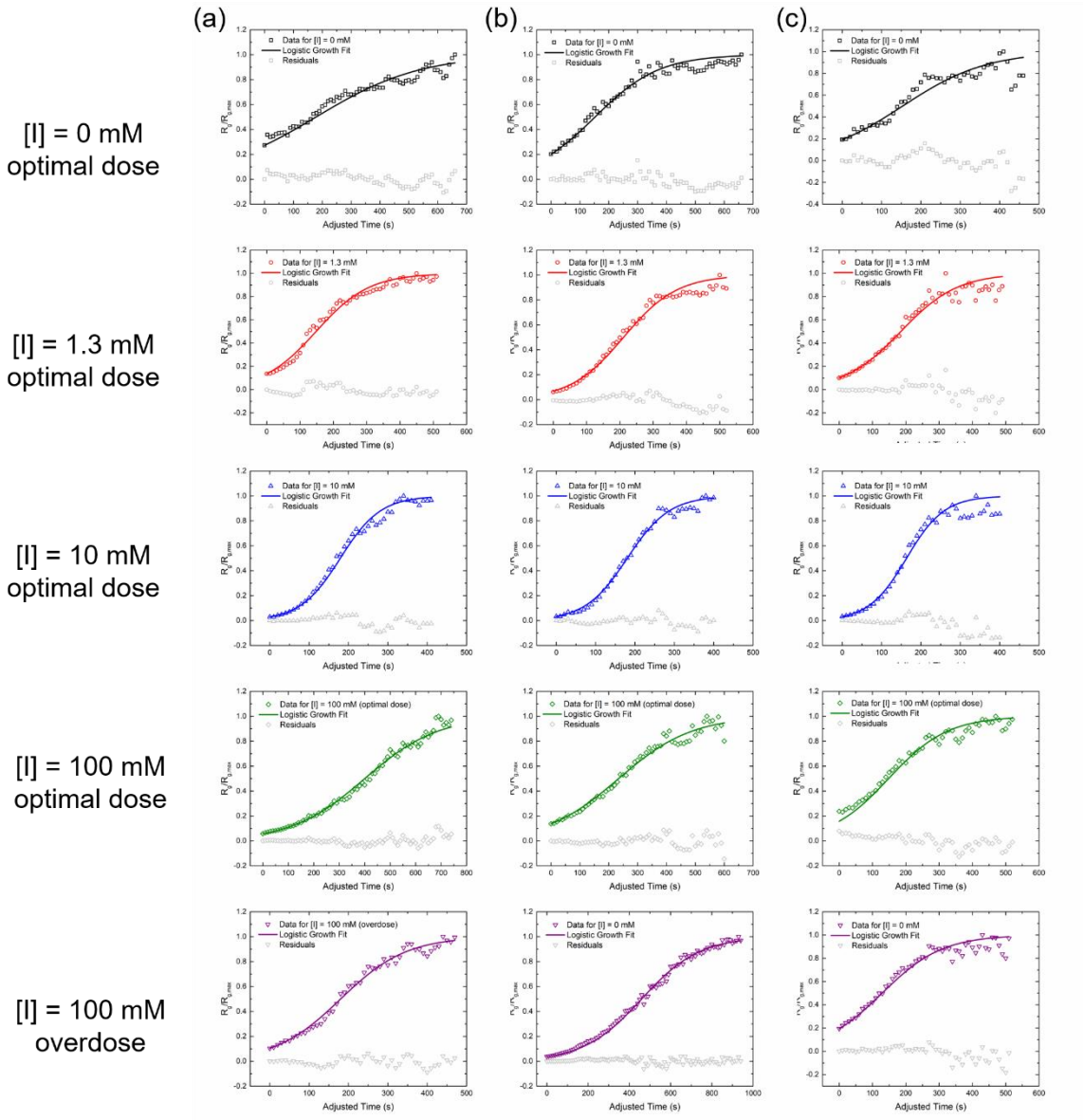


**Figure 5.11**: Logistic growth fits to floc size data over time for (a) trial 1, (b) trial 2, and (c) trial 3. The fits represent the solutions containing the higher molecular weight polyelectrolyte (4190SSH) at all tested solution ionic strengths. For each plot, the open colored circles represent the $R_g$ data collected experimental data points, normalized by the maximum value of $R_g$ in the fitting range, at the floc size plateaus. The solid colored line indicates the logistic growth fit. The open gray circles represent the residuals of the fit, which is the data point calculated by the logistic growth model subtracted from the original data at each corresponding time point. The time was adjusted so that the beginning of floc growth occurs at t = 0 s.

For both polyelectrolytes tested in this study, the floc growth rate initially increases from 0.010 ± 0.002 mm·s$^{-1}$ for 4190SH and 0.008 ± 0.004 mm·s$^{-1}$ for 4190SSH at [I] = 0 mM to 0.020 ± 0.003 mm·s$^{-1}$ for 4190SH and 0.020 ± 0.002 mm·s$^{-1}$ for 4190SSH at [I] = 10 mM as shown in **Table 5-1**. Once the solution ionic strength is increased to [I] = 100 mM, the growth rates decrease to 0.007 ± 0.003 mm·s$^{-1}$ for 4190SH and 0.009 ± 0.005 mm·s$^{-1}$ for 4190SSH. This initial increase in growth rate followed by a decrease as the solution ionic strength increases is due to the interplay of two factors: (1) the bentonite aggregate size increases with ionic strength and (2) the persistence length, and therefore how stretched out the polyelectrolyte conformation is in solution, decreases.[50,90] In particular, the change in persistence length of the polyelectrolytes affects how effectively the polyelectrolyte bridges multiple bentonite aggregates. When there are no or very few additional ions in solution (*i.e.*, [I] = 0 mM and [I] = 1.3 mM), the positive charges of the quaternary ammonium cation functional groups on the polyelectrolyte backbone repulse each other, forcing the polyelectrolyte to adopt a more rigid, expanded conformation with a larger persistence length compared to those at higher ionic strengths.[50,194,201]

Similarly to the bentonite sheets and aggregates, as the solution ionic strength increases ([I] = 10 mM and [I] = 100 mM), the positive charges of the quaternary ammonium functional groups on the polymer backbone are increasingly screened due to an increase in negative $Cl^-$ ions present in solution. This then allows for the polyelectrolyte to adopt a more flexible, coiled conformation and the persistence length therefore decreases.[50,194] Walldal and Åkerman[194] found that for the same CPAM with a molecular weight in the same range as the ones used in this study (5 x 10$^6$ g·mol$^{-1}$), the persistence length decreased from ~8.5 nm at [I] = 0 mM to ~5.5 nm at [I] = 10 mM until it finally plateaued to ~2 nm at [I] = 45 mM. The [I] = 10 mM appears to be an inflection point as at that point the bentonite aggregates prior to the addition of CPAM are two orders of magnitude larger than those at [I] = 0 mM as shown by Wilkinson *et al.*,[90] but the persistence lengths of the polyelectrolytes are not so small that the bridging capability of the CPAM is significantly decreased, which could explain why the growth rate has increased and why there is a delay in the growth at [I] = 100 mM compared to the other

ionic strengths tested. At [I] = 100 mM, the bentonite aggregate size prior to the addition of CPAM is another order of magnitude larger than that at [I] = 10 mM, but the persistence lengths of the polyelectrolytes have continued to decrease, as the polymer chains cannot bridge the now much larger bentonite aggregates as effectively, leading to smaller floc sizes and growth rates. The images in **Figure 5.3** and **Figure 5.4** illustrate this point as the flocs are visibly larger at the lower ionic strengths and smaller at the higher ionic strengths.

As the flocs are formed and grow during flocculation, they can eventually break due to fluid shear forces.[59,61] After some time, the process will approach a steady state between floc growth and breakage.[58,80,164] Prior studies have shown that the maximum floc size is on the order of the Kolmogorov microscale and floc size decreases with increasing global velocity gradient via the global dissipation rate of turbulent kinetic energy.[59,87,88,185] However, the global velocity gradient in this study does not vary significantly, if at all, because the kinematic viscosities of the suspensions are quite similar to each other (~1 cSt to ~1.2 cSt) and the same inner cylinder speed and vortex flow type were used in all experiments. Here, the global velocity gradient, $G \approx 2\pi R_i \Omega_i / d$, is 25.1 $s^{-1}$ for Stage 1 mixing and 23.3 $s^{-1}$ for Stage 2 mixing. Because the global velocity gradient does not vary between experiments, the differences in floc size and floc growth rate are largely due to the interplay between increasing bentonite aggregate size and less expanded polyelectrolyte conformation from decreased persistence length as the solution ionic strength increases.

What is interesting to note is that there is no appreciable difference in the growth rates between the lower and higher molecular weight polyelectrolytes. This largely has to do with using TWV flow for all experiments, which implies that the intervortex mass transfer during mixing does not significantly vary. Intervortex mass transfer can be quantified by an effective dispersion coefficient determined for this particular TC cell by Wilkinson and Dutcher,[95] which can be expressed as

$$D_z^* = 2\lambda k_{cb} \tag{5.4}$$

where $D_z^*$ is the effective dispersion coefficient in $m^2 \cdot s^{-1}$, $\lambda$ is the axial wavelength of the vortex (~1 cm for vortices present here), and $k_{cb}$ is the intermixing coefficient in m $s^{-1}$[195,186]. The values of $D_z^*$ vary from 5.3 x $10^{-5}$ $m^2 \cdot s^{-1}$ at [I] = 0 mM and 1.3 mM, 6.7 x $10^{-5}$ $m^2 \cdot s^{-1}$ at [I] = 10 mM, and 6.2 x $10^{-5}$ $m^2 \cdot s^{-1}$ at [I] = 100 mM for 4190SH and from 5.6 x $10^{-5}$ $m^2 \cdot s^{-1}$ at [I] = 0 mM, 6.3 x $10^{-5}$ $m^2 \cdot s^{-1}$ at [I] = 1.3 mM, 6.2 x $10^{-5}$ $m^2 \cdot s^{-1}$ at [I] = 10 mM, and 5.9 x $10^{-5}$ $m^2 \cdot s^{-1}$ at [I] = 100 mM for 4190SSH for Stage 1 mixing. The trend is similar during Stage 2 mixing, where the values of $D_z^*$ vary from 5.0 x $10^{-5}$ $m^2 \cdot s^{-1}$ at [I] = 0 mM to 5.8 x $10^{-5}$ $m^2 \cdot s^{-1}$ at [I] = 100 mM for 4190SH and from 5.2 x $10^{-5}$ $m^2 \cdot s^{-1}$ at [I] = 0 mM to 5.5 x $10^{-5}$ $m^2 \cdot s^{-1}$ at [I] = 100 mM for 4190SSH. The effective dispersion coefficient is highest at [I] = 10 mM which correlates with this case having the highest growth rate well, which indicates that the solution properties do indeed affect the trends described previously. There is a small delay in the floc growth curves for the 4190SH case at [I] = 0 mM and [I] = 1.3 mM compared to the 4190SSH by approximately 30 s and 100 s, respectively, which is due to the small increase in the effective dispersion coefficient for the 4190SSH case during Stage 1 mixing.

### *5.3.3. Ionic Strength and Molecular Weight Effects on Floc Morphology and Number Distribution*

Another key parameter to examine in addition to floc size and floc growth rate is floc morphology as a function of ionic strength and polyelectrolyte molecular weight. Sedimentation and filtration of flocs for effective separation from water depend on the floc morphology and is related to both floc size and density.[62] Shear gradients present during the mixing process can alter the floc structure with time, which can also have consequences for removal efficiency. Floc morphology can be quantified using a non-dimensional parameter known as a fractal dimension. To obtain a three-dimensional mass fractal dimension, light scattering techniques are typically used. This requires the removal of sample flocs from their native environment.[164,188,189] One of the major advantages of the TC cell in this study is that the combination of the optically clear, glass outer cylinder and the radial injection capabilities of the inner cylinder allows for the determination of the fractal dimension throughout the duration of the flocculation process via image analysis

without floc removal. The only difference between determining a fractal dimension with image analysis versus light scattering is that image analysis yields a two-dimensional, rather than a three-dimensional fractal dimension, fractal dimension.[61,62,190]

The two-dimensional fractal dimension was obtained by linearly regressing the log of the cross-sectional floc area against the log of the floc perimeter for each ten second data set. The closer the $D_{sf}$ value is to 1, the more circular in cross-section the floc becomes, whereas the closer $D_{sf}$ is to 2, the less circular and more rod-like shape the cross-section of the floc is. **Figure 5.12** shows the evolution of $D_{sf}$ with time during Stage 1 and Stage 2 mixing as a function of ionic strength and polyelectrolyte molecular weight. The flocs are initially less circular (*i.e.*, $D_{sf}$ is closer to 2 than to 1) due to increased aggregate-aggregate collisions from orthokinetic aggregation, which is the driving force for flocculation.[48,58,190] The fractal dimension asymptotically decreases toward unity in all cases, indicating that the floc morphology is more circular. This suggests that shear-induced rounding dominates aggregate-aggregate collisions, particularly because a turbulent flow type was used throughout the duration of the experiment, which echoes what was observed in a prior study by Metaxas *et al*.[88]

Another factor to consider here is how the individual bentonite sheets interaction with each other prior to the addition of CPAM. It was previously mentioned that bentonite sheets adopt a porous, edge-face structure at lower ionic strengths. As the ionic strength increases, the bentonite sheets adopt a more edge-edge structure to ultimately, a denser, face-face packed structure.[71,72] **Figure 5.12** and **Table 5-1** show that the $D_{sf}$ values increase with increasing ionic strength, indicating that the flocs are less circular in cross-section. At the end of the logistic growth fits, the $D_{sf}$ values increased from 1.21 ± 0.01 at [I] = 0 mM to 1.4 ± 0.1 at [I] = 100 mM for 4190SH, and increased from 1.22 ± 0.06 at [I] = 0 mM to 1.3 ± 0.1 at [I] = 100 mM for 4190SSH. This implies that flocs at higher ionic strengths are more resistant to shear-induced rounding, which is most likely due to the denser nature of the bentonite aggregates at higher ionic strengths. Interestingly, these results contradict what Wilkinson *et al*.[90] found, where the flocs at [I] = 100 mM had smaller fractal dimensions than those at [I] = 10 mM. However, it should be noted that the

fractal dimension for flocs at [I] = 0 mM or [I] = 1.3 mM were not measured in the Wilkinson study, and jar tests were used, where the flow field is not nearly as homogeneous as the TWV flow used in the present study.[87] Between the two polyelectrolytes used, there was a statistically insignificant difference between the fractal dimension values at injection, at the speed change, and at the end of the logistic growth fit. This result further suggests that the initial bentonite aggregate structure due to the ionic strength of the solutions determines the fractal dimension trends.

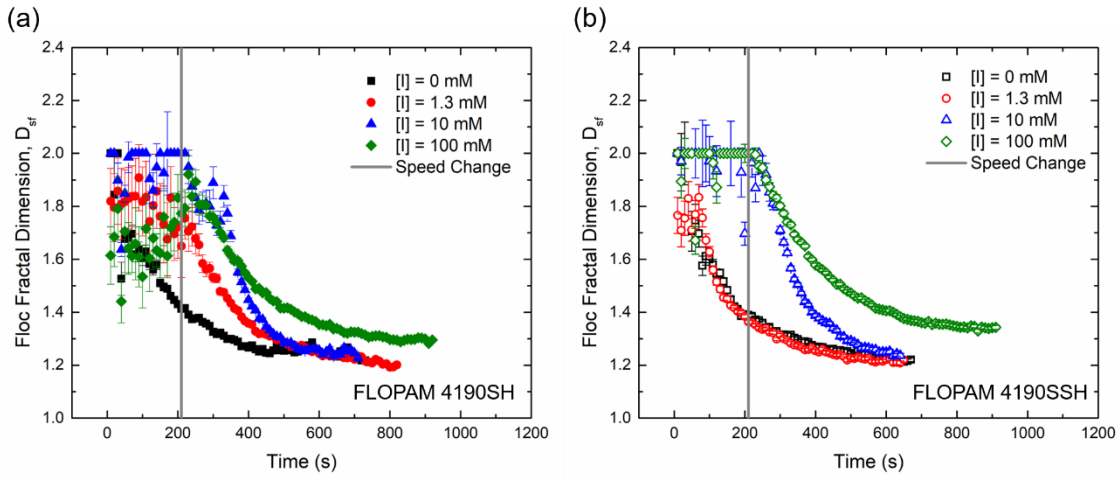


**Figure 5.12**: Floc morphology quantified as a 2-D perimeter-based fractal dimension, $D_{sf}$, as a function of ionic strength with time for the (a) lower molecular weight cationic polyacrylamide flocculant (4190SH) and the (b) higher molecular weight cationic polyacrylamide flocculant (4190SSH). The vertical gray line depicts the point where the inner cylinder speed transitions from $\Omega_i$ = 0.5 $s^{-1}$ to $\Omega_i$ = 0.46 $s^{-1}$.

In addition to differences in floc morphology as a function of ionic strength, the number of flocs present in the suspension differs with ionic strength. Because the persistence lengths of the polyelectrolytes are longer and the initial bentonite aggregate sizes are lower at lower ionic strengths, and the initial bentonite aggregate sizes are lower at lower ionic strengths as compared to higher ionic strengths, more of the bentonite aggregates present in the suspension can be incorporated to form a floc. This is reflected in the larger floc sizes observed at lower ionic strengths in **Figure 5.8** and **Table 5-1**. Larger floc sizes indicate less flocs in the suspension, which is observed in **Figure 5.13**. The maximum number of flocs increases from ~3000 flocs up to ~8000 flocs for 4190SH

and from ~3500 flocs up to ~10,000 flocs for 4190SSH as ionic strength increases. The numbers are slightly higher for the 4190SSH as its longer length compared to 4190SH allows it to adsorb to more bentonite aggregates in the suspension.

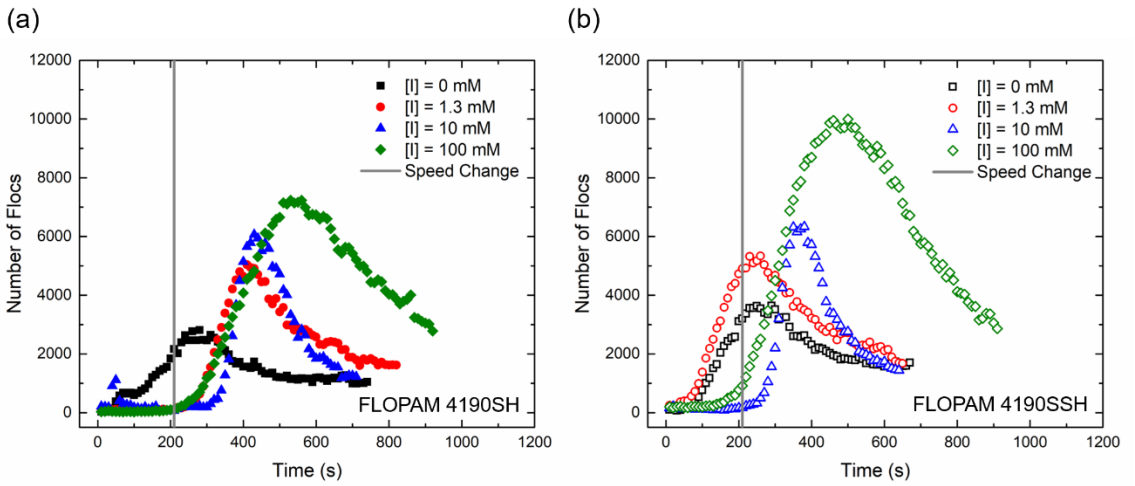


**Figure 5.13**: Number of flocs as a function of solution ionic strength with time for the (a) lower molecular weight cationic polyacrylamide flocculant (4190SH) and the (b) higher molecular weight cationic polyacrylamide flocculant (4190SSH). The vertical gray line depicts where the inner cylinder speed transitions from $\Omega_i$ = 0.5 $s^{-1}$ to $\Omega_i$ = 0.46 $s^{-1}$.

**Table 5-1**: Summary of relevant parameters including: the solution ionic strength, the polyelectrolyte concentration used with optimal dose or overdose, the maximum floc size, the floc growth rate, and the fractal dimension where the polyelectrolyte is injected (30 s), at the Stage 1 to Stage speed change (210 s), and where growth plateaus (varies for each condition). The errors for the mean values represent 95% confidence intervals.

| | Ionic Strength (mM) | Polyelectrolyte Concentration (ppm) | Max Floc Size, $R_g$ (mm) | Floc Grow Rate, $r$ (mm·$s^{-1}$) | $D_{sf}$ at Injection | $D_{sf}$ at Speed Change | $D_{sf}$ at End of Fit |
|---|---|---|---|---|---|---|---|
| FLOPAM 4190SH (MW = 4-6 x $10^6$ g·$mol^{-1}$) | 0 | 8.0 (optimal) | 1.8 ± 0.3 | 0.010 ± 0.002 | 1.8 ± 0.6 | 1.5 ± 0.1 | 1.21 ± 0.01 |
| | 1.3 | 11.9 (optimal) | 1.5 ± 0.5 | 0.011 ± 0.001 | 1.8 ± 0.4 | 1.7 ± 0.2 | 1.24 ± 0.06 |
| | 10 | 4.0 (optimal) | 1.5 ± 0.5 | 0.020 ± 0.003 | 2.0 ± 0.1 | 2.0 ± 0.0 | 1.25 ± 0.09 |
| | 100 | 1.0 (optimal) | 0.7 ± 0.9 | 0.007 ± 0.003 | 1.9 ± 0.2 | 1.9 ± 0.3 | 1.4 ± 0.1 |
| | 100 | 8.0 (overdose) | 0.7 ± 0.4 | 0.0101 ± 0.0001 | 2.0 ± 0.0 | 1.55 ± 0.06 | 1.36 ± 0.08 |
| | Ionic Strength (mM) | Polyelectrolyte Concentration (ppm) | Max Floc Size, $R_g$ (mm) | Floc Grow Rate, $r$ (mm·$s^{-1}$) | $D_{sf}$ at Injection | $D_{sf}$ at Speed Change | $D_{sf}$ at End of Fit |
| FLOPAM 4190SSH (MW = 8-11 x $10^6$ g·$mol^{-1}$) | 0 | 7.0 (optimal) | 1.9 ± 0.2 | 0.008 ± 0.004 | 2.0 ± 0.2 | 1.41 ± 0.04 | 1.22 ± 0.06 |
| | 1.3 | 7.0 (optimal) | 1.7 ± 0.6 | 0.012 ± 0.001 | 1.9 ± 0.3 | 1.4 ± 0.1 | 1.3 ± 0.1 |
| | 10 | 5.0 (optimal) | 1.6 ± 0.1 | 0.020 ± 0.002 | 2.0 ± 0.0 | 2.0 ± 0.0 | 1.22 ± 0.03 |
| | 100 (optimal) | 1.5 (optimal) | 0.9 ± 1.0 | 0.009 ± 0.005 | 1.9 ± 0.3 | 1.8 ± 0.3 | 1.3 ± 0.1 |
| | 100 (overdose) | 7.0 (overdose) | 0.9 ± 0.8 | 0.010 ± 0.005 | 2.0 ± 0.0 | 1.7 ± 0.3 | 1.33 ± 0.07 |

*5.3.4. Effects of Optimal Dosing and Overdosing on Floc Growth*

To further illustrate the effects of overdosing a suspension with polyelectrolyte flocculant, an experiment was conducted to compare the floc size and floc growth rates between the optimal dose required for [I] = 100 mM as determined in **Figure 5.7** for both polyelectrolytes used in this study. **Figure 5.14a** shows the floc size for the optimal dose cases (green symbols) with the corresponding overdose cases (purple symbols) for the lower molecular weight CPAM (closed diamonds) and the higher molecular weight CPAM (open triangles). The concentrations for the overdose case are 8.0 ppm for 4190SH and 7.0 ppm for 4190SSH, which are the concentrations used for the [I] = 0 mM case as shown in **Table 5-1**. There is no statistical difference in the maximum floc size and the floc growth rate between the optimal and overdose cases for both polyelectrolytes according to **Table 5-1**.

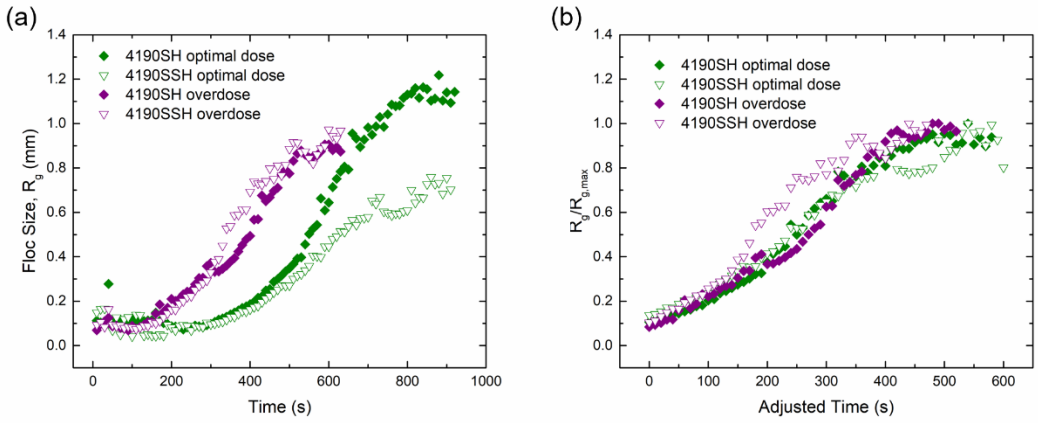


**Figure 5.14**: (a) Comparison of optimal dose (green diamonds) and overdose (purple triangles) floc growth with time using the lower (4190SH, solid symbols) and higher (4190SSH, open symbols) molecular weight polyelectrolyte flocculants at [I] = 100 mM. To better compare the floc growth of the optimal dose to overdose conditions, (b) shows the time adjusted such that all growth curves start at 0 s and the floc sizes normalized by the maximum floc size ($R_g/R_{g,max}$). There is no statistical difference in floc size or growth rate between optimal dose and overdose conditions for both flocculants studied.

To make it more apparent that there is no appreciable difference between the optimal and overdose cases, the floc size normalized by the maximum floc size was plotted against the adjusted time (where all growth starts at 0 s) in **Figure 5.14b**. Using a higher

concentration polyelectrolyte does not result in an increased flocculation performance compared to the smaller, optimal dose. Using more of the polyelectrolyte could potentially result in restabilization of the particulate as described earlier.[44] At an industrial scale, using more flocculant than needed can be cost-prohibitive as more polyelectrolyte would be used and any excess polyelectrolyte would have to be filtered downstream prior to discharging the water. This would result in increased operating costs for a utility.[46]

## *5.4. Conclusion*

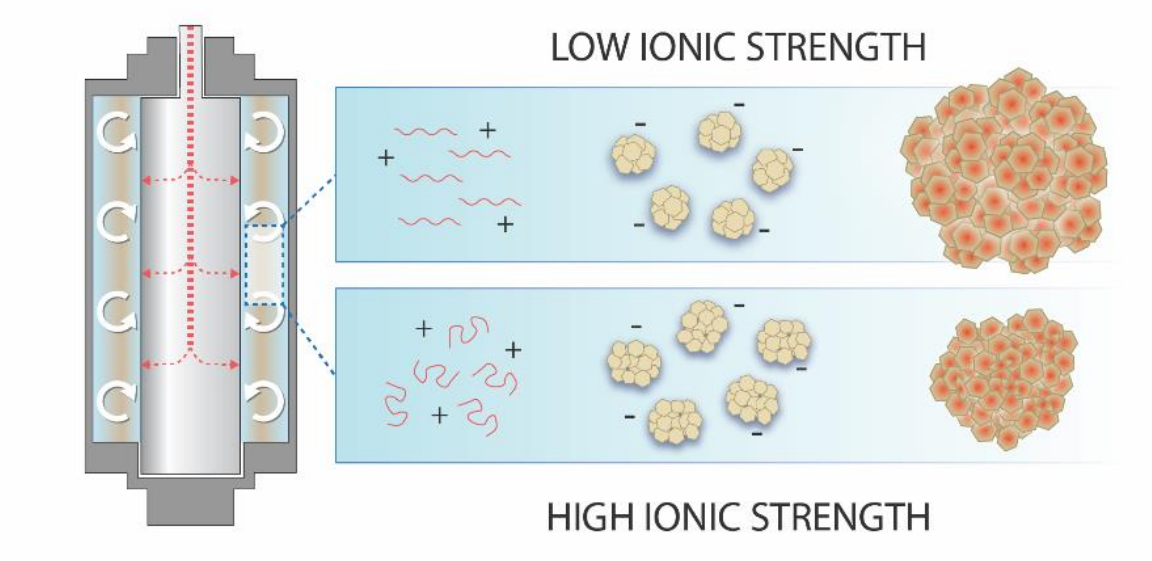


**Figure 5.15**: Graphical summary of findings. Increased charge screening from increased ionic strength of a bentonite-laden suspension for flocculation in a Taylor-Couette cell capable of radial injection results in an interplay between increased bentonite aggregate size and decreased ability for the polyelectrolyte to bridge multiple aggregates due to decreasing persistence length, resulting in a less expanded polymer conformation in solution.

The unique ability to non-intrusively inject one fluid into another fluid while harnessing the precise mixing capabilities of a TC cell offers unprecedented access to the entire flocculation process without having to remove flocs for further analysis. In this study, the ionic strength was varied in a bentonite suspension and two different molecular weights of polyelectrolyte flocculant were used at the same turbulent wavy vortex flow state generated by the TC cell to obtain the floc size, floc growth rate, 2-D floc fractal dimension, and floc numbers with time. As the ionic strength increased, the floc size

generally decreased while the floc growth rate initially increased then decreased. This was due to charge screening effects, where the initial bentonite aggregate size increases but the polyelectrolyte persistence length decreases and its conformation is less expanded, hindering its ability to adsorb to and bridge multiple bentonite aggregates. The $D_{sf}$ values increased (became less circular in cross-section) with ionic strength due to densification of bentonite aggregates because of charge screening, rendering the flocs more resistant to shear-induced breakage. An increase in ionic strength resulted in an increased in the number of flocs due to the inability of the polyelectrolytes to effectively bridge multiple bentonite aggregates as their respective persistence lengths decrease with increasing ionic strength, resulting in a less expanded conformation in solution. There were no appreciable differences between the two molecular weights of CPAM tested in this study, with the exceptions of smaller optimal doses and slightly higher effective dispersion coefficients for the larger molecular weight polyelectrolyte.

Flocculation is a highly dynamic process, with results that depend on both the physicochemical properties of the solution, as well as the hydrodynamic properties of the mixing environment. With respect to the myriad of factors affecting polyelectrolyte-mediated flocculation, this study only begins to scratch the surface. Here, only one turbulent vortex type (TWV) was used to study the flocculation of bentonite with cationic polyacrylamide as a function of ionic strength and polymer molecular weight. It would be of interest to study how the results presented here compare with a different turbulent flow state or with a laminar flow state, such as laminar wavy vortex flow. Fundamental understanding of the effect of solution properties and flow parameters can potentially be used to optimize processes that utilized polymer-driven flocculation of a solid particulate, such as water treatment operations.

# Chapter 6
# Effects of Humic Acid on Polyelectrolyte-Clay Flocculation

## *6.1. Introduction*

The flocculation studies discussed in the previous chapters examine a two-component system of bentonite and cationic polyacrylamide flocculant, where in Chapter 4, the mixing speed of the Taylor-Couette cell was varied and in Chapter 5, the solution ionic strength and flocculant molecular weight were varied. A particulate system consisting of just bentonite clay and NaCl as described previously appears deceptively simple. However, the anisotropic nature of bentonite with respect to its charge distribution renders it highly susceptible to changes in surface aggregate morphology due to changes in pH or ionic strength.[71,72,84] These changes in surface aggregate morphology ultimately influence the manner in which the polyelectrolyte flocculant can interact with the bentonite aggregates.[73]

Significant progress has been made in studying this already complex system as a function of two key solution properties: pH and ionic strength. Wilkinson *et al*.[90] showed that increasing the solution ionic strength increases the bentonite aggregate size due to charge screening effects, which resulted in a decrease the optimal polyelectrolyte flocculant dose. In addition, laser scanning confocal microscopy showed that the internal floc structure also changed with increasing ionic strength, from a more network-like

structure at lower ionic strength ([I] < 10 mM) to a electrostatic "patchy" structure at higher ionic strength ([I] > 10 mM. Further work by Wilkinson *et al*.[91] showed that changes in solution pH did not appreciably affect neither the initial bentonite aggregate size nor the floc morphology. What was observed was that as the pH increased, the optimal polyelectrolyte flocculant dose also increased. From these studies it appears that the initial bentonite aggregate size largely decides the internal floc structure while the initial bentonite morphology decides the extent of polymer adsorption, as shown by the changes in required flocculant dosing.

Realistically, the particulate matter in surface waters consists of organic and inorganic components. Most of the natural organic matter present is in the form of humic substances (HS), of which can broadly be categorized into humic acids, fulvic acids and humin, which largely vary by their phenolic and carboxyl content.[202,203] The origin of humic substances in water sources come primarily from either terrestrial origin (*allochthonous* substances) or from the natural decay process of biological material (*autochthonous* substances).[204] This complicates treating surface waters, as the relative fraction of humic acids and fulvic acids will vary, depending on the source of the natural organic matter. Removing HS from source waters via flocculation is a non-trivial process, as the HS need to be converted from a soluble form to an insoluble form. Addition of cationic polyelectrolytes only partially removes HS from surface waters, but the presence of suspended solids, such as bentonite, has shown increased removal from water.[74] Adsorption of HS onto the clay is highly dependent on solution conditions and generally proceeds via ion exchange and surface complexation mechanisms.[75–77] From a health and safety perspective, removal of HS is critical because if they are not properly removed prior to the chlorination step of the water treatment process, HS can react with chlorination chemicals and form toxic byproducts, such as dihaloacetonitriles.[78,79]

Recent analyses of the HS structure describe them as anionic "supramolecular associations."[44,205] It is thought that the charge neutralization of the HS is its predominant mechanism of removal from water and is best done using cationic polyelectrolytes. Kvinnesland and Odegaard[206] showed that there is a stochiometric relationship between the

cationic charge density of the polyelectrolyte and the anionic charge density of the HS present. Therefore, the higher charge density polyelectrolytes are more effective in removing most HS from water.[207,208] One further complication is that the solubility of the fractions present in HS are largely pH dependent. Humic acid, which is what is used in this study, tends to be insoluble at lower pH values (*i.e.*, below its pKa value) and exists in a multi-step equilibrium state in solution. Because there is not one specific chemical structure associated with humic acid, the pKa can vary between 3 and 9 depending on its source, chemical functional groups present (particularly carboxylic acid content), and method of preparation.[202,203,209] These additional complexities further complicate the adsorption of polyelectrolyte to the bentonite aggregate surfaces, as there is now competition for the polyelectrolyte between the bentonite and the humic acid.

To make the flocculation particulate system in this study more realistic in nature, natural organic matter was added in the form of humic acid (HA), as shown in **Figure 6.1**. The pH of the system was systematically varied, and the polyelectrolyte flocculation performance was evaluated in the form of jar tests. Humic acids from different sources were studied to examine possible differences in flocculation performance holding all other factors (*i.e.*, ionic strength, mixing protocol, pH range tested) the same. Laser scanning confocal microscopy experiments were conducted to image the internal floc structure to determine possible differences as the pH range, flocculant doses, and humic acid sources varied.

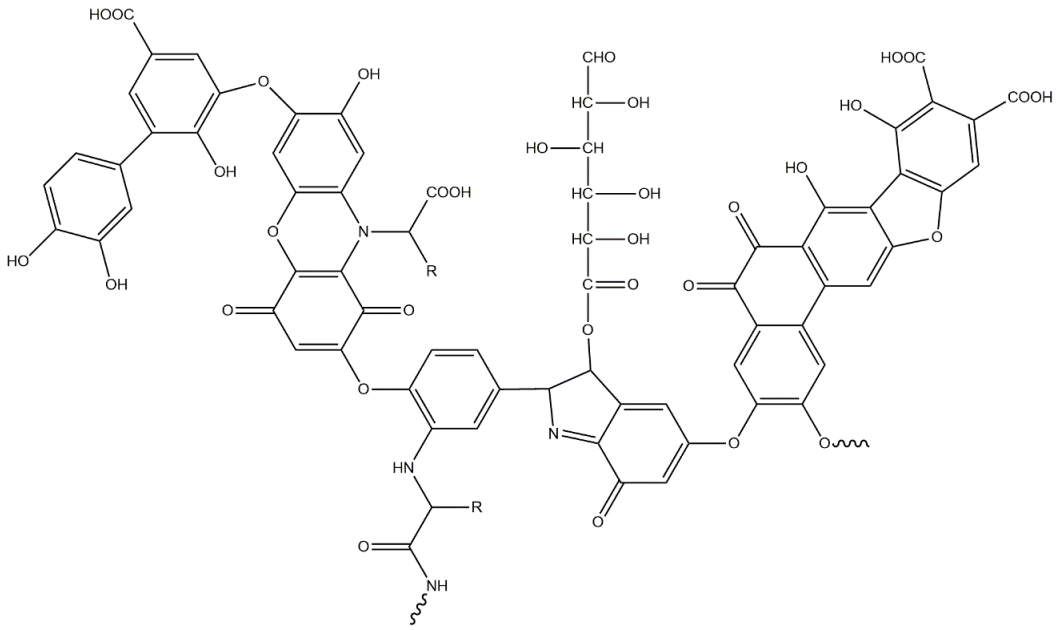


**Figure 6.1**: A typical chemical structure for humic acid (HA). Variation can exist with respect to the functional groups presented here.

## *6.2. Materials and Methods*

### *6.2.1. Materials*

Three different samples of humic acid were used in this study: a coal-based technical grade HA from Sigma Aldrich, a Leonardite-based HA standard (1S104H Leonardite) from the International Humic Substances Society (IHSS) and a peat-based HA standard (1S103H Pahokee Peat). A 1 $g \cdot L^{-1}$ stock solution of each sample was prepared by dissolving 0.5 g of humic acid in 500 mL of 0.1 M NaOH solution in a volumetric flask. The solution was stirred before each use to re-disperse any precipitated humic acid and allowed to warm to room temperature. When not in use, the stock solution was stored in the refrigerator. Distilled water used in the studies was from Premium Waters, Inc. Powdered Na-bentonite from Alfa Aesar and ACS grade NaCl from Fisher Scientific were used as received.

The commercial polyelectrolyte flocculant used in the jar tests study is a cationic polyacrylamide (FLOPAM FO 4190SH, SNF Polydyne, $M_w$ = 4-6 x $10^6$ $g \cdot mol^{-1}$) with 10 mol% of the monomer groups containing a quaternary ammonium cation with a permanent

positive charge, regardless of solution pH. To make a 0.2 wt% stock solution of the flocculant, 0.2 g of the solid pellets was mixed with a Jiffy mixer attachment in 400 mL of distilled water for 30 min. The stock rested overnight (~12 h) in the refrigerator prior to initial and any subsequent use. Before any experiment, the stock solution was allowed to warm to room temperature and was remade every two weeks according to the supplier's instructions.

For the laser scanning confocal microscopy studies, a fluorescent analog of the commercial cationic polyacrylamide (CPAM) was used. Cyanine5-labeled PAEMAm-s-PMAAPTA (polyN-(2-aminoethyl) methacrylamide-s-poly[3-(methacryloylamino)propyl] trimethylammonium chloride) ($M_n$ = 3.3 MDa, *dn/dc* (experimental) = 0.1081, $Đ$ =1.247) was synthesized according to a prior study by Wilkinson *et al.*[89] The chemical structures of the commercial grade CPAM and the fluorescent analog are shown in **Figure 6.2**. While there are some minor structural differences between the two polymers, both the commercial and fluorescent versions have the 10 mol% charge from the quaternary ammonium functional group.

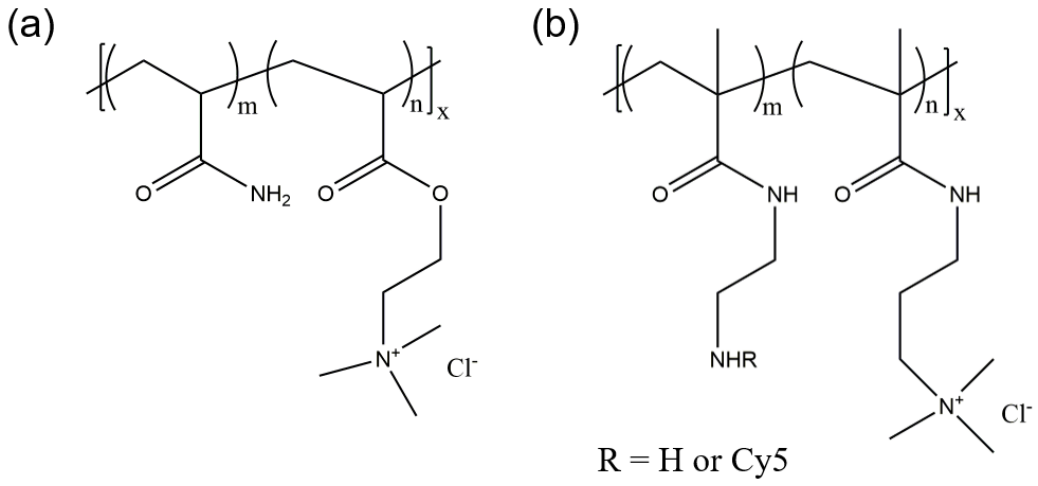


**Figure 6.2**: Chemical structures of (a) the commercial cationic polyacrylamide (FLOPAM 4190SH) and (b) the fluorescent analog. Both structures contain a quaternary ammonium functional group which renders the polymer permanently cationic in solution. Cy5 denotes the Cyanine5 fluorophore labeled to a fraction of the polymer chains in the fluorescent analog.

*6.2.2. Jar Tests*

For all experiments, 2 mL of a 1 $g \cdot L^{-1}$ stock solution of humic acid was added to 1 L of distilled water in 2 L Pyrex jars. The final concentration of humic acid in solution is 2 $mg \cdot L^{-1}$. This was chosen because it falls in the concentration range of humic substances present in river water.[204] River water was appropriate to model here, as the source of drinking water for the city of Minneapolis is the Mississippi River. The pH of the solution was adjusted using 0.1 M NaOH or 0.1 M HCl to produce solutions at pH 3, 5, 6.6, 9 and 11. The pH of the solutions was measured using a Mettler Toledo SevenExcellence pH meter. For solutions at pH 3 or 11, acid or base could be added before the bentonite was added to the solution. However, when the solution pH was adjusted to 5, 6.6, and 9 before adding bentonite, interactions of the bentonite with dissolved $CO_2$ in water and humic acid caused the solution to drift to pH 6.[178] Therefore, for solutions at pH 5, 6.6, and 9, HCl or NaOH were mixed for 2 minutes at 200 RPM immediately after bentonite dispersion. The ionic strength of all solutions remained constant at [I] = 1.3mM. A pre-determined amount of NaCl by the amount of acid or base added to the suspension for pH adjustments, was added concurrently with humic acid. Ionic strength calculations included the contributions from NaCl, NaOH, and HCl. Humic acid was omitted from these calculations because of its varying chemical structure and size, which makes accurate quantification of the contributions to the total ionic strength impractical.

As described previously, 30 mg of bentonite was added before or after adjusting the pH and dispersed at 300 RPM for 30 min in a VELP Sceintifica JTL4 flocculator. The speed of flocculator was then reduced to 200 RPM and the desired commercial polyelectrolyte dose was injected simultaneously into each jar. After 3 min of rapid mixing at 200 RPM, the speed was further reduced to 30 RPM for 30 min. Once the mixing finished, the suspension settled for 5 min. Afterwards, the final turbidity of the supernatant was measured using a LaMotte turbidity meter. A schematic of the procedure is shown in **Figure 6.3**.

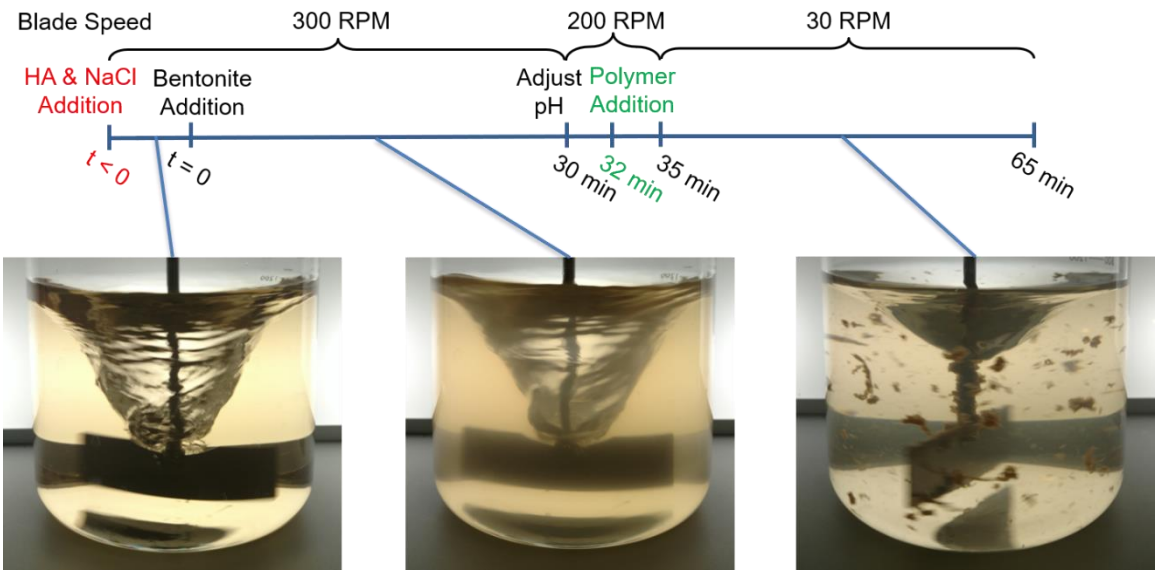


**Figure 6.3**: A schematic of the jar test procedure including mixing speeds and time points for addition of humic acid (HA), NaCl, and the polymer flocculant.

*6.2.3. Laser Scanning Confocal Microscopy*

To prepare the flocs for laser scanning confocal microscopy, the same jar test procedure described in the previous section was used with a few changes added. Smaller 600 mL jars instead of 1 L jars were used and the volume of distilled water was decreased from 1 L to 250 mL. The mixing times and speeds were reduced to 150 RPM for 30 s for the rapid mix and 20 RPM for 20 min for the slow mix. These changes were made to the sample volumes and mixing protocol to account for a smaller supply of the fluorescently tagged polyelectrolyte. The dosage of the fluorescent polyelectrolyte analog was measured proportionally to what was used in the full-size jar tests that used the commercial polyelectrolyte. The flocs were gently aspirated from the bottom of the jars using a plastic pipette onto a glass microscope slide with ~3.2 mm deep poly(dimethyl siloxane) wells. The well openings were then covered with a glass coverslip.

A Nikon C2+ laser confocal instrument coupled to a Nikon Eclipse Ti inverted microscope with a 20× objective lens was used to obtain confocal images of the internal floc structure. The bentonite does not fluoresce on its own; however, the Cy5 fluorophore in the fluorescent analog and the humic acid do fluoresce. To image the fluorescent

polymer, a Cy5 filter cube with excitation wavelengths of 488 nm and 637 nm and an emission wavelength of 447 nm was used. To image the humic acid, a FITC-Texas Red filter cube with an excitation wavelength of 490-510 nm and 560-580 nm and emission wavelengths of 450-470nm, 520-550 nm, and 600-650 nm was used. The FITC-Texas Red filter cube was chosen as the excitation wavelength of most humic acids is around 470-490 nm and the emission is between 450-500 nm.[210–212] The confocal images were recorded with a resolution of 0.62 μm per pixel (2048 × 2048), and the depth resolution was 10 μm.

#### *6.2.4. Aggregate Size and Zeta Potential Measurements*

To measure the bentonite aggregate size distribution as a function of pH, a Microtrac BLUEWAVE Particle Size Analyzer was used. This laser diffraction system is capable of measuring both spherical and irregularly shaped particles from 0.01 to 2000 μm using modified Mie scattering calculations that meet ISO TC24 standard specifications. A Microtrac Stabino Particle Charge Titration Analyzer was used to measure the zeta potential of the suspensions. Each sample was measured in each apparatus immediately after the mixing procedure in the flocculator outline in the first section of the Methods. Note that here, the polyelectrolyte flocculant was not added to the suspension, as it is the bentonite-humic acid aggregate behavior that is of interest in these measurements.

## *6.3. Results and Discussion*

#### *6.3.1. Effect of pH on Turbidity Reduction*

Flocculation performance is defined here by the way the final turbidity increases or decreases with increasing polyelectrolyte dosage. Ideally, an optimal dosage would be present, which is the smallest amount of flocculant required to achieve a minimum in final turbidity of the supernatant post-flocculation. The first set of experiments, as shown in **Figure 6.4**, varied the pH of the solution using the coal-based HA, while the ionic strength is kept constant at [I] = 1.3 mM. **Figure 6.4a** depicts all the experimental trials plotted together but can be a bit difficult to interpret. Therefore, **Figure 6.4b** depicts the extreme pH values tested (pH 3 and pH 11) with the median pH value of 6.6, while **Figure 6.4c** depicts the intermediate pH values tested (pH 5 and pH 9) with the median pH value of 6.6. In general, the final turbidity values increased with increasing pH. This is most likely

due to the HA being insoluble at the lowest pH value of 3 tested here, indicating minimal competition with the bentonite for the polyelectrolyte adsorption.

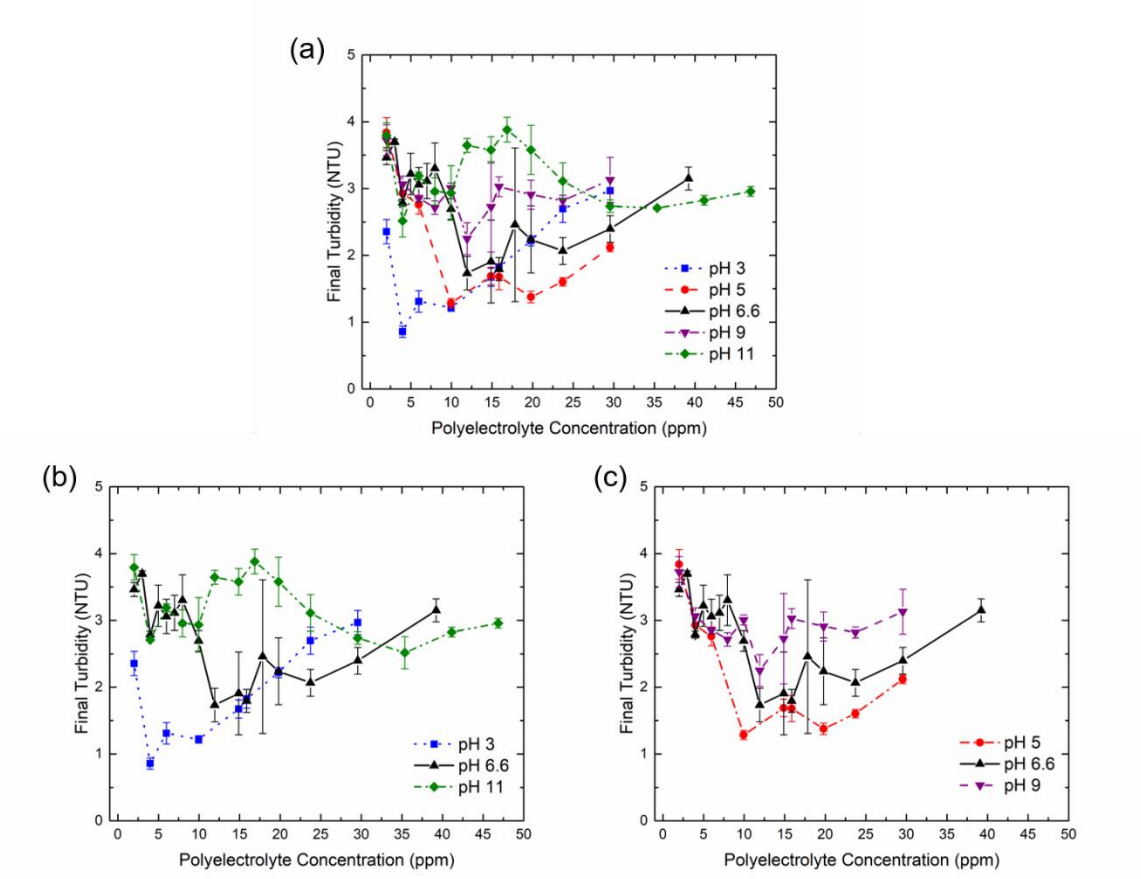


**Figure 6.4**: Turbidity curves expressed in nephelometric turbidity units (NTU) as a function of solution pH and polyelectrolyte dose in parts per million (ppm) using the coal-based humic acid. Curve (a) depicts all the superimposed curves, while (b) depicts the two extreme pH levels of pH 3 and 11 alongside the median pH 6.6 and (c) depicts the two intermediate pH levels of 5 and 9 alongside the median pH 6.6. The global minimum in each curve represents the optimal dosage of polyelectrolyte flocculant required for particulate removal *i.e.*, the lowest final turbidity. For all experiments, the solution ionic strength was [I] = 1.3 mM.

The optimal dosage also increased with increasing pH, from 10.0 ppm at pH 3 and 5 to 11.9 ppm at pH 6.6 and 9 to finally 35.4 ppm at pH 11. This trend is what was also seen in a previous study by Wilkinson *et al.*[91] and is postulated to be a consequence of a change from a porous edge-face bentonite aggregate morphology to a dense face-face morphology. The pH 3 case is the only curve where there is only a global minimum,

indicating optimal flocculant dosage, before an observed rise in turbidity with increasing polyelectrolyte dose as a result of particulate restabilization.[197] The other pH curves show a global minimum and at least one local minimum and/or maximum. It is likely this behavior is observed due to HA being partially or mostly soluble in solution at more elevated pH, which subsequently competes with bentonite for adsorption to the polyelectrolyte.

The zeta potential comparison of a bentonite-only and a bentonite with humic acid suspension is shown in **Figure 6.5**. As expected, the magnitude of the zeta potential increases with increasing pH from approximately -65 mV to -110 mV, as the hydroxyl edge groups from bentonite and the carboxylic acid groups from the HA are deprotonated. To determine if the initial bentonite aggregate size in the presence of humic acid has a potential effect on the flocculation behavior observed in **Figure 6.4**, the area-averaged aggregate size was measured using laser diffraction particle sizing as a function of pH. An aggregate size comparison between a bentonite only suspension and bentonite with HA suspension is shown along with the zeta potential **Figure 6.5**. At pH 3, the average aggregate size for both suspensions is higher than at the higher pH values ($4.5 \pm 0.4$ μm for bentonite only and $3.2 \pm 0.5$ μm for bentonite with humic acid at pH 3). At all other pH values, the average size for both types of suspensions is between 2.0 and 2.6 μm, with no statistical difference between the suspension types and the pH values. The results here reflect what was previously seen in the bentonite-polyelectrolyte flocculation pH study by Wilkinson *et al*.[91], where there was no appreciable difference in initial particulate aggregate size. Therefore, the size does not play an appreciable role in the differences seen in the flocculation performance. It is more likely that the aggregate morphology plays a larger role in the flocculation performance by influencing the internal floc structure, which is discussed in the following section.

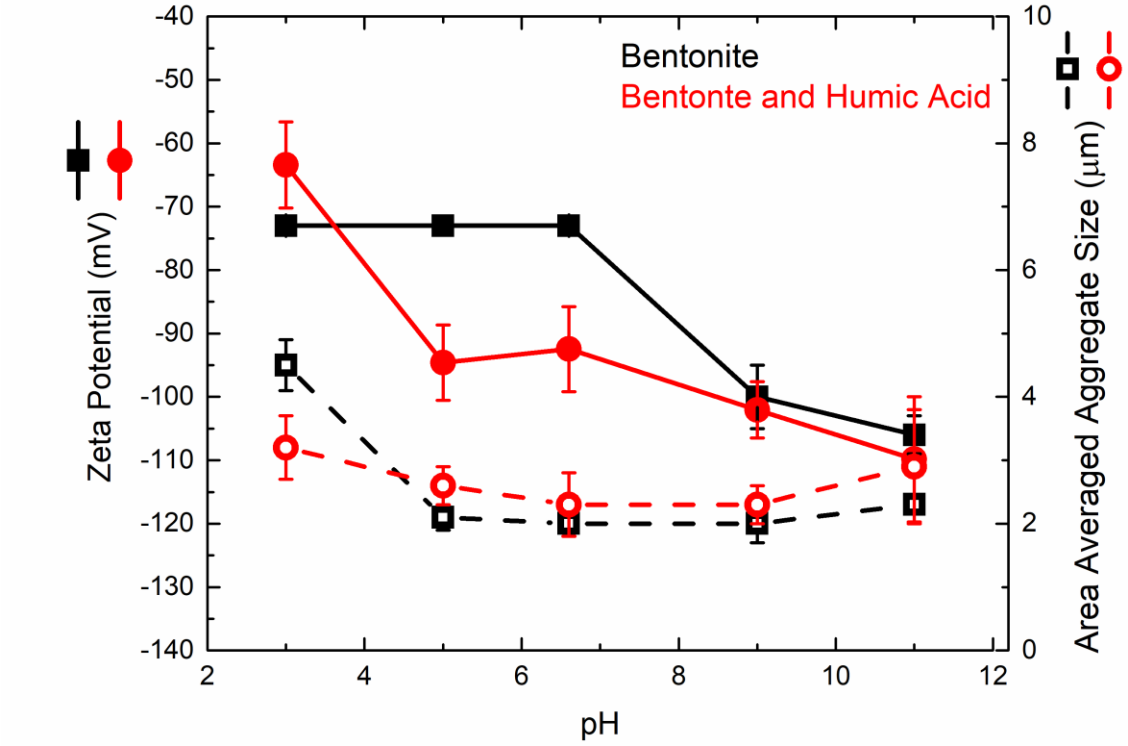


**Figure 6.5**: Zeta potential (filled symbols) and area-average aggregate size (open symbols) of a bentonite only (black) and bentonite and humic acid (red) suspension as a function of solution pH. The error bars represent the standard deviation of the mean of three measurements at each point.

### *6.3.2. Effect of Dosing and pH on Internal Floc Structure*

The fluorophore-tagged analog of the commercial polyelectrolyte flocculant was used to form flocs that can be imaged via laser scanning confocal microscopy. Conveniently, the filter cubes required for imaging the fluorescent polyelectrolyte and the humic acid do not have overlapping excitation/emission signals, therefore the location of both components within the floc structure were simultaneously collected. A representative example is shown in **Figure 6.6** at pH 11 for the coal-based HA, where most of the HA should be dissolved in solution.[202,209] The internal floc structure at the global minimum (35.4 ppm) and local minimum (4.0 ppm) respectively are shown. Here, the internal floc structure for both minima is made of highly networked structures. The humic acid appears

to be adsorbed onto the same areas as the polyelectrolyte, which suggests the humic acid has adsorbed onto the polyelectrolyte and formed a coating around the floc.

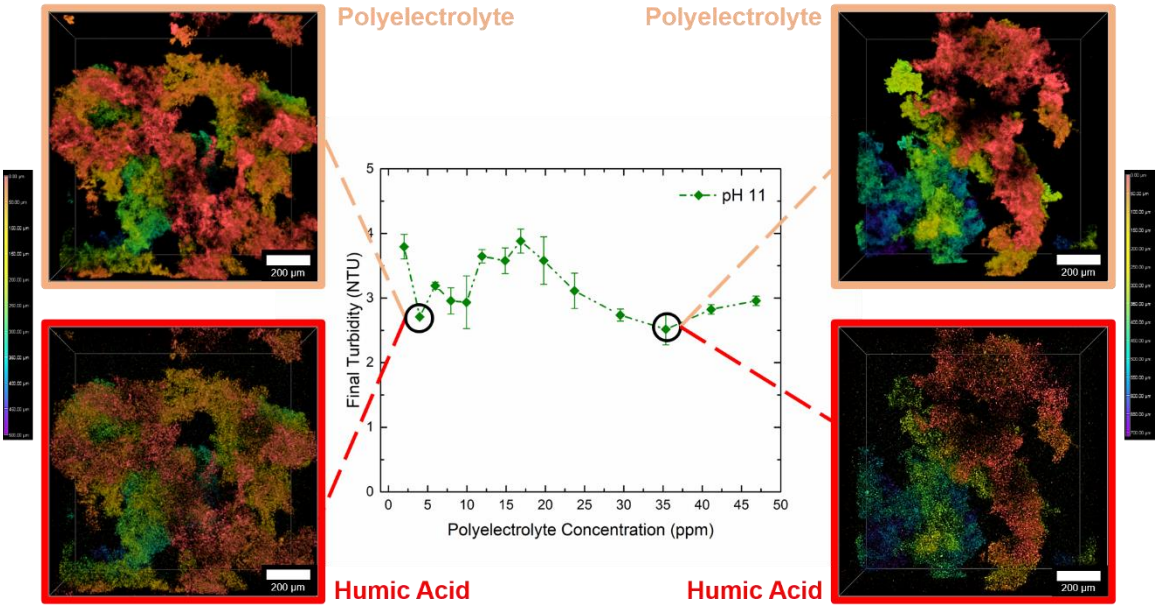


**Figure 6.6**: Laser confocal 3D renders of a floc composed of bentonite, coal-based humic acid, and Cy5-tagged polyelectrolyte at two turbidity minima. The turbidity curve is data taken from jar tests performed at pH 11 at an ionic strength of [I] = 1.3 mM. Circles indicate the dosage of polyelectrolyte which correspond to the confocal images. Images bordered in orange are taken with the Cy5 filter cube, which shows the areas where the polyelectrolyte fluoresces. Images bordered in red are taken with the FITC-Texas Red filter cube, which shows areas where the humic acid fluoresces. The vertical colored scale bars represent depth. All scale bars represent 200 µm.

The internal floc structure at the global maximum, however, appears quite different to that of the structure at the two minima. The images in **Figure 6.7** show that it is patchier in structure and not nearly as interconnected into a network structure. Based on the colored scalebar that codes for depth, the flocs also appear to be smaller at the maximum compared to the minima. It is possible in this scenario the competition between the bentonite and HA for adsorption onto the polyelectrolyte was in favor of the HA. If the HA and polyelectrolyte adsorbed to each other first, their overall net positive charge density would decrease. The bentonite aggregates, which at pH 11 possess a net negative charge, have more free adsorption sites than cationic functional groups available to adsorb onto those sites. This could potentially explain why the patchier, smaller flocs are visible. As the

polyelectrolyte dose increases, the amount of positive charge from the quaternary ammonium groups on the polymer backbone increases, which could explain why a return to the larger, networked flocs is seen here.

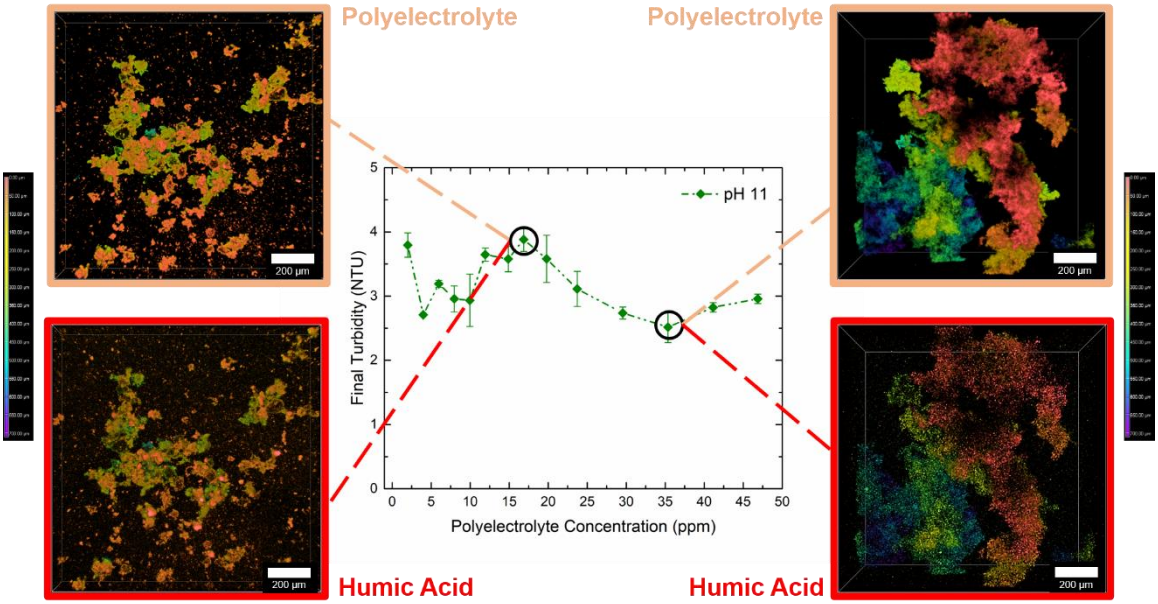


**Figure 6.7**: Laser confocal 3D renders of a floc composed of bentonite, coal-based humic acid, and Cy5-tagged polyelectrolyte at the turbidity global maximum and minimum. The turbidity curve is data taken from jar tests performed at pH 11 at an ionic strength of [I] = 1.3 mM. Circles indicate the dose of polyelectrolyte, which correspond to the confocal images. Images bordered in orange are taken with the Cy5 filter cube, which shows the areas where the polyelectrolyte fluoresces. Images bordered in red are taken with the FITC-Texas Red filter cube, which shows areas where the humic acid fluoresces. The vertical colored scale bars represent depth. All scale bars represent 200 µm.

At the opposite pH extreme where humic acid is mostly insoluble in water, the adsorption behavior is markedly different. **Figure 6.8** shows a comparison of a representative floc at the respective global minima at pH 3 (4.0 ppm) and pH 11 (35.4 ppm). The polyelectrolyte signal shows the expected networked polymer structure, but the HA signal shows very different structural behavior. Here, it appears that the humic acid is only adsorbed to several areas of the polyelectrolyte-covered bentonite aggregate. This suggests that the fraction of HA that did dissolve in solution has been adsorbed onto the polyelectrolyte as observed in the pH 11 case. It is likely that the remaining fraction has failed to be incorporated into the floc because it is undissolved in solution. The behavior

shown here is quite complex due to the pH dependent nature of the humic acid present in the system.

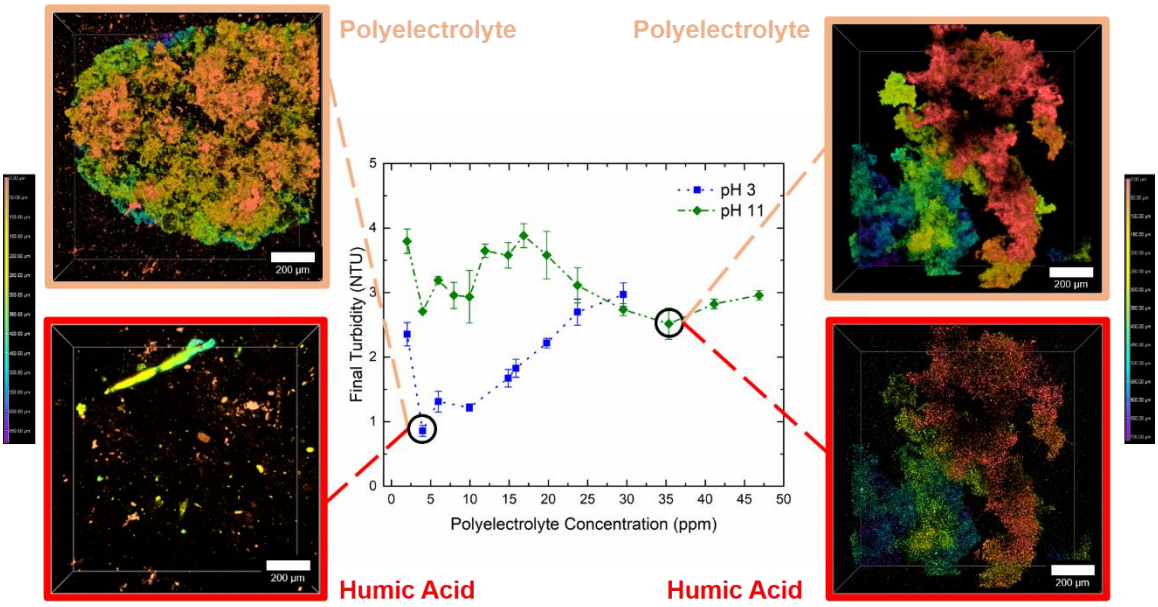


**Figure 6.8**: Laser confocal 3D renders of a floc composed of bentonite, coal-based humic acid, and Cy5-tagged polyelectrolyte at the turbidity global minima. The turbidity curves are data taken from jar tests performed at pH 3 and 11 at an ionic strength of [I] = 1.3 mM. Circles indicate the dose of polyelectrolyte, which correspond to the confocal images. Images bordered in orange are taken with the Cy5 filter cube, which shows the areas where the polyelectrolyte fluoresces. Images bordered in red are taken with the FITC-Texas Red filter cube, which shows areas where the humic acid fluoresces. The vertical colored scale bars represent depth. All scale bars represent 200 µm.

### *6.3.3. Comparison Between Humic Acids from Various Sources*

The turbidity tests and laser scanning confocal microscopy were performed for two additional humic acid standards (one that is Leonardite-based and another that is peat-based) and all three humic acid samples are displayed in **Figure 6.9**. For better comparison, the flocculation results between all three humic acid samples for each pH value are shown in **Figure 6.10** and are remarkably similar with very minor differences within experimental error. It is possible that the behavior of these three humic acids samples is similar because they are from terrestrial sources, which means their phenolic and carboxylic content are similar, according to the International Humic Substances Society (IHSS).[203]

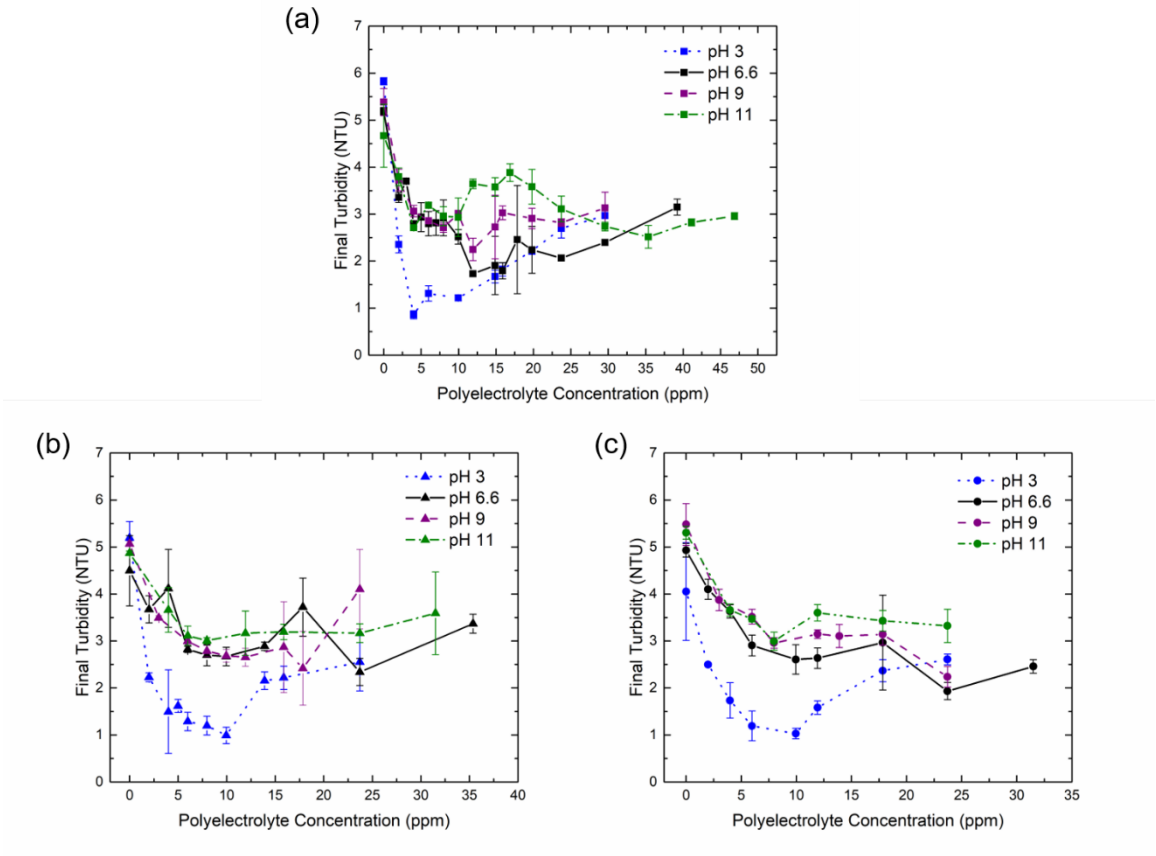


**Figure 6.9**: Turbidity curves for (a) coal-based humic acid, (b) Leonardite-based humic acid, and (c) peat-based humic acid as a function of pH and polyelectrolyte dose. The solution ionic strength was kept constant at [I] = 1.3 mM.

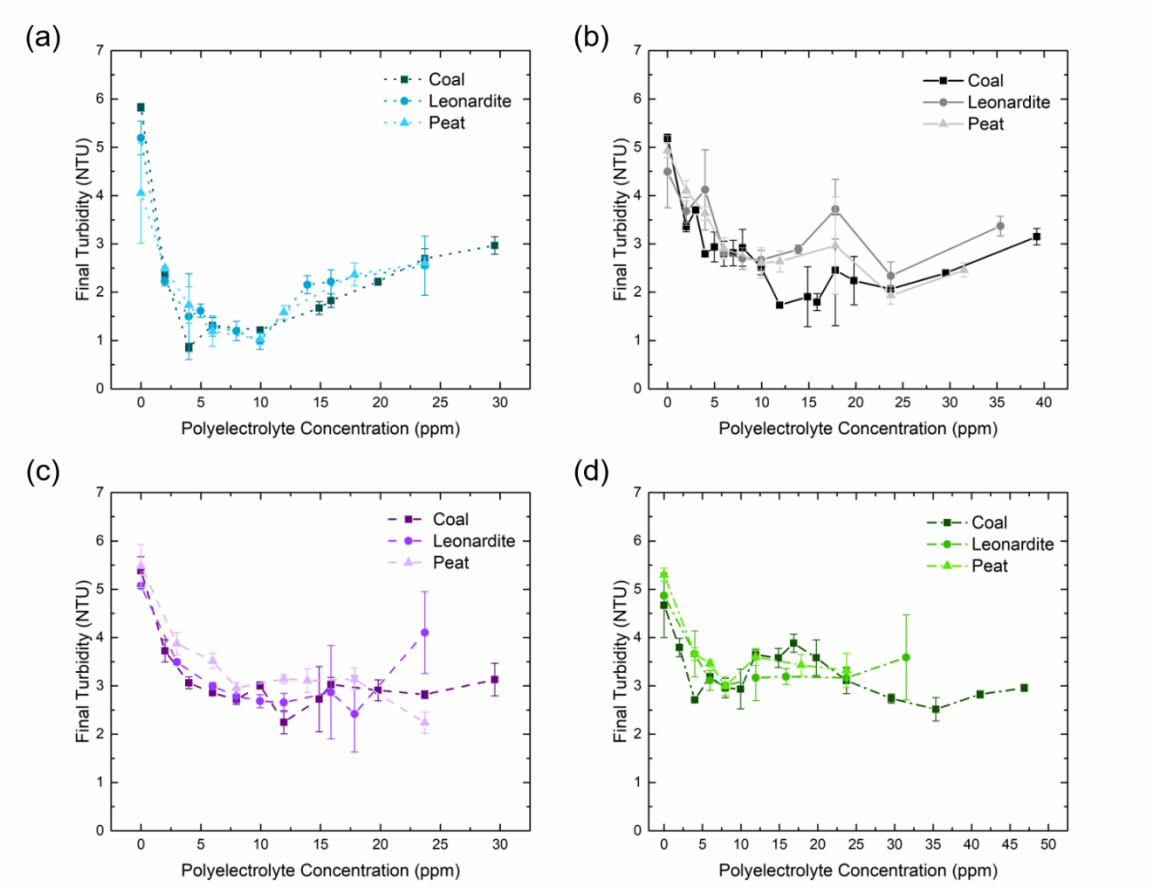


**Figure 6.10**: Turbidity curves for all three humic acid samples at (a) pH 3 (b) pH 6.6, (c) pH 9, and (d) pH 11. The curves are rearranged in this fashion to allow direct comparison between the three HA samples at each pH tested. The solution ionic strength was kept constant at [I] = 1.3 mM.

Confocal microscopy was also performed at the polyelectrolyte concentration corresponding to the global minimum of each of the three humic acid samples at pH 3, 6.6, and 11 as shown in **Figure 6.11**, **Figure 6.12**, and **Figure 6.13**, respectively. The internal floc structure between the three samples are largely similar, with networked flocs observed in the phase contrast microscopy images (column iii) and in the confocal renders at pH 3 and pH 6.6 using the Cy5 filter cube (*i.e.*, the polyelectrolyte signal-column, i) for all three humic acid samples and at pH 11 for the coal-based sample. One marked difference in this set is that the flocs consisting of Leonardite-based and peat-based HA appear to have the polyelectrolyte adsorbed to the bentonite in a patchier fashion. As expected, there is hardly

any signal from the FITC-Texas Red filter cube (*i.e.*, the humic acid signal-column ii) at pH 3, as it is largely insoluble. There is a humic acid signal at pH 6.6 and an even more intense signal at pH 11, suggesting that the solubility of the HA matters for incorporation into the floc.

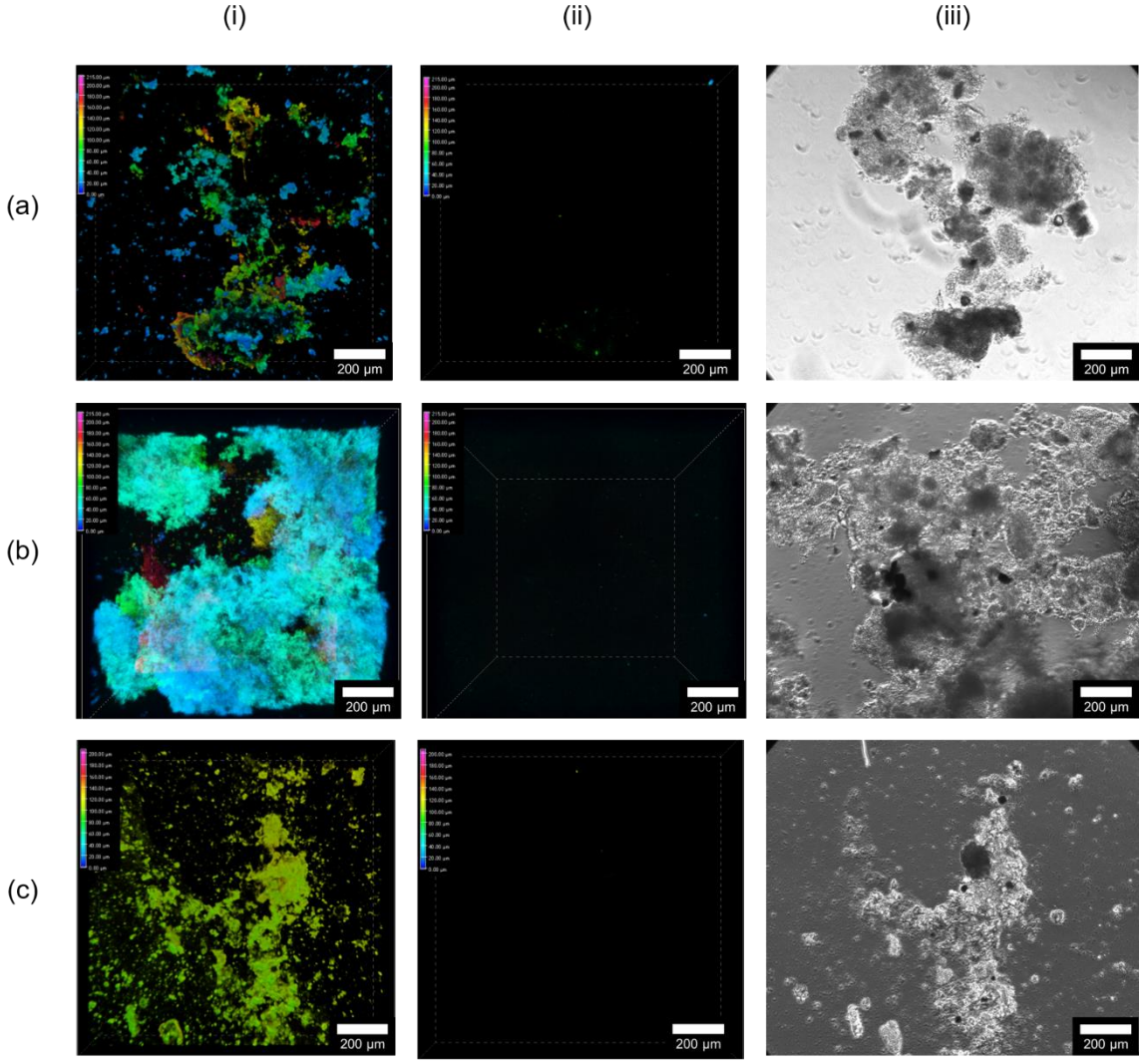


**Figure 6.11**: By column, laser confocal 3D renders using the (i) Cy5 filter cube (polyelectrolyte signal), (ii) FITC-Texas Red filter cube (humic acid signal), and (iii) phase contrast optical microcopy of bentonite flocs consisting of a Cy5-tagged polyelectrolyte and, by row, (a) coal-based humic acid, (b) Leonardite-based HA, or (c) peat-based HA. These are all at pH 3 and a solution ionic strength of [I] = 1.3 mM. All scale bars represent 200 µm.

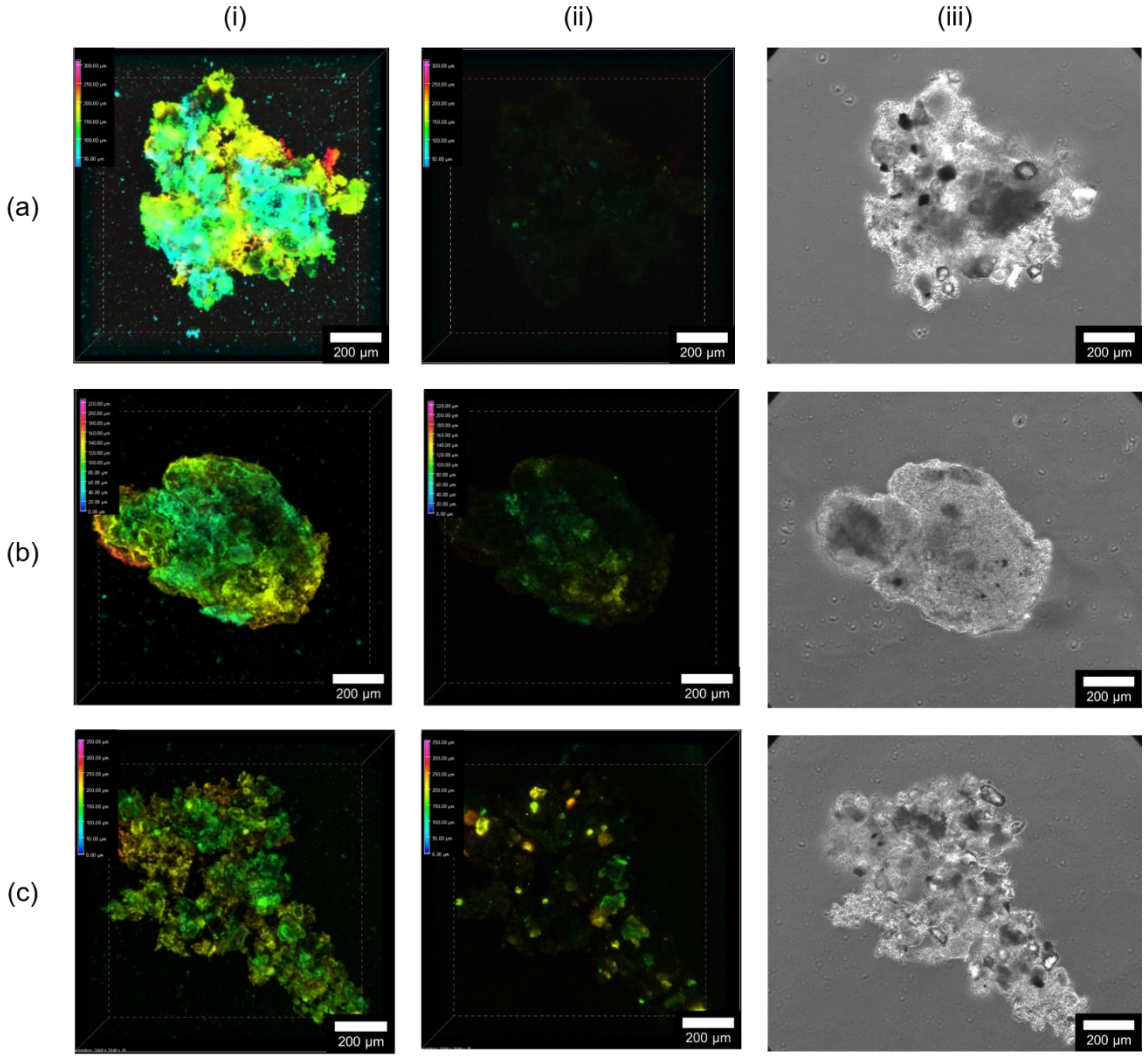


**Figure 6.12**: By column, laser confocal 3D renders using the (i) Cy5 filter cube (polyelectrolyte signal), (ii) FITC-Texas Red filter cube (humic acid signal), and (iii) phase contrast optical microcopy of bentonite flocs consisting of a Cy5-tagged polyelectrolyte and, by row, (a) coal-based humic acid, (b) Leonardite-based HA, or (c) peat-based HA. These are all at pH 6.6 and a solution ionic strength of [I] = 1.3 mM. All scale bars represent 200 µm.

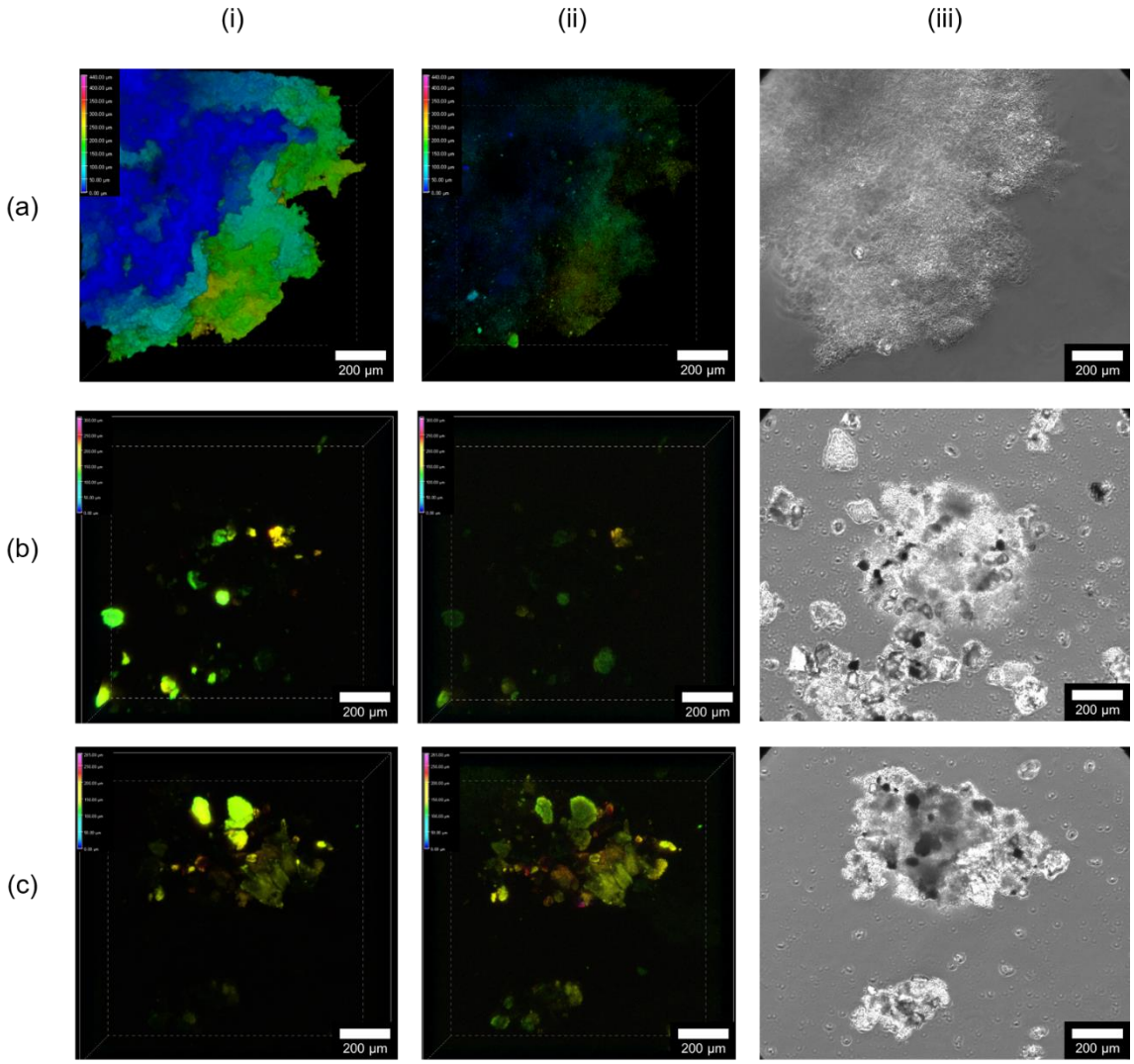


**Figure 6.13**: By column, laser confocal 3D renders using the (i) Cy5 filter cube (polyelectrolyte signal), (ii) FITC-Texas Red filter cube (humic acid signal), and (iii) phase contrast optical microcopy of bentonite flocs consisting of a Cy5-tagged polyelectrolyte and, by row, (a) coal-based humic acid, (b) Leonardite-based HA, or (c) peat-based HA. These are all at pH 11 and a solution ionic strength of [I] = 1.3 mM. All scale bars represent 200 µm.

## *6.4. Conclusion*

The flocculation and confocal microscopy studies of three humic acid samples as a function of pH from different terrestrial sources give some insight into how changing a deceivingly simple solution parameter, such as pH, can yield complex results. In this study, humic acid charge density and solubility increase with increasing pH, which impacts how

the polyelectrolyte will interact with the humic acid, and ultimately, the bentonite, to form flocs. Competitive flocculation of bentonite and humic acid with the cationic polyacrylamide results in a few extreme responses, as observed in the turbidity curves. While the confocal microscopy does show what the structure of these flocs looks like and where the polyelectrolyte and humic acid are located within a floc, they fail to provide a quantitative measure of how much humic acid in particular has been incorporated into the floc. UV-Vis or fluorescence spectroscopy could potentially provide a way to calculate how much of the humic acid is incorporated into a floc by determining the HA concentration in the supernatant, after flocculation.[74,205,212–215] Since the total concentration of humic acid is fixed and the concentration of HA in the supernatant could potentially be measured, the concentration of HA incorporated into the flocs can be determined.

# Chapter 7
# Summary and Future Directions

## *7.1. Summary*

This thesis examined the behavior of polymers in solution under complex physicochemical and hydrodynamic flow fields, specifically the self-association of polymer chains and together with suspended particulate matter in flow. Brief summaries of each chapter are presented here.

Chapter 2 looked at the characterization of the extensional properties of semi-dilute aqueous methylcellulose (MC) solutions. Pure aqueous MC solutions are shear-thinning fluids at room temperature. The addition of 8 wt% NaCl results in a fraction of MC self-assembling into long fibrils, which modify the rheological properties of the original MC solution. Capillary breakup extensional rheometry (CaBER) was used to characterize NaCl-free and 8 wt% NaCl solutions of 530 kg·mol$^{-1}$ MC at room temperature. The NaCl-free solutions exhibit only power law behavior, whereas solutions with NaCl exhibit both power law and elastic regimes. As MC concentration increases, the extensional relaxation time also increases strongly, from 0.04 s at 0.5 wt% MC to 4 s at 1 wt% MC. In addition, the apparent extensional viscosity rapidly increases as a function of increasing MC concentration, from ~40 Pa·s at 0.5 wt% to ~1300 Pa·s at 1 wt%. This behavior is attributed to the presence of fibrils in the MC solutions containing NaCl.[28]

Chapter 3 studied the extensional rheological properties of lower molecular weight, lower viscosity MC solutions as a function of NaCl concentration via filament stretching with a flow-focusing microfluidic device. The flow-driven extensional viscosity can be calculated from transient filament diameter thinning behavior of 1 wt% MC with a molecular weight of 150 $kg \cdot mol^{-1}$ and was found to increase as the concentration of NaCl increased, from ~1 Pa·s to ~15.1 Pa·s between 0 wt% to 8 wt% NaCl, respectively. Like the CaBER study, the increase in extensional viscosity is attributed to the presence of fibrils in the MC solutions containing NaCl annealed at room temperature, as demonstrated with cryogenic transmission electron microscopy (cryo-TEM). The study of the extensional behavior of this commercially relevant polymer using the methods explored in Chapters 2 and 3 should inform and enable new ways to process MC, such as fiber spinning and extrusion.

Chapter 4 explored floc assembly dynamics using a commercially available cationic polyacrylamide which is commonly used in drinking water treatment, and anisotropic Na-bentonite clay particles under a variety of hydrodynamic mixing conditions. A Taylor-Couette cell with the unique ability to radially inject fluid into the rotating annulus was used to study how specific hydrodynamic flow fields affect assembly and structure of these materials during the flocculation process. Faster floc growth rates and decreased floc fractal dimensions were observed for higher order flow states, indicating improved mass transfer of the polymer flocculant and breakage at the edges of the flocs (shear rounding), respectively.[88]

Chapter 5 built on the work from Chapter 4 by examining floc formation and growth behavior using samples of the commercially available cationic polyacrylamide in Chapter 4 having two different molecular weights and under a variety of solution ionic strengths. The floc size generally decreased with increasing ionic strength whereas the floc growth rate initially increased then decreased. This likely occurred due to the interplay between increased bentonite aggregate size and a decreased ability for the polyelectrolyte to bridge multiple aggregates because of its decreasing persistence length with increased ionic strength. The densification of bentonite aggregates at higher ionic strengths resulted

in floc morphologies that were more resistant to shear-induced breakage. Apart from optimal dose concentration and dispersion coefficients, there were no clear differences in the floc growth rate behaviors for the two molecular weights studied. The work in Chapters 4 and 5 sheds more light on the physicochemical complexities of polyelectrolyte-driven flocculation that can point to the dosing requirements for more efficient industrial water treatment operations.

Chapter 6 examined the flocculation effects of humic acid, an organic contaminant, to the now familiar bentonite-NaCl system as a function of pH. The charge density and solubility of humic acid increase as a function of increasing pH. This impacts the way a polyelectrolyte will interact with the humic acid, and ultimately, the bentonite, to form flocs. Competitive flocculation of bentonite and humic acid with the cationic polyacrylamide resulted in various responses, as observed in the turbidity curves. Confocal microscopy showed the structure of these flocs and provided information on the location of the polyelectrolyte and humic acid within a floc. Ultimately, however, the confocal images were not successful with providing a quantitative measure of the humic acid amount incorporated into the floc. A subsequent section will address future directions to attempt to quantify humic acid uptake in flocs.

## *7.2. Future Directions*

While the work in this thesis provides new understanding of polymer assembly in flow, the work also provides a platform for several future directions of research. In this section, five potential directions for follow-up studies are detailed based on new ideas or lingering questions that emerged during the current thesis efforts. These ideas and preliminary work, if any, are presented here.

### *7.2.1. Validation of Measured Extensional Properties of Methylcellulose Using Dripping-onto-Substrate Rheology*

The continued progress in developing methods to measure extensional properties of solutions, particularly at lower solution viscosities, allows for a greater variety of materials to be studied, including methylcellulose (MC), as mentioned in this thesis. To the

best of our knowledge, the studies presented here are the first attempt to measure extensional properties of MC. Therefore, it would be prudent to compare these measurements using CaBER for the 530 kg·mol$^{-1}$ MC and the filament stretching microfluidic devices for the 150 kg·mol$^{-1}$ MC by using another technique to test the accuracy of the resulting extensional relaxation times and extensional viscosities. One such method discussed in Chapter 1 that could be used for both molecular weight MC variants is dripping-onto-substrate (DOS) rheology.

The setup for DOS would be relatively simple, as the laboratory is already equipped with a syringe pump and a high-speed camera. The only other required equipment would be a light diffuser and finding an appropriate substrate onto which the MC can be dripped. DOS has become a popular technique for measuring extensional properties of fluids because it is relatively easy to setup, does not require the purchase of large capital equipment such as a rheometer, and is capable of measuring low elasticity (relaxation times < 1 ms) and low viscosity fluids (shear viscosity < 20 mPa·s).[21,23] It has been shown to be effective at determining extensional properties and capillarity-driven pinching for a whole host of fluids, including, but not limited to dilute, semi-dilute, and entangled solutions.[11,12,104,149,216–218] Therefore, DOS is a suitable candidate for validating the accuracy of the results in the CaBER and microfluidic filament thinning studies of MC.

### *7.2.2. Temperature Effects on the Extensional Rheological Properties of Methylcellulose*

The present MC studies looked at the way fibrils formed under the influence of NaCl at room temperature and how this affected their extensional properties. As previously discussed, increasing the temperature of the MC solution is another way to induce fibril formation in MC solutions.[32,33] Modifications to the microfluidic setup presented in Chapter 3 could allow for measuring the extensional properties of methylcellulose as a function of temperature. To achieve this, a device based on the work of Stan *et al*.[219] was designed and is currently under development and testing in the Dutcher lab. In brief, the setup will incorporate a platform consisting of resistive heating elements and resistive temperature devices placed underneath a microfluidic device, where the microfluidic device will consist of relatively large reservoirs to allow for even heating of

methylcellulose prior to flowing through the device. Depending on the microfluidic device used, this temperature-controlled setup can be adopted to study the shear and extensional properties of methylcellulose as a function of temperature history.

### *7.2.3. Ionic Strength Effects on the Extensional Rheology of Polyelectrolytes*

The presence of charge-bearing ionic groups along the backbone of polyelectrolytes alters their conformation in both shear and extensional flows compared to non-ionic polymers. When subjected to an extensional flow field, dilute solutions of polyelectrolytes show either a rigid rod-like extension or a coil-stretch transition depending on factors such as molecular weight, ionic strength, and type of added salt.[220,221] For dilute solutions of polyelectrolytes, stretching due to electrostatic interactions results in more expanded conformations in the polyelectrolytes as compared to their non-ionic counterparts.[195] Chain behavior in semi-dilute solutions has been more complicated to study due to additional interchain interactions on account of the higher concentration of polyelectrolyte present.[222] The presence of additional salt in solution further complicates matters. Extensional rheology techniques such as CaBER and DOS can elucidate the behavior of polyelectrolyte solutions as a function of concentration, ionic strength, molecular weight, ionic strength, and salt type.[223–225]

Preliminary extensional rheological studies with CaBER have been performed for a set of polyelectrolyte flocculants that were donated by Nalco (an Ecolab company). The 179A variant is a cationic polyelectrolyte with 42% of the monomers consisting of positively charged functional groups while the 184A variant is an anionic polyelectrolyte with 50% of the monomers consisting of negatively charged functional groups. Both are linear in structure and are approximately the same molecular weight (> 5 MDa as reported by Nalco). The concentration of both polyelectrolytes is 1 wt% in a solution of synthetic tap water consisting of $CaCl_2$ and $MgCl_2$ at solution ionic strengths of 10.25 mM and 102.5 mM. Steady shear rheology in **Figure 7.1** shows that the solution is shear thinning for both polyelectrolytes at 10.25 mM. For the cationic polyelectrolyte, the solution is still shear thinning at 102.5 mM but to a lesser degree, whereas for the anionic polyelectrolyte at 102.5 mM, the solution appears Newtonian-like. The enhance charge screening at higher

ionic strength results in the polyelectrolytes adopting a less expanded conformation, resulting in isolated clusters which results in decreased shear viscosity.[226,227]

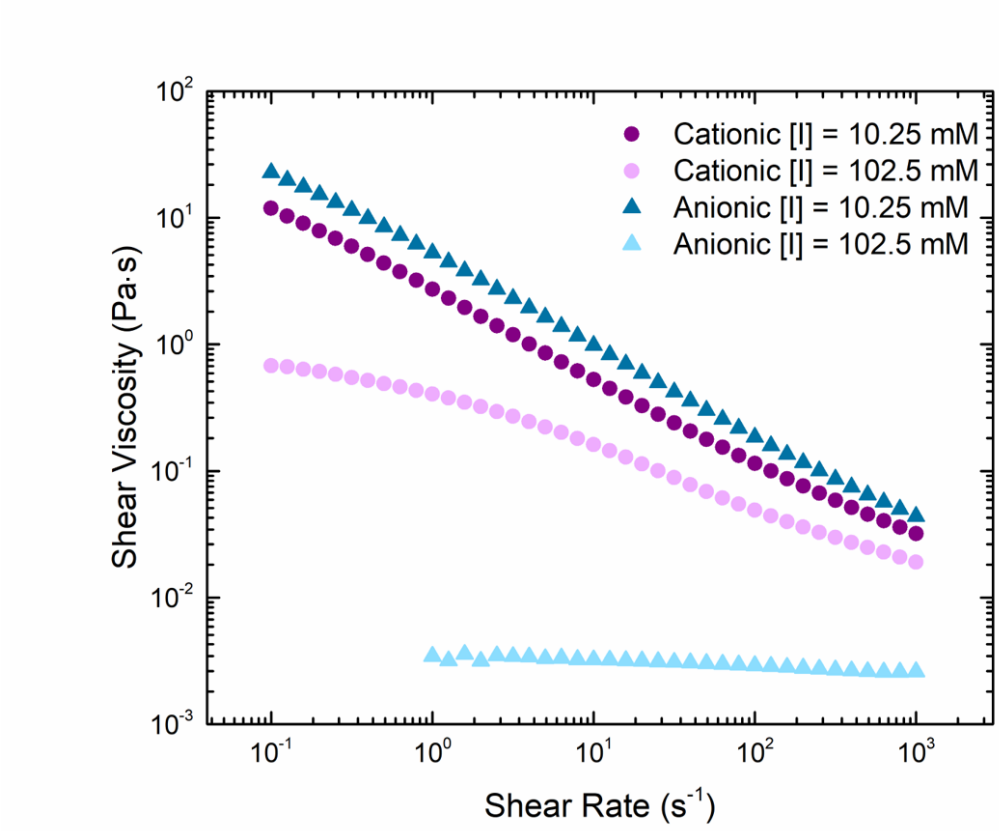


**Figure 7.1**: Steady shear viscosity traces of the cationic (179A series, circles) and anionic (184A series, triangles) polyelectrolytes at solution ionic strengths of 10.25 mM (darker colors) and 102.5 mM (lighter colors). The experiments were performed on an AR-G2 rotational rheometer using the cone and plate geometry at a temperature of 22°C.

Representative results from CaBER tests of both polyelectrolytes are shown in **Figure 7.2**, where in both cases, the critical breakup time decrease from ~1.7 s at 10.25 mM for both polyelectrolytes to ~0.9 s at 102.5 mM for the cationic variant and ~0.1 s for the anionic variant. The extensional relaxation times from the elasto-capillary fits also decrease with increasing ionic strength from 63 ± 1 ms to 44 ± 4 ms for the cationic variant and 20 ± 3 ms to 4.3 ± 0.9 ms for the anionic variant. The apparent extensional viscosities also decrease with increasing ionic strength, which was what was also observed for the

shear viscosities. The reasoning for the decrease in extensional relaxation times and viscosity is largely attributed to charge screening.

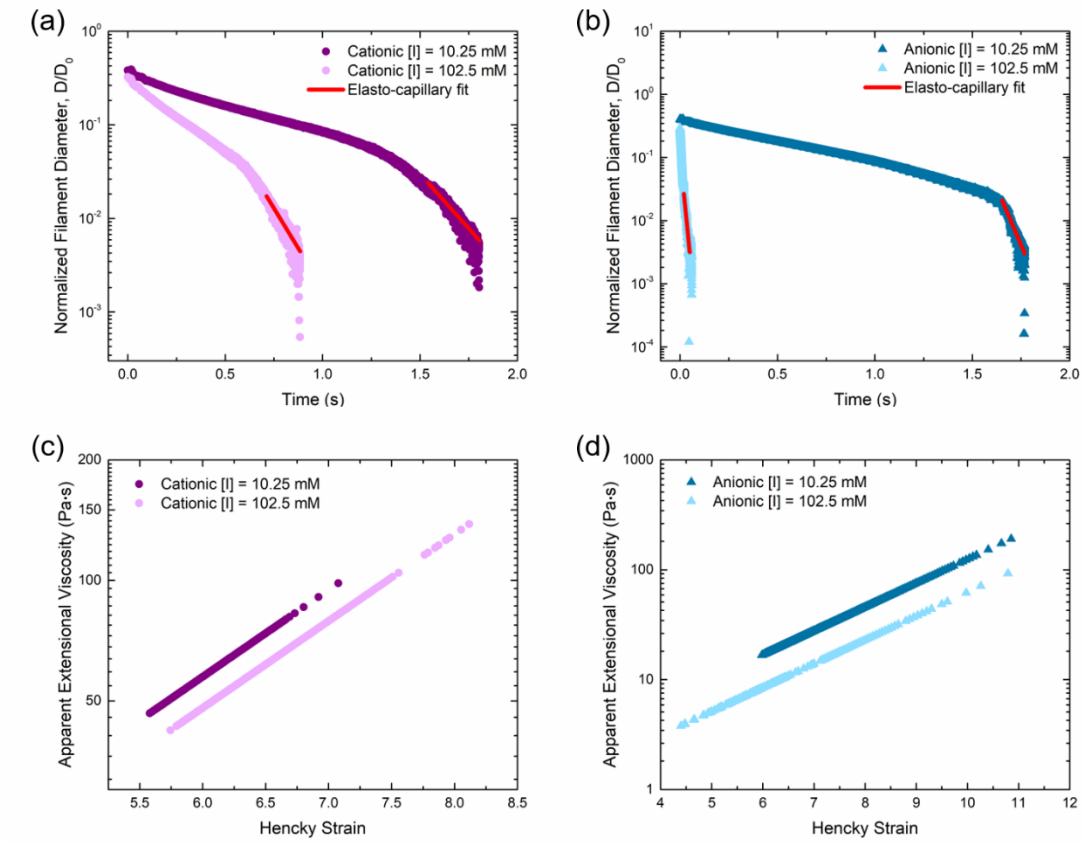


**Figure 7.2**: CaBER results for the 1 wt% cationic (179A series, purple) and 1 wt% anionic (184A series, cyan) polyelectrolytes. Normalized filament diameters with time are shown along with corresponding elasto-capillary fits (solid red lines) for (a) cationic and (b) anionic polyelectrolytes. The plate diameter was 6 mm and the initial height between plates was 3 mm with a strike time of 50 ms for solutions with [I] = 10.25 mM and 30 ms for solutions with [I] = 102.5 mM. The final heights between the plates for the cationic variant were 11.21 mm for [I] = 10.25 mM and 10 mm for [I] = 102.5 mM, while the final heights for the anionic variant were 11.17 mm for [I] = 10.25 mM and 6.33 mm for [I] = 102.5 mM. The calculated apparent extensional viscosities are shown for both the (c) cationic polyelectrolyte and the (d) anionic polyelectrolyte.

It should be noted, however, that because $CaCl_2$ and $MgCl_2$, which are divalent salts, were used in the synthetic tap water mixture, the mechanism of interaction with the polyelectrolytes differs from that with monovalent salts.[228] Additional studies with a

monovalent salt such as NaCl and studies examining both dilute and semi-dilute concentrations of the polyelectrolytes would be required to study differences in their respective rheological responses. It should also be noted that the calculated relaxation times for the anionic polyelectrolyte fall at or below the limitations of the CaBER, therefore the use of either the DOS or microfluidic filament thinning would be a more appropriate alternative to accurately measure its extensional properties.

### *7.2.4. Additional Flocculation Studies in the Taylor-Couette Cell*

The surface has only been scratched with respect to the variety of parameters that can be used to study the polyelectrolyte flocculation with suspended particulates. One of the most important characteristics of a polymer flocculant, other than its molecular weight, is its charge density. Because more positive charges are available to interact with the negatively charged surfaces of bentonite sheets at higher polyelectrolyte charge densities, the bentonite is neutralized and destabilized with smaller doses of polyelectrolyte.[44] **Figure 7.3** shows preliminary jar tests performed for varying charge densities of the same molecular weight of cationic polyacrylamide in the flocculation studies discussed in Chapter 5 (the 4190SSH variant). As expected, the optimal dosing drastically decreased with increasing charge density. What would be interesting to study is how polyelectrolytes of different charge densities behave under flow, as they will undoubtedly possess a different conformation in solution. In this context, it might therefore be useful to pair this study with the shear and extensional behavior of polyelectrolytes of varying charge densities to better understand their behavior in solution.

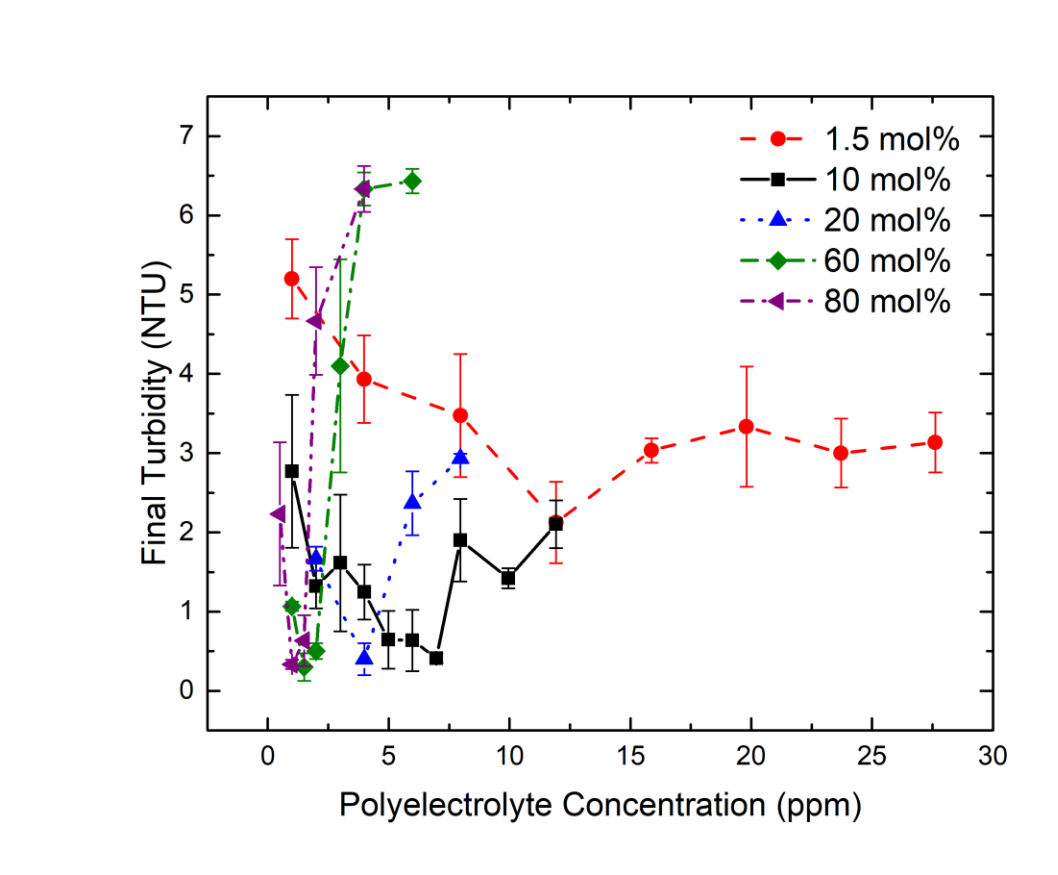


**Figure 7.3**: Jar test results for cationic polyacrylamide (4190SSH variant) at varying charge densities in mol%. The final turbidity is reported in nephelometric turbidity units (NTU) while the flocculant dosage is reported in parts per million (ppm). The corresponding polyelectrolyte dose at the minimum final turbidity is known as the optimal dose level.

Salt valency is another important parameter to consider in polyelectrolyte-driven flocculation since there is several salts present with varying concentrations in source waters. Holding the concentration of salts of different valency constant (*i.e.*, a monovalent salt such as NaCl or a divalent salt such as $CaCl_2$) results in a higher ionic strength for the higher valency salt. The Debye length will therefore be smaller for the higher valency salt system compared to one with a lower valency salt[48]. The identity of the cation or anion also plays a role in the way it interacts with both the bentonite and the polyelectrolyte. Stawinski *et al.*[71] showed that the bentonite aggregates will be larger in size and more compact in structure in the presence of $Ca^{2+}$ ions, as compared to $Na^{+}$ ions. Chremos and Douglas[228]

showed that higher order valency ions reduce the persistence length of charged polymer chains and tend to be more highly coiled compared to monovalent ions. The TC cell is therefore the perfect candidate to observe how floc growth and structure change with time as a function of varying salt valency and type.

### *7.2.5. Elucidation of Humic Acid Behavior During Flocculation*

The qualitative analysis from the confocal images of flocs containing bentonite, humic acid, and fluorescently tagged cationic polyacrylamide provide some idea in the way the humic acid was incorporated into the floc as a function of pH. To summarize: it was generally found that as pH decreased, there was a decreased presence of humic acid, as seen in the confocal images, because of the decreased solubility of humic acid.[202,209] What this analysis did not provide is a quantitative measure of humic acid in the floc. UV-Vis spectroscopy at an absorption wavelength of 254 nm could be used to measure the concentration of the supernatant after flocculation from calibrated standards.[74,205,212,215] Since the concentration of humic acid is fixed for all experiments, the concentration incorporated into the floc can be determined.

One major concern with the UV-Vis method is that the concentration of humic acid in the supernatant might be below the UV-Vis detection limit. An alternative method is excitation-emission fluorescence spectroscopy, as it is some orders of magnitude more sensitive than UV-Vis spectroscopy. For fluorescence spectroscopy, an excitation wavelength of 280 nm would be used and the resultant intensity can be related to calibration standards.[212–215] One caveat for both UV-Vis and fluorescence spectroscopy is that, even if there is a discernable signal, this might not accurately reflect the concentration of humic acid in the supernatant. This is because, at lower solution pH (pH < 5 on average), the humic acid decreases in solubility. Nevertheless, this information would be valuable at pH > 5 since most incoming water for treatment tend to not be below pH 5.

## *7.3. Concluding Thoughts*

Polymers are all around us and used in countless industrial processes and applications. When put in solutions, the dynamics of the polymer itself, and the way in

which it interacts with other suspended polymers and particles, have a dramatic impact on how the solution flows. This is especially true for charged polymers (polyelectrolytes), where the salinity of the solution changes the shape of the polymer chain and the particle aggregates, as well as the degree of attraction between the macromolecular species. The information presented in this thesis, *Polymer Solutions in Complex Flows: Fibrils, Filaments, and Flocs*, in conjunction with the future directions proposed in this final chapter, can be used to further advance understanding of the behavior and assembly of polymers under a variety of solution and flow conditions.

# Bibliography


(1) Fernando, R. H.; Xing, L. L.; Glass, J. E. Rheology Parameters Controlling Spray Atomization and Roll Misting Behavior of Waterborne Coatings. *Prog. Org. Coatings* **2000**, *40* (1–4), 35–38.

(2) Basaran, O. A.; Gao, H.; Bhat, P. P. Nonstandard Inkjets. *Annu. Rev. Fluid Mech.* **2013**, *45* (1), 85–113.

(3) Zehev Tadmor, C. G. G.; Gogos, C. G. *Principles of Polymer Processing*, 2nd ed.; John Wiley & Sons, Inc.: Hoboken, New Jersey, USA, 2006.

(4) Fong, H.; Chun, I.; Reneker, D. H. Beaded Nanofibers Formed during Electrospinning. *Polymer (Guildf).* **1999**, *40* (16), 4585–4592.

(5) Xiaochun, Y.; Sai, L.; Guangjian, H.; Guizhen, Z.; Jinping, Q. Experimental Study of the Extrusion Characteristic of a Vane Extruder Based on Extensional Flow. *Adv. Polym. Technol.* **2016**, *35* (2), 215–220.

(6) Hooshyar, S.; Germann, N. The Investigation of Shear Banding Polymer Solutions in Die Extrusion Geometry. *J. Nonnewton. Fluid Mech.* **2019**, *272*, 104161.

(7) Shaikh, S. M.; Nasser, M.; Hussein, I. A.; Benamor, A. Investigation of the Effect of Polyelectrolyte Structure and Type on the Electrokinetics and Flocculation Behavior of Bentonite Dispersions. *Chem. Eng. J.* **2017**, *311*, 265–276.

(8) Galindo-Rosales, F. J.; Alves, M. A.; Oliveira, M. S. N. Microdevices for Extensional Rheometry of Low Viscosity Elastic Liquids: A Review. *Microfluid. Nanofluidics* **2013**, *14* (1–2), 1–19.

(9) Macosko, C. W. *Rheology: Principles, Measurements, and Applications*; Wiley-VCH, 1994.

(10) Jones, D. M.; Walters, K.; Williams, P. R. On the Extensional Viscosity of Mobile Polymer Solutions. *Rheol. Acta* **1987**, *26* (1), 20–30.

(11) Dinic, J.; Zhang, Y.; Jimenez, L. N.; Sharma, V. Extensional Relaxation Times of Dilute, Aqueous Polymer Solutions. *ACS Macro Lett.* **2015**, *4* (7), 804–808.

(12) Dinic, J.; Jimenez, L. N.; Sharma, V. Pinch-off Dynamics and Dripping-onto-Substrate (DoS) Rheometry of Complex Fluids. *Lab Chip* **2017**, *17* (3), 460–473.

(13) Keshavarz, B.; Sharma, V.; Houze, E. C.; Koerner, M. R.; Moore, J. R.; Cotts, P. M.; Threlfall-Holmes, P.; McKinley, G. H. Studying the Effects of Elongational Properties on Atomization of Weakly Viscoelastic Solutions Using Rayleigh Ohnesorge Jetting Extensional Rheometry (ROJER). *J. Nonnewton. Fluid Mech.* **2015**, *222*, 171–189.

(14) Sharma, V.; Haward, S. J.; Serdy, J.; Keshavarz, B.; Soderlund, A.; Threlfall-Holmes, P.; McKinley, G. H. The Rheology of Aqueous Solutions of Ethyl Hydroxy-Ethyl Cellulose (EHEC) and Its Hydrophobically Modified Analogue (HmEHEC): Extensional Flow Response in Capillary Break-up, Jetting (ROJER) and in a Cross-Slot Extensional Rheometer. *Soft Matter* **2015**, *11* (16), 3251–3270.

(15) Huang, Q.; Mangnus, M.; Alvarez, N. J.; Koopmans, R.; Hassager, O. A New Look at Extensional Rheology of Low-Density Polyethylene. *Rheol. Acta* **2016**, *55* (5), 343–350.

(16) Román Marín, J. M.; Huusom, J. K.; Alvarez, N. J.; Huang, Q.; Rasmussen, H. K.; Bach, A.; Skov, A. L.; Hassager, O. A Control Scheme for Filament Stretching Rheometers with Application to Polymer Melts. *J. Nonnewton. Fluid Mech.* **2013**, *194*, 14–22.

(17) Anna, S. L.; Rogers, C.; McKinley, G. H. On Controlling the Kinematics of a Filament Stretching Rheometer Using a Real-Time Active Control Mechanism. *J. Nonnewton. Fluid Mech.* **1999**, *87* (2–3), 307–335.

(18) McKinley, G. H.; Brauner, O.; Yao, M. Kinematics of Filament Stretching in Dilute and Concentrated Polymer Solutions. *Korea-Australia Rheol. J.* **2001**, *13* (1), 29–35.

(19) Anna, S. L.; McKinley, G. H. Elasto-Capillary Thinning and Breakup of Model Elastic Liquids. *J. Rheol. (N. Y. N. Y).* **2001**, *45* (1), 115–138.

(20) Babcock, H. P.; Teixeira, R. E.; Hur, J. S.; Shaqfeh, E. S. G.; Chu, S. Visualization of Molecular Fluctuations near the Critical Point of the Coil-Stretch Transition in Polymer Elongation. *Macromolecules* **2003**, *36* (12), 4544–4548.

(21) Campo-Deaño, L.; Clasen, C. The Slow Retraction Method (SRM) for the Determination of Ultra-Short Relaxation Times in Capillary Breakup Extensional Rheometry Experiments. *J. Nonnewton. Fluid Mech.* **2010**, *165* (23–24), 1688–1699.

(22) Greiciunas, E.; Wong, J.; Gorbatenko, I.; Hall, J.; Wilson, M. C. T.; Kapur, N.; Harlen, O. G.; Vadillo, D.; Threlfall-Holmes, P. Design and Operation of a Rayleigh Ohnesorge Jetting Extensional Rheometer (ROJER) to Study Extensional Properties of Low Viscosity Polymer Solutions. *J. Rheol. (N. Y. N. Y).* **2017**, *61* (467), 467–476.

(23) Rodd, L. E.; Scott, T. P.; Cooper-White, J. J.; McKinley, G. H. Capillary Break-up Rheometry of Low-Viscosity Elastic Fluids. *Appl. Rheol.* **2005**, *15* (1), 12–27.

(24) Ober, T. J.; Haward, S. J.; Pipe, C. J.; Soulages, J.; McKinley, G. H. Microfluidic Extensional Rheometry Using a Hyperbolic Contraction Geometry. *Rheol. Acta* **2013**, *52* (6), 529–546.

(25) Haward, S. J.; Ober, T. J.; Oliveira, M. S. N.; Alves, M. A.; McKinley, G. H. Extensional Rheology and Elastic Instabilities of a Wormlike Micellar Solution in a Microfluidic Cross-Slot Device. *Soft Matter* **2012**, *8* (2), 536–555.

(26) Keshavarz, B.; McKinley, G. H. Micro-Scale Extensional Rheometry Using Hyperbolic Converging/Diverging Channels and Jet Breakup. *Biomicrofluidics* **2016**, *10* (4), 043502.

(27) Rodd, L. E.; Cooper-White, J. J.; Boger, D. V.; McKinley, G. H. Role of the Elasticity Number in the Entry Flow of Dilute Polymer Solutions in Micro-Fabricated Contraction Geometries. *J. Nonnewton. Fluid Mech.* **2007**, *143* (2–3), 170–191.

(28) Morozova, S.; Schmidt, P. W.; Metaxas, A.; Bates, F. S.; Lodge, T. P.; Dutcher, C. S. Extensional Flow Behavior of Methylcellulose Solutions Containing Fibrils. *ACS Macro Lett.* **2018**, *7* (3), 347–352.

(29) Chatterjee, T.; Nakatani, A. I.; Adden, R.; Brackhagen, M.; Redwine, D.; Shen, H.; Li, Y.; Wilson, T.; Sammler, R. L. Structure and Properties of Aqueous Methylcellulose Gels by Small-Angle Neutron Scattering. *Biomacromolecules* **2012**, *13* (10), 3355–3369.

(30) Xu, Y.; Wang, C.; Tam, K. C.; Li, L. Salt-Assisted and Salt-Suppressed Sol-Gel Transitions of Methylcellulose in Water. *Langmuir* **2004**, *20* (3), 646–652.

(31) Xu, Y.; Li, L.; Zheng, P.; Lam, Y. C.; Hu, X. Controllable Gelation of Methylcellulose by a Salt Mixture. *Langmuir* **2004**, *20* (15), 6134–6138.

(32) Lott, J. R.; McAllister, J. W.; Arvidson, S. A.; Bates, F. S.; Lodge, T. P. Fibrillar Structure of Methylcellulose Hydrogels. *Biomacromolecules* **2013**, *14* (8), 2484–2488.

(33) Lott, J. R.; McAllister, J. W.; Wasbrough, M.; Sammler, R. L.; Bates, F. S.; Lodge, T. P. Fibrillar Structure in Aqueous Methylcellulose Solutions and Gels. *Macromolecules* **2013**, *46* (24), 9760–9771.

(34) Sarkar, N. Thermal Gelation Properties of Methyl and Hydroxypropyl Methylcellulose. *J. Appl. Polym. Sci.* **1979**, *24* (4), 1073–1087.

(35) Haque, A.; Morris, E. R. Thermogelation of Methylcellulose. Part I: Molecular Structures and Processes. *Carbohydr. Polym.* **1993**, *22* (3), 161–173.

(36) Kobayashi, K.; Huang, C. I.; Lodge, T. P. Thermoreversible Gelation of Aqueous

Methylcellulose Solutions. *Macromolecules* **1999**, *32* (21), 7070–7077.

(37) Li, L.; Thangamathesvaran, P. M.; Yue, C. Y.; Tam, K. C.; Hu, X.; Lam, Y. C. Gel Network Structure of Methylcellulose in Water. *Langmuir* **2001**, *17* (26), 8062–8068.

(38) Bodvik, R.; Dedinaite, A.; Karlson, L.; Bergström, M.; Bäverbäck, P.; Pedersen, J. S.; Edwards, K.; Karlsson, G.; Varga, I.; Claesson, P. M. Aggregation and Network Formation of Aqueous Methylcellulose and Hydroxypropylmethylcellulose Solutions. *Colloids Surfaces A Physicochem. Eng. Asp.* **2010**, *354* (1–3), 162–171.

(39) McAllister, J. W.; Lott, J. R.; Schmidt, P. W.; Sammler, R. L.; Bates, F. S.; Lodge, T. P. Linear and Nonlinear Rheological Behavior of Fibrillar Methylcellulose Hydrogels. *ACS Macro Lett.* **2015**, *4* (5), 538–542.

(40) Lodge, T. P.; Maxwell, A. L.; Lott, J. R.; Schmidt, P. W.; McAllister, J. W.; Morozova, S.; Bates, F. S.; Li, Y.; Sammler, R. L. Gelation, Phase Separation, and Fibril Formation in Aqueous Hydroxypropylmethylcellulose Solutions. *Biomacromolecules* **2018**, *19* (3), 816–824.

(41) Schmidt, P. W.; Morozova, S.; Owens, P. M.; Adden, R.; Li, Y.; Bates, F. S.; Lodge, T. P. Molecular Weight Dependence of Methylcellulose Fibrillar Networks. *Macromolecules* **2018**, *51* (19), 7767–7775.

(42) Bonn, D.; Amarouchène, Y.; Wagner, C.; Douady, S.; Cadot, O. Turbulent Drag Reduction by Polymers. *J. Phys. Condens. Matter* **2005**, *17* (14), S1195–S1202.

(43) Nasser, M. S.; James, A. E. Effect of Polyacrylamide Polymers on Floc Size and Rheological Behaviour of Kaolinite Suspensions. *Colloids Surfaces A Physicochem. Eng. Asp.* **2007**, *301* (1–3), 311–322.

(44) Bolto, B.; Gregory, J. Organic Polyelectrolytes in Water Treatment. *Water Res.* **2007**, *41* (11), 2301–2324.

(45) Shaikh, S. M. R.; Nasser, M. S.; Hussein, I.; Benamor, A.; Onaizi, S. A.; Qiblawey, H. Influence of Polyelectrolytes and Other Polymer Complexes on the Flocculation and Rheological Behaviors of Clay Minerals: A Comprehensive Review. *Sep. Purif. Technol.* **2017**, *187*, 137–161.

(46) Lee, C. S.; Robinson, J.; Chong, M. F. A Review on Application of Flocculants in Wastewater Treatment. *Process Saf. Environ. Prot.* **2014**, *92* (6), 489–508.

(47) Oyegbile, B.; Ay, P.; Narra, S. Introduction Flocculation Kinetics and Hydrodynamic Interactions in Natural and Engineered Flow Systems: A Review. *Environ. Eng. Res* **2016**, *21* (1), 1–14.

(48) Berg, J. C. *An Introduction to Interfaces and Colloids*; World Scientific, 2009.

(49) Zhu, Z.; Wang, H.; Yu, J.; Dou, J. On the Kaolinite Floc Size at the Steady State of Flocculation in a Turbulent Flow. *PLoS One* **2016**, *11* (2), e0148895.

(50) Feng, L.; Stuart, M. C.; Adachi, Y. Dynamics of Polyelectrolyte Adsorption and Colloidal Flocculation upon Mixing Studied Using Mono-Dispersed Polystyrene Latex Particles. *Adv. Colloid Interface Sci.* **2015**, *226*, 101–114.

(51) Biggs, S.; Habgood, M.; Jameson, G. J.; Yan, Y. Aggregate Structures Formed via a Bridging Flocculation Mechanism. *Chem. Eng. J.* **2000**, *80* (1), 13–22.

(52) Zhou, Y.; Franks, G. V. Flocculation Mechanism Induced by Cationic Polymers Investigated by Light Scattering. *Langmuir* **2006**, *22* (16), 6775–6786.

(53) Szilagyi, I.; Trefalt, G.; Tiraferri, A.; Maroni, P.; Borkovec, M. Polyelectrolyte Adsorption, Interparticle Forces, and Colloidal Aggregation. *Soft Matter* **2014**, *10* (15), 2479.

(54) Adachi, Y.; Xiao, J. Initial Stage of Bridging Flocculation of PSL Particles Induced by an Addition of Polyelectrolyte under High Ionic Strength. *Colloids Surfaces A Physicochem. Eng. Asp.* **2013**, *435*, 127–131.

(55) Barbot, E.; Dussouillez, P.; Bottero, J. Y.; Moulin, P. Coagulation of Bentonite Suspension by Polyelectrolytes or Ferric Chloride: Floc Breakage and Reformation. *Chem. Eng. J.* **2010**, *156* (1), 83–91.

(56) Rasteiro, M. G.; Pinheiro, I.; Garcia, F. A. P.; Ferreira, P.; Hunkeler, D. Using Light Scattering to Screen Polyelectrolytes (PEL) Performance in Flocculation. *Polymers (Basel).* **2011**, *3* (4), 915–927.

(57) Hoogeveen, N. G.; Stuart, M. A. C.; Fleer, G. J. Polyelectrolyte Adsorption on Oxides: I. Kinetics and Adsorbed Amounts. *J. Colloid Interface Sci.* **1996**, *182* (1), 133–145.

(58) Yu, W.; Gregory, J.; Campos, L.; Li, G. The Role of Mixing Conditions on Floc Growth, Breakage and Re-Growth. *Chem. Eng. J.* **2011**, *171* (2), 425–430.

(59) Bouyer, D.; Coufort, C.; Liné, A.; Do-Quang, Z. Experimental Analysis of Floc Size Distributions in a 1-L Jar under Different Hydrodynamics and Physicochemical Conditions. *J. Colloid Interface Sci.* **2005**, *292* (2), 413–428.

(60) Rossini, M.; Garrido, J. G.; Galluzzo, M. Optimization of the Coagulation–Flocculation Treatment: Influence of Rapid Mix Parameters. *Water Res.* **1999**, *33* (8), 1817–1826.

(61) Vlieghe, M.; Coufort-Saudejaud, C.; Frances, C.; Liné, A. *In Situ* Characterization of Floc Morphology by Image Analysis in a Turbulent Taylor-Couette Reactor. *AIChE J.* **2014**, *60* (7), 2389–2403.

(62) Spicer, P. T.; Keller, W.; Pratsinis, S. E. The Effect of Impeller Type on Floc Size and Structure during Shear-Induced Flocculation. *J. Colloid Interface Sci.* **1996**, *184* (1), 112–122.

(63) Roussy, J.; Van Vooren, M.; Dempsey, B. A.; Guibal, E. Influence of Chitosan

Characteristics on the Coagulation and the Flocculation of Bentonite Suspensions. *Water Res.* **2005**, *39* (14), 3247–3258.

(64) Levy, N.; Magdassi, S.; Bar-Or, Y. Physico-Chemical Aspects in Flocculation of Bentonite Suspensions by a Cyanobacterial Bioflocculant. *Water Res.* **1992**, *26* (2), 249–254.

(65) Waajen, G.; Van Oosterhout, F.; Douglas, G.; Lürling, M. Management of Eutrophication in Lake De Kuil (The Netherlands) Using Combined Flocculant-Lanthanum Modified Bentonite Treatment. *Water Res.* **2016**, *97*, 83–95.

(66) Duman, O.; Tunç, S. Electrokinetic and Rheological Properties of Na-Bentonite in Some Electrolyte Solutions. *Microporous Mesoporous Mater.* **2009**, *117* (1), 331–338.

(67) M'bodj, O.; Ariguib, N. K.; Ayadi, M. T.; Magnin, A. Plastic and Elastic Properties of the Systems Interstratified Clay–Water–Electrolyte–Xanthan. *J. Colloid Interface Sci.* **2004**, *273* (2), 675–684.

(68) Durán, J. D. G.; Ramos-Tejada, M. M.; Arroyo, F. J.; González-Caballero, F. Rheological and Electrokinetic Properties of Sodium Montmorillonite Suspensions. *J. Colloid Interface Sci.* **2000**, *229* (1), 107–117.

(69) Cadene, A.; Durand-Vidal, S.; Turq, P.; Brendle, J. Study of Individual Na-Montmorillonite Particles Size, Morphology, and Apparent Charge. *J. Colloid Interface Sci.* **2005**, *285*, 719–730.

(70) Żbik, M. S.; Williams, D. J.; Song, Y.-F.; Wang, C.-C. The Formation of a Structural Framework in Gelled Wyoming Bentonite: Direct Observation in Aqueous Solutions. *J. Colloid Interface Sci.* **2014**, *435*, 119–127.

(71) Stawiński, J. Influence of Calcium and Sodium Concentration on the Microstructure of Bentonite and Kaolin. *Clays Clay Miner.* **1990**, *38* (6), 617–622.

(72) Chen, J. S. Rheological Behavior of Na-Montmorillonite Suspensions at Low Electrolyte Concentration. *Clays Clay Miner.* **1990**, *38* (1), 57–62.

(73) Yan, X.; Zhang, X. Interactive Effects of Clay and Polyacrylamide Properties on Flocculation of Pure and Subsoil Clays. *Soil Res.* **2014**, *52* (7), 727.

(74) Bolto, B.; Dixon, D.; Eldridge, R.; King, S. Cationic Polymer and Clay or Metal Oxide Combinations for Natural Organic Matter Removal. *Water Res.* **2001**, *35* (11), 2669–2676.

(75) Bradl, H. B. Adsorption of Heavy Metal Ions on Soils and Soils Constituents. *J. Colloid Interface Sci.* **2004**, *277* (1), 1–18.

(76) Salman, M.; El-Eswed, B.; Khalili, F. Adsorption of Humic Acid on Bentonite. *Appl. Clay Sci.* **2007**, *38* (1–2), 51–56.

(77) Yang, S.; Li, J.; Lu, Y.; Chen, Y.; Wang, X. Sorption of Ni(II) on GMZ Bentonite: Effects of PH, Ionic Strength, Foreign Ions, Humic Acid and Temperature. *Appl. Radiat. Isot.* **2009**, *67* (9), 1600–1608.

(78) Oliver, B. G. Dihaloacetonitriles in Drinking Water: Algae and Fulvic Acid as Precursors. *Environ. Sci. Technol.* **1983**, *17* (2), 80–83.

(79) Peters, R. J. B.; de Leer, E. W. B.; de Galan, L. Dihaloacetonitriles in Dutch Drinking Waters. *Water Res.* **1990**, *24* (6), 797–800.

(80) Guibai, L.; Gregory, J. Flocculation and Sedimentation of High-Turbidity Waters. *Water Res.* **1991**, *25* (9), 1137–1143.

(81) Adachi, Y.; Wada, T. Initial Stage Dynamics of Bridging Flocculation of Polystyrene Latex Spheres with Polyethylene Oxide. *J. Colloid Interface Sci.* **2000**, *229* (1), 148–154.

(82) Axford, S. D. T.; Herrington, T. M. Determination of Aggregate Structures by Combined Light-Scattering and Rheological Studies. *J. Chem. Soc. Faraday Trans.* **1994**, *90* (14), 2085.

(83) Bushell, G. C.; Yan, Y. D.; Woodfield, D.; Raper, J.; Amal, R. On Techniques for the Measurement of the Mass Fractal Dimension of Aggregates. *Adv. Colloid Interface Sci.* **2002**, *95* (1), 1–50.

(84) Rice, J. A.; Tombácz, E.; Malekani, K. Applications of Light and X-Ray Scattering to Characterize the Fractal Properties of Soil Organic Matter. *Geoderma* **1999**, *88* (3–4), 251–264.

(85) Lee, B. J.; Molz, F. Numerical Simulation of Turbulence-Induced Flocculation and Sedimentation in a Flocculant-Aided Sediment Retention Pond. *Environ. Eng. Res* **2014**, *19* (2), 165–174.

(86) Laurent, J.; Samstag, R. W.; Ducoste, J. M.; Griborio, A.; Nopens, I.; Batstone, D. J.; Wicks, J. D.; Saunders, S.; Potier, O. A Protocol for the Use of Computational Fluid Dynamics as a Supportive Tool for Wastewater Treatment Plant Modelling. *Water Sci. Technol.* **2014**, *70* (10), 1575.

(87) Coufort, C.; Bouyer, D.; Liné, A. Flocculation Related to Local Hydrodynamics in a Taylor–Couette Reactor and in a Jar. *Chem. Eng. Sci.* **2005**, *60* (8–9), 2179–2192.

(88) Metaxas, A.; Wilkinson, N.; Raethke, E.; Dutcher, C. S. In Situ Polymer Flocculation and Growth in Taylor-Couette Flows. *Soft Matter* **2018**, *14* (42), 8627–8635.

(89) Wilkinson, N.; Metaxas, A.; Ruud, E.; Raethke, E.; Wickramaratne, S.; Reineke, T. M.; Dutcher, C. S. Internal Structure Visualization of Polymer - Clay Flocculants Using Fluorescence. *Colloids Interface Sci. Commun.* **2016**, *10–11*, 1–5.

(90) Wilkinson, N.; Metaxas, A.; Brichetto, E.; Wickramaratne, S.; Reineke, T. M.;

Dutcher, C. S. Ionic Strength Dependence of Aggregate Size and Morphology on Polymer-Clay Flocculation. *Colloids Surfaces A Physicochem. Eng. Asp.* **2017**, *529*, 1037–1046.

(91) Wilkinson, N.; Metaxas, A.; Quinney, C.; Wickramaratne, S.; Reineke, T. M.; Dutcher, C. S. PH Dependence of Bentonite Aggregate Size and Morphology on Polymer-Clay Flocculation. *Colloids Surfaces A Physicochem. Eng. Asp.* **2018**, *537*, 281–286.

(92) Soos, M.; Ehrl, L.; Bäbler, M. U.; Morbidelli, M. Aggregate Breakup in a Contracting Nozzle. *Langmuir* **2010**, *26* (1), 10–18.

(93) Selomulya, C.; Bushell, G.; Amal, R.; Waite, T. D. Aggregate Properties in Relation to Aggregation Conditions under Various Applied Shear Environments. *Int. J. Miner. Process.* **2004**, *73* (2–4), 295–307.

(94) Wilkinson, N.; Dutcher, C. S. Taylor-Couette Flow with Radial Fluid Injection. *Rev. Sci. Instrum.* **2017**, *88* (8), 083904.

(95) Wilkinson, N. A.; Dutcher, C. S. Axial Mixing and Vortex Stability to in Situ Radial Injection in Taylor-Couette Laminar and Turbulent Flows. *J. Fluid Mech.* **2018**, *854*, 324–347.

(96) Basaran, O. A. Small-Scale Free Surface Flows with Breakup: Drop Formation and Emerging Applications. *AIChE J.* **2002**, *48* (9), 1842–1848.

(97) McKinley, G. H.; Sridhar, T. Filament Stretching Rheometry of Complex Fluids. *Annu. Rev. Fluid Mech.* **2002**, *34* (1), 375–415.

(98) McKinley, G. H. Visco-Elasto-Capillary Thinning and Break-up of Complex Fluids. *Rheol. Rev.* **2005**, 1–48.

(99) Haward, S. J.; Sharma, V.; Butts, C. P.; McKinley, G. H.; Rahatekar, S. S. Shear and Extensional Rheology of Cellulose/Ionic Liquid Solutions. *Biomacromolecules* **2012**, *13* (5), 1688–1699.

(100) Duxenneuner, M. R.; Fischer, P.; Windhab, E. J.; Cooper-White, J. J. Extensional Properties of Hydroxypropyl Ether Guar Gum Solutions. *Biomacromolecules* **2008**, *9* (11), 2989–2996.

(101) Yu, D.-G.; Li, X.-X.; Ge, J.-W.; Ye, P.-P.; Wang, X. The Influence of Sheath Solvent's Flow Rate on the Quality of Electrospun Ethyl Cellulose Nanofibers. *Model. Numer. Simul. Mater. Sci.* **2013**, *03* (04), 1–5.

(102) Pipe, C. J.; McKinley, G. H. Microfluidic Rheometry. *Mech. Res. Commun.* **2009**, *36* (1), 110–120.

(103) Haward, S. J. Microfluidic Extensional Rheometry Using Stagnation Point Flow. *Biomicrofluidics* **2016**, *10* (4), 043401.

(104) Dinic, J.; Biagioli, M.; Sharma, V. Pinch-off Dynamics and Extensional Relaxation Times of Intrinsically Semi-Dilute Polymer Solutions Characterized by Dripping-onto-Substrate Rheometry. *J. Polym. Sci. Part B Polym. Phys.* **2017**, *55* (22), 1692–1704.

(105) Entov, V. M.; Hinch, E. J. Effect of a Spectrum of Relaxation Times on the Capillary Thinning of a Filament of Elastic Liquid. *J. Nonnewton. Fluid Mech.* **1997**, *72* (1), 31–53.

(106) Schümmer, P.; Tebel, K. H. Design and Operation of the Free Jet Elongational Rheometer. *Rheol. Acta* **1982**, *21* (4–5), 514–516.

(107) McKinley, G. H.; Tripathi, A. How to Extract the Newtonian Viscosity from Capillary Breakup Measurements in a Filament Rheometer. *J. Rheol. (N. Y. N. Y).* **2000**, *44* (115).

(108) Clasen, C.; Plog, J. P.; Kulicke, W.-M.; Owens, M.; Macosko, C.; Scriven, L. E.; Verani, M.; McKinley, G. H. How Dilute Are Dilute Solutions in Extensional Flows? *J. Rheol. (N. Y. N. Y).* **2006**, *50* (6), 849–881.

(109) Heymann, E. Studies on Sol-Gel Transformations. I. The Inverse Sol-Gel Transformation of Methylcellulose in Water. *Trans. Faraday Soc.* **1935**, *31*, 846–864.

(110) Heymann, E.; Bleakley, H. G.; Docking, A. R. Studies on the Lyotropic Series. I: The Adsorption of Salts on Methylcellulose. *J. Phys. Chem.* **1938**, *42* (3), 353–368.

(111) Kundu, P. P.; Kundu, M. Effect of Salts and Surfactant and Their Doses on the Gelation of Extremely Dilute Solutions of Methyl Cellulose. *Polymer (Guildf).* **2001**, *42* (5), 2015–2020.

(112) Lin, L.; Wang, Q.; Xu, Y. Thermoreversible Association and Gelation of Methylcellulose in Aqueous Solutions. *Nihon Reoroji Gakkaishi* **2003**, *31* (5), 287–296.

(113) Villetti, M. a.; Soldi, V.; Rochas, C.; Borsali, R. Phase-Separation Kinetics and Mechanism in a Methylcellulose/Salt Aqueous Solution Studied by Time-Resolved Small-Angle Light Scattering (SALS). *Macromol. Chem. Phys.* **2011**, *212* (10), 1063–1071.

(114) Arvidson, S. A.; Lott, J. R.; McAllister, J. W.; Zhang, J.; Bates, F. S.; Lodge, T. P.; Sammler, R. L.; Li, Y.; Brackhagen, M. Interplay of Phase Separation and Thermoreversible Gelation in Aqueous Methylcellulose Solutions. *Macromolecules* **2013**, *46* (1), 300–309.

(115) McAllister, J. W.; Schmidt, P. W.; Dorfman, K. D.; Lodge, T. P.; Bates, F. S. Thermodynamics of Aqueous Methylcellulose Solutions. *Macromolecules* **2015**, *48* (19), 7205–7215.

(116) Papageorgiou, D. T. On the Breakup of Viscous Liquid Threads. *Phys. Fluids* **1995**,

*7* (7), 1529–1544.

(117) Doshi, P.; Suryo, R.; Yildirim, O. E.; McKinley, G. H.; Basaran, O. A. Scaling in Pinch-off of Generalized Newtonian Fluids. *J. Nonnewton. Fluid Mech.* **2003**, *113* (1), 1–27.

(118) Huisman, F. M.; Friedman, S. R.; Taborek, P. Pinch-off Dynamics in Foams, Emulsions and Suspensions. *Soft Matter* **2012**, *8* (25), 6767–6774.

(119) Clasen, C. Capillary Breakup Extensional Rheometry of Semi-Dilute Polymer Solutions. *Korea-Australia Rheol. J.* **2010**, *22* (4), 331–338.

(120) Sachsenheimer, D.; Oelschlaeger, C.; Müller, S.; Küstner, J.; Bindgen, S.; Willenbacher, N. Elongational Deformation of Wormlike Micellar Solutions. *J. Rheol. (N. Y. N. Y).* **2014**, *58* (6), 2017–2042.

(121) Arnolds, O.; Buggisch, H.; Sachsenheimer, D.; Willenbacher, N. Capillary Breakup Extensional Rheometry (CaBER) on Semi-Dilute and Concentrated Polyethyleneoxide (PEO) Solutions. *Rheol. Acta* **2010**, *49* (11), 1207–1217.

(122) Liu, Y.; Jun, Y.; Steinberg, V. Concentration Dependence of the Longest Relaxation Times of Dilute and Semi-Dilute Polymer Solutions. *J. Rheol. (N. Y. N. Y).* **2009**, *53* (5), 1069–1085.

(123) Milner, S. T.; Mc Leish, T. C. B. Reptation and Contour-Length Fluctuations in Melts of Linear Polymers. *Phys. Rev. Lett.* **1998**, *81* (3), 725–728.

(124) Lodge, T. P. Reconciliation of the Molecular Weight Dependence of Diffusion and Viscosity in Entangled Polymers. *Phys. Rev. Lett.* **1999**, *83* (16), 3218–3221.

(125) Flory, P. J. *Principles of Polymer Chemistry*; Cornell University Press: Ithaca, 1953.

(126) Miller, E.; Clasen, C.; Rothstein, J. P. The Effect of Step-Stretch Parameters on Capillary Breakup Extensional Rheology (CaBER) Measurements. *Rheol. Acta* **2009**, *48* (6), 625–639.

(127) Dutcher, C. S.; Wexler, A. S.; Clegg, S. L. Surface Tensions of Inorganic Multicomponent Aqueous Electrolyte Solutions and Melts. *J. Phys. Chem. A* **2010**, *114* (46), 12216–12230.

(128) Metcalf, A. R.; Boyer, H. C.; Dutcher, C. S. Interfacial Tensions of Aged Organic Aerosol Particle Mimics Using a Biphasic Microfluidic Platform. *Environ. Sci. Technol.* **2016**, *50* (3), 1251–1259.

(129) Boyer, H. C.; Dutcher, C. S. Atmospheric Aqueous Aerosol Surface Tensions: Isotherm-Based Modeling and Biphasic Microfluidic Measurements. *J. Phys. Chem. A* **2017**, *121* (25), 4733–4742.

(130) Narayan, S.; Moravec, D. B.; Hauser, B. G.; Dallas, A. J.; Dutcher, C. S. Removing Water from Diesel Fuel: Understanding the Impact of Droplet Size on Dynamic

Interfacial Tension of Water-in-Fuel Emulsions. *Energy & Fuels* **2018**, *32* (7), 7326–7337.

(131) Schröder, A.; Sprakel, J.; Schroën, K.; Spaen, J. N.; Berton-Carabin, C. C. Coalescence Stability of Pickering Emulsions Produced with Lipid Particles: A Microfluidic Study. *J. Food Eng.* **2018**, *234*, 63–72.

(132) Chacon Orellana, L. A.; Baret, J. Rapid Stabilization of Droplets by Particles in Microfluidics: Role of Droplet Formation. *ChemSystemsChem* **2019**, *1* (1–2), 16–24.

(133) Arratia, P. E.; Thomas, C. C.; Diorio, J.; Gollub, J. P. Elastic Instabilities of Polymer Solutions in Cross-Channel Flow. *Phys. Rev. Lett.* **2006**, *96* (14), 144502.

(134) Arratia, P. E.; Gollub, J. P.; Durian, D. J. Polymeric Filament Thinning and Breakup in Microchannels. *Phys. Rev. E* **2008**, *77* (3), 036309.

(135) Haward, S. J.; Oliveira, M. S. N.; Alves, M. A.; McKinley, G. H. Optimized Cross-Slot Flow Geometry for Microfluidic Extensional Rheometry. *Phys. Rev. Lett.* **2012**, *109* (12), 128301.

(136) Del Giudice, F.; Haward, S. J.; Shen, A. Q. Relaxation Time of Dilute Polymer Solutions: A Microfluidic Approach. *J. Rheol. (N. Y. N. Y).* **2017**, *61* (2), 327–337.

(137) Anna, S. L.; Bontoux, N.; Stone, H. A. Formation of Dispersions Using "Flow Focusing" in Microchannels. *Appl. Phys. Lett.* **2003**, *82* (3), 364–366.

(138) Bruss, I. R.; Grason, G. M. Topological Defects, Surface Geometry and Cohesive Energy of Twisted Filament Bundles. *Soft Matter* **2013**, *9* (34), 8327.

(139) Hall, D. M.; Bruss, I. R.; Barone, J. R.; Grason, G. M. Morphology Selection via Geometric Frustration in Chiral Filament Bundles. *Nat. Mater.* **2016**, *15* (7), 727–732.

(140) Hall, D. M.; Grason, G. M. How Geometric Frustration Shapes Twisted Fibres, inside and out: Competing Morphologies of Chiral Filament Assembly. *Interface Focus* **2017**, *7* (4), 20160140.

(141) Sethuraman, V.; Dorfman, K. D. Simulating Precursor Steps for Fibril Formation in Methylcellulose Solutions. *Phys. Rev. Mater.* **2019**, *3* (5), 055601.

(142) Schmidt, P. W.; Morozova, S.; Ertem, S. P.; Coughlin, M. L.; Davidovich, I.; Talmon, Y.; Reineke, T. M.; Bates, F. S.; Lodge, T. P. Internal Structure of Methylcellulose Fibrils. *Macromolecules* **2020**, *53* (1), 398–405.

(143) Micklavzina, B. L.; Metaxas, A. E.; Dutcher, C. S. Microfluidic Rheology of Methylcellulose Solutions in Hyperbolic Contractions and the Effect of Salt in Shear and Extensional Flows. *Soft Matter* **2020**, *16* (22), 5273–5281.

(144) Lee, H. S.; Muller, S. J. A Differential Pressure Extensional Rheometer on a Chip

with Fully Developed Elongational Flow. *J. Rheol. (N. Y. N. Y).* **2017**, *61* (5), 1049–1059.

(145) Funami, T.; Kataoka, Y.; Hiroe, M.; Asai, I.; Takahashi, R.; Nishinari, K. Thermal Aggregation of Methylcellulose with Different Molecular Weights. *Food Hydrocoll.* **2007**, *21* (1), 46–58.

(146) Xia, Y.; Whitesides, G. M. Soft Lithography. *Annu. Rev. Mater. Sci.* **1998**, *28* (1), 153–184.

(147) McDonald, J. C.; Whitesides, G. M. Poly(Dimethylsiloxane) as a Material for Fabricating Microfluidic Devices. *Acc. Chem. Res.* **2002**, *35* (7), 491–499.

(148) Qin, D.; Xia, Y.; Whitesides, G. M. Soft Lithography for Micro- and Nanoscale Patterning. *Nat. Protoc.* **2010**, *5* (3), 491–502.

(149) Dinic, J.; Sharma, V. Power Laws Dominate Shear and Extensional Rheology Response and Capillarity-Driven Pinching Dynamics of Entangled Hydroxyethyl Cellulose (HEC) Solutions. *Macromolecules* **2020**, *53*, 3424–3437.

(150) Daly, E.; Saunders, B. R. Study of the Effect of Electrolyte on the Swelling and Stability of Poly(N-Isopropylacrylamide) Microgel Dispersions. *Langmuir* **2000**, *16* (13), 5546–5552.

(151) Polotsky, A. A.; Plamper, F. A.; Borisov, O. V. Collapse-to-Swelling Transitions in PH- and Thermoresponsive Microgels in Aqueous Dispersions: The Thermodynamic Theory. *Macromolecules* **2013**, *46* (21), 8702–8709.

(152) Zavgorodnya, O.; Kozlovskaya, V.; Liang, X.; Kothalawala, N.; Catledge, S. A.; Dass, A.; Kharlampieva, E. Temperature-Responsive Properties of Poly(N-Vinylcaprolactam) Multilayer Hydrogels in the Presence of Hofmeister Anions. *Mater. Res. Express* **2014**, *1* (3), 035039.

(153) Amarouchene, Y.; Bonn, D.; Meunier, J.; Kellay, H. Inhibition of the Finite-Time Singularity during Droplet Fission of a Polymeric Fluid. *Phys. Rev. Lett.* **2001**, *86* (16), 3558–3561.

(154) Oliveira, M. S. N.; McKinley, G. H. Iterated Stretching and Multiple Beads-on-a-String Phenomena in Dilute Solutions of Highly Extensible Flexible Polymers. *Phys. Fluids* **2005**, *17* (7), 071704.

(155) Dangla, R.; Lee, S.; Baroud, C. N. Trapping Microfluidic Drops in Wells of Surface Energy. *Phys. Rev. Lett.* **2011**, *107*, 124501.

(156) Juarez, G.; Arratia, P. E. Extensional Rheology of DNA Suspensions in Microfluidic Devices. *Soft Matter* **2011**, *7* (19), 9444–9452.

(157) Sessoms, D. A.; Belloul, M.; Engl, W.; Roche, M.; Courbin, L.; Panizza, P. Droplet Motion in Microfluidic Networks: Hydrodynamic Interactions and Pressure-Drop Measurements. *Phys. Rev. E* **2009**, *80*, 016317.

(158) Vanapalli, S. A.; Banpurkar, A. G.; Van Den Ende, D.; Duits, M. H. G.; Mugele, F. Hydrodynamic Resistance of Single Confined Moving Drops in Rectangular Microchannels. *Lab Chip* **2009**, *9* (7), 982–990.

(159) Brun, P.-T.; Nagel, M.; Gallaire, F. Generic Path for Droplet Relaxation in Microfluidic Channels. *Phys. Rev. E* **2013**, *88*, 43009.

(160) Torres, M. D.; Hallmark, B.; Wilson, D. I.; Hilliou, L. Natural Giesekus Fluids: Shear and Extensional Behavior of Food Gum Solutions in the Semidilute Regime. *AIChE J.* **2014**, *60* (11), 3902–3915.

(161) Torres, M. D.; Hallmark, B.; Wilson, D. I. Effect of Concentration on Shear and Extensional Rheology of Guar Gum Solutions. *Food Hydrocoll.* **2014**, *40*, 85–95.

(162) Różańska, S. *Advances in Food Rheology and Its Applications*; Ahmed, J., Ptaszek, P., Basu, S., Eds.; Woodhead Publishing, 2017.

(163) Wingstrand, S. L.; Alvarez, N. J.; Huang, Q.; Hassager, O. Linear and Nonlinear Universality in the Rheology of Polymer Melts and Solutions. *Phys. Rev. Lett.* **2015**, *115*, 078302.

(164) Peter Jarvis; Bruce Jefferson, A.; Parsons, S. A. Breakage, Regrowth, and Fractal Nature of Natural Organic Matter Flocs. *Environ. Sci. Technol.* **2005**, *39* (7), 2307–2314.

(165) Andereck, C. D.; Liu, S. S.; Swinney, H. L. Flow Regimes in a Circular Couette System with Independently Rotating Cylinders. *J. Fluid Mech.* **2006**, *164* (1), 155.

(166) Dutcher, C. S.; Muller, S. J. Explicit Analytic Formulas for Newtonian Taylor-Couette Primary Instabilities. *Phys. Rev. E. Stat. Nonlin. Soft Matter Phys.* **2007**, *75* (4 Pt 2), 047301.

(167) Dutcher, C. S.; Muller, S. J. Spatio-Temporal Mode Dynamics and Higher Order Transitions in High Aspect Ratio Newtonian Taylor–Couette Flows. *J. Fluid Mech.* **2009**, *641*, 85.

(168) Fardin, M. A.; Perge, C.; Taberlet, N. "The Hydrogen Atom of Fluid Dynamics" – Introduction to the Taylor–Couette Flow for Soft Matter Scientists. *Soft Matter* **2014**, *10* (20), 3523.

(169) Zbik, M. S.; Smart, R. S. C.; Morris, G. E. Kaolinite Flocculation Structure. *J. Colloid Interface Sci.* **2008**, *328* (1), 73–80.

(170) Majji, M. V.; Banerjee, S.; Morris, J. F. Inertial Flow Transitions of a Suspension in Taylor–Couette Geometry. *J. Fluid Mech.* **2018**, *835*, 936–969.

(171) Dutcher, C. S.; Muller, S. J. The Effects of Drag Reducing Polymers on Flow Stability : Insights from the Taylor-Couette Problem. *Korea-Australia Rheol. J.* **2009**, *21* (4), 213–233.

(172) Dutcher, C. S.; Muller, S. J. Effects of Moderate Elasticity on the Stability of Co- and Counter-Rotating Taylor–Couette Flows. *J. Rheol. (N. Y. N. Y).* **2013**, *57* (3), 791.

(173) Nemri, M.; Charton, S.; Climent, E. Mixing and Axial Dispersion in Taylor–Couette Flows: The Effect of the Flow Regime. *Chem. Eng. Sci.* **2016**, *139*, 109–124.

(174) Tilton, N.; Martinand, D.; Serre, E.; Lueptow, R. M. Pressure-Driven Radial Flow in a Taylor–Couette Cell. *J. Fluid Mech.* **2010**, *660*, 527–537.

(175) Guérin, L.; Coufort-Saudejaud, C.; Liné, A.; Frances, C. Dynamics of Aggregate Size and Shape Properties under Sequenced Flocculation in a Turbulent Taylor-Couette Reactor. *J. Colloid Interface Sci.* **2017**, *491*, 167–178.

(176) Nemri, M.; Climent, E.; Charton, S.; Lanoë, J.-Y.; Ode, D. Experimental and Numerical Investigation on Mixing and Axial Dispersion in Taylor–Couette Flow Patterns. *Chem. Eng. Res. Des.* **2013**, *91* (12), 2346–2354.

(177) Nemri, M.; Cazin, S.; Charton, S.; Climent, E. Experimental Investigation of Mixing and Axial Dispersion in Taylor–Couette Flow Patterns. *Exp. Fluids* **2014**, *55* (7), 1769.

(178) Kaufhold, S.; Dohrmann, R.; Koch, D.; Houben, G. The PH of Aqueous Bentonite Suspensions. *Clays Clay Miner.* **2008**, *56* (3), 338–343.

(179) Yukselen, M. A.; Gregory, J. The Effect of Rapid Mixing on the Break-up and Re-Formation of Flocs. *J. Chem. Technol. Biotechnol.* **2004**, *79* (7), 782–788.

(180) Lewis, G. S.; Swinney, H. L. Velocity Structure Functions, Scaling, and Transitions in High-Reynolds-Number Couette-Taylor Flow. *Phys. Rev. E* **1999**, *59* (5), 5457–5467.

(181) Kargi, F. Re-Interpretation of the Logistic Equation for Batch Microbial Growth in Relation to Monod Kinetics. *Lett. Appl. Microbiol.* **2009**, *48* (4), 398–401.

(182) Bukhman, Y. V.; DiPiazza, N. W.; Piotrowski, J.; Shao, J.; Halstead, A. G. W.; Bui, M. D.; Xie, E.; Sato, T. K. Modeling Microbial Growth Curves with GCAT. *BioEnergy Res.* **2015**, *8* (3), 1022–1030.

(183) Mikeš, D. A Simple Floc-Growth Function for Natural Flocs in Estuaries. *Math Geosci* **2011**, *43*, 593–606.

(184) Su, Kui-Zu and Yu, H.-Q. Formation and Characterization of Aerobic Granules in a Sequencing Batch Reactor Treating Soybean-Processing Wastewater. *Environ. Eng. Sci.* **2005**, *39* (8), 2818–2827.

(185) Bouyer, D.; Liné, A.; Do-Quang, Z. Experimental Analysis of Floc Size Distribution under Different Hydrodynamics in a Mixing Tank. *AIChE J.* **2004**, *50* (9), 2064–2081.

(186) Ohmura, N.; Kataoka, K.; Shibata, Y.; Makino, T. Effective Mass Diffusion over Cell Boundaries in a Taylor-Couette Flow System. *Chem. Eng. Sci.* **1997**, *52* (11), 1757–1765.

(187) Dusting, J.; Balabani, S. Mixing in a Taylor–Couette Reactor in the Non-Wavy Flow Regime. *Chem. Eng. Sci.* **2009**, *64* (13), 3103–3111.

(188) Li, T.; Zhu, Z.; Wang, D.; Yao, C.; Tang, H. Characterization of Floc Size, Strength and Structure under Various Coagulation Mechanisms. *Powder Technol.* **2006**, *168* (2), 104–110.

(189) Li, T.; Zhu, Z.; Wang, D.; Yao, C.; Tang, H. The Strength and Fractal Dimension Characteristics of Alum–Kaolin Flocs. *Int. J. Miner. Process.* **2007**, *82* (1), 23–29.

(190) Zhu, Z.; Yu, J.; Wang, H.; Dou, J.; Wang, C. Fractal Dimension of Cohesive Sediment Flocs at Steady State under Seven Shear Flow Conditions. *Water* **2015**, *7* (12), 4385–4408.

(191) Tinland, B.; Pluen, A.; Sturm, J.; Weill, G. *Persistence Length of Single-Stranded DNA*; 1997.

(192) Heath, D.; Tadros, T. . Influence of PH, Electrolyte, and Poly(Vinyl Alcohol) Addition on the Rheological Characteristics of Aqueous Dispersions of Sodium Montmorillonite. *J. Colloid Interface Sci.* **1983**, *93* (2), 307–319.

(193) Mayordomo, N.; Degueldre, C.; Alonso, U.; Missana, T. Size Distribution of FEBEX Bentonite Colloids upon Fast Disaggregation in Low-Ionic Strength Water. *Clay Miner.* **2016**, *51* (2), 213–222.

(194) Walldal, C.; Åkerman, B. Effect of Ionic Strength on the Dynamic Mobility of Polyelectrolytes. *Langmuir* **1999**, *15*, 5237–5243.

(195) Colby, R. H. Structure and Linear Viscoelasticity of Flexible Polymer Solutions: Comparison of Polyelectrolyte and Neutral Polymer Solutions. *Rheol Acta* **2010**, *49*, 425–442.

(196) Guérin, L.; Coufort-Saudejaud, C.; Liné, A.; Frances, C. Dynamics of Aggregate Size and Shape Properties under Sequenced Flocculation in a Turbulent Taylor-Couette Reactor. *J. Colloid Interface Sci.* **2017**, *491*, 167–178.

(197) Blanco, A.; Negro, C.; Fuente, E.; Tijero, J. Effect of Shearing Forces and Flocculant Overdose on Filler Flocculation Mechanisms and Floc Properties. *Ind. Eng. Chem. Res.* **2005**, *44* (24), 9105–9112.

(198) Daryabeigi Zand, A.; Hoveidi, H. *Comparing Aluminium Sulfate and Poly-Aluminium Chloride (PAC) Performance in Turbidity Removal from Synthetic Water*; 2015; Vol. 2.

(199) Sakhawoth, Y.; Michot, L. J.; Levitz, P.; Malikova, N. Flocculation of Clay Colloids Induced by Model Polyelectrolytes: Effects of Relative Charge Density and Size.

*ChemPhysChem* **2017**, *18* (19), 2756–2765.

(200) Deepnarain, N.; Kumari, S.; Ramjith, J.; Swalaha, F. M.; Tandoi, V.; Pillay, K.; Bux, F. A Logistic Model for the Remediation of Filamentous Bulking in a Biological Nutrient Removal Wastewater Treatment Plant. *Water Sci. Technol.* **2015**, *72* (3), 391–405.

(201) Durand, G.; Lafuma, F.; Audebert, R. Adsorption of Cationic Polyelectrolytes at Clay-Colloid Interface in Dilute Aqueous Suspensions — Effect of the Ionic Strength of the Medium. In *Trends in Colloid and Interface Science II*; Steinkopff: Darmstadt, 1988; pp 278–282.

(202) Klučáková, M.; Pekař, M. Behaviour of Partially Soluble Humic Acids in Aqueous Suspension. *Colloids Surfaces A Physicochem. Eng. Asp.* **2008**, *318* (1–3), 106–110.

(203) Ritchie, J. D.; Perdue, E. M. Proton-Binding Study of Standard and Reference Fulvic Acids, Humic Acids, and Natural Organic Matter. *Geochim. Cosmochim. Acta* **2003**, *67* (1), 85–96.

(204) Frimmel, F. H. Aquatic Humic Substances. In *Biopolymers*; Steinbuchel, A., Ed.; Wiley-VCH Verlag GmbH & Co. KGaA, 2005; pp 301–320.

(205) Piccolo, A.; Spaccini, R.; Drosos, M.; Vinci, G.; Cozzolino, V. The Molecular Composition of Humus Carbon: Recalcitrance and Reactivity in Soils. In *The Future of Soil Carbon: Its Conservation and Formation*; Elsevier Inc., 2018; pp 87–124.

(206) Kvinnesland, T.; Ødegaard, H. The Effects of Polymer Characteristics on Nano Particle Separation in Humic Substances Removal by Cationic Polymer Coagulation. *Water Sci. Technol.* **2004**, *50* (12), 185–191.

(207) Kam, S. K.; Gregory, J. The Interaction of Humic Substances with Cationic Polyelectrolytes. *Water Res.* **2001**, *35* (15), 3557–3566.

(208) Bolto, B.; Abbt-Braun, G.; Dixon, D.; Eldridge, R.; Frimmel, F.; Hesse, S.; King, S.; Toifl, M. Experimental Evaluation of Cationic Polyelectrolytes for Removing Natural Organic Matter from Water. *Water Sci. Technol.* **1999**, *40* (9), 71–79.

(209) Klučáková, M.; Kolajová, R. Dissociation Ability of Humic Acids: Spectroscopic Determination of PKa and Comparison with Multi-Step Mechanism. *React. Funct. Polym.* **2014**, *78*, 1–6.

(210) Ghosh, K.; Schnitzer, M. Fluorescence Excitation Spectra of Humic Substances. *Can. J. Soil Sci.* **1980**, *60* (2), 373–379.

(211) Senesi, N.; Miano, T. M.; Provenzano, M. R.; Brunetti, G. Spectroscopic and Compositional Comparative Characterization of I.H.S.S. Reference and Standard Fulvic and Humic Acids of Various Origin. *Sci. Total Environ.* **1989**, *81–82* (C), 143–156.

(212) Chen, W.; Westerhoff, P.; Leenheer, J. A.; Booksh, K. Fluorescence

Excitation−Emission Matrix Regional Integration to Quantify Spectra for Dissolved Organic Matter. *Environ. Sci. Technol.* **2003**, *37*, 5701–5710.

(213) Sierra, M. M. D.; Giovanela, M.; Parlanti, E.; Soriano-Sierra, E. J. Fluorescence Fingerprint of Fulvic and Humic Acids from Varied Origins as Viewed by Single-Scan and Excitation/Emission Matrix Techniques. *Chemosphere* **2005**, *58* (6), 715–733.

(214) Chen, J.; LeBoeuf, E. J.; Dai, S.; Gu, B. Fluorescence Spectroscopic Studies of Natural Organic Matter Fractions. *Chemosphere* **2003**, *50* (5), 639–647.

(215) Westerhoff, P.; Aiken, G.; Amy, G.; Debroux, J. Relationships between the Structure of Natural Organic Matter and Its Reactivity towards Molecular Ozone and Hydroxyl Radicals. *Water Res.* **1999**, *33* (10), 2265–2276.

(216) Dinic, J.; Sharma, V. Flexibility, Extensibility, and Ratio of Kuhn Length to Packing Length Govern the Pinching Dynamics, Coil-Stretch Transition, and Rheology of Polymer Solutions. *Macromolecules* **2020**, *14*, 11.

(217) Dinic, J.; Sharma, V. Macromolecular Relaxation, Strain, and Extensibility Determine Elastocapillary Thinning and Extensional Viscosity of Polymer Solutions. *Proc. Natl. Acad. Sci. U. S. A.* **2019**, *116* (18), 8766–8774.

(218) Sousa, P. C.; Vega, E. J.; Sousa, R. G.; Montanero, J. M.; Alves, M. A. Measurement of Relaxation Times in Extensional Flow of Weakly Viscoelastic Polymer Solutions. *Rheol Acta* **2017**, *56*, 11–20.

(219) Stan, C. A.; Schneider, G. F.; Shevkoplyas, S. S.; Hashimoto, M.; Ibanescu, M.; Wiley, B. J.; Whitesides, G. M. A Microfluidic Apparatus for the Study of Ice Nucleation in Supercooled Water Drops. *Lab Chip* **2009**, *9* (16), 2293–2305.

(220) Carrington, S.; Odell, J.; Fisher, L.; Mitchell, J.; Hartley, L. Polyelectrolyte Behaviour of Dilute Xanthan Solutions: Salt Effects on Extensional Rheology. *Polymer (Guildf).* **1996**, *37* (13), 2871–2875.

(221) Narh, K. A.; Keller, A. The Effect of Counterions on the Chain Conformation of Polyelectrolytes, as Assessed by Extensibility in Elongational Flow: The Influence of Multiple Valency. *J. Polym. Sci. Part B Polym. Phys.* **1994**, *32* (10), 1697–1706.

(222) Ashok, B.; Muthukumar, M. Crossover Behavior of the Viscosity of Dilute and Semidilute Polyelectrolyte Solutions. *J. Phys. Chem. B* **2009**, *113* (17), 5736–5745.

(223) Nallely Jimenez, L.; Dinic, J.; Parsi, N.; Sharma, V. Extensional Relaxation Time, Pinch-Off Dynamics, and Printability of Semidilute Polyelectrolyte Solutions. *Macromolecules* **2018**, *51*, 5191–5208.

(224) Szopinski, D.; Handge, U. A.; Kulicke, W.-M.; Abetz, V.; Luinstra, G. A. Extensional Flow Behavior of Aqueous Guar Gum Derivative Solutions by Capillary Breakup Elongational Rheometry (CaBER). *Carbohydr. Polym.* **2016**, *136*, 834–840.

(225) Walter, A. V; Jimenez, L. N.; Dinic, J.; Sharma, V.; Erk, K. A. Effect of Salt Valency and Concentration on Shear and Extensional Rheology of Aqueous Polyelectrolyte Solutions for Enhanced Oil Recovery. *Rheol. Acta* **2019**, *58*, 145–157.

(226) Tam, K. C.; Jenkins, R. D.; Winnik, M. A.; Bassett, D. R. A Structural Model of Hydrophobically Modified Urethane-Ethoxylate (HEUR) Associative Polymers in Shear Flows. *Macromolecules* **1998**, *31* (13), 4149–4159.

(227) Kujawa, P.; Audibert-Hayet, A.; Selb, J.; Candau, F. Effect of Ionic Strength on the Rheological Properties of Multisticker Associative Polyelectrolytes. *Macromolecules* **2006**, *39*, 384–392.

(228) Chremos, A.; Douglas, J. F. Influence of Higher Valent Ions on Flexible Polyelectrolyte Stiffness and Counter-Ion Distribution. *J. Chem. Phys.* **2016**, *144* (16), 164904.

# Appendix A
# Copyright Permissions

Figure 1.1 in Chapter 1 was adapted with permission from Springer Nature Customer Service Centre GmBH: Springer, Microfluidics and Nanofluidics 14, Microdevices for extensional rheometry of low viscosity elastic liquids: a review, F. J. Galindo-Rosales and M. A. Alves, Copyright (2013). Figure 1.4 in Chapter 1 is adapted with permission from *Microporous and Mesoporous Materials*, 33, O. Duman and S. Tunç, Electrokinetic and rheological properties of Na-bentonite in some electrolyte solutions, 331-338, Copyright (2009), with permission from Elsevier.

Chapter 2 consists of portions of a journal article reprinted with permission from S. Morozova, P. W. Schmidt, A. Metaxas, F. S. Bates, T. P. Lodge, and C. S. Dutcher, Extensional Flow Behavior of Methylcellulose Solutions Containing Fibrils, *ACS Macro Letters*, 7, 347-352, Copyright (2018) American Chemical Society.

Chapter 3 consists of portions of a journal article currently under review in A. E. Metaxas, M. L. Coughlin, C. K. Hansen, F. S. Bates, T. P. Lodge, and C. S. Dutcher, Microfluidic filament thinning of aqueous, fibrillar methylcellulose solutions, *Physical Review Fluids* (2020) Submitted.

Chapter 4 consists of portions of a journal article cited as A. Metaxas, N. Wilkinson, E. Raethke, and C. S. Dutcher, *In situ* polymer flocculation and growth in Taylor-Couette

flows, *Soft Matter*, 14, 8627-8635 (2018), reproduced by permission of The Royal Society of Chemistry.

Chapter 5 consists of portions of a journal article currently under review in A. E. Metaxas, V. Panwar, R. L. Olson, and C. S. Dutcher, Ionic strength and molecular weight effects on floc formation and growth in Taylor-Couette flows, *Soft Matter* (2020) Submitted.

# Appendix B

# LabVIEW and MATLAB Codes

## *LabVIEW: On Demand Injection Control*

The following is the LabVIEW user interface and circuit diagram used to specify the drive pressure (in psi) and duration of injection (in ms) for the injection assembly.

**"Voltage – On Demand Output.vi."**

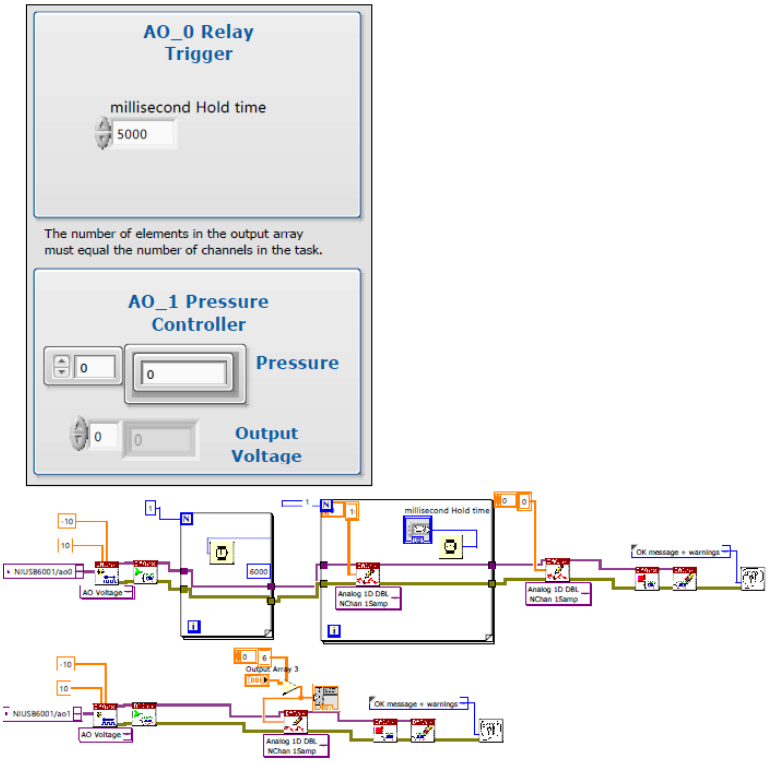

## *LabVIEW: Simultaneous Camera and Injection Control*

The following is the LabView user interface and circuit diagram for injection flocculant from the injection cylinder into the annulus while simultaneously recording the entire flocculation process. The first image indicates where the user can specify the file name, injection time (in ms), the recording time (in min), and the drive pressure (in psi). The frame rate read-out is also shown in the lower left-hand corner. The second image shows the live recording.

**"Camera Control Subsection & Injection Control 8-10-17.vi."**

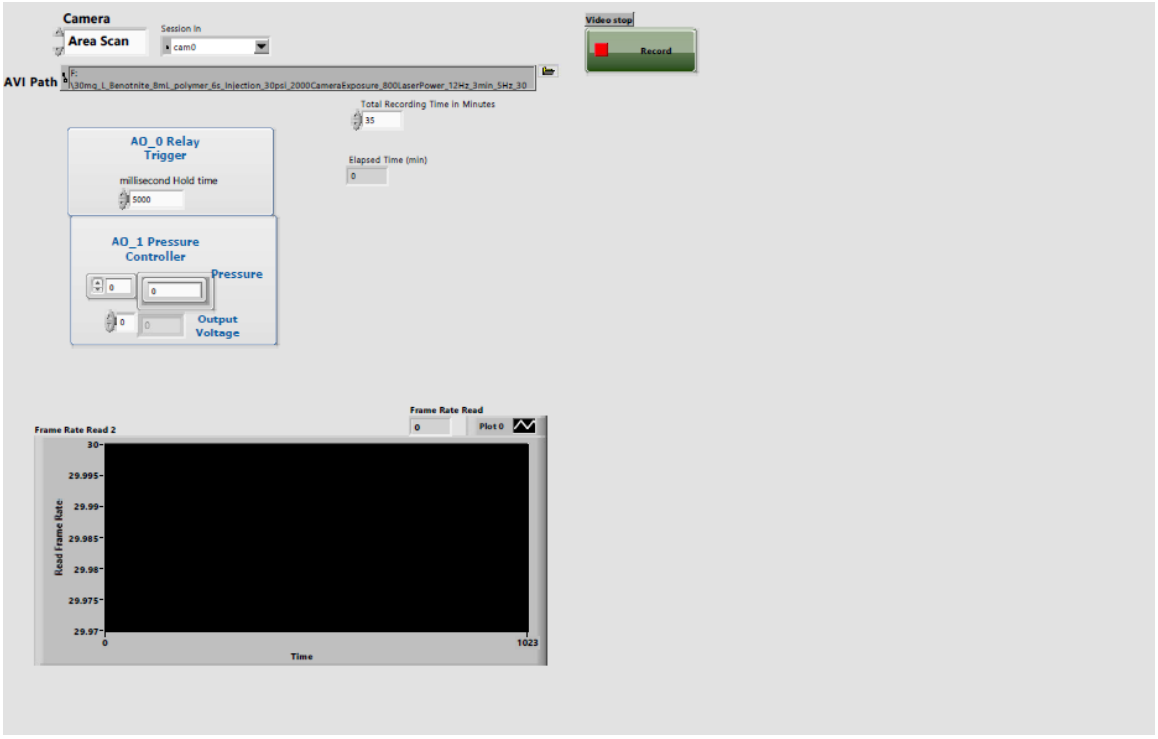


Live Image

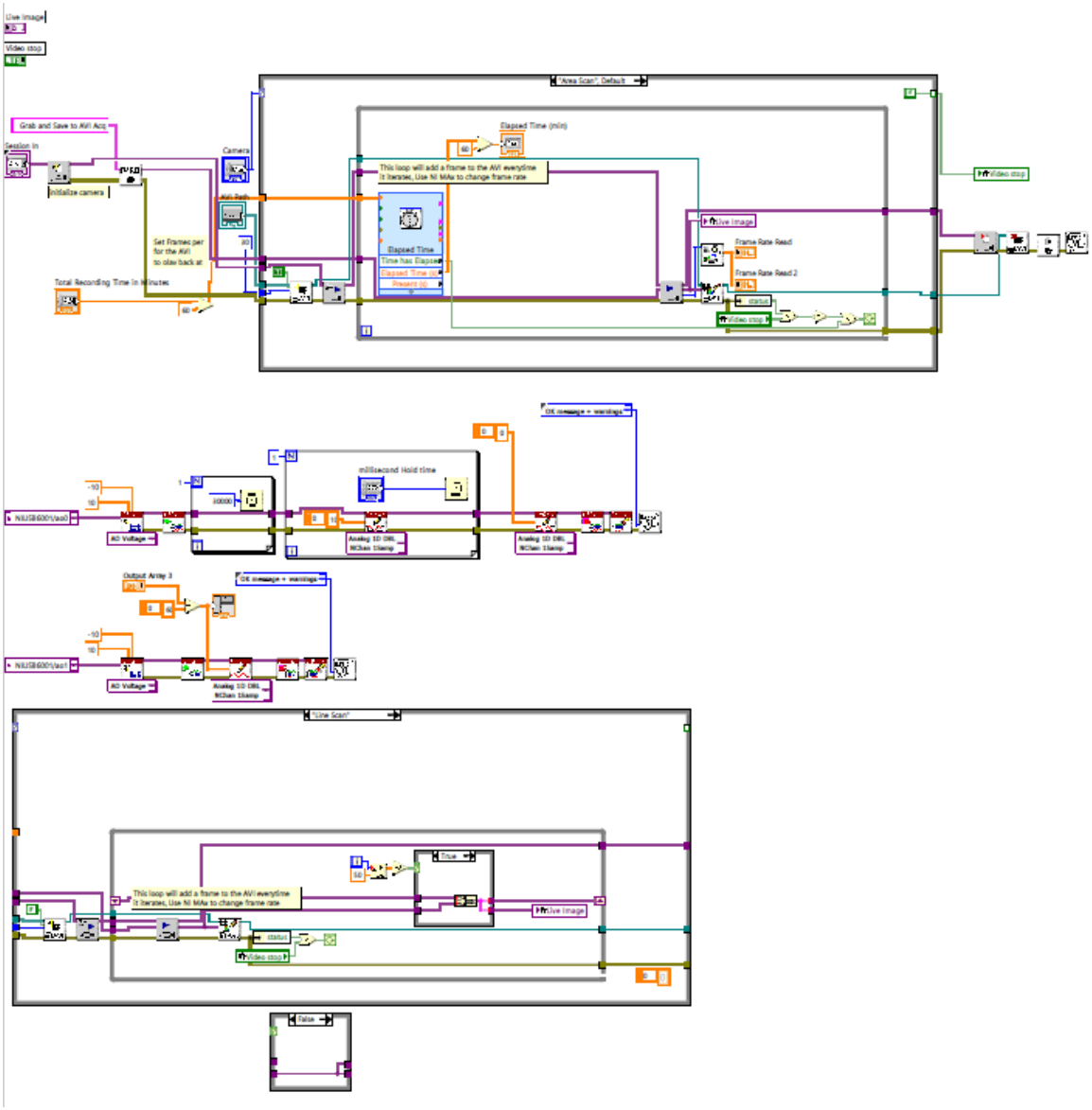
Live Image
Video stop
Grab and Save to AVI Acq
Session In
Initialize camera
Camera
Set Frames per for the AVI to play back at
Total Recording Time In Minutes
"Area Scan" Default
Elapsed Time (min)
This loop will add a frame to the AVI everytime it iterates, Use NI MAx to change frame rate
Elapsed Time
Time has Elapsed
Frame Rate Read
Frame Rate Read 2
status
millisecond Hold time
AO Voltage
Output Array 3
"Line Scan"
True
False

## *MATLAB: CaBER Data Fitting Code*

This code fits to the elasto-capillary region of the CaBER data file. The user defines the start and end time of the fit, and those times must match the times listed in the data file to the fifth place past the decimal point, otherwise MATLAB will generate an error. Both "createFit" and "fitpolymersmaster" are required for the code to operate (the former is the function that the latter calls). The code will calculate the extensional relaxation time, *lamda* (make sure to divide it by three as this considers $3\lambda_E$ as a single fit parameter), the pre-factor, *a*, and the root mean square error, *RMSE*. An example of the output figure is shown below.

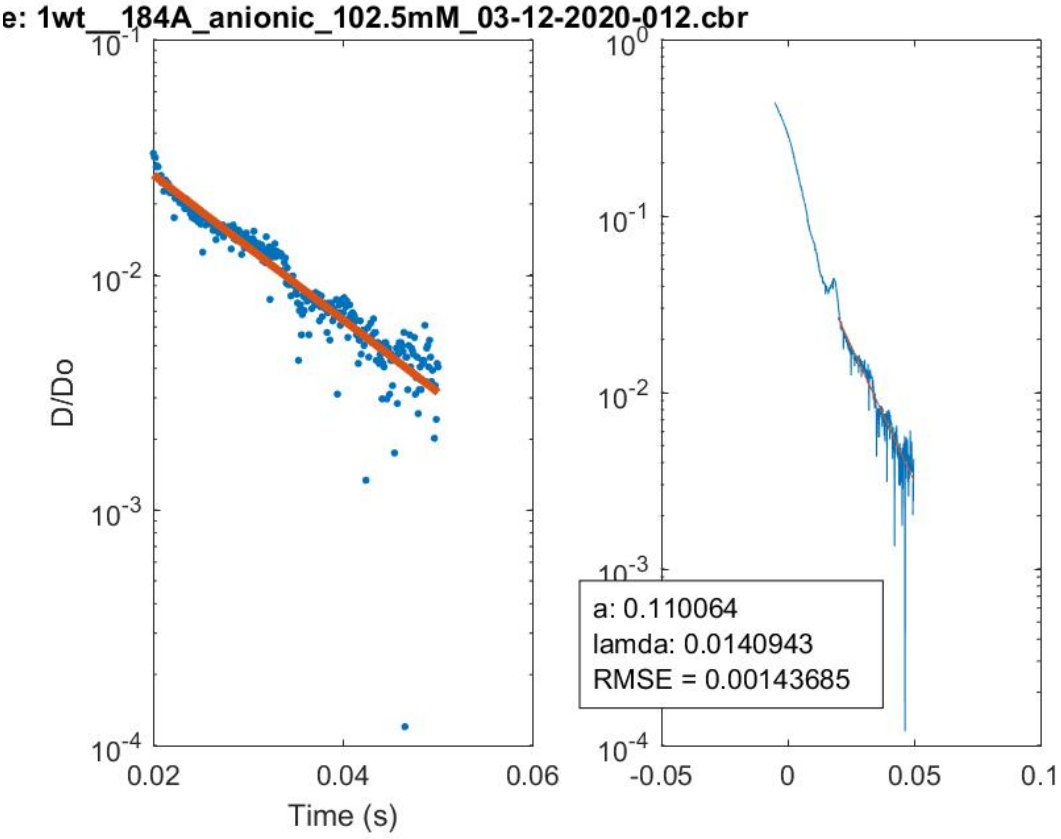


**"createFit.m"**

```
function [fitresult, gof] = createFit(x, y)
%CREATEFIT(X,Y)
%  Create a fit.
%
```

```
%  Data for 'untitled fit 1' fit:
%      X Input : x
%      Y Output: y
%  Output:
%      fitresult : a fit object representing the fit.
%      gof : structure with goodness-of fit info.
%
%  See also FIT, CFIT, SFIT.

%  Auto-generated by MATLAB on 17-Feb-2016 11:00:38


%% Fit: 'untitled fit 1'.
[xData, yData] = prepareCurveData( x, y );

% Set up fittype and options.
ft = fittype( 'a*exp(-x/l)', 'independent', 'x',
'dependent', 'y' ); %+a2*exp(-x/l2)
opts = fitoptions( 'Method', 'NonlinearLeastSquares' );
opts.Display = 'Off';
opts.Lower = [0 0 0 0];
opts.StartPoint = [0.01 2.0];

% Fit model to data.
[fitresult, gof] = fit( xData, yData, ft, opts );

% Plot fit with data.
% figure( 'Name', 'untitled fit 1' );
% h = plot( fitresult, xData, yData );
% legend( h, 'y vs. x', 'untitled fit 1', 'Location',
'NorthEast' );
% % Label axes
% xlabel x
% ylabel y
% grid on
```

**“fitpolymersmaster.m”**

```
clc, clear, close all;
timestart  = 0.02001;%enter start time here
timeend = 0.05002;%enter end time here
[GFileName,PathName] = uigetfile('*.cbr','Data to be
analyzed','MultiSelect','on');
if ischar(GFileName);
```

```
    VarNumMovs = 1;
    MFileName{1,1} = GFileName;
else VarNumMovs = length(GFileName);
    MFileName = GFileName;
end;
%%
for i=1:VarNumMovs
    %%
    FileName=MFileName{i};
    clf;
    % 40 is the line where we start reading, it skips some
data since the
    % comment field pushes data down depending on the
number of lines
    m = dlmread([PathName,FileName(1:end-
4),'.cbr'],'\t',32);
    % fields in m
    % t [s] D [mm]  D/D0 [-]    epsilon [-] epsilon dot
[1/s]   eta [Pa.s]

    x = m(:,1);
    y = m(:,3);
    rawx{i} = x;
    % rawx{i,2} = FileName;
    rawy{i} = y;
    % rawy{i,2} = FileName;
%    hold on;
%     hFig = figure(1);
%     set(hFig, 'Position', [1 1 1600 800])
%     subplot(2,2,1)
%     semilogy(x,y,'.','MarkerSize',2)
%     title('Original plot');
%     [x_user,~] = ginput(2); % Let the user select two x-
values from which to crop.
%     start = x>min(x_user);
%     stop = x<max(x_user);
%     index = start+stop-1;
%     index = 1 - index;
%     x(index==1) = [];
%     y(index==1) = [];
%     subplot(2,2,2);
%     semilogy(x,y,'.','MarkerSize',2)
%     title('New plot with cropped values');
%     xlim([min(x(:)) max(x(:))]);
%     x = x-x(1);
```

```
%     y = y/y(1);
%
    I_end = find(x == timeend); %0.03501); %this is the
first time data point
    I_start = find(x == timestart); %0.00001); %this is the
last time data point
    x = x(I_start:I_end); %this truncates the data to the
range desired
    y = y(I_start:I_end); %this truncates the data to the
range desired
    [fitresult, gof] = createFit(x,y); %this does the
actual fitting
    k=i;
    resultmatrix=coeffvalues(fitresult);
    a(k)=resultmatrix(1);
    l(k)=resultmatrix(2);
    %a2(k)=resultmatrix(3);
    %l2(k)=resultmatrix(4);
    %beg(k) = min(x_user);
    %fin(k) = max(x_user);

    %ft = a(k)*exp(-x/a2(k))+l(k)*exp(-x/l2(k));
    ft = a(k)*exp(-x/l(k));
    fit(k)=gof.rmse;
    figure(1)
    %subplot(2,2,3)


subplot(1,2,1);semilogy(x,y,'.',x,ft,'MarkerSize',8,'LineWi
dth',3)
    xlabel('Time (s)');
    ylabel('D/Do');
    title(sprintf('name: %s',FileName));

    annotation('textbox',[.5 .2 .1 .1],'String',{...
        %sprintf('a: %g',a(k)),sprintf('a2:
%g',l(k)),sprintf('lamda: %g',a2(k)),sprintf('lamda2:
%g',l2(k)),sprintf('RMSE = %g',...
        %fit(k))},'BackgroundColor',[1 1 1])
        sprintf('a: %g',a(k)),sprintf('lamda:
%g',l(k)),sprintf('RMSE = %g',...
        fit(k))},'BackgroundColor',[1 1 1])
```

```
    subplot(1,2,2);
semilogy(rawx{i}(I_start/2:I_end),rawy{i}(I_start/2:I_end),
x,ft)
    print([PathName,FileName(1:end-4),'.jpg'],'-djpeg');
    %  end
    pause;

end

% %% Write results to XLS spreadsheet
%
% results = cell((k+1),10);
% results(1,1:7) = {'A', 'Lamda', 'Time Start','Time
Stop','RMSE', 'intercept', 'Filename'};
%
% for i=1:k;
%     results(i+1, 1:6) = {a(i), l(i), beg(i), fin(i),
fit(i), n(i)};
%     results(i+1, 6) = {MFileName{i}};
% end
%
% if exist([PathName,'results.xlsx'],'file')==0;
%     xlswrite([PathName,'results.xlsx'],results)
% else
%     k=1;
%     while
exist([PathName,'results',num2str(k),'.xlsx'],'file')==2;
%         k=k+1;
%     end
%
xlswrite([PathName,'results',num2str(k),'.xlsx'],results)
% end
%
%
save([PathName,'results',num2str(k),'.mat'],'rawx','rawy');
```

### *MATLAB: Filament Thinning Image Analysis Code*

This code takes an uncompressed AVI movie of a filament thinning event in a microfluidic device, applies an intensity threshold, and uses edge-finding to calculate the filament width with time at five user-defined locations.

**"video_analysis_030719_1.m"**

```
%Script for analyzing AVI files of filament thinning.
%11-09-18 - Clay Hansen - Dutcher Group - University of MN
- Twin Cities

%%  Data Aquisition
clear
clc

[video,video_path] = uigetfile('*.AVI'); %prompt for file
choice
cd(video_path); %change working directory to that folder
v = VideoReader(video);
w = VideoWriter('edge_output.AVI') %create AVI file to
write to.
%w = VideoWriter('edge_output.AVI', 'Uncompressed AVI') %%
use this to output uncompressed AVI
open(w) %open above AVI file
frame_rate = input('Enter the video framerate in frames per
second: ');
frames_per_second = 1/frame_rate;
%col_spacing = input('Enter the spacing between capture
columns in pixels: ');
%% Data input
vidframe = readFrame(v);

%%  Establish Physical Scale
hFig = figure('Name', 'Click on two locations with a known
distance between them.  Left click first, right click
second.', 'NumberTitle', 'off');

scaleImage = vidframe;
hIm = imshow(scaleImage);
hSP = imscrollpanel(hFig,hIm);
api = iptgetapi(hSP);
api.setMagnification(2);
hMagBox = immagbox(hFig,hIm);
```

```
pos = get(hMagBox,'Position');
set(hMagBox,'Position',[0 0 pos(3) pos(4)])
imoverview(hIm)
%imshow(scaleImage); %display image
title('Left click 1st point, right click 2nd point');
%set(gcf, 'units','normalized','outerposition',[0 0 1 1]);
full scale image
[xi,yi] = getpts;
close

lineLengthInPixels = round(sqrt((xi(1)-xi(2))^2+ (yi(1)-
yi(2))^2))
lineLengthInMicrons = input('Enter the real world distance
between these points in microns: ');
pixelsPerMicron = lineLengthInPixels/lineLengthInMicrons;
micronsPerPixel = lineLengthInMicrons/lineLengthInPixels;

%% Determine region of interest and choose vertical slice
to study.
repeat_region = 1
while repeat_region == 1

hFig = figure('Name', 'Crop the region of interest.  5
evenly spaced vertical columns will be generated in the
region of interest.', 'NumberTitle', 'off');

scaleImage = vidframe;
hIm = imshow(scaleImage);
hSP = imscrollpanel(hFig,hIm);
api = iptgetapi(hSP);
api.setMagnification(1);
hMagBox = immagbox(hFig,hIm);
pos = get(hMagBox,'Position');
set(hMagBox,'Position',[0 0 pos(3) pos(4)])
imoverview(hIm)

[x, rect] = imcrop();
close

top_pixel = round(rect(2));
bottom_pixel = round(rect(2)+ rect(4));
%pixel_column2 = round(rect(1) + rect(3)/2);
column_1 = round(rect(1));
column_2 = round(rect(1)+rect(3)/4);
column_3 = round(rect(1)+rect(3)/2);
```

```
column_4 = round(rect(1)+3* rect(3)/4)
column_5 = round(rect(1)+rect(3));
imshow(scaleImage);
hold on


line([column_1 column_1], [top_pixel bottom_pixel],
'color', 'white')
line([column_2 column_2], [top_pixel bottom_pixel],
'color', 'white')
line([column_3 column_3], [top_pixel bottom_pixel],
'color', 'white')
line([column_4 column_4], [top_pixel bottom_pixel],
'color', 'white')
line([column_5 column_5], [top_pixel bottom_pixel],
'color', 'white')
hold off
answer = questdlg('Are the columns positioned correctly?',
'Column Positioning');
switch answer
    case 'Yes'
        repeat_region =0;
    case 'No'
        repeat_region = 1;
end
end
close
%Pixel_Column = 300;
%I = imread(origImages(1).name);
%I = imcrop(I,rect);
%I = mean(I,3);
%I(:,Pixel_Column2-2:Pixel_Column2+2,1) = 256; %make
selected pixel column black for display (to validate)
%figure(2); imagesc(I); colormap(gray);
%%
v.currenttime = input('Enter start time in seconds: ')
end_time = input ('Enter end time in seconds: ')
duration = end_time - v.currenttime;
num_frames = round(v.framerate*duration);
%% Edgefinding from emulsion stability script(establish
appropriate threshold value for further use)

[vidframeBW,threshold] = edge(vidframe,'Sobel');
repeat = 1;
```

```
while repeat == 1
     imshow(vidframeBW)
    answer = questdlg('Is the edgefinding good enough?',
'Edgefinding');
switch answer
    case 'Yes'
        repeat =0;
    case 'No'
        repeat = 1;
disp('The previous threshold value was: ')
disp(threshold)
threshold = input('Enter a new threshold value: ');
vidframeBW = edge(vidframe,'Sobel',threshold);
close
end
end


vidframeBW = edge(vidframe,'Sobel',threshold);


%% loop structure to read entire video (cannot use parallel
proc. in this manner)
%{
while hasFrame(v)
    vidframe = readFrame(v);
    vidframeBW = edge(vidframe,'Sobel',threshold);


end
%}

%%
%pixel_column = round(xi(1));
% top_pixel = round(rect(2));
% bottom_pixel = round(rect(2)+ rect(4));



%%  sample: read - edgefind - write to video
k = 1;
f = waitbar(k/num_frames, 'Processing...');
for k = 1:num_frames
waitbar(k/num_frames, f);
vidframe = readFrame(v);
```

```
vidframeBW = edge(vidframe,'Sobel',threshold); %perform
edgefinding on frame using established threshhold value
Column_Pixel_Frame1(:,k)= vidframeBW(top_pixel:bottom_pixel
, column_1);
Column_Pixel_Frame2(:,k)= vidframeBW(top_pixel:bottom_pixel
, column_2);
Column_Pixel_Frame3(:,k)= vidframeBW(top_pixel:bottom_pixel
, column_3);
Column_Pixel_Frame4(:,k)= vidframeBW(top_pixel:bottom_pixel
, column_4);
Column_Pixel_Frame5(:,k)= vidframeBW(top_pixel:bottom_pixel
, column_5);


vidframeGray = uint8(255*vidframeBW);%converts vidframeBW
(bin image) to greyscale for writing out to video frame

vidframe(top_pixel:bottom_pixel,column_1) = 255;  %the next
ten lines of code are for adding white columns
vidframe(top_pixel:bottom_pixel,column_2) = 255; %in the
video frames to indicate where measurements are being taken
vidframe(top_pixel:bottom_pixel,column_3) = 255;
vidframe(top_pixel:bottom_pixel,column_4) = 255;
vidframe(top_pixel:bottom_pixel,column_5) = 255;

vidframeGray(top_pixel:bottom_pixel,column_1) = 255;
vidframeGray(top_pixel:bottom_pixel,column_2) = 255;
vidframeGray(top_pixel:bottom_pixel,column_3) = 255;
vidframeGray(top_pixel:bottom_pixel,column_4) = 255;
vidframeGray(top_pixel:bottom_pixel,column_5) = 255;


comboFrame = cat(2,vidframe,vidframeGray); %combine source
video and edge-found video into single frame for writing
out to video
writeVideo(w, comboFrame); %writes to video

end
close(f)
%{
while v.currenttime < 15
    vidframe = readFrame(v); % read next frame from
videoreader object
    vidframeBW = edge(vidframe,'Sobel',threshold); %perform
edgefinding on frame using established threshhold value
```

```
    vidframeGray = uint8(255*vidframeBW); %converts
vidframeBW (bin image) to greyscale for writing out to
video frame
    writeVideo(w, vidframeGray);




    end

    %}

close(w); %close avi file that is being written to.


%% Find width of filament

[height,length] = size(Column_Pixel_Frame1);
thickness_in_pixels = zeros(length,5);

for j = 1:length


    if isempty(find(Column_Pixel_Frame1(:,j), 1))
        white_pixels1 = [0,0];
        thickness_in_pixels(j,1) = 0;
    else
        white_pixels1 = find(Column_Pixel_Frame1(:,j));
        thickness_in_pixels(j,1) = max(white_pixels1)-
min(white_pixels1);
    end

    if isempty(find(Column_Pixel_Frame2(:,j), 1))
        white_pixels2 = [0,0];
        thickness_in_pixels(j,2) = 0;
    else
        white_pixels2 = find(Column_Pixel_Frame2(:,j));
        thickness_in_pixels(j,2) = max(white_pixels2)-
min(white_pixels2);
    end

    if isempty(find(Column_Pixel_Frame3(:,j), 1))
        white_pixels3 = [0,0];
        thickness_in_pixels(j,3) = 0;
    else
```

```
        white_pixels3 = find(Column_Pixel_Frame3(:,j));
        thickness_in_pixels(j,3) = max(white_pixels3)-
min(white_pixels3);
    end

    if isempty(find(Column_Pixel_Frame4(:,j), 1))
        white_pixels4 = [0,0];
        thickness_in_pixels(j,4) = 0;
    else
        white_pixels4 = find(Column_Pixel_Frame4(:,j));
        thickness_in_pixels(j,4) = max(white_pixels4)-
min(white_pixels4);
    end

    if isempty(find(Column_Pixel_Frame5(:,j), 1))
        white_pixels5 = [0,0];
        thickness_in_pixels(j,5) = 0;
    else
        white_pixels5 = find(Column_Pixel_Frame5(:,j));
        thickness_in_pixels(j,5) = max(white_pixels5)-
min(white_pixels5);
    end
   %white_pixels1 = find(Column_Pixel_Frame1(:,j));
   %white_pixels2 = find(Column_Pixel_Frame2(:,j));
   %white_pixels3 = find(Column_Pixel_Frame3(:,j));
   %white_pixels4 = find(Column_Pixel_Frame4(:,j));
   %white_pixels5 = find(Column_Pixel_Frame5(:,j));

    %thickness_in_pixels(j,1) = max(white_pixels1)-
min(white_pixels1);
    %thickness_in_pixels(j,2) = max(white_pixels2)-
min(white_pixels2);
    %thickness_in_pixels(j,3) = max(white_pixels3)-
min(white_pixels3);
    %thickness_in_pixels(j,4) = max(white_pixels4)-
min(white_pixels4);
    %thickness_in_pixels(j,5) = max(white_pixels5)-
min(white_pixels5);
end

%% Format data for export and write to CSV

thickness_in_microns = thickness_in_pixels *
micronsPerPixel; %convert width in pixels to width in
microns
```

```
time_col = [0:frames_per_second:((num_frames-
1)*frames_per_second)]'; %create column for time based on
20000fps (.00005 sec/frame)
data_to_write = horzcat(time_col,thickness_in_microns);
%combine time column with data columns
csv_filename = strrep(video,'avi','csv'); %harvest source
file name and convert to csv filename
csvwrite(csv_filename, data_to_write) %write to csv
%% Notes and snippets for later



%Specify starting time
%v.CurrentTime = xx.xx (seconds from beginning of video)
```

## *MATLAB: Flocculation Image Analysis Code*

This code extracts every frame of a flocculation movie, applies a user-defined intensity threshold, binarizes the frames, and uses the built-in *regionprops* function in MATLAB to calculate the transient floc size (in terms of radius of gyration), floc morphology (in terms of a 2-D perimeter-based fractal dimension), and the number of flocs.

**"Particle_Size_Analysis_1_24_17.m"**

```
%%
clear
[FileName,PathName,FilterIndex] = uigetfile('*','Select The
Movie File(s)');%,'MultiSelect','on');
tic;

mm_Per_Pixel = 28.5/550; %6/61; %6/114; %6/120; %0.078;
graythresh_min = 0.7;

RecordMovie = 0 %0 is no and 1 is yes
FrameSkip = 1
%endFrame = floor(30*60*5/FrameSkip);
%floor(numFrames/FrameSkip);
average_num_amount = 10*30 %how many frames to average
together for final plot
Break_Data_Number1 = 200; %how many breaks in frame groups
to make
Break_Data_Number2 = 3;

movinfo = VideoReader(FileName);
numFrames = movinfo.NumberOfFrames
framerate = movinfo.FrameRate;
movinfo = VideoReader(FileName);
toAverageFrame = mean(read(movinfo,[1,500]),4);
AverageFrame = mean(toAverageFrame,3);
figure(1)
DispFrame = read(movinfo,50);
DispFrame = max(read(movinfo,[50,100]),[],4);
[I2, rect] = imcrop(DispFrame);


Frame_Breaks_temp =
round(linspace(1,(numFrames),Break_Data_Number1));
Frame_Breaks_temp2 =
round(linspace(1,Frame_Breaks_temp(2),Break_Data_Number2));
```

```
Frame_Breaks = [Frame_Breaks_temp2,
Frame_Breaks_temp(3:end)];

movinfo = VideoReader(FileName);
aa=0;

particleMeans = matfile(strjoin({FileName(1:end-
4),'_ParticelMeansPerFrame.mat'},''),'Writable',true);
particleMeans.RgAllPerFrame = zeros(2000,1);
particleMeans.AreaAllPerFrame = zeros(2000,1);
particleMeans.PerimeterAllPerFrame = zeros(2000,1);

 H1 = figure(1);
 H2 = figure(2);
 H3 = figure(3);
 if RecordMovie == 1
    Bianary_movie =
matfile('BinaryMovie.mat','Writable',true);
    Gray_movie = matfile('GrayMovie.mat','Writable',true);
    %Bianary_movie.Frame = zeros(rect(2)-rect(1), rect(4)-
rect(3));
 end
%tic;
%%
for mm = 1:length(Frame_Breaks)-1
    parfor_progress(-Frame_Breaks(mm) +
Frame_Breaks(mm+1));
    gThresh = zeros(1,-Frame_Breaks(mm) +
Frame_Breaks(mm+1));
    particleMeansCirc = zeros(-Frame_Breaks(mm) +
Frame_Breaks(mm+1),1);
    particleMeansRgNUM = zeros(-Frame_Breaks(mm) +
Frame_Breaks(mm+1),1);
    particleMeansNumParticles = zeros(-Frame_Breaks(mm) +
Frame_Breaks(mm+1),1);
    start_index = Frame_Breaks(mm)-1;
    RgHolder={0};
    AreaHolder={0};
    PerimeterHolder = {0};

    parfor ii = Frame_Breaks(mm) : Frame_Breaks(mm+1)

        thisFrame = read(movinfo,ii*FrameSkip);
        thisFrame_Raw = thisFrame;
        thisFrame = mean(thisFrame,3) - AverageFrame;
```

```
        belowZeroValues = find(thisFrame<0);
        thisFrame(belowZeroValues) = 0;
        thisFrame = imcrop(thisFrame,rect);
        thisFrameGray = mat2gray(thisFrame,[0 255]);



        gThresh(ii-start_index) =
graythresh(thisFrameGray);
          if gThresh(ii-start_index) < graythresh_min
              gThresh(ii-start_index) = graythresh_min;
          end
        Bianary_Frame = im2bw(thisFrameGray,gThresh(ii-
start_index));
        if RecordMovie == 1
            %Gray_movie.Frame(:,:,ii) = thisFrameGray;
            %Bianary_movie.Frame(:,:,ii) = Bianary_Frame;
            %only works for non parfor
        end
        if mod(ii,50) == 0;
            figure(5); subplot(1,3,1);
imagesc(Bianary_Frame);
            subplot(1,3,2); imagesc(thisFrame); colorbar
            subplot(1,3,3); imagesc(thisFrame_Raw);
        end

        StructureHolder =
regionprops(Bianary_Frame,'Perimeter','Area','EquivDiameter
','PixelList','Centroid','MajorAxisLength','MinorAxisLength
');
        for jj = 1:length(StructureHolder)
            StructureHolder(jj).Circularity =
StructureHolder(jj).EquivDiameter/StructureHolder(jj).Perim
eter;
            StructureHolder(jj).RgSquared =
1/StructureHolder(jj).Area*(sum((StructureHolder(jj).PixelL
ist(:,1) -
StructureHolder(jj).Centroid(:,1)).^2+(StructureHolder(jj).
PixelList(:,2) - StructureHolder(jj).Centroid(:,2)).^2));


        end
        particleInfo{ii-start_index} =  StructureHolder;
        if isfield(StructureHolder,'Circularity') == 1
```

```
            Circularity  =
cat(1,StructureHolder.Circularity);
            Circularity(find(Circularity==Inf)) = [];
            RgSquared = cat(1,StructureHolder.RgSquared);
            RgSquared(find(RgSquared==0)) = [];
            particleMeansCirc(ii-start_index) =
mean(Circularity);
            particleMeansRgNUM(ii-start_index) =
sqrt(mean(RgSquared));
            particleMeansRgAREA(ii-start_index) =
sum(sqrt(RgSquared).^3)/sum(sqrt(RgSquared).^2);
            particleMeansNumParticles(ii-start_index) =
length(RgSquared);
            RgHolder{ii-start_index} = sqrt(RgSquared);
            PerimeterHolder{ii-start_index} =
cat(1,StructureHolder.Perimeter);
            AreaHolder_temp = cat(1,StructureHolder.Area);
            AreaHolder{ii-start_index} =
AreaHolder_temp(AreaHolder_temp>1);
        else
            particleMeansRgNUM(ii-start_index) = 0;
            particleMeansRgAREA(ii-start_index)= 0;
            particleMeansNumParticles(ii-start_index) = 0;
            particleMeansCirc(ii-start_index) = 0;
            RgHolder{ii-start_index} = 0;
            PerimeterHolder{ii-start_index} = 0;
            AreaHolder{ii-start_index} = 0;


        end
        %progressbar(ii/numFrames)
        parfor_progress;
    end
    parfor_progress(0);
    fprintf('Parfor loop finished\n')

    RgHolderMat = [];
    AreaHolderMat = [];
    PerimeterHolderMat =[];
    for bb= 1:length(RgHolder)
        if isempty(RgHolder{bb})==0
            [i1,j1] =
ndgrid(1:size(RgHolderMat,1),1:size(RgHolderMat,2));
```

```
            [i2,j2] =
ndgrid(1:size(RgHolder{bb},1),(1:size(RgHolder{bb},2))+size
(RgHolderMat,2));
            RgHolderMat =
accumarray([i1(:),j1(:);i2(:),j2(:)],[RgHolderMat(:);RgHold
er{bb}(:)]);
        else
            A = [0;0];
            [i1,j1] =
ndgrid(1:size(RgHolderMat,1),1:size(RgHolderMat,2));
            [i2,j2] =
ndgrid(1:size(A,1),(1:size(A,2))+size(RgHolderMat,2));
            RgHolderMat =
accumarray([i1(:),j1(:);i2(:),j2(:)],[RgHolderMat(:);A(:)])
;
        end
    end
    fprintf('test1')
    for bb= 1:length(AreaHolder)
        if isempty(AreaHolder{bb})==0
        [i1,j1] =
ndgrid(1:size(AreaHolderMat,1),1:size(AreaHolderMat,2));
        [i2,j2] =
ndgrid(1:size(AreaHolder{bb},1),(1:size(AreaHolder{bb},2))+
size(AreaHolderMat,2));
        AreaHolderMat =
accumarray([i1(:),j1(:);i2(:),j2(:)],[AreaHolderMat(:);Area
Holder{bb}(:)]);
        else
            A = [0;0];
            [i1,j1] =
ndgrid(1:size(AreaHolderMat,1),1:size(AreaHolderMat,2));
            [i2,j2] =
ndgrid(1:size(A,1),(1:size(A,2))+size(AreaHolderMat,2));
            AreaHolderMat =
accumarray([i1(:),j1(:);i2(:),j2(:)],[AreaHolderMat(:);A(:)
]);
        end
    end
    fprintf('test2')

    for bb= 1:length(PerimeterHolder)
        if isempty(PerimeterHolder{bb})==0
```

```
        [i1,j1] =
ndgrid(1:size(PerimeterHolderMat,1),1:size(PerimeterHolderM
at,2));
        [i2,j2] =
ndgrid(1:size(PerimeterHolder{bb},1),(1:size(PerimeterHolde
r{bb},2))+size(PerimeterHolderMat,2));
        PerimeterHolderMat =
accumarray([i1(:),j1(:);i2(:),j2(:)],[PerimeterHolderMat(:)
;PerimeterHolder{bb}(:)]);
        else
            A = [0;0];
            [i1,j1] =
ndgrid(1:size(PerimeterHolderMat,1),1:size(PerimeterHolderM
at,2));
            [i2,j2] =
ndgrid(1:size(A,1),(1:size(A,2))+size(PerimeterHolderMat,2)
);
            PerimeterHolderMat =
accumarray([i1(:),j1(:);i2(:),j2(:)],[PerimeterHolderMat(:)
;A(:)]);
        end
    end


particleMeans.RgNUM(Frame_Breaks(mm):Frame_Breaks(mm+1),1)
= particleMeansRgNUM;

particleMeans.RgAREA(1,Frame_Breaks(mm):Frame_Breaks(mm+1))
= particleMeansRgAREA;

particleMeans.Circ(Frame_Breaks(mm):Frame_Breaks(mm+1),1) =
particleMeansCirc;

particleMeans.gThresh(1,Frame_Breaks(mm):Frame_Breaks(mm+1)
) = gThresh;

particleMeans.NumParticles(Frame_Breaks(mm):Frame_Breaks(mm
+1),1) = particleMeansNumParticles;
    fprintf('test3')

%     if mm ==1
%         particleMeans.RgAllPerFrame = RgHolderMat;
%         particleMeans.AreaAllPerFrame = AreaHolderMat;
%     else
```

```
%         [i1,j1] =
ndgrid(1:size(particleMeans.RgAllPerFrame,1),1:size(particl
eMeans.RgAllPerFrame,2));
%         [i2,j2] =
ndgrid(1:size(RgHolderMat,1),(1:size(RgHolderMat,2))+size(p
articleMeans.RgAllPerFrame,2));
%         particleMeans.RgAllPerFrame =
accumarray([i1(:),j1(:);i2(:),j2(:)],[reshape(particleMeans
.RgAllPerFrame,numel(particleMeans.RgAllPerFrame),1);RgHold
erMat(:)]);
%         fprintf('test4')
%         [i1,j1] =
ndgrid(1:size(particleMeans.AreaAllPerFrame,1),1:size(parti
cleMeans.AreaAllPerFrame,2));
%         [i2,j2] =
ndgrid(1:size(AreaHolderMat,1),(1:size(AreaHolderMat,2))+si
ze(particleMeans.AreaAllPerFrame,2));
%         particleMeans.AreaAllPerFrame =
accumarray([i1(:),j1(:);i2(:),j2(:)],[reshape(particleMeans
.AreaAllPerFrame,numel(particleMeans.AreaAllPerFrame),1);Ar
eaHolderMat(:)]);
%     end
    [rowsRg, columnsRg] = size(RgHolderMat);

particleMeans.RgAllPerFrame(1:rowsRg,Frame_Breaks(mm):Frame
_Breaks(mm+1)) = RgHolderMat;
    fprintf('test4')
    [rowsArea, columnsArea] = size(AreaHolderMat);

particleMeans.AreaAllPerFrame(1:rowsArea,Frame_Breaks(mm):F
rame_Breaks(mm+1)) = AreaHolderMat;
    [rowsPerimeter, columnsPerimeter] =
size(PerimeterHolderMat);

particleMeans.PerimeterAllPerFrame(1:rowsPerimeter,Frame_Br
eaks(mm):Frame_Breaks(mm+1)) = PerimeterHolderMat;

    fprintf('test5')

    figure(1); plot(particleMeans.gThresh,'.')
    figure(2); subplot(2,1,1); plot(particleMeans.Circ);
title('Circularity vs Frame')
    subplot(2,1,2); plot(particleMeans.RgAREA,'.');
title('Rg vs Frame')
```

```
    %fprintf('Saving\n')
    %save(strjoin({FileName(1:end-
4),'_subdata_for_frames_', num2str(Frame_Breaks(mm)),
'_to_', num2str(Frame_Breaks(mm+1)), '.mat'},''),'-
v7.3','gThresh','particleMeansCirc','particleMeansRg','star
t_index') %'particleInfo',
    %fprintf('Done Saving. Now Frame Averaging\n')



%     particleMeansNumParticles =
zeros(length(particleInfo),1);
%
%     for ii = 1:length(particleInfo)
%         particleMeansNumParticles(ii) =
length(cat(1,particleInfo{ii}.Area));
%     end
%
%
particleMeans.NumParticles(Frame_Breaks(mm):Frame_Breaks(mm
+1),1) = particleMeansNumParticles;
%
%     for ii =
average_num_amount:average_num_amount:length(particleMeansR
g)
%         aa=aa+1;
%         this_particleMeansRg = particleMeansRg(ii-
average_num_amount+1:ii);
%
this_particleMeansRg(find(this_particleMeansRg==0)) = [];
%
this_particleMeansRg(find(isnan(this_particleMeansRg)==1))
= [];
%         particleMeansRg_multiFrameAvg(aa) =
mean(this_particleMeansRg);
%         this_particleMeansCirc = particleMeansCirc(ii-
average_num_amount+1:ii);
%
this_particleMeansCirc(find(this_particleMeansCirc==0)) =
[];
%
this_particleMeansCirc(find(isnan(this_particleMeansCirc)==
1)) = [];
```

```
%         particleMeansCirc_multiFrameAvg(aa) =
mean(this_particleMeansCirc);
%         this_particleMeansNumParticles =
particleMeansNumParticles(ii-average_num_amount+1:ii);
%         particleMeansNumParticles_multiFrameAvg(aa) =
sum(this_particleMeansNumParticles);
%
%     end
%
%     figure(3); subplot(3,1,1);
plot(particleMeansCirc_multiFrameAvg);
title(strjoin({'Circularity
vs',num2str(average_num_amount),' Frame Average'},''))
%     subplot(3,1,2); plot(particleMeansRg_multiFrameAvg);
title(strjoin({'Rg vs ',num2str(average_num_amount),' Frame
Average'},''))
%     subplot(3,1,3);
semilogy(particleMeansNumParticles_multiFrameAvg);
title(strjoin({'Number of Particles vs
',num2str(average_num_amount),' Frame Average'},''))



    clear particleInfo particleMeansNumParticles
particleMeansRgNUM particleMeansRgAREA particleMeansCirc
gThresh RgHolder particleMeansRgAREA AreaHolder
MajorAxisHolder
    save(strjoin({FileName(1:end-
4),'_workspace.mat'},''),'-v7.3')
    clc
    toc
    fprintf('Finished Frame group %d of %d\n',mm,
length(Frame_Breaks)-1)
end

fprintf('Saving Workspace')
save(strjoin({FileName(1:end-4),'_workspace.mat'},''),'-
v7.3')
savefig(H1,'gThresh plot.fig')
savefig(H2,'Rg and Circ per Frame.fig')
savefig(H3,'Frame Averaged Data.fig')
toc
fprintf('\ntotal elapsed time is %d hours',toc/3600)
```

```
%%
clear particleMeansRg_multiFrameAvg
particleMeansCirc_multiFrameAvg jj
particleMeansNumParticles_multiFrameAvg
particleMeansMajorAxis_multiFrameAvg;
clear xData yData thisFitX thisFitY this_particleMeansArea
this_particleMeansPerimeter ft opts fitresult gof
resultmatrix D_sf D_sfRsquared
clear ConfidenceErrorMatrix resultsConfidenceMatrix
%average_num_amount = 1*30;
%particleMeansNumParticles = zeros(length(particleInfo));
% for ii = 1:length(particleInfo)
%     particleMeansNumParticles(ii) =
length(cat(1,particleInfo{ii}.Area));
% end

jj=0;

for ii =
average_num_amount:average_num_amount:length(particleMeans.
RgAllPerFrame)
    jj=jj+1;
    this_particleMeansRg =
particleMeans.RgAllPerFrame(:,ii-average_num_amount+1:ii);
    %this_particleMeansRg(find(this_particleMeansRg==0)) =
[];

%this_particleMeansRg(find(isnan(this_particleMeansRg)==1))
= [];
    this_particleMeansRg =
this_particleMeansRg(this_particleMeansRg>0);
    particleMeansRg_multiFrameAvg(jj) =
sum(this_particleMeansRg.^3)/sum(this_particleMeansRg.^2);

    this_particlePerimeter =
particleMeans.PerimeterAllPerFrame(:,ii-
average_num_amount+1:ii);
    this_particlePerimeter =
this_particlePerimeter(this_particlePerimeter>0);
    this_particleArea = particleMeans.AreaAllPerFrame(:,ii-
average_num_amount+1:ii);
    this_particleArea =
this_particleArea(this_particleArea>0);
```

```
    thisFitX = log(this_particlePerimeter);
    thisFitY = log(this_particleArea);
    if length(thisFitX)>2
    [xData, yData] = prepareCurveData( thisFitX, thisFitY);
    % Set up fittype and options.
    ft = fittype( '2/Df*x+c', 'independent', 'x',
'dependent', 'y' );
    opts = fitoptions( 'Method', 'NonlinearLeastSquares' );
    opts.Display = 'Off';
    opts.Lower = [1 -Inf];
    opts.StartPoint = [1.5 -1];
    opts.Upper = [2 Inf];
    [fitresult, gof] = fit( xData, yData, ft, opts );
    resultmatrix=coeffvalues(fitresult);
    resultsConfidenceMatrix(1:2,1:2,jj) =
confint(fitresult);
    ConfidenceErrorMatrix(jj) = resultmatrix(1) -
resultsConfidenceMatrix(1,1,jj);
    D_sf(jj) = resultmatrix(1);
    D_sfRsquared(jj) = gof.rsquare;
    end

%    particleMeansMajorAxis_multiFrameAvg(jj) =
sum(this_particleMeansMajorAxis.^3)/sum(this_particleMeansM
ajorAxis.^2);

    this_particleMeansCirc = particleMeans.Circ(ii-
average_num_amount+1:ii,1);
    this_particleMeansCirc(find(this_particleMeansCirc==0))
= [];

this_particleMeansCirc(find(isnan(this_particleMeansCirc)==
1)) = [];
    particleMeansCirc_multiFrameAvg(jj) =
mean(this_particleMeansCirc);
    %this_particleMeansNumParticles =
particleMeans.NumParticles(ii-average_num_amount+1:ii,1);
    particleMeansNumParticles_multiFrameAvg(jj) =
numel(this_particleMeansRg(this_particleMeansRg>0));
    clc
    fprintf('Completed Process Loop %d of
%d\n',jj,round(length(particleMeans.RgAREA)/average_num_amo
unt,0))
end
```

```
figure(3); hold off;subplot(3,1,1); hold off;
plot((1:length(particleMeansCirc_multiFrameAvg))*average_nu
m_amount/30,particleMeansCirc_multiFrameAvg);
title(strjoin({'Circularity vs
',num2str(average_num_amount),' Frame Average'},''))
hold on; xlabel('time (s)'); ylabel('Circularity')
subplot(3,1,2); hold off;
semilogy((1:length(particleMeansRg_multiFrameAvg))*average_
num_amount/30,particleMeansRg_multiFrameAvg*mm_Per_Pixel);
title(strjoin({'Rg vs ',num2str(average_num_amount),' Frame
Average'},''))
hold on; xlabel('time (s)'); ylabel('Rg (mm)')
subplot(3,1,3);  hold off;
semilogy((1:length(particleMeansNumParticles_multiFrameAvg)
)*average_num_amount/30,particleMeansNumParticles_multiFram
eAvg); title(strjoin({'Number of Particles vs
',num2str(average_num_amount),' Frame Average'},''))
hold on; xlabel('time (s)'); ylabel('Number of Particles')
savefig(H3,'Frame Averaged Data.fig')

H6 = figure(6);
subplot(2,1,1);
errorbar((1:length(D_sf))*average_num_amount/30,D_sf,Confid
enceErrorMatrix,'o'); title(strjoin({'D_s_f vs
',num2str(average_num_amount),' Frame Average'},''))
xlabel('time (s)'); ylabel('D_s_f'); ylim([1 2])
subplot(2,1,2);
plot((1:length(D_sfRsquared))*average_num_amount/30,D_sfRsq
uared); title(strjoin({'R^2 of D_s_f vs
',num2str(average_num_amount),' Frame Average'},''))
xlabel('time (s)'); ylabel('R^2 of D_s_f'); ylim([0.5 1])
savefig(H6,'Fractal Dimension over Time.fig')

fprintf('Saving Workspace')
save(strjoin({FileName(1:end-4),'_workspace.mat'},''),'-
v7.3')
toc
fprintf('\ntotal elapsed time is %d hours',toc/3600)
%%
aa = 0;
H5 = figure(5);
hold off
for ii = [3,5,8,10]
    aa = aa+1;
```

```
    C =
particleMeans.RgAllPerFrame(:,ii*30*60:ii*30*60+900);
    edges =
logspace(log10(min(min(C(C>0)))/2),log10(max(max(C(C>0)))*2
),100);
    [NRg, EDGESRg] = histcounts(C(C>0),edges);
    f_i = NRg.*EDGESRg(2:end)/sum(NRg.*EDGESRg(2:end));
    f_is =
f_i.*EDGESRg(2:end)*sum(NRg.*EDGESRg(2:end))/sum(NRg.*EDGES
Rg(2:end).^2);
    times(aa) = ii;
    f_isStore{aa} = f_is;
    EDGESRgStore{aa} = EDGESRg*mm_Per_Pixel;

semilogx(EDGESRg(2:end)*mm_Per_Pixel,f_is,'LineWidth',2.5)
    hold on

end
legend(strjoin({'30s average at t = ',num2str(times(1)),'
minutes'},''),strjoin({'30s average at t =
',num2str(times(2)),' minutes'},''),strjoin({'30s average
at t = ',num2str(times(3)),' minutes'},''),strjoin({'30s
average at t = ',num2str(times(4)),'
minutes'},''),'Location','NorthWest')
xlabel('Rg (mm)');ylabel('Fractional Frequency')
hold off
savefig(H5,'Area Averaged Diameter Distibutions over
time.fig')
fprintf('Saving Workspace')
save(strjoin({FileName(1:end-4),'_workspace.mat'},''),'-
v7.3')
fprintf('Saving Workspace Complete\n')




%%
if RecordMovie ==1
    v = VideoWriter('BianaryMovie.avi','Uncompressed AVI');
    open(v)

    for ii = 1:length(Bianary_movie)
        Frame = [Gray_movie{ii}
ones(size(Gray_movie{ii},1),4)
mat2gray(Bianary_movie{ii})];
```

```
        writeVideo(v,Frame);
        progressbar(ii/length(Bianary_movie))
    end

    close(v)
end
%%
DataOutToOrigin(:,1) =
[(1:length(particleMeansRg_multiFrameAvg))*average_num_amou
nt/30]';
DataOutToOrigin(:,2) = D_sf';
DataOutToOrigin(:,3) = ConfidenceErrorMatrix';
DataOutToOrigin(:,4) =
particleMeansRg_multiFrameAvg*mm_Per_Pixel';
DataOutToOrigin(:,5) =
particleMeansNumParticles_multiFrameAvg';
DataOutToOrigin_Labels = {'Time','Dsf','Dsf
Error','Rg','NumFlocs'};
% for ii = 1: length(Bianary_movie)
% figure(4); subplot(1,2,2); imshow(Bianary_movie{ii})
% subplot(1,2,1); imshow(Gray_movie{ii})
% pause(.005)
% end
```

**“parfor_progress.m”**

```
function percent = parfor_progress(N)
%PARFOR_PROGRESS Progress monitor (progress bar) that works
with parfor.
%   PARFOR_PROGRESS works by creating a file called
parfor_progress.txt in
%   your working directory, and then keeping track of the
parfor loop's
%   progress within that file. This workaround is necessary
because parfor
%   workers cannot communicate with one another so there is
no simple way
%   to know which iterations have finished and which
haven't.
%
%   PARFOR_PROGRESS(N) initializes the progress monitor for
a set of N
%   upcoming calculations.
%
```

```
%   PARFOR_PROGRESS updates the progress inside your parfor
loop and
%   displays an updated progress bar.
%
%   PARFOR_PROGRESS(0) deletes parfor_progress.txt and
finalizes progress
%   bar.
%
%   To suppress output from any of these functions, just
ask for a return
%   variable from the function calls, like PERCENT =
PARFOR_PROGRESS which
%   returns the percentage of completion.
%
%   Example:
%
%      N = 100;
%      parfor_progress(N);
%      parfor i=1:N
%         pause(rand); % Replace with real code
%         parfor_progress;
%      end
%      parfor_progress(0);
%
%   See also PARFOR.

% By Jeremy Scheff - jdscheff@gmail.com -
http://www.jeremyscheff.com/

error(nargchk(0, 1, nargin, 'struct'));

if nargin < 1
    N = -1;
end

percent = 0;
w = 50; % Width of progress bar

if N > 0
    f = fopen('parfor_progress.txt', 'w');
    if f<0
        error('Do you have write permissions for %s?',
pwd);
    end
```

```
    fprintf(f, '%d\n', N); % Save N at the top of
progress.txt
    fclose(f);

    if nargout == 0
        disp(['  0%[>', repmat(' ', 1, w), ']']);
    end
elseif N == 0
    delete('parfor_progress.txt');
    percent = 100;

    if nargout == 0
        disp([repmat(char(8), 1, (w+9)), char(10), '100%[',
repmat('=', 1, w+1), ']']);
    end
else
    if ~exist('parfor_progress.txt', 'file')
        error('parfor_progress.txt not found. Run
PARFOR_PROGRESS(N) before PARFOR_PROGRESS to initialize
parfor_progress.txt.');
    end

    f = fopen('parfor_progress.txt', 'a');
    fprintf(f, '1\n');
    fclose(f);

    f = fopen('parfor_progress.txt', 'r');
    progress = fscanf(f, '%d');
    fclose(f);
    percent = (length(progress)-1)/progress(1)*100;

    if nargout == 0
        perc = sprintf('%3.0f%%', percent); % 4 characters
wide, percentage
        disp([repmat(char(8), 1, (w+9)), char(10), perc,
'[', repmat('=', 1, round(percent*w/100)), '>', repmat(' ',
1, w - round(percent*w/100)), ']']);
    end
end
```

# Appendix C

# CaBER Operation

1. You will need: gloves, a syringe (1 mL is perfectly adequate), a needle, and your sample. The small box on the right contains metal plates of various diameters you can use for your experiment.

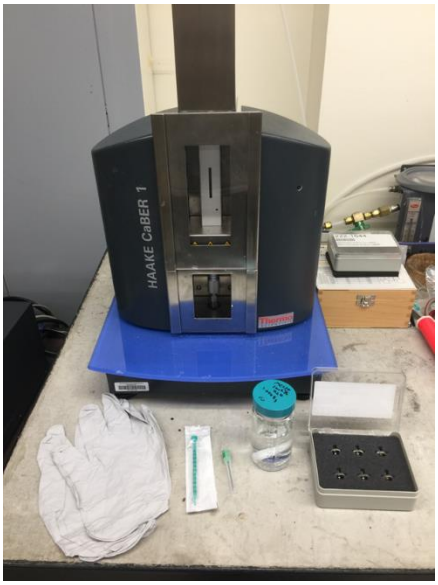


2. Turn on the laser power supply to allow it to warm up while setting up for your experiment.

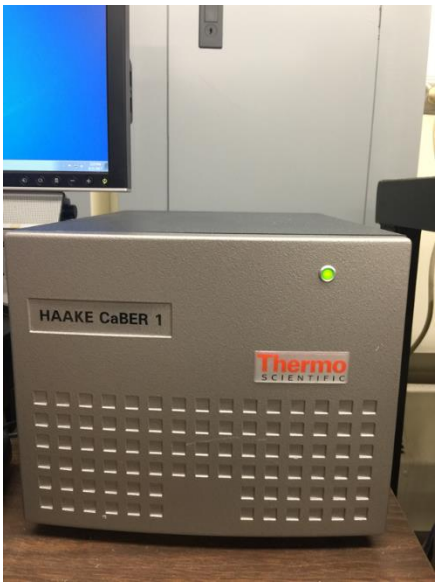


3. Slide the metal barrier up from where the metal plate holders are located. This is also where you will deposit your sample and where the laser is housed.

4. Select a set of plates (diameters include: 4 mm, 6 mm, and 8 mm) and screw into the top plate holder. Repeat for the bottom plate holder.

5. The lower portion of the CaBER houses the micrometer screw. This adjusts the position of the bottom plate to determine the final strike height of your experiment. A full turn on the micrometer screw (0.5 mm) roughly corresponds to a 1 mm change in the final strike height.

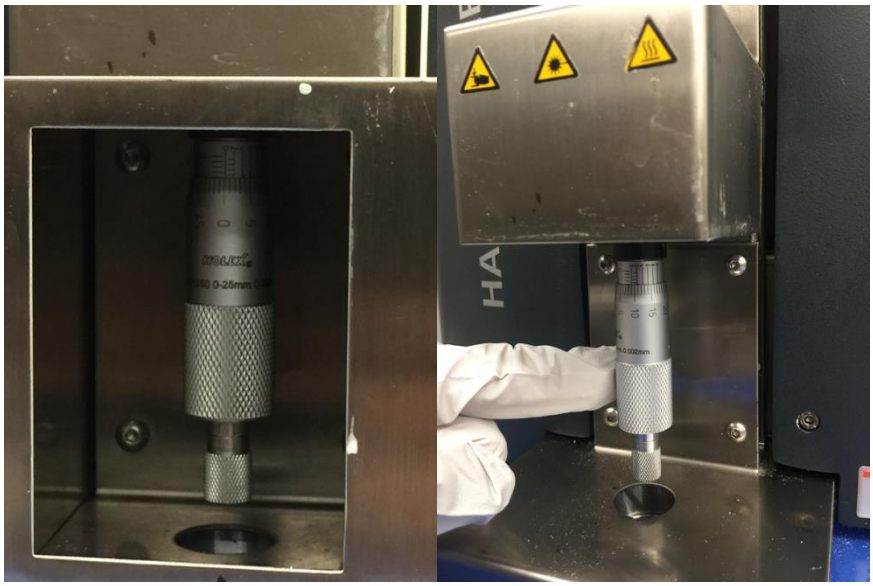

6. Once you have adjusted the micrometer, open the CaBER Control software. Mouse over the **Configuration** tab and select **Define Geometry**. Here you can adjust the initial gap between the two plates and the plate diameter. Typically, the initial gap is set such that the aspect ratio of the initial gap to the plate diameter is between 0.5 and 1.

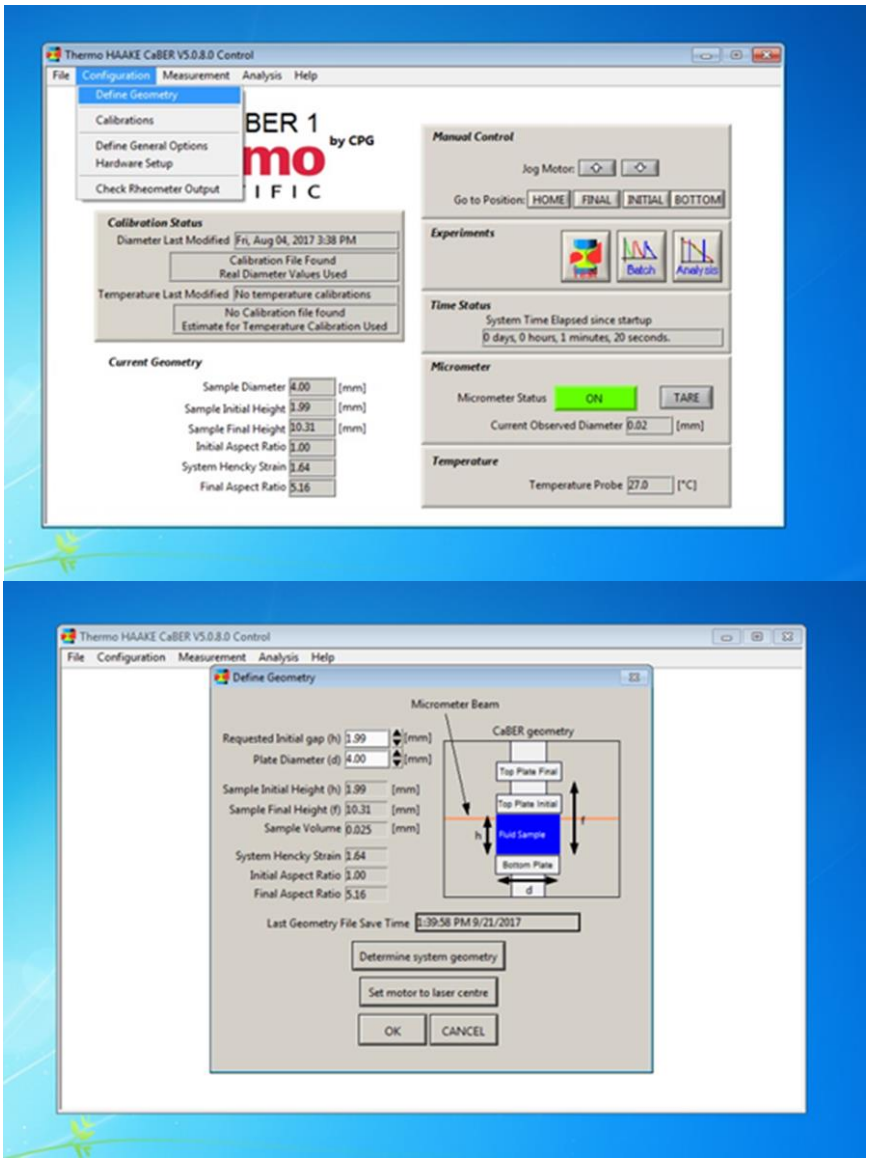


7. Click on **Determine system geometry**. The instrument will then proceed to calculate the final height between the two plates after the initial separation as shown by the red arrow in the image on the right. Click **Set motor to laser centre** and then click **OK** when finished.

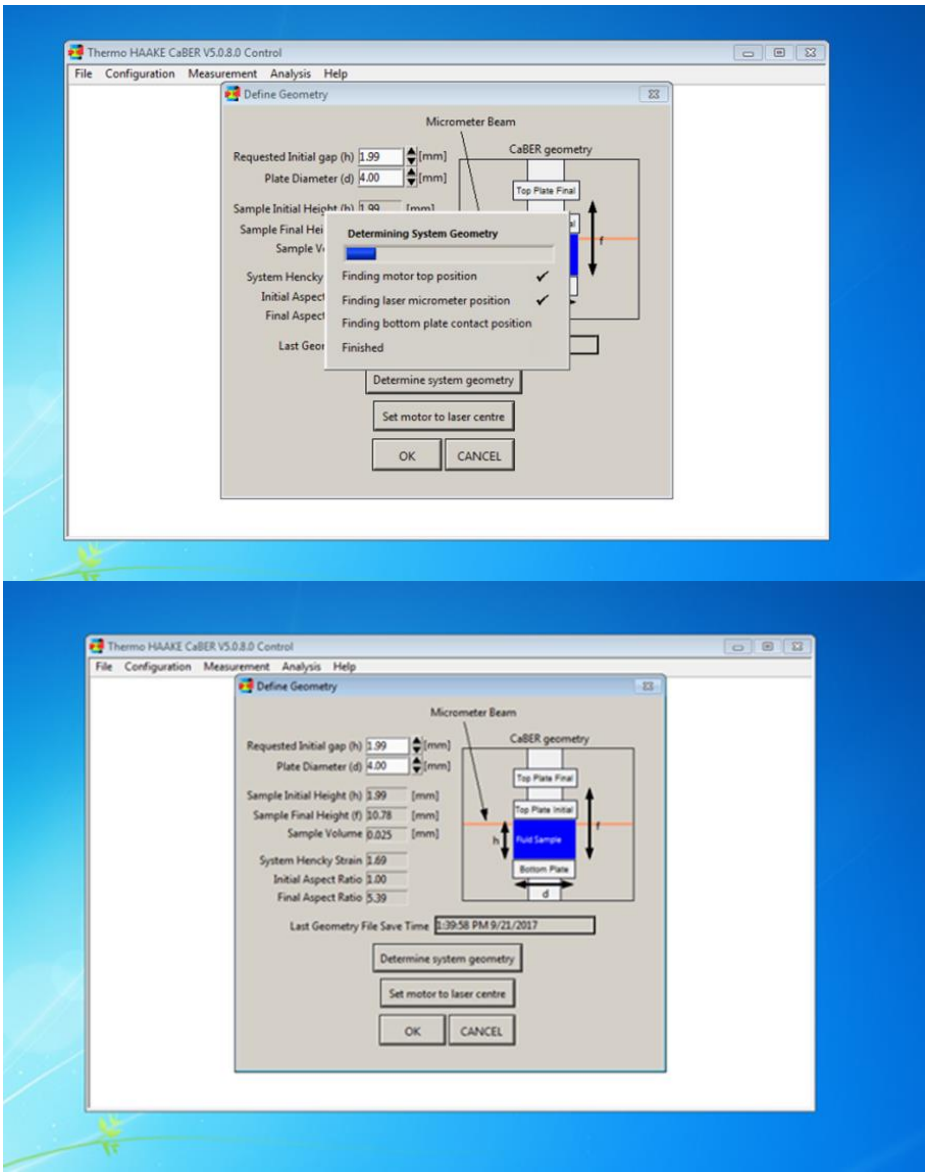


8. Click on **Measurement** and mouse over to **Define Stretch Profile**. Here, you can indicate the stretch profile you would like for you sample (Linear, Exponential, and "Cushioned Strike") in addition to the strike time for your sample. The strike time (step strain deformation rate) needs to be fast enough to finish stretching the fluid before capillary forces cause it to breakup. Generally speaking, a faster strike time needs to be used for lower viscosity materials. The stretch profile can also be changed from a simple linear motion to an exponentially accelerating motion ("Exponential") or exponential deceleration ("Cushioned Strike") to reduce any problems caused by fast deceleration. These parameters will need to be adjusted for each sample. Click **OK** when finished.

*Note: The strike time DOES NOT influence strain rate since the extensional flow measured depends only upon sample properties (this is unlike conventional rotational geometry).

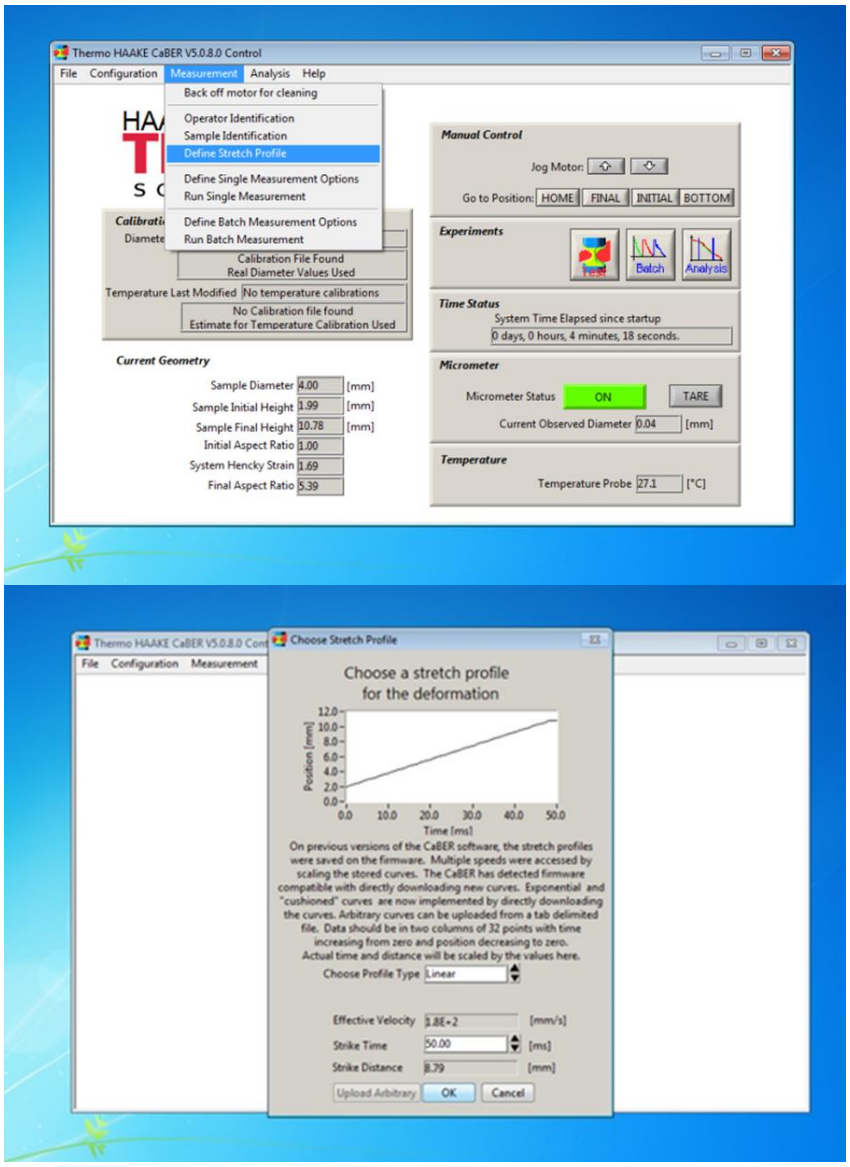


9. In the **Measurement** tab, click on **Define Single Measurement Options**. In Sampling Mode, you can either choose: Real-Time Measurement, which will continuously measure your sample until the fluid filament breaks, or High-Speed Measurement, where you have to set the sample rate and sample duration for your experiment. It is recommended to run a Real-Time experiment first to get an idea for the sample duration, then run High-Speed experiments since they offer better resolution. The equilibration time refers to how long the sample rests between the plates before applying the step strain. Typically, the more viscous the fluid, the

longer it needs to rest (usually at least 3 times its relaxation if previously known). When done, click **OK**. Next, click on the **Test** icon.

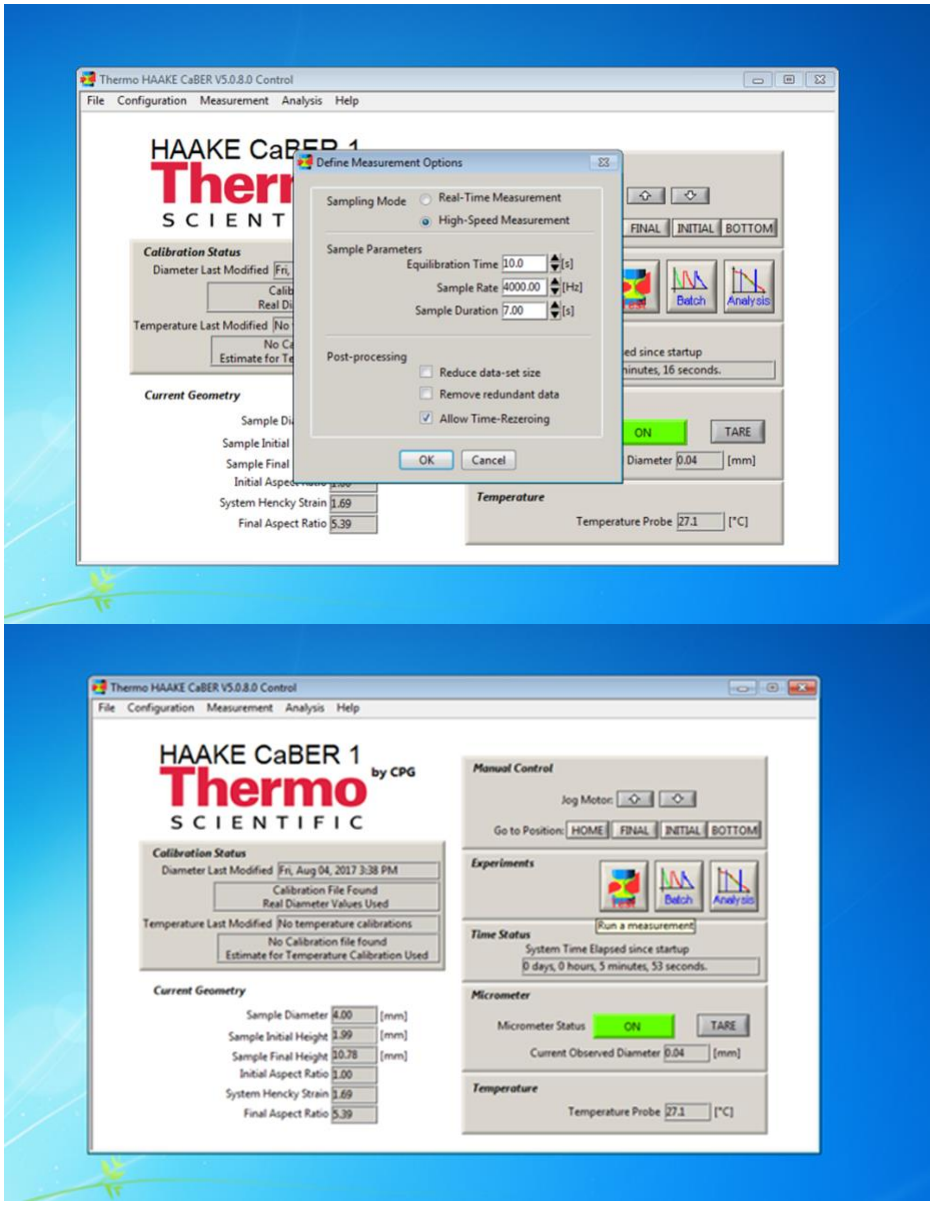


10. Upon clicking the **Test** icon, the **Identification** window will appear. The **Operator** tab is where you can input your name or initials, your affiliation, the directory you would like to save the data, and any other comments you would like to write. The **Sample** tab is where you can input sample information. The surface tension and density are only needed if you choose to analyze your data in the CaBER software. It is highly recommended to use an alternate data work-up method as the software is glitchy and tends to eliminate data points. The **Notes** tab is where you can input any additional information you would like.

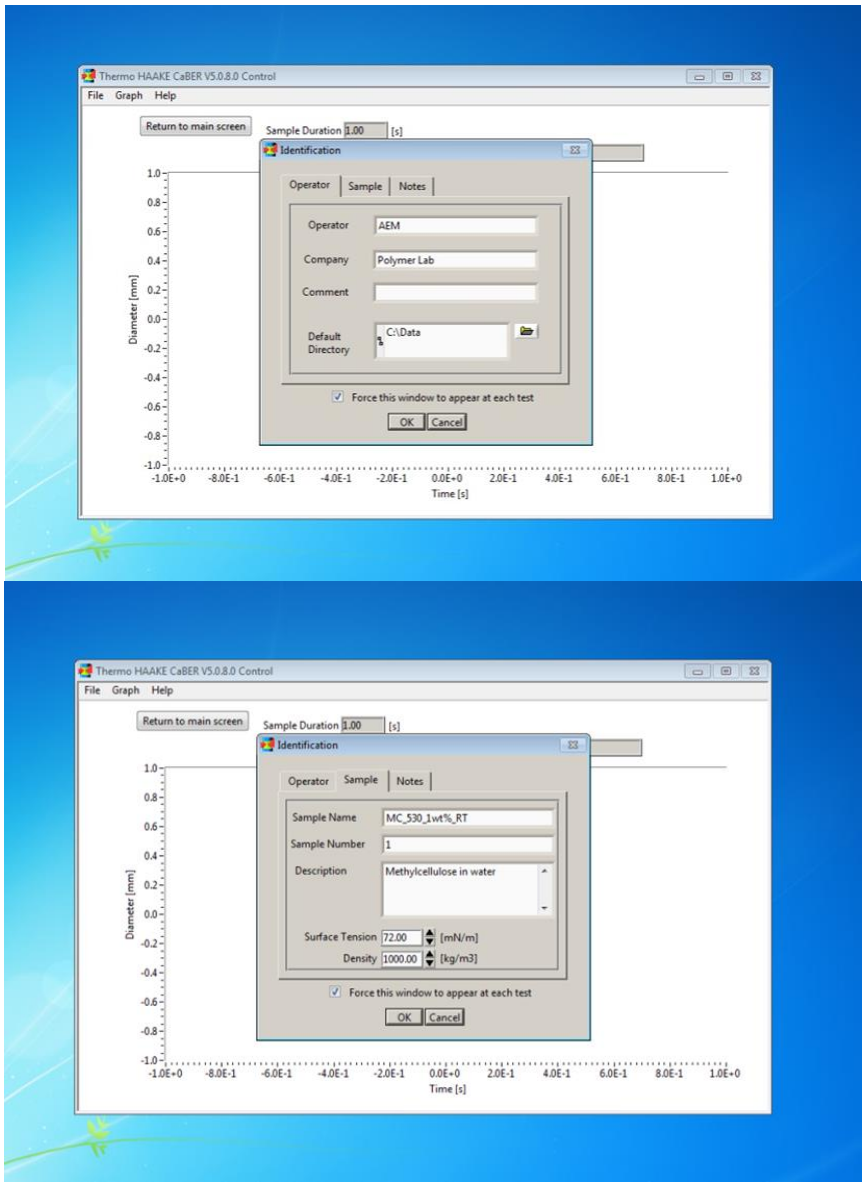


11. Once you click **OK** on the **Identification** tab, this window will appear, and you will see and hear the plates moving to their initial position for sample loading. DO NOT click **OK** until the sample is properly loaded. You can use arrows to jog the motor up and down for ease of loading, then click **Initial position** to return the plates to their starting position.

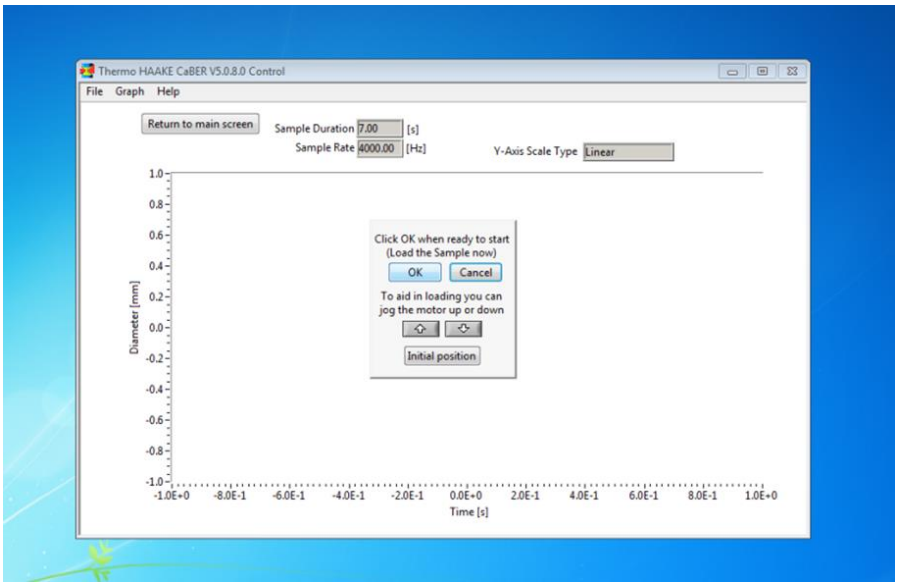


12. Draw up some of your sample into the syringe and wipe off any excess around the outside of the syringe using a Kimwipe. Remove the needle from its protective case and using one hand, place it onto the syringe. Squeeze some of the sample out of the needle for priming purposes.


13. Loading Method 1: Insert the tip of the needle between the two plates and touch the tip of it to the top plate. Gently squeeze out the sample until loaded properly (see the next slide for what the sample should look like when properly loaded).

    Loading Method 2: Jog the top plate motor up and squeeze out enough sample for proper loading (see the next slide for what the sample should look like when properly loaded). Once finished, click on **Initial position**. Knowing the correct amount may take some trial and error.

Loading Method 1 (Less Viscous Samples)

Loading Method 2 (More Viscous Samples)

14. When properly loaded, the sample should be slightly convex from the edges of the plates as indicated on the right. Too little sample may cause early breakup and too much sample may result in fluid droplets flying out of the column and disrupting the measurements from the laser. Sample loading is of the utmost importance in this experiment, and it takes some practice to get the sample loaded correctly.

Bad Sample Loading

Good Sample Loading

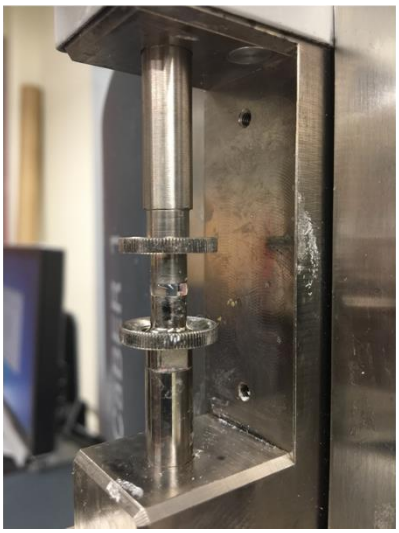

15. When finished loading, click OK. A window will appear that will time the equilibration period before the plates separate.

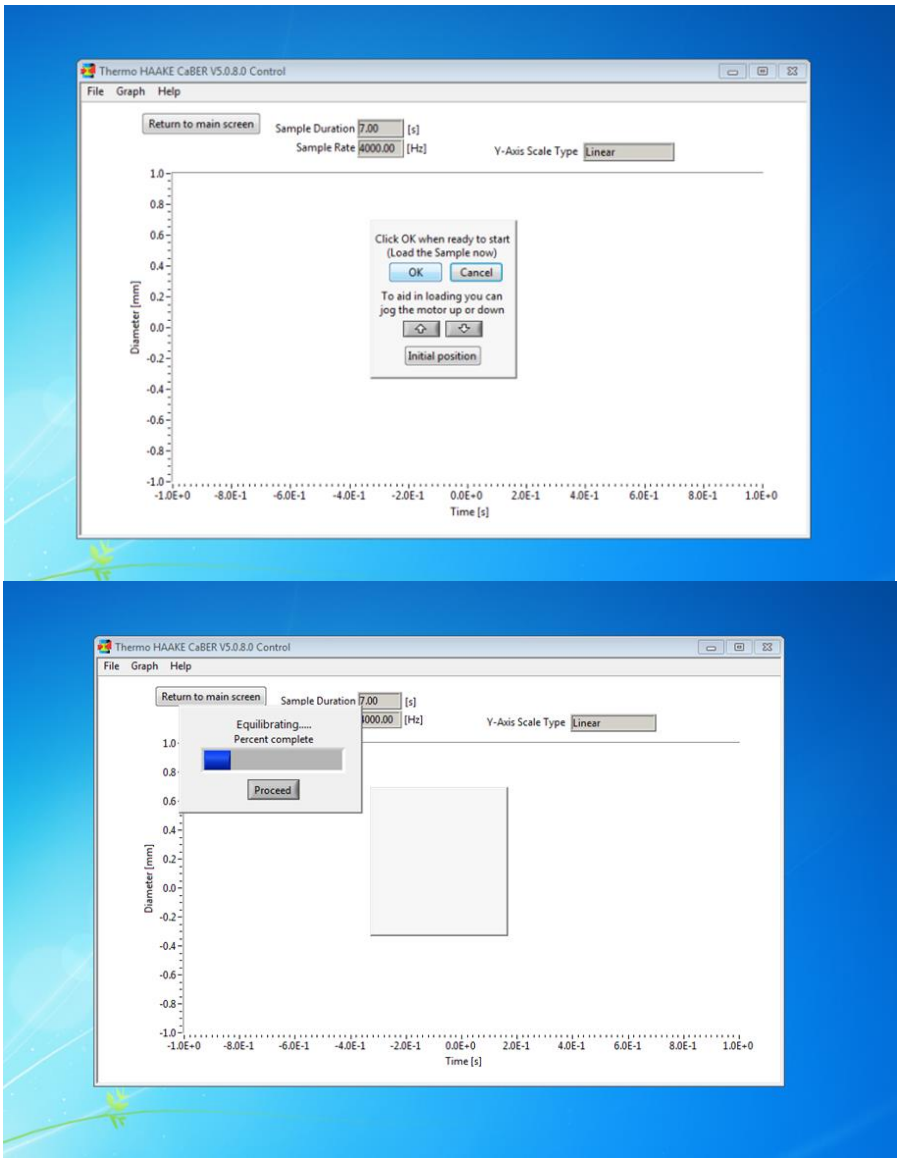


16. Once the plates separate, a separate window will appear with the "WORKING…" indicating that the data is being collected during the experiment. Once finished, two windows will appear. One of them is the plots of diameter vs. time from the experiment, and the other is the File Explorer window. Type in the desired file name and the location where you would like to save the file into the File Explorer window. The file extension, .cbr, is a text file and can be opened in any text-based program or can be imported into Excel.

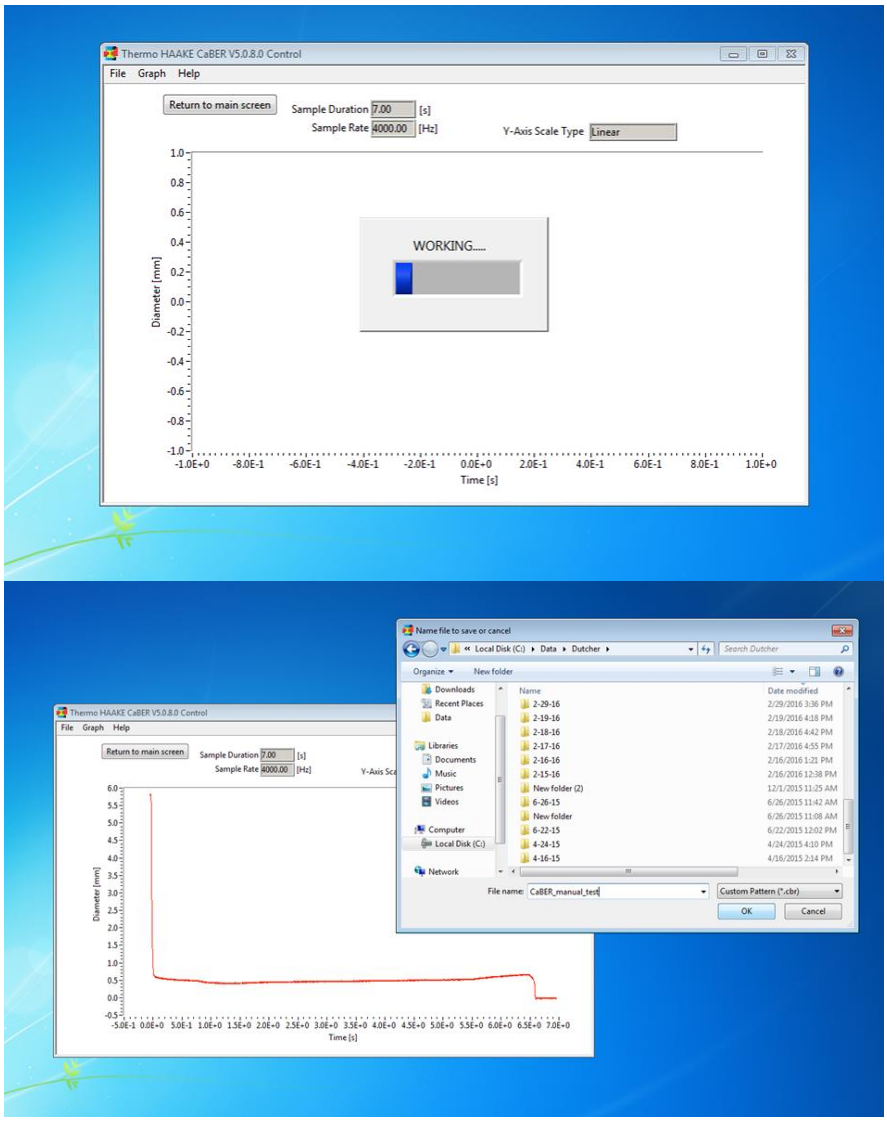


17. Once finished, hover over File and click on Quit.

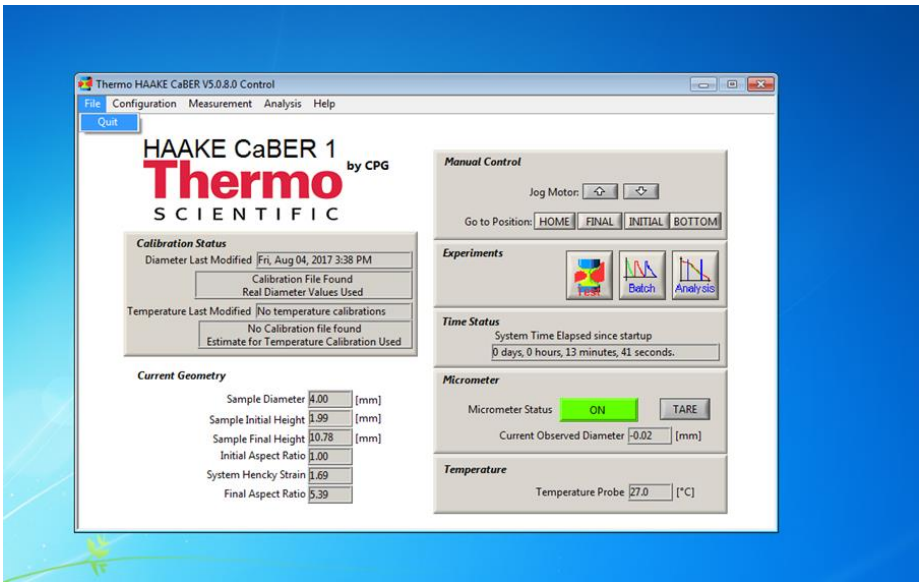


18. Wipe off the excess sample with a Kimwipe. Squirt some DI water onto a Kimwipe and wipe down both the top and bottom plates. If necessary, use acetone or ethanol to clean off the plates.

19. Turn off the laser power supply. Cover the plate holders with the metal sliding barrier when finished. Happy CaBERing!


HAAKE CaBER 1
Thermo

# Appendix D

# Full TC Cell Assembly and Disassembly

## A. Full TC Cell Assembly

1. Grease O-Rings (364 series on bottom cap, 256 series on top cap) and bearings in the cylinder caps.

2. Insert outer glass cylinder into bottom cap carefully. It helps to have two people perform this step.

3. Place the 8 hex key socket head screws securing the bottom cap of the cell to the outer cylinder. Alternate tightening the screws like you are tightening a car tire with a hex screwdriver.

4. Use C-Clamps to secure the bottom of the cylinders to the wooden holder. Be careful not to scratch or hit the glass.

5. Insert foam into the glass outer cylinder. Attach gold thread attachment to the drive shaft of one of the inner cylinders (either the blank inner cylinder or the injection inner cylinder). Screw eyelet into gold threat attachment and hook onto loading crane. Gently lower the inner cylinder into glass outer cylinder. Make sure the bottom hub is secured to the wooden holder before lowering. Push down on the inner cylinder after lowering to ensure the bottom seals.

6. Unscrew eyelet from gold thread attachment. Repeat step 3 with respect to the top cap. Make sure the tension rod screw holes line up across the top and bottom caps.

7. Blow off the cell with compressed air. Attach tension rods and screw in the eyelet to the gold thread attachment. Insert foam sheet around the walls of the Plexiglass container. Lift the cell with the crane and place into the Plexiglass container that is sitting on the holding cart.

8. Remove the tension rods. Remove the eyelet from the gold thread attachment and place the eyelet into the top plate of the cell for later use with the yellow loading straps.

9. Place the taper bearing on the bottom with the washer below it. Screw the hex-nut to the bottom. *Do not forget to apply grease on the threads to assist this process.*

10. Attach adjustable chain-wrench to the hex nut located at the bottom of the cell surrounding the outer cylinder shaft to prevent it from rotating while screwing on the hex-nuts. Position one C-Clamp vertically on the bottom of the nut and tighten the hex-nuts until the washer is just flush with the bottom plate. Insert the small, rectangular shear key into the rectangular groove in the shaft. Insert the lower timing belt pulley and attach it to the spacer with a hex key.

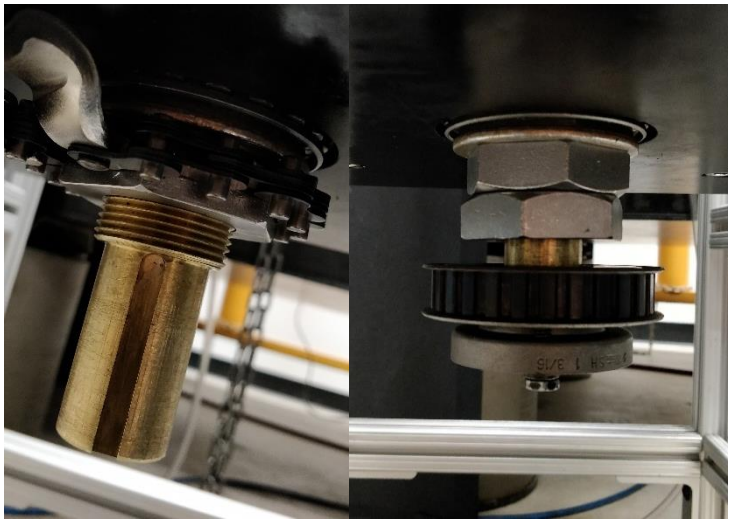

11. Thread yellow loading straps through the eyelets on the top plate, which should be resting on the 8020 support rods. Attach the straps to the loading crane and lift the top plate so that the hole in the center hovers over the assembled cylinders. Slowly lower the top plate.

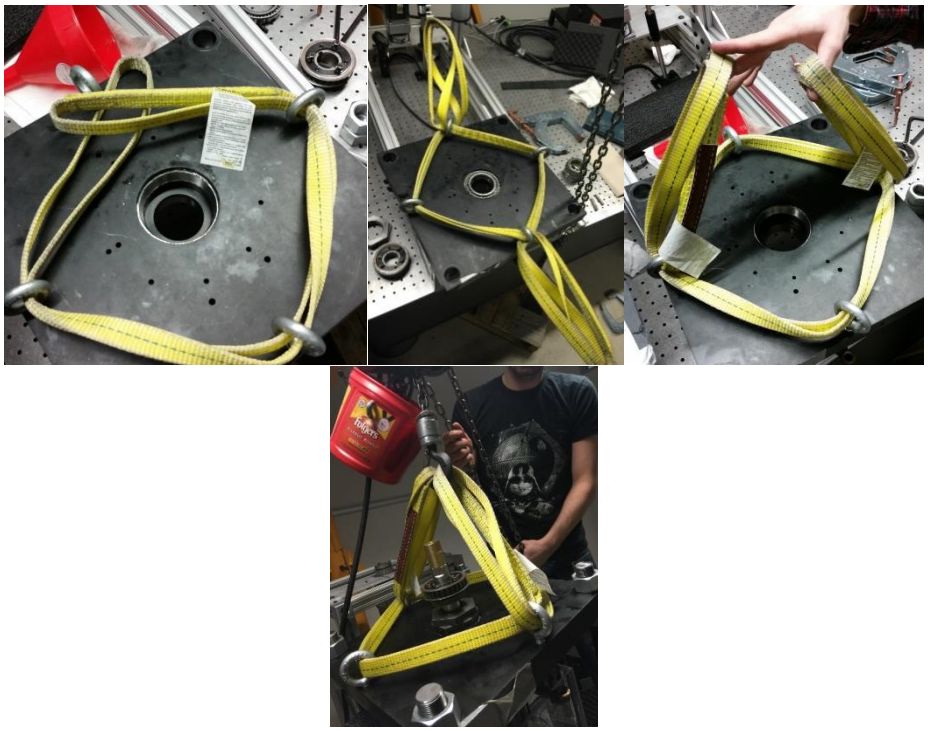

12. While positioning the top plate, make sure the inner cylinder is in center of the outer cylinder to avoid any scratching between them. This can be done by adjusting the four nuts on which it is held. Check with a level to ensure the top plate has not been loaded in a crooked fashion.

13. Tighten down top support nuts around the four corners of the top plate. Screw in the gold thread attachment and screw in an eyelet. Attach the eyelet to loading

crane, *slowly* lift the cell from the cart until it *just* hovers over the 8020 frame. Gently push the apparatus back until it is flush with the rear 8020 frame and lower onto the bottom frame. Screw in place to the black, round-topped screws located outside the lower portion of the 8020 frame.

14. Unscrew the gold thread attachment. Screw on the two hex-nuts on the center shaft to secure the inner cylinder shaft on the top of the cell. Attach C-Clamps to the nuts. Position one C-Clamp horizontally on the bottom nut and one C-Clamp vertically on the top of the nut and tighten. Unthread yellow loading straps from the eyelets.

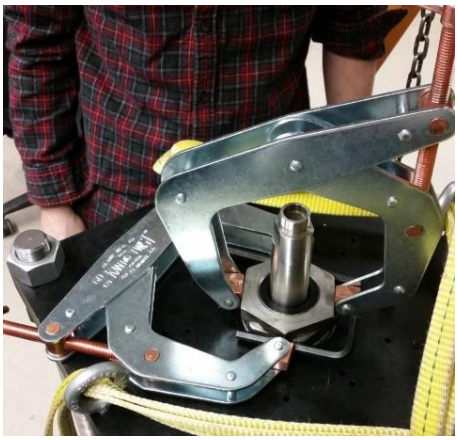

15. Insert the small, rectangular shear key into the rectangular groove in the shaft. The sides with small circles engraved into the surface should face outwards. Insert the upper timing belt pulley and attach it to the spacer with a hex key.

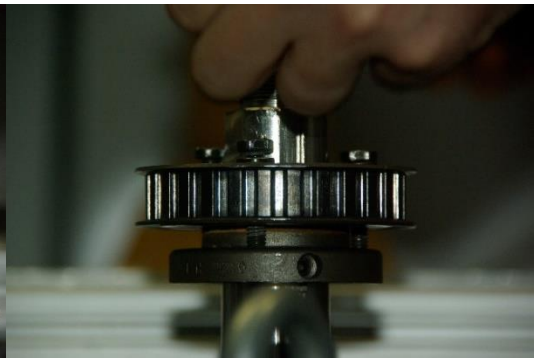

16. Attach and tighten the rubber timing belts to the lower and upper pulleys. Make sure the belts are level using the level. The belts should be tight, but not so tight that they are forcing the inner cylinder to tilt toward the motors.

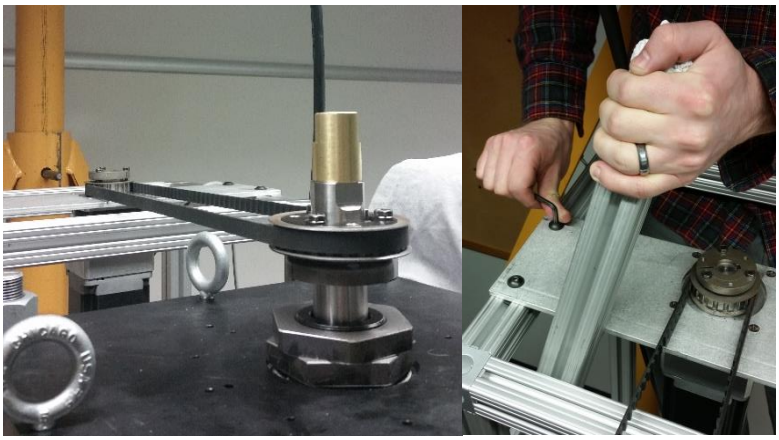

17. If using the injection cylinder, attach the rotary injection tube assembly. Tighten the brass portion with the chain wrench so that it does not loosen during operation.

18. Insert support structure for the rotary injection tube assembly and tighten screws. The support structure consists of two anodized aluminum rectangular plates.

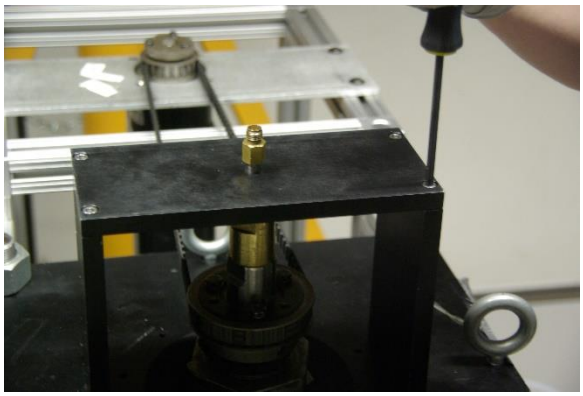

19. Prime injection tubing opening if needed with required fluid. Attach tubing from pressurized fluid reservoirs. Make sure tubing is not bent or tangled.

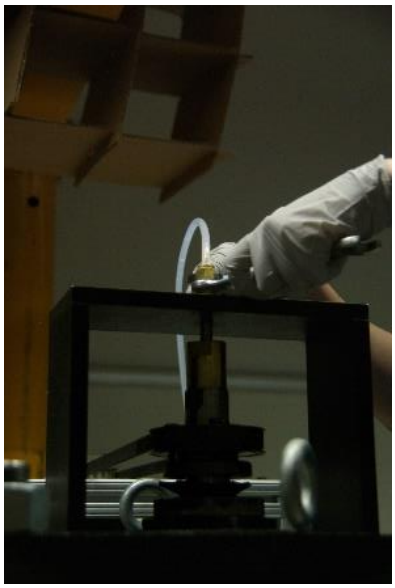

20. Align camera and laser light sheet or flicker-free light as needed, depending on the experiment.

## B. Full Cell Disassembly

1. Drain the paraffin oil in the Plexiglass tank by opening the yellow tabbed valve. Use a sieve while draining the oil back into the oil barrels periodically to filter out hair or particulates. When finished, close the valve. Drain any fluid in the cell annulus.

2. If you had installed the injection support structure and injection tube assembly, uninstall those. If not, proceed to the next step.

3. Thread yellow loading straps through eyelets located on the top of the cell and attach to the loading crane. Remove timing belts from the upper and lower pulleys.

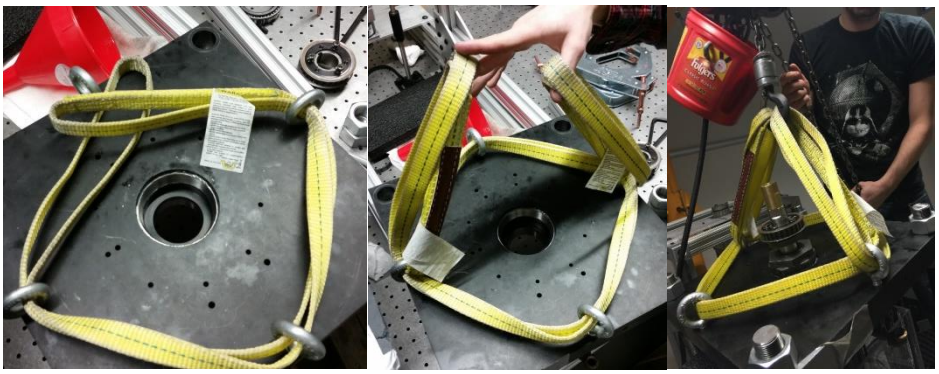

4. Unscrew the round-topped black bolts from both sides of the 8020 frame to detach the cell. Lift the cell from the frame using the crane and move to the holding cart. Screw 2-3 black, round-topped bolts on the sides of the cell to attach it to the holding cart.

5. Unscrew the gold thread attachment and remove upper pulley.

6. Attach C-Clamps to the nuts located at the top of the cell surrounding the inner cylinder shaft. Position one C-Clamp horizontally on the bottom nut and one C-Clamp vertically on the top of the nut and unscrew the nuts.

7. Unscrew the 4 nuts in each corner that attach the top plate of the cell to the support rods.

8. Clip in yellow loading straps to the crane hook. Lift the top plate of the cell and place on 8020 frame. Watch out for trapped liquid and make sure to lift the top off slowly and evenly.

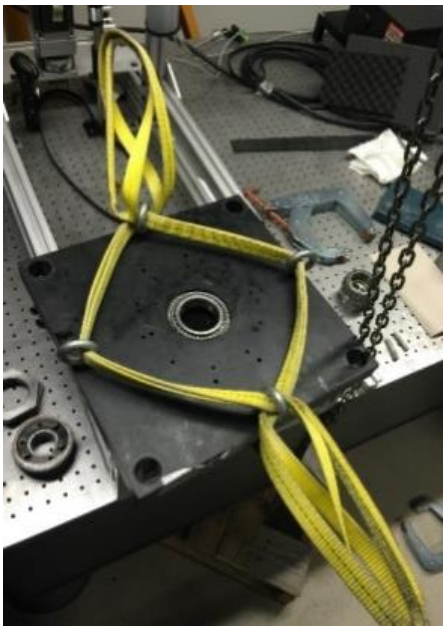

9. Place a drainage bucket under the yellow-tabbed drainage valve. Unscrew the round-topped screws and lift the apparatus such that the plate that houses the round-topped screw farthest away from the drainage valve is resting in the groove of the 8020 on the holding cart. Open the drainage valve. Using a sponge, scrub the inside of the Plexiglass container and outside of the glass cylinder a solution of Micro-90 cleaner (one or two capfuls of Micro-90 for about a gallon's worth of water). Rinse out the container with water. After rinsing, close the valve and empty the drainage bucket. Dry the water off with paper towels.

10. Screw in gold thread attachment to drive shaft, followed by an eyelet. Place foam sheet in Plexiglass container to form a barrier between the Plexiglass and the glass outer cylinder.

11. Attach tension rods to the cylinders. Hook the loading crane through the eyelet and lift the cylinders. Lift, move, and lower the cylinders into the wooden holder. Use C-Clamps to secure the bottom of the cylinders to the wooden holder. Be careful not to scratch or hit the glass outer cylinder. Remove the tension rods and wipe down the cylinders.

12. Unscrew the eyelet from the gold thread attachment. Remove the 8 Allen key socket head screws securing the top cap of the cell to the inner cylinder.

13. Remove the top cap of the cylinders. Rinse the top cap with water and clean it with the Micro-90 solution if needed. Remove the shaft seal and clean the roller bearing. Dry all components. If the bearing is rusty, it will need to be replaced with a new one by the Machine Shop.

14. Keep the C-Clamps attached to the wooden holder. Screw in the eyelet to the gold thread attachment and attach to loading crane. Insert foam in between the inner cylinder and the glass outer cylinder. Carefully lift the inner cylinder out and lower it into a drainage bucket.

15. Scrub the inner cylinder with the Micro 90 solution and rinse with water. Dry the inner cylinder. If the apparatus needs to be used shortly after disassembly, place out of the way until it can be re-assembled. If the apparatus is disassembled and will not be used soon, lower the inner cylinder into an empty bucket. Grasp onto the drive shaft and unscrew the gold thread attachment. Carefully place cylinder into its foam-lined cardboard box on the shelf to the right of the computer terminal.

16. Repeat steps 12 and 13 with respect to the bottom cap and screws (disregard the eyelet/gold thread attachment).

17. Spray some Windex into a paper towel and clean off the inside and outside of the glass cylinder. If the cell will not be used soon, carefully remove the glass outer cylinder by gently wiggling it out of the bottom cap. With another person to help, lift the glass cylinder and place into its bubble-wrap lined box.

18. Clean the bottom cap with water and the Micro-90 solution, if needed. Remove, clean, and dry the shaft seal. Clean and dry the roller bearing and check for rusting. If the bearing is rusted through, it will need to be replaced with a new one by the Machine Shop. For maintenance purposes, the bearings and shaft seals should be replaced once a year.

# Appendix E

# Injection Cylinder and Injection Port Assembly, Disassembly, and Cleaning

## A. Injection Cylinder Assembly

1. Grease O-ring (364 series) on the bottom cap. Carefully slide the outer cover over the drive shaft.

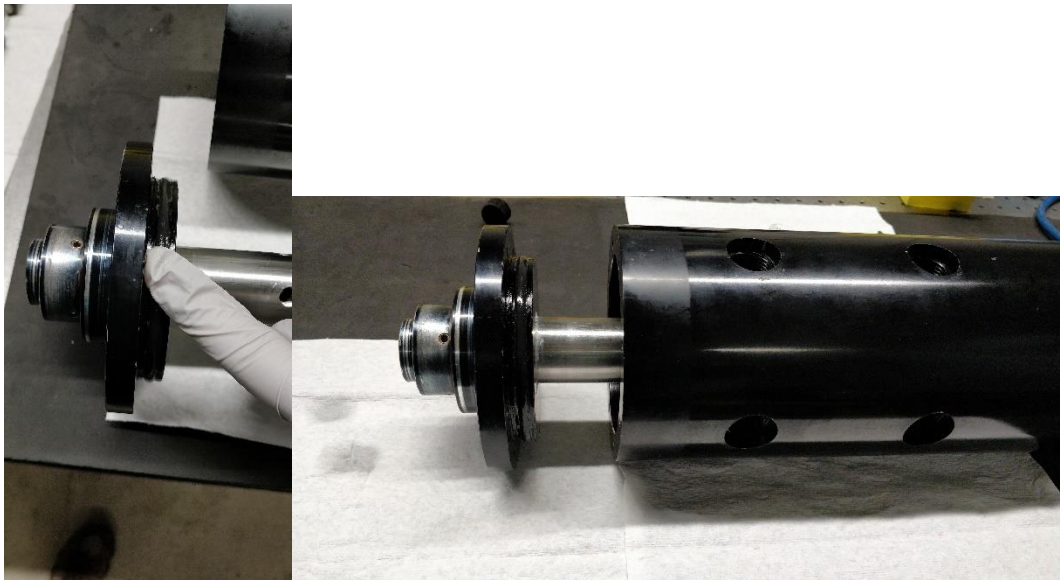

2. Line up screw-holes in bottom cap assembly with those on the outer cover. Carefully lift cell and place into a paper-towel lined bucket. Stabilize drive shaft with a clamp attached to a ring stand with a counterweight (here, the blue water

container). Push down on the top of the outer cover to seal the bottom cap/drive shaft to the outer cover.

3. Carefully lift cylinder back onto the laser table. Place the 8 hex key socket head screws securing the bottom cap of the cell to the outer cover. Alternate tightening the screws like you are tightening a car tire with a hex screwdriver. Tighten the set screws at the top of the cylinder to secure the drive shaft.

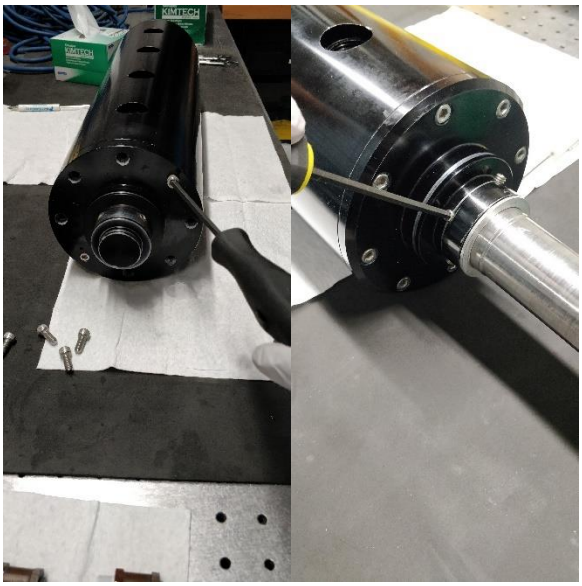

4. Carefully insert the injection ports into their assigned location and screw partway into their respective holes. Each column has an assigned letter (A, B, C, or D), which is engraved into the drive shaft. Each row has an assigned number (1, 2, 3, or 4) where Row 1 is closest the top of the cell and Row 4 is the row closest to the

bottom of the cell. The column and row information (*e.g.*, A1) is engraved into the outer cover of each injection port. It is **critical** that the ports are placed into their proper location for accurate fluid injection.

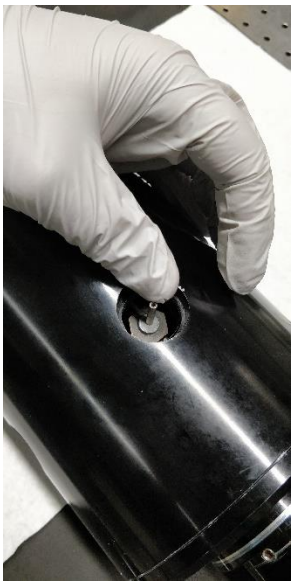

5. Use the socket wrench attachment and the large flathead screwdriver to tighten the injection ports. These need to be as tight as possible to ensure no leaking. Use the four-pronged tool to gently screw in the white plugs. These should only be hand tight. Place black port covers into warm water to help soften them. Attach them to outside of the port making sure the two legs rest in the groove of the white plug.

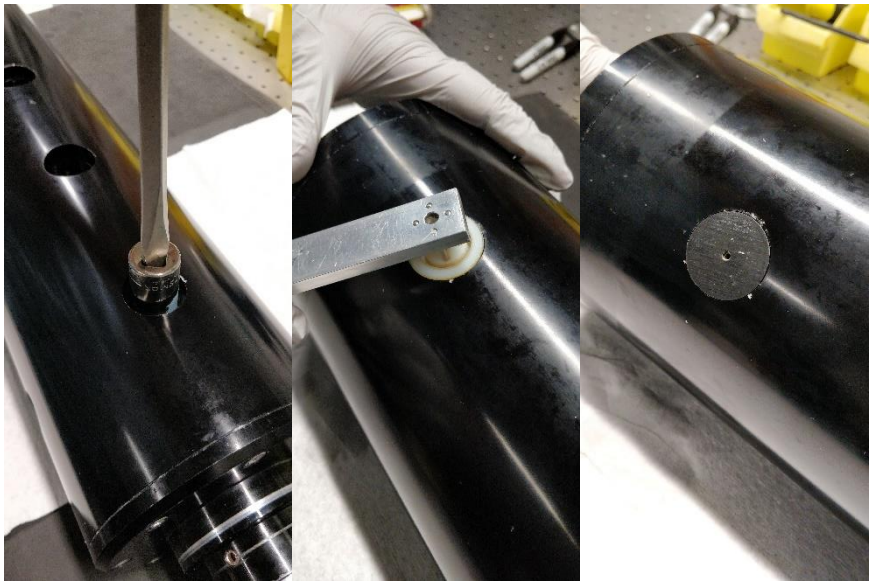

6. If the cell does not need to be used after assembly, store it in its foam-lined box and place on the shelves by the TC cell computer terminal.

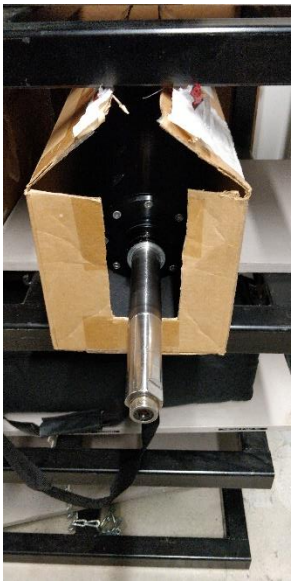

## B. Injection Cylinder Priming and Insertion

1. Carefully place injection cylinder into a bucket and stabilize with a clamp attached to a ring stand with a counterweight. Place a funnel into the drive shaft opening. Pour fluid of choice into the drive shaft until it is just full. Remove funnel. Connect the pressure tubing from the pressurized fluid containers. Using the "Voltage On Demand" LabView code, prime the injection ports by flowing fluid until the fluid emerges from all 16 ports (usually 3-5 times of pumping for 10 s at 30 psi does the trick). Wash the outer surface of the injection cylinder with a Micro-90 solution followed by a rinse with distilled water to remove any fluid on the cover surface. **Be careful to avoid removing the fluid inside the tubes coming from the check valves. This will make subsequent injections no longer accurate with the calibrations.**

2. Insert foam sheet into glass cylinder and lower injection cylinder into the cell. Secure the cell to the wooden holder before lowering. Push down on inner cylinder after lowering to ensure the bottom seals.

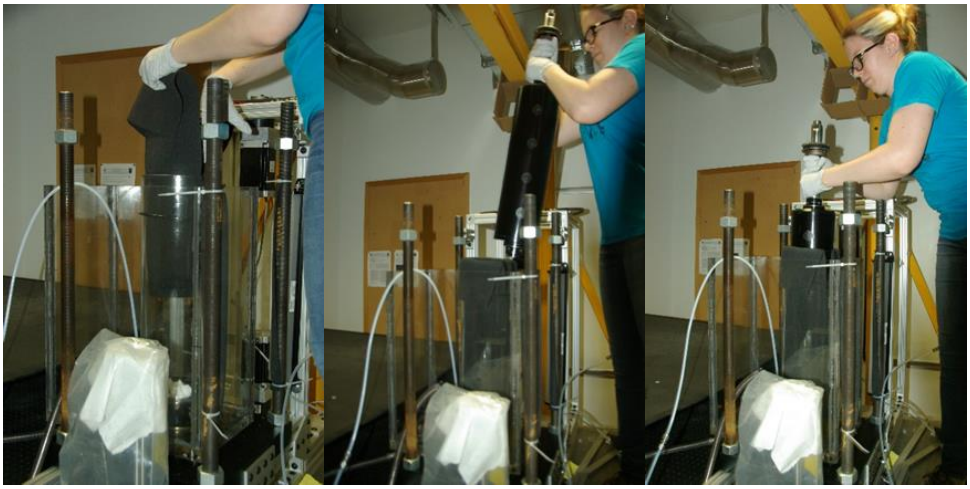

3. Place the top cap onto the glass cylinder and insert the small foam sheets into the sides to prevent damage to the glass if one pushes too hard on the cap upon insertion. Make sure the tension rod screw holes line up across the top and bottom caps. Push top cap in (this requires a bit of force).

4. Attach the Delrin sleeve by sliding it up with the O-ring around the outer cylinder. Secure the sleeve to the top cap with 8 hex-screws. Continue with the normal assembly process described in the Full Assembly/Disassembly manual.

5. The entire TC injection setup is shown below with all the labeled components.

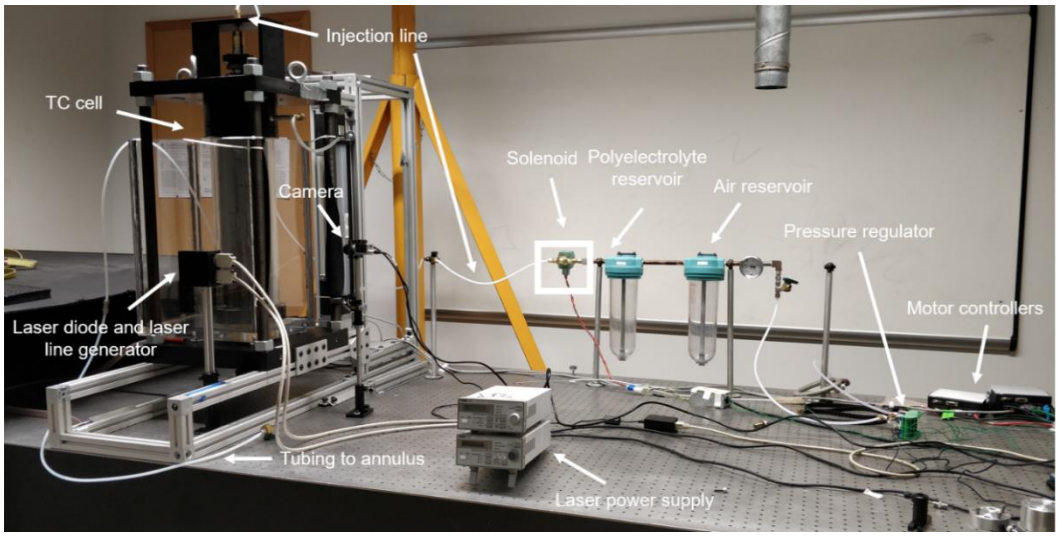


## C. Injection Cylinder Disassembly

1. Continue with normal disassembly of the TC cell apparatus up until the top plate needs to be removed. Remove the top plate as normal, but leave the top plate hanging on the crane and slide over to the side. Perform the reverse of Steps 2-4 in Section B here.

2. To remove the fluid remaining in the injection cylinder, attach it to the pressurized fluid reservoirs as described in Step 1 of Section B. Make sure that both fluid reservoirs are empty and clean prior to this step. Flow air through the injection cylinder until fluid stops coming out of the ports. When finished, remove the injection tubing, and overturn the injection cylinder into the bucket to drain the last of the fluid in the drive shift. If you feel capable enough to do so, you can drain the fluid from the drive shift before attaching to the reservoir to speed the draining process.

3. Prime the injection tubing with distilled water and reattach to the rotary injection assembly. Continuously flow water followed by air through the injection cylinder until only air comes out from the ports.

4. Thoroughly wash the outside of the cylinder with the Micro-90 solution and rinse with distilled water. Lift cylinder onto paper-towel covered foam sheet onto laser table and wipe down with paper towels.

5. Carefully remove black port covers with a small flathead screwdriver. Remove the white plugs using the four-pronged tool.

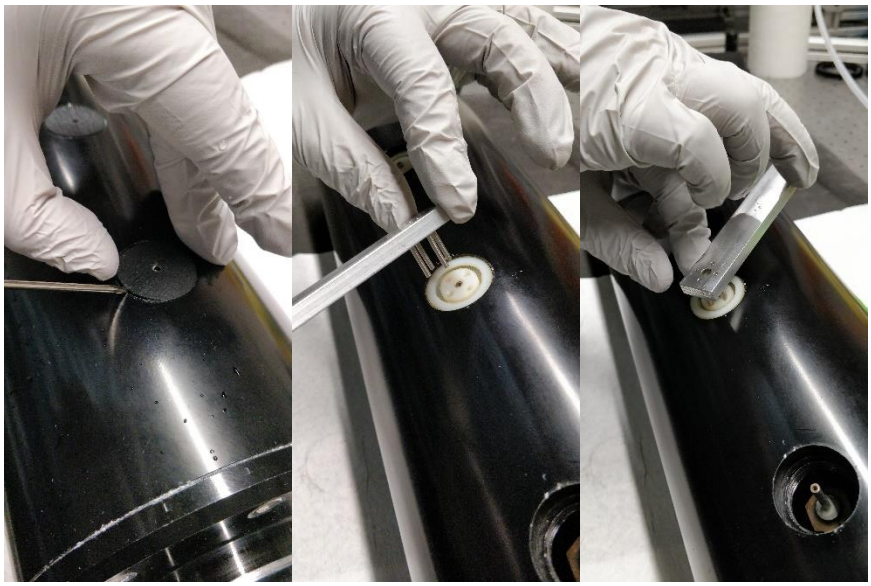

6. Use socket wrench attachment with the large flathead screwdriver to partially unscrew the injection ports. Use your fingers to completely unscrew the ports. Be careful not to let the ports fall into the cavity.

7. Unscrew the 8 hex-screws on the bottom cap. Unscrew set screws where the drive shaft meets the cylinder cover.

8. Use the small flathead screwdriver to pry the seal between the bottom cap and the cylinder cover. Be careful to not scratch the surface of the cylinder.

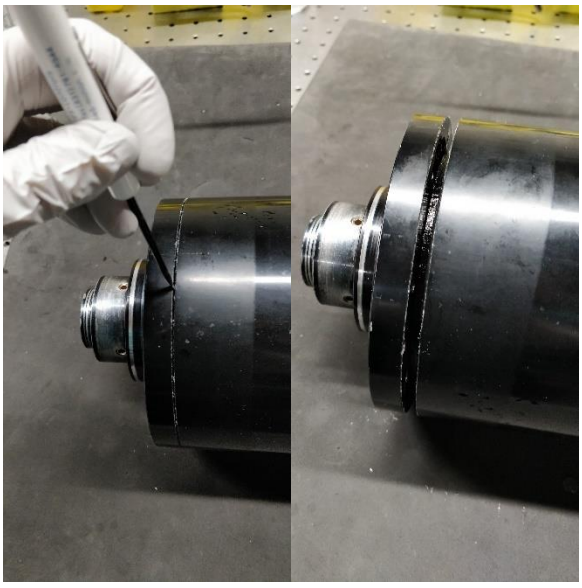

9. With the rubber mallet, hammer the top of the drive shaft to separate the bottom cap/drive shaft from the cylinder cover. You might need another person to hold the cylinder steady while the drive shaft is hammered.

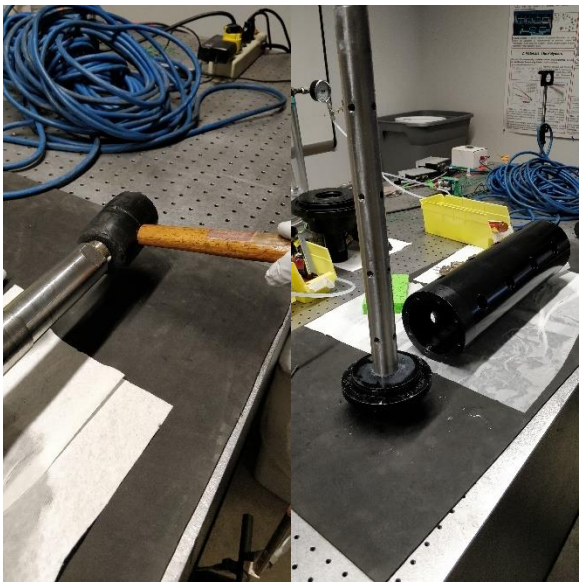

10. Thoroughly scrub the drive shaft/bottom cap assembly and cylinder cover with the Micro-90 solution and rinse with distilled water. Dry with paper towels and place aside to then clean the injection ports.

## D. Injection Port Cleaning Protocol

1. Scrape off the Teflon tape from the injection ports with the wired brush.

2. Remove the injection tubing connected to the pressurized fluid reservoirs while the system is depressurized. Remove the brass Swagelok component.

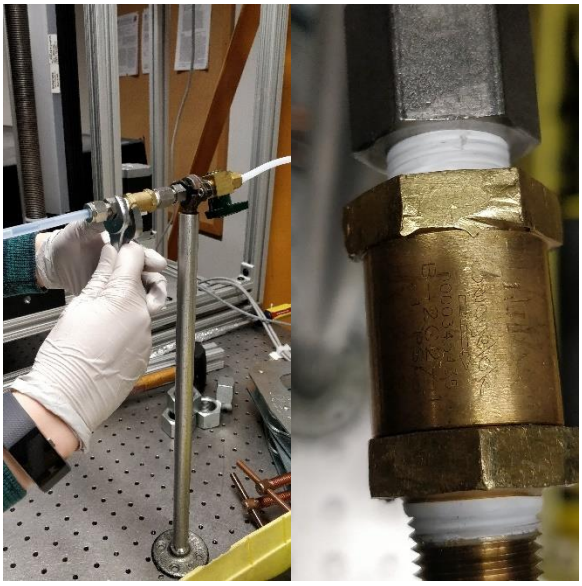

3. Take apart the brass Swagelok component by steadying the fused end with a 5/8 wrench and placing another 5/8 wrench on the removable end slight above in position relative to the wrench on the fused end. Using the palm of your hand, push down on the wrench on the removable end to loosen it. Remove the O-ring, check valve, and spring and clean them with the Micro-90 solution and rinse with water. Dry the components and apply Teflon tape to the screwed ends.

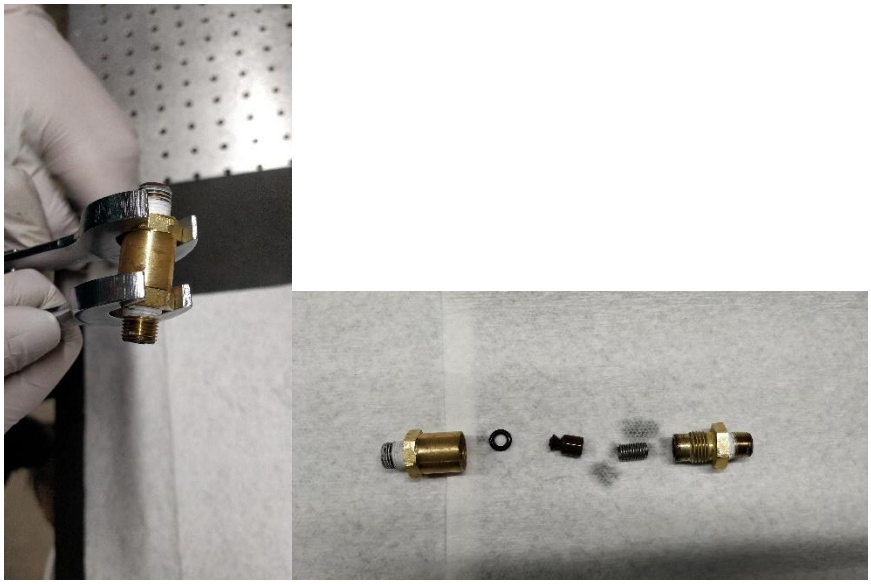

4. Screw component with the smaller opening (the rightmost component in the figure on the right in Step 3) back into the pressured injection tubing assembly. Fill the leftmost fluid reservoir with distilled water and pressurize the system to 30 psi.

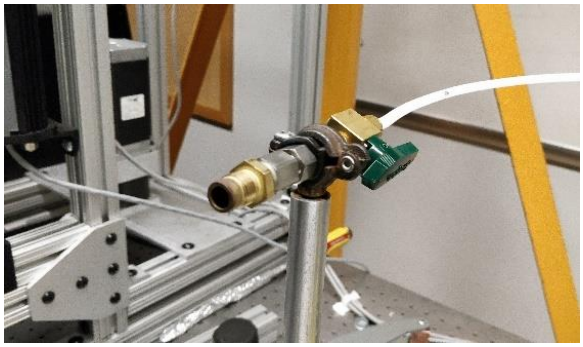

5. Following the same procedure in Step 3, take apart an injection port. **It is critical that you do this and following steps one at a time for each injection port. The check valves and injection components are unique to each port. DO NOT MIX THEM UP as only the outer portion of each port is engraved with its identifying letter-number combination (*e.g.*, A1, A2, etc.).**

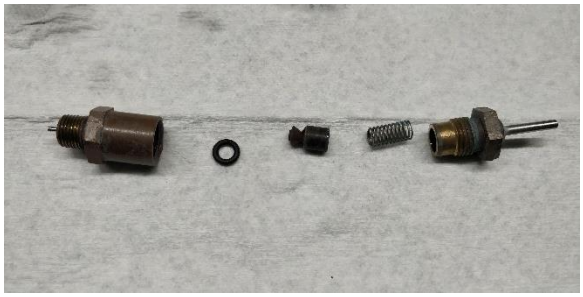

6. Screw in the component of the injection port housing the flow restrictor (the end with the short, skinny metal tube set into the plastic retainer) into the pressurized injection system. Place a beaker underneath and drive water through for 15 s at 30 psi. If the port is clogged, it might take several tries to get water to flow through.

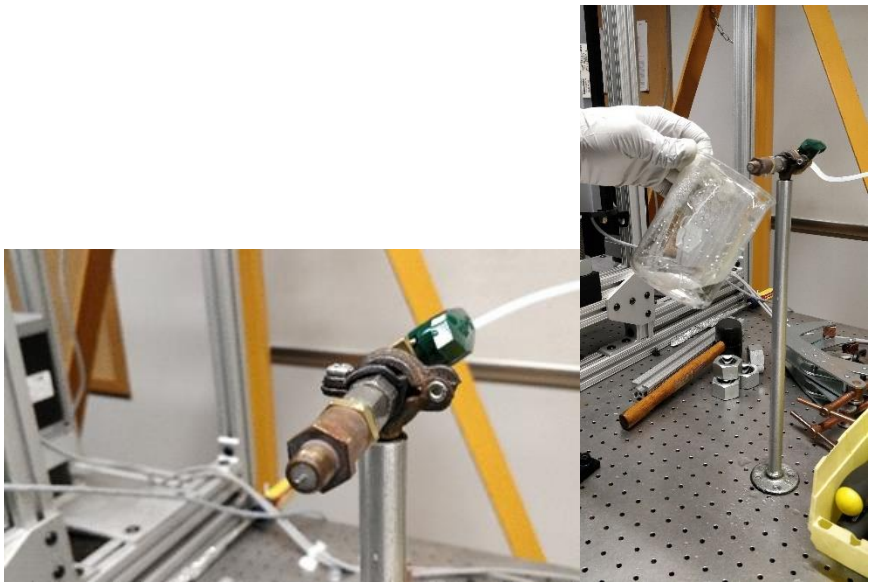

7. When finished, dry off all the port components with a paper towel and reapply Teflon tape to the screwed ends. Put together components in the order shown in the picture below. To tighten the injection port, steady the fused end with a 5/8 wrench and place another 5/8 wrench on the removable end slight below in position relative to the wrench on the fused end. Using the palm of your hand, pull up on the wrench on the removable end to tighten it.

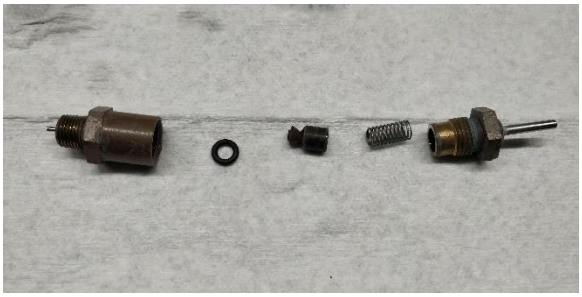

8. Repeat Steps 5-7 for the rest of the injection ports (16 total).

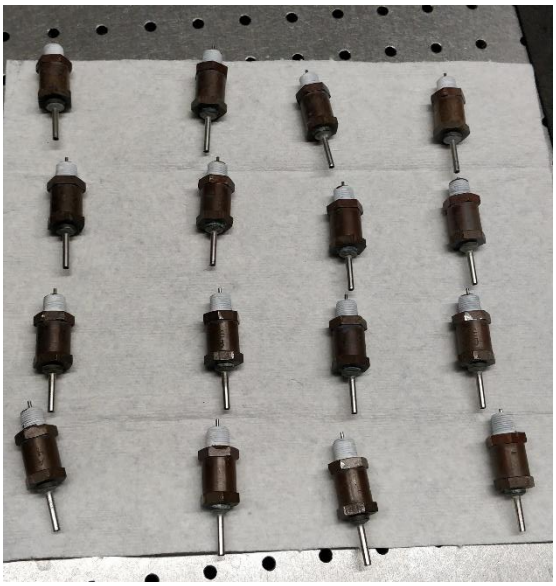

9. Put the brass Swagelok component back together and screw it back into the injection tubing system so that the arrow on the cover faces out away from the fluid reservoirs. Reattach tubing to the Swagelok component.

10. Proceed with injection cylinder assembly described in Section A.

# Appendix F

# TC Cell Maintenance Guidelines

There are several parts that need to be replaced every so often to ensure safe and successful operation of the TC cell. The most critical of these parts are listed below:

1. Drive shaft seal (replace once a year or earlier if it looks rusty)
    a. Product Description:0.394” ID x 0.748” OD TC automotive shaft seal
    b. Catalog Number: 36677177
    c. Supplier: MSC Industrial Supply
2. Top and bottom cap seals (replace once a year or earlier if it looks rusty)
    a. Product Description: Value collection 2-3/4" ID, 7/16" thick, TA, automotive shaft seal 3-3/4" OD, nitrile
    b. Catalog Number: 36680221
    c. Supplier: MSC Industrial Supply
3. Top and bottom ball bearings (replace once a year or earlier if it looks rusty)
    a. Product Description: Precision ball bearing, sealed, number 6210-2RS, for 50 mm shaft diameter
    b. Catalog Number: 6661K112
    c. Supplier: McMaster-Carr